D5.3: REPORT ON MULTI-CONSTELLATION GNSS BASED MULTI-MODE AUGMENTATION TECHNOLOGY RESEARCH

SECURITY: PUBLIC

GREAT
GREENER AIR TRAFFIC OPERATIONS

Lead beneficiary: Nanjing University of Aeronautics and Astronautics (NUAA)

Contractual Due Date: M36

Actual Submission Date:

17/01/20223 (M37)

Grant Agreement number:	875154
Project acronym:	GREAT
Project title:	GREENER AIR TRAFFIC OPERATIONS
Funding scheme:	RIA/H2020
Start date of the project:	January 1st, 2020
Duration:	42 months
Project coordinator (organization):	Michael Finke (DLR)
Phone:	+49 531 295-2921
E-mail:	Michael.Finke@dlr.de
Project website address:	www.project-great.eu

This project has received funding from the European Union's Horizon 2020 research and innovation programme under grant agreement No 875154 GreAT.

DOCUMENT INFORMATION

DOCUMENT NAME	D5.3 Research on multi-constellation GNSS based multi-mode augmentation technology research
VERSION	VF (final version)
VERSION DATE	17/01/2023
AUTHORS	Rui Sun (NUAA), Hanzhi Chen (NUAA), Li Ji (NUAA), Siyu Deng (NUAA), et al.
SECURITY	Public

DOCUMENT APPROVALS

	NAME	ORGANISATION	DATE
COORDINATOR			
WP LEADER			
TASK LEADER	Rui Sun	NUAA	10/12/2022
OTHER (QUALITY)	Jetta Keranen	L-UP	17/12/2023

DOCUMENT HISTORY AND LIST OF AUTHORS

VERSION	DATE	MODIFICATION	NAME (ORGANISATION)
V0.01	15/8/2022	First draft	NUAA
V0.02	02/9/2022	Draft	NUAA
V0.03	26/9/2022	Draft	NUAA
V0.04	16/10/2022	Draft	NUAA
V0.05	1/11/2022	Review and improvements	NUAA
V1.00	10/12/2022	Final version for submission	NUAA
VF	17/12/2023	Quality assessment	L-UP

DISTRIBUTION LIST

FULL NAME OR GROUP
GreAT Consortium EU
GreAT Consortium China
Project Officer
Other

EXECUTIVE SUMMARY

Addressing environmental challenges, especially global warming, is more than ever a must for the community. This matter is becoming an increasing priority at regional and global level. Europe has made commitments to reduce the aviation's environment footprint; hence, it is contributing to climate change, increasing noise, affecting local air quality and consequently affecting the health and quality of life of European citizens. Due to Covid-19, the air traffic is drastically reduced and it is expected that it will need five to ten years to recover to 2019 numbers. This offers the chance to rebuild it greener than before. The air traffic in Europe was growing until 2019 and is expected to continue increasing significantly in the future again in order to cope with the growing demand for mobility and connectivity. A long-term effect on the environment from aviation sector, mainly caused by aircraft noise and exhaust gases (especially CO_2, nitrogen oxides NO_x and methane), make it a clear target for mitigation efforts. The future growth of aviation shall go hand in hand with environment sustainability policies. Therefore, studies and research are being conducted in Europe exploring possible optimization of the aircraft technologies as well as Air Traffic Management operations. Given the close interdependency between flight routing and environment impact, optimization in flight trajectory design and ATC operations are an appropriate means to reduce the emissions in short- and medium-term periods.

The international project "Greener Air Traffic Operations" (GreAT) has been launched in line with this perspective. This project will be conducted in cooperation between Chinese and European partners.

Within this technology document, the multi-constellation GNSS based multi-mode augmentation technology is developed for developing and advancing greener ATM. This is done by proposing a set of GNSS positioning and integrity monitoring algorithm according to navigation performance requirements of G-ATM.

The navigation performance requirements for G-ATM were investigated firstly. Then, a set of GNSS positioning error correction models, including Genetic Algorithm-Back Propagation (GA-BP)-based ionospheric delay prediction model and the Grouped Method of Data Handling (GMDH)-based tropospheric delay prediction model, was proposed to satisfy the accuracy requirement of G-ATM. As for the integrity requirement of G-ATM, a set of Fault Detection and Exclusion (FDE) algorithms, including double detectors based FDE and adaptive noise variance based FDE was proposed. Besides, a multiple-variable and multiple-constraint gradient descent learning based integrity risk and continuity risk allocation strategy was proposed to optimize protection level calculation. In the experiments, the proposed technology provided great accuracy and reliability improvements of GNSS positioning. It is very beneficial for efficient air traffic management and greener air traffic.

TABLE OF CONTENTS

LIST OF FIGURES

GLOSSARY

Acronym	Signification
ARAIM	Advanced Receiver Autonomous Integrity Monitoring
BDS	BeiDou Navigation Satellite System
CODE	Center for Orbit Determination in Europe
DOP	Dilution of Precision
ESA	European Space Agency
EU	European Union
FDE	Fault Detection and Exclusion
GA-BP	Genetic Algorithm – Back Propagation
GALILEO	Galileo satellite navigation system
G-ATM	green air traffic management
GIM	Global Ionosphere Map
GLONASS	GLObal NAvigation Satellite System
GMDH	Group Method of Data Handling
GNSS	Global Navigation Satellite System
GPS	Global Positioning System
IGS	International GNSS Service, IGS
IMU	Inertial Measurement Unit
LOS	Line-of-Sight
PNT	Positioning, Navigation and Timing
MI	Multipath Interference
NLOS	Non-Line-of-Sight
RAIM	Receiver Autonomous Integrity Monitoring
ZTD	Zenith Tropospheric Delay
ARAIM	Advanced Receiver Autonomous Integrity Monitoring
BDS	BeiDou Navigation Satellite System
CODE	Center for Orbit Determination in Europe
DOP	Dilution of Precision

ESA	European Space Agency
EU	European Union
FDE	Fault Detection and Exclusion
GA-BP	Genetic Algorithm – Back Propagation
GALILEO	Galileo satellite navigation system
G-ATM	green air traffic management
GIM	Global Ionosphere Map
GLONASS	GLObal NAvigation Satellite System
GMDH	Group Method of Data Handling
GNSS	Global Navigation Satellite System
GPS	Global Positioning System
IGS	International GNSS Service, IGS
IMU	Inertial Measurement Unit
LOS	Line-of-Sight
PNT	Positioning, Navigation and Timing
MI	Multipath Interference
NLOS	Non-Line-of-Sight
RAIM	Receiver Autonomous Integrity Monitoring
ZTD	Zenith Tropospheric Delay

1. INTRODUCTION

With the development of economic globalization, the communication between China and European countries becomes more and more frequent. However, the rapidly growing flights not only increase the pressure on air traffic management, but also cause great challenges to global environmental protection due to the emission of harmful or greenhouse gases. The Positioning, Navigation and Timing (PNT) technology is critical for green air traffic management (G-ATM). Global Navigation Satellite System (GNSS) is able to provide constant PNT service worldwide with low cost and high accuracy [Groves 2015]. In civil aviation, GNSS is the main PNT source for air traffic management (ATM), Performance-Based Navigation (PBN) [ICAO 2008], Automatic Dependent Surveillance-Broadcast (ADS-B) [Manesh 2017] and et al. As internationally acknowledged GNSS, BeiDou Navigation Satellite System (BDS) of China and Galileo satellite navigation system of Europe can be coupled to obtain greater navigation performance than single system [Odolinski 2015]. Hence, the integrated BDS/Galileo is expected to play a more important role in future civil navigation.

GNSS signals, however, would be contaminated by errors including tropospheric error, ionosphere error and multipath error due to the environmental interference. Those errors, especially mutipath error, seriously degrade accuracy and reliability of GNSS, which reduces efficiency of air trafic operations, and even threatens safety of flights. To deal with GNSS errors in measurenment domain, there are generally error modelling method and Receiver Autonomous Integrity Monitoring (RAIM). The GNSS error modelling method is knowledge driven or data driven. The knowledge driven GNSS error model, which is based on physical principle of specific error, has strong appliabilty but low accuracy [Wang 2016]. The data driven GNSS error model, which is constructed by training machine learning or deep learning model with a great amount of data, provided obvious accuracy improvement in tests. But it is generally difficult to be applied in other scenarios and demands large calculation comsumption [Chen 2011]. As for RAIM, it usually detects and excludes measurements with unacceptable errors by consistency checking. RAIM also involves protection level calculation to envelope positioning errors for GNSS integrity monitoring [Zhu 2018]. Traditional RAIM is based on single fault hypothesis, so it is only effective in single fault scenario [Lee 1986; Parkinson 1988; Sturza 1988]. With the development of multi-constellation GNSS, multiple hypothesis solutions separation (MHSS) based Advanced Receiver Autonomous Integrity Monitoring (ARAIM) was proposed to handle with simultaneous multiple faults [Blanch 2012]. Nevertheless, complex and massive computation are required to implement ARAIM. Besides, ARAIM has only been validated in simulated experiments.

Therefore, to satisfy navigation and positioning requirement for future civil aviation, it is necessary to develop muti-constellation GNSS based multi-mode augmentation technology. This subproject firstly figured out the navigation performance requirement of G-ATM. Then the high-accuracy GNSS error models were constructed. In addition, the GNSS integrity algorithms including highly reliable fault detection and exclusion algorithm and optimized protection level calculation model were proposed. The research of this subproject greatly improves GNSS navigation performance in all stages of flights, which means great contribution to greener air traffic operation.

1.1. PURPOSE OF THE DOCUMENT

The purpose of this document is to describe the research on multi-constellation GNSS based multi-mode augmentation technology, including navigation performance requirement of G-ATM, high-accuracy GNSS error models and high-reliability GNSS

integrity algorithm. These models and algorithm will lead to high-performance GNSS navigation and positioning system for G-ATM.

1.2. SCOPE

The document will present new GNSS augmentation technology. The requirements of navigation performance for G-ATM was investigated and clarified. GNSS error sources were modeled to support the accuracy requirement of navigation system for G-ATM. And the integrity algorithm was developed to support the integrity requirement of navigation system for G-ATM.

1.3. INTENDED READERSHIP

This section describes the intended audience for this document. In general, readers of this document can be:

1) Readers internal to the project, using this document as input for their own activities.
2) Readers of GreAT sister projects (ACACIA, CLIMOP, ALTERNATE), using to follow latest developments and approaches, and to drive scientific exchange between the sister projects. This is for aligning the activities of all four projects and identifying synergy effects. Finally, this document can also serve as reference for scientific publications.
3) Readers from the GreAT Advisory board, in order to provide input and to follow the developments from a stakeholder point of view.
4) Readers involved in current and future projects dealing with reducing the impact of aviation on climate change and other environmental parameters, especially to build upon the approaches described in this document; and to align other developments (e.g. modifications to aircraft propulsion and airframe) with it.
5) Readers from air navigation service providers or other stakeholders not involved in the project but effected from its developments (especially airports, airlines or ATC equipment providers).
6) Standardization bodies and regulating authorities and organizations like ICAO, EASA, EUROCONTROL or CAAC.
7) All other interested members of aviation community.

1.4. STRUCTURE OF THE DOCUMENT

This document contains the following sections:

Chapter 1 Introduction – describes the purpose and scope of the document, the intended audience and the document structure.

Chapter 2 Fundamental GNSS Theory – describes fundamental theory of GNSS involved in this subproject.

Chapter 3 Navigation Performance Requirements of G-ATM – introduces required navigation performance mainly including accuracy and integrity requirements of G-ATM.

Chapter 4 Multi-constellation GNSS Error Model for G-ATM – describes the proposed high-accuracy ionospheric error model, tropospheric error model and multipath error model.

Chapter 5 Multi-constellation GNSS Fault Detection and Exclusion model for G-ATM – describes the proposed double detectors based FDE and adaptive noise variance based FDE.

Chapter 6 High-accuracy Multi-constellation GNSS Positioning Model for G-ATM– describes the data-driven multi-constellation GNSS positioning model.

Chapter 7 Multi-constellation GNSS Protection Level Calculation Model for G-ATM - describes the optimized GNSS protection level calculation algorithm.

Chapter 8 Summary – brief summary of the document content.

Chapter 9 References – contains the references.

2. FUNDAMENTAL GNSS THEORY

In a broad sense, GNSS includes all navigation satellite systems that achieve global coverage and only regional coverage, and in a narrow sense, only satellite systems that achieve global coverage. The current navigation systems for global coverage are Chinese BDS, American GPS, Russian GLONASS and EU Galileo, and only regional coverage are Japanese QZSS (quasi-ceiling satellite system) and Indian IRNSS (India). This report studies the GNSS in the narrow sense. This chapter mainly introduces the basic theory of GNSS.

2.1. GNSS CONSTELLATION

The GNSS constellation consists of the constellations of each subsystem, and the basic situation is shown in Table 2-1.

Table 2-1: Basic information of the GNSS constellations.

Constellation characteristics	GPS	GLONASS	Galileo	BDS
Number of mid-orbit satellites	21+3*	21+3*	27+3*	24+3*
Near-circular orbit radius / m	26560623.7	25489581.7	29378137	27899000
Number of track planes	6	3	3	3
Track plane inclination / °	55	64.8	56	55
The crossing point of adjacent track ascensional difference / °	60	120	120	120
Identical orbital plane satellite latitude difference / °	90	45	36	40

Note: The number in the number of medium-orbit satellites by * indicates the number of alternate satellites.

It should be noted that unlike GPS, GLONASS, and Galileo constellation completely composed of mid-orbit satellites, BDS constellation, in addition to 27 mid-round orbit satellites (three are standby), includes five geostationary orbit satellites (east longitude 58.75°, 80°, 110.5°, 140° and 160°, 35786km) and three inclined geostationary orbit satellites (orbital inclination 55°, phase difference 120°).

2.2. GNSS MULTIPLE FREQUENCIES

The GNSS is a multi-frequency and multimode system, can provide users with multi-system, multi-type, multi-frequency signals, It significantly increases the number of satellite and ranging signals that the user can observe, While the precision attenuation factor decreases, Users thus obtain a much richer observational data, Under the single

satellite navigation and positioning system, the number of visible stars is insufficient for some reasons, and the satellite navigation system fails, The probability of not achieving positioning is therefore reduced; Users can flexibly process GNSS multi-frequency multi-mode observation data, For example, the observations can be combined to fix the ambiguity and detect multi-frequency cycle Slips, To achieve the purpose of eliminating the error, improving the accuracy, reducing the convergence time and speeding up the positioning speed.

The types of GNSS satellite launch carriers and corresponding frequencies are shown in Table 2-2.

Table 2-2: GNSS multiple frequencies.

The carrier type	GPS			Galileo			BDS		
	L1	L2	L5	E1	E5a	E5b	B1I	B2a	B2b
frequency (MHz)	1575.42	1227.6	1176.45	1575.42	1176.45	1207.14	1561.098	1176.45	1207.1
The carrier type	GLONASS								
	G1			G2					
frequency (MHz)	$(f_1)_i = 1602.5265 + (i-1)\times 0.5625$ $(i = -7,-6,\cdots,6)$			$(f_2)_i = 1246.4375 + (i-1)\times 0.4375$ $(i = -7,-6\cdots,6)$					

2.3. GNSS TIME SYSTEM

Using the satellite navigation system to realize the positioning of the ground user only needs to determine the location of the instantly visible satellite and the distance between the satellite and the ground user, but it is not easy to accurately obtain these data. The data in the following example illustrate the importance of accurate measurement time: navigation satellites are running in orbit at high speed. For example, GPS satellites are running at about 3.9 km/s, and the observation time error of $1\,\mu s$ will cause a 3.9mm satellite position error. The carrier signal propagates in space at speeds close to the speed of light, and if the ranging error is to be controlled within 300m, the signal propagation time measurement error should be less than $1\,\mu s$. Because of this, GNSS must establish a time system with high precision and high stability. The coordinated UTC adopts the definition of seconds of an atomic clock with high stability and high accuracy, and is associated with the Earth's rotation. GPS, GLONASS, Galileo and BDS all established their own reference time systems on the basis of UTC, using GNSS multiple systems for navigation and positioning must consider the interaction between the various time systems.

2.3.1. GNSS TIME

GPS, GLONASS, Galileo, and BDS all established an internal reference time system based on TC UTC, namely GPST, GLST, GST, and BDT. The following is a brief description of the reference time systems and their conversion relationship to the coordinating world UTC.

(1) Reference time system for the GPS, GPST
GPST time changes continuously, no leap seconds, from UTC (USNO) 0:0 seconds on January 6,19800:0 minutes 0 seconds, take the same seconds when the international

atoms, with the number of weeks and the number of seconds from Sunday 0:0 minutes 0 seconds to describe the time calendar, reach 1024 weeks after the timing. The conversion relationship between GPST and UTC is:

$$GPST = UTC(USNO) + t_1 - t_2 = UTC - t_3 + t_1 - t_2 \quad \textbf{(2-1)}$$

Where, t1Is the integer second difference between the UTC time maintained by the UTC (GPST and the USNO); t2Is the second difference between GPST and UTC (USNO); t3Is the second difference between UTC and UTC (USNO).

(2) GLONASS reference time system GLST
GLST belongs to a non-continuous time system with jumping seconds. The UTC (SU) takes 0:0:0 seconds on January 1,1996 as the starting time, taking the same seconds of the international atomic time, the cumulative day of the above leap year and the daily number of seconds describe the time calendar. The conversion relationship between GLST and UTC is:

$$GLST = UTC(SU) + 3h - t_1' = UTC - t_2' + 3h - t_1' \quad \textbf{(2-2)}$$

Where, t_1' is GLST and UTC (SU); t_2' is the second difference between UTC and UTC (SU).

(3) Galileo reference time system GST
In order to improve its interoperability and compatibility with GPS system, its reference time system, GST, adopts the same starting time, second length, and time calendar description as GPST, which is also a continuous time system without skipping seconds. The difference is that GST starts timing at 4096 weeks. The conversion relationship between GST and UTC is:

$$GST = UTC + t_1 - \Delta t'' \quad \textbf{(2-3)}$$

Where, t_1 is the integer second difference between GST and UTC, the same as that in equation (4-1); $\Delta t''$ is the second difference between UTC and GST.

(1) BDS Reference Time System BDT
BDT belongs to a continuous time system, from UTC (NTSC) 2006 January 1,0:0:00 seconds, take the second length and epoch consistent with GPST description. The conversion relationship between BDT and UTC is:

$$BDT = UTC(NTSC) + t_1''' - t_2''' = UTC - t_3''' + t_1''' - t_2'''BDT = UTC \quad \textbf{(2-4)}$$

Where, t_1''' is the integer second difference between BDT and UTC (NSTC); t_2''' is the second difference between BDT and UTC (NSTC); t_3''' is the second difference between UTC (NSTC) and UTC.

2.3.2. TRANSFORMATION BETWEEN GNSS TIME SYSTEMS

In order to achieve compatibility and interoperability between the GNSS subsystems, the conversion between different navigation satellite systems must be considered. The time systems established by each GNSS system are all related to the coordinated UTC, and the conversion relationship between the various satellite navigation systems can be obtained.

The conversion relationship between GPST and GLST is:

$$GPST - GLST = t_1 - 3h - \Delta t + \Delta t' \quad \textbf{(2-5)}$$

The conversion relationship between GPST and GST is the following:

$$GPST - GST = \Delta t'' - \Delta t \quad \textbf{(2-6)}$$

The conversion relationship between GPST and BDT is the following:

$$GPST - BDT = t_1 - t_1''' - \Delta t + \Delta t''' \quad (2\text{-}7)$$

The conversion relationship between GLST and GST is the following:

$$GLST - GST = 3h - t_1 - \Delta t' + \Delta t'' \quad (2\text{-}8)$$

The conversion relationship between GLST and BDT is the following:

$$GLST - BDT = 3h - t_1''' - \Delta t' + \Delta t''' \quad (2\text{-}9)$$

The conversion relationship between GST and BDT is the following:

$$GST - BDT = t_1 - t_1''' - \Delta t'' + \Delta t''' \quad (2\text{-}10)$$

The time difference between GPST, GLST, GST and BDT can be divided into second difference and integer second difference, and the second difference can be released from the relevant timing center or broadcast by the satellite navigation messages. The integer second difference will only change when it is adjusted in the navigation system.

2.4. GNSS COORDINATE SYSTEM

In the GNSS system, different objects have different requirements under different scenarios for coordinate systems. In order to facilitate the description of the spatial position and motion rules of objects, different coordinate systems are defined according to the actual requirements, and the position of the same object also needs to be transformed between different coordinate systems. This section describes the Earth reference model and the general coordinate system built based on the Earth reference model, and gives the conversion relationship between the general coordinate systems.

2.4.1. EARTH ELLIPTICAL MODEL

The Earth ellipsoid model is described by the long half axis a, the short half axis b, the flat rate f, the first eccentricity e, and the second eccentricity e', and the relationship between them is

$$f = \frac{a-b}{a}, e = \frac{\sqrt{a^2-b^2}}{a}, e' = \frac{\sqrt{a^2-b^2}}{b} \quad (2\text{-}11)$$

The ellipsoid reference models and related parameters used by GPS, GLONASS, Galileo, and BDS are shown in Table 2-3.

Table 2-3: Earth ellipsoid parameters of GNSS.

GNSS system	Elliptic reference model	Major semiaxis a/m	Oblatenes f	Geocentric gravitational constant $GM/m^3 \cdot s^{-2}$	Rotational-angular velocity of the earth $\omega/rad \cdot s^{-1}$
GPS	WGS-84	6378137	1/298.257 223 563	3 986 005.0×108	7 292 115.0×10-11
GLONASS	PZ-90	6378136	1/292.578 393 03	3 986 004.4×108	7 292 115.0×10-11

Galileo	ITRF96	6378137	1/298.257 222 101	3 986 004.418×108	7 292 115.0×10-11
BDS	CGCS2000	6378137	1/298.257 222 101	3 986 004.418×108	7 292 115.0×10-11

2.4.2. COMMON COORDINATE SYSTEMS

(1) Earth-Centered-Inertial (ECI) coordinate system

The ECI coordinate system does not rotate relative to the earth's rotation. It can study the motion law of satellites under the ECI coordinate system.

(2) Earth-Centered,Earth-Fixed (ECEF) coordinate system

Due to the rotation of the earth, the inertial coordinates of the center point on the earth will change continuously over time. In order to describe the position of the point on the earth, The ECEF coordinate system is defined as rotating around the Z-axis with respect to the Earth's rotation, i.e., the ECEF coordinate system is stationary with respect to the Earth.

(3) Local coordinate system

In order to facilitate the description of the motion law of objects in local areas, the local coordinate system is defined, such as the North East Up (ENU) coordinate system, which can take any point of the earth's surface as the coordinate origin. The above three common coordinate systems all belong to the right-handed Cartesian coordinate system.

Table 2-4: Common right-handed Cartesian coordinate systems

Coordinate system types	ECI	ECEF	Local coordinate system (ENU)
Origin of coordinate	Center of the earth	Center of the earth	Any point on the earth's surface
X axis points to	J2000.0 Spring Equinox	Average Greenwich Meridian	east
Z axis points to	International Agreement Origin (CIO)	The Z-axis is perpendicular to the equatorial plane pointing to the geographic Arctic	The zenith direction

(4) Geocentric geodetic coordinate system

The geocentric geodetic coordinate system represents the position of the ground point by the longitude, latitude and height of the earth. It is a coordinate system that represents the position of the point on the earth's surface by the spherical angle and normal distance of the object relative to the Earth reference model.

2.4.3. TRANSFORMATION BETWEEN COORDINATE SYSTEMS

GNSS system simulations and observational data processing often involve transformations between different coordinate systems. This section first introduces the transformation

formula between the right-hand Cartesian coordinate system with different origin and not parallel coordinate axis, which is applicable to the transformation between the ECI coordinate system, ECEF coordinate system and local coordinate system, and then introduces the transformation between the ECEF coordinate system and geocentric geodetic coordinate system.

(1) Conversion between the right-hand Cartesian coordinate systems

As shown in Figure 2-1, coordinate system 1 (XYZ) and coordinate system 2 $(X_1Y_1Z_1)$ are right-hand Cartesian coordinate system with different origin and axes are not parallel. Suppose that the coordinate system 2 is rotated around the axis X_1 , Angle α , around, axis rotation, corner, around, axis rotation Angle (positive counterclockwise from the yearning origin direction of the coordinate axis), the resulting axes of the coordinate system 3 are parallel to each axis of the coordinate system 1.

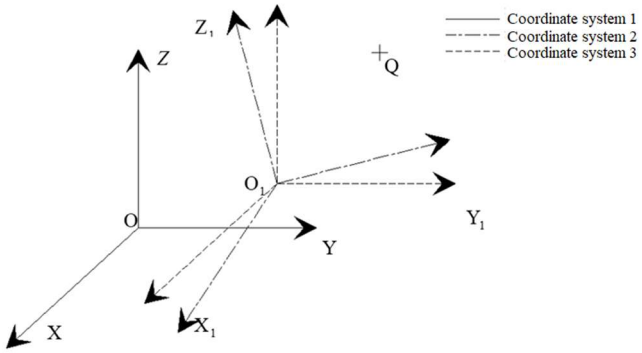

Figure 2-1: Transformation between right-hand cartesian coordinate systems

If the coordinate of a point Q in space in the coordinate system 2 is $(X_1Y_1Z_1)$

$$Q = \begin{bmatrix} x_0 \\ y_0 \\ z_0 \end{bmatrix} \tag{2-12}$$

Considering that the coordinate system 2 rotates the coordinate system 3, the coordinate of the Q point in the coordinate system 3 is Q'

$$Q' = RQ \tag{2-13}$$

The rotation matrix is R

$$\begin{aligned} R &= R_x(\alpha)R_y(\beta)R_z(\gamma) \\ &= \begin{pmatrix} 1 & 0 & 0 \\ 0 & \cos\alpha & \sin\alpha \\ 0 & -\sin\alpha & \cos\alpha \end{pmatrix} \begin{pmatrix} \cos\beta & 0 & -\sin\beta \\ 0 & 1 & 0 \\ \sin\beta & 0 & \cos\beta \end{pmatrix} \begin{pmatrix} \cos\gamma & -\sin\gamma & 0 \\ \sin\gamma & \cos\gamma & 0 \\ 0 & 0 & 1 \end{pmatrix} \\ &= \begin{pmatrix} \cos\beta\cos\gamma & \cos\beta\sin\gamma & -\sin\beta \\ \cos\alpha\cos\beta\cos\gamma - \cos\alpha\sin\gamma & \sin\alpha\sin\beta\sin\gamma + \cos\alpha\cos\gamma & \sin\alpha\cos\beta \\ \cos\alpha\cos\gamma\sin\beta + \sin\alpha\sin\gamma & \cos\alpha\sin\beta\sin\gamma - \cos\gamma\sin\alpha & \cos\alpha\cos\beta \end{pmatrix} \end{aligned} \tag{2-14}$$

Since the angles of α、β、γ are very small, the following approximation can be carried out:

$$\begin{aligned} &\sin\alpha \approx \alpha, \sin\beta \approx \beta, \sin\gamma \approx \gamma \\ &\cos\alpha \approx 1, \cos\beta \approx 1, \sin\gamma \approx 1 \end{aligned} \tag{2-15}$$

$$R = \begin{pmatrix} 1 & r & -\beta \\ -\gamma & 1 & \alpha \\ \beta & -\alpha & 1 \end{pmatrix} \tag{2-16}$$

$$Q' = RQ_1 = \begin{pmatrix} 1 & \gamma & -\beta \\ -\gamma & 1 & \alpha \\ \beta & -\alpha & 1 \end{pmatrix} Q_1 \tag{2-17}$$

If the origin of coordinate system 3 in coordinate system 1 is

$$O_1 = \begin{pmatrix} \Delta x \\ \Delta y \\ \Delta z \end{pmatrix} \tag{2-18}$$

Since coordinate system 1 is in parallel to the respective axes of coordinate system 3, it can be considered that coordinate system 3 is obtained by the translation of coordinate system 1.

Thus the coordinates of the Q points in coordinate system 1 are

$$Q'' = Q' + O_1 = RQ_1 + O_1 = \begin{pmatrix} 1 & \gamma & -\beta \\ -\gamma & 1 & \alpha \\ \beta & -\alpha & 1 \end{pmatrix} \begin{pmatrix} x_0 \\ y_0 \\ z_0 \end{pmatrix} + \begin{pmatrix} \Delta x \\ \Delta y \\ \Delta z \end{pmatrix} \tag{2-19}$$

This equation is the principle of realizing the transformation of coordinates between geocentric inertial coordinate system, geocentric solid coordinate system and local geographic coordinate system.

(2) The conversion between the geocentric solid coordinate system and the geocentric geodetic coordinate system

As shown in Figure 2-2, the geocentric coordinates of a point Q near the Earth surface are $Q = (\varphi, \lambda, h)^T$.

According to the geometric knowledge, it is easy to get the coordinates of the point in the geocentric coordinate system

$$Q' = \begin{pmatrix} x_0 \\ y_0 \\ z_0 \end{pmatrix} = \begin{pmatrix} (r+h)\sin\lambda\cos\varphi \\ (r+h)\sin\lambda\sin\varphi \\ (r+h)\cos\varphi \end{pmatrix} \tag{2-20}$$

Where, r is the radius of the Earth reference ellipsoid model corresponding to the solid coordinate system.

Similarly, if the geocentric fixed coordinates of the point $Q' = (x_0, y_0, z_0)^T$ are known, the geocentric geodetic coordinates of the point are:

$$Q = \begin{pmatrix} \varphi \\ \lambda \\ h \end{pmatrix} = \begin{pmatrix} \arctan\left(\dfrac{x_0}{y_0}\right) \\ \arctan\left(\dfrac{z_0}{\sqrt{x_0^2 + y_0^2}}\right) \\ \sqrt{x_0^2 + y_0^2 + z_0^2} - r \end{pmatrix} \tag{2-21}$$

Equation (2-20) and equation (2-21) are the conversion relationship between geocentric solid coordinate system and geocentric geodetic coordinate system.

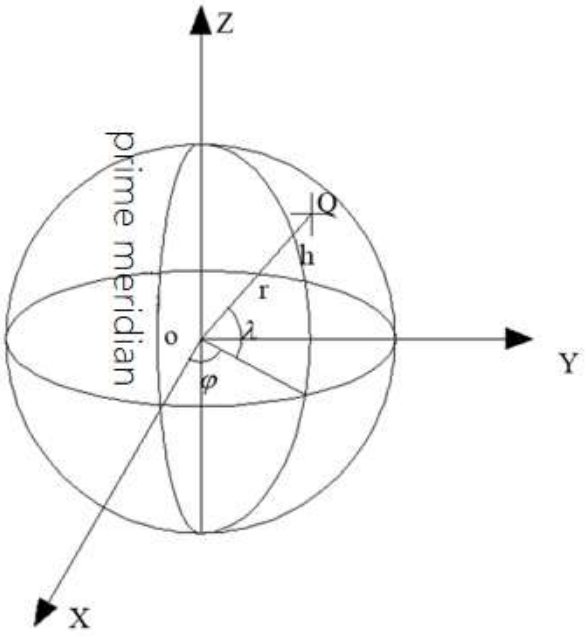

Figure 2-2: Transformation between the geocentric and geodetic coordinate systems.

2.5. GNSS ERROR SOURCE

From the perspective of the whole process of GNSS positioning, GNSS positioning results are affected by satellite, satellite signal propagation process and receiver, so GNSS positioning error has satellite, signal propagation process and receiver from the error source. To realize the simulation of GNSS system, the formation mechanism and mathematical model of various GNSS localization errors must be studied.

2.5.1. SATELLITE RELATED ERROR

(1) Satellite ephemeris errors

The difference between the satellite position and velocity given by the satellite calendar and the actual satellite is called the satellite ephemeris error. The size of the ephemeris error mainly depends on the quality of the satellite orbit setting system, such as the number and geographical distribution of the orbit setting, the number and accuracy of the observed values, the mathematical and mechanical model used and the perfection of the orbit setting software. In addition, it is also directly related to the extrapolation time interval of the ephemeris (the measured ephemeris time interval can be regarded as zero).

(2) Clock error of satellite clock

In GNSS, the time of satellite broadcasting signals is determined using the satellite clock and transmitted to the user through the satellite signals. Although the satellite bell is an atomic bell with high stability and high precision, there is inevitably an error. The deviation relative to the standard satellite navigation system is called the satellite clock error. This error includes both systematic error (such as clock difference, clock speed, frequency drift,

etc.), as well as random error. The systematic error is much larger than the value of the random error, and can be determined by inspection and alignment and corrected by the model; while the random error can only be described by the stability of the clock, and the sign and size cannot be determined. The satellite clock error at time t can generally be expressed as:

$$\Delta t_R = a_0 + a_1(t - t_0) + a_2(t - t_0)^2 + \int_{t_0}^{t} y(t)dt \quad (2\text{-}22)$$

where, t_0 is time, a_0, a_1, a_2 is the clock difference, clock speed, and clock aging rate (frequency drift) of the reference moment of the satellite clock, respectively, and $\int_{t_0}^{t} y(t)dt$ is a random term.

(3) Relativistic effect

According to the Einstein relativistic effect, the time between the gravity and the speed of motion is different between objects. Therefore, the relativistic effect refers to the phenomenon that the relative clock error occurs between the two clocks occurs because the satellite clock and the receiver clock are in different states (motion speed and gravity position). In the field of navigation and positioning, the following methods are generally used to calculate the satellite clock delay caused by the relativistic effect:

$$\Delta t_r = F e_s \sqrt{a_s} \sin E_k \quad (2\text{-}23)$$

where, F is the constant, $F = -4.442807633 \times 10^{-10} \left[s / m^{1/2} \right]$; e_s is the eccentricity of the satellite orbit; a_s is the long radius of the satellite orbit; E_k is a near Earth angle and can be calculated from the satellite star calendar data.

2.5.2. SIGNAL PROPAGATION PROCESS BASED ERROR

During the propagation process of the GNSS satellite signals, the speed and the propagation path of the satellite signals are affected by the actual space atmospheric environment, leading to some errors contained in the GNSS observations.

IONOSPHERIC ERROR

The ionosphere refers to the earth's atmosphere between 50 and 1000 km above the ground. Gas molecules in the ionosphere, due to the radiation from various rays of the sun and other celestial objects, produce a strong ionization that forms a large number of free electrons and positive ions. When a satellite signal passes through the ionosphere, like other electromagnetic waves, the signal path bends and the propagation speed changes. So the distance obtained by multiplying the propagation time of the signal by the speed of light in the vacuum does not equal the geometric distance between the satellite and the receiver. This deviation is called the ionospheric refraction error.

The ionosphere contains a higher density of electrons, which is a diffusion medium, within which electromagnetic waves propagate at a frequency-dependent velocity. Theory shows that the group refractive index of the ionosphere is:

$$n_G = 1 + 40.28 N_e f^{-2} \quad (2\text{-}24)$$

Therefore, the group speed is:

$$v_G = \frac{C}{n_G} = C\left(1 - 40.28 N_e f^{-2}\right) \quad (2\text{-}25)$$

Where, N_e is the electron density (number of electrons/m^3); f is the frequency (Hz) of the signal; C is the speed of light in vacuum.

When making the pseudo-distance measurement, the modulation code travels in the ionosphere at a group speed v_G. If the propagation time Δt of the signal is measured in the pseudo measurement, the true distance S from the satellite to the receiver is

$$S = \int_{\Delta t} v_G dt = \int_{\Delta t} C\left(1 - 40.28 N_e f^{-2}\right) dt = C\Delta t - C\frac{40.28}{f^2}\int_{S'} N_e ds$$
$$= \rho - C\frac{40.28}{f^2}\int_{S'} N_e ds = \rho + d_{ion} \quad \textbf{(2-26)}$$

The above equation indicates that the ionospheric correction item must be added to the distance $\rho = C \cdot \Delta t$ calculated by the signal propagation time Δt and the light speed C to equal to the correct distance of S.

$$d_{ion} = -C\frac{40.28}{f^2}\int_{s'} N_e ds \quad \textbf{(2-27)}$$

The integral $\int_{S'} N_e ds$ in equation (2-27) represents the integration of the electron density N_e, the total electron number, along the signal propagation path s. The magnitude of visible ionospheric correction mainly depends mainly on the total number of electrons and signal frequency. The number of ionosphere refraction correction during carrier phase measurement and the correction during pseudodistance measurement are the same size with opposite symbols. For signals, this distance correction can reach 50m maximum in the zenith direction and 150m near the horizon direction (height angle of 20°), so it must be carefully corrected to seriously damage the accuracy of the observed value.

TROPOSPHERE ERROR

Troposphere delay generally refers to the refraction of electromagnetic waves by the non-ionized atmosphere. The non-ionized atmosphere includes the troposphere and the stratosphere, about 60km from the ground. Because the main refraction occurs in the troposphere, it is usually called the troposphere refraction. The refraction of the troposphere is closely related to the ground climate, atmospheric pressure, temperature, and humidity changes, which also makes the troposphere refraction more complex than the ionospheric refraction. Through the troposphere, not only the speed changes, but also the propagation direction changes, and the path is curved. The effect on tropospheric refraction is related to the height angle of the signal, with the impact of up to 2-3m in the zenith direction (90°) and 20m in the ground direction (10°). The smaller the height Angle of the observation satellite, the greater the impact of the troposphere on the GNSS signal. Because the signal must pass through a longer route for the satellite to cross the troposphere, and the resulting error also increases. Therefore, the cut-off height Angle lower than 15° should be avoided in the process of positioning calculation. The troposphere refraction in the propagation path is usually expressed as the product of the troposphere refraction $\delta\rho_z$ in the zenith direction and product of mapping function $M(E)$ satellite elevation angle E :

$$\delta\rho_{Trop} = \delta\rho_z M(E) \quad \textbf{(2-28)}$$

Ninety percent of the tropospheric refraction is caused by the dry gas in the atmosphere, but because the water and gas distribution in the atmosphere varies greatly in time and space, it is difficult to accurately predict it, so an empirical model can only be used to correct the troposphere refraction error. Common models used in GNSS localization are

Saastamoinen and Hopfield models, and the modified parameters of the model are formulated as follows.

The Saastamoinen model comes from gas laws and simplified assumptions that pressure, temperature and humidity change with height. Zenith dry, wet delay is expressed as

$$\tilde{T}_{z,d} = 0.002277\left(1 + 0.0026\cos 2\varphi + 0.00028H\right)P_0 \quad \textbf{(2-29)}$$

$$\tilde{T}z,w = 0.002277\left(\frac{1255}{T_0} + 0.05\right)e_0 \quad \textbf{(2-30)}$$

T_0 is temperature, P_0 is pressure, and e_0 is local pressure caused by water vapor (both in millibar). The values of these parameters are either measured in the antenna regions, or derived from models of the standard atmosphere. ϕ For latitude, H for the local height of the antenna (in km).

$$N_d(h) = N_{d0}\left(1 - \frac{h}{h_d}\right)^4 \quad \textbf{(2-31)}$$

where, h represents the height of the measuring station; N_{d0} is the surface dry refraction; h_d (about 43km) is the height corresponding to zero dry refractivity: $N_d(h_d) = 0$.

As can be seen from the above, the correction effect of tropospheric refraction is affected by many real-time meteorology, so the real-time meteorological data around the observation station should be fully grasped as correctly as possible, so as to achieve the best correction effect of the error model.

MULTIPATH ERROR

In GNSS positioning, if the satellite signal (reflected wave) reflected by the reflector around the measuring station enters the receiver antenna, this will interfere with the signal directly from the satellite (direct wave), so that the observation value deviates from the true value to produce the so-called "multipath error". This interference delay effect caused by the signal propagation of the multipath is called the multipath effect. Multipath effect is an important source of error in GNSS positioning, which will seriously damage the accuracy of GNSS positioning, and will also cause signal failure. The reasons for the multipath effect are briefly described below.

(1) Reflective wave

As shown in Figure 2-3, the signal received by the receiver antenna is a combined signal after interference generated by direct and reflected waves. Antenna A also receives the direct signal S from the satellite and the reflected signal S' reflected from the ground. Obviously, the path length of the two signals is different. The path length of the reflected signal is called the range difference, which is represented by Δ. As can be seen from Figure 2-3:

$$\Delta = GA - OA = GA\left(1 - \cos 2z\right) = \frac{H}{\sin z}\left(1 - \cos 2z\right) = 2H\sin z \quad \textbf{(2-32)}$$

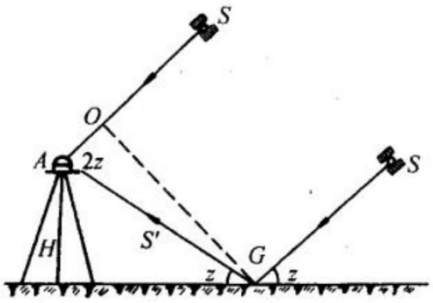

Figure 2-3: Ground-level emission wave

where, H is the height of the antenna from the ground.

The phase delay θ between the reflected waves and the direct waves is:

$$\theta = \Delta\frac{2\pi}{\lambda} = 4\pi H \sin z / \lambda \tag{2-33}$$

Where, λ is the wavelength of the carrier wave.

Since part of the energy of the reflected wave is absorbed by the reflected surface, the receiver receiving antenna is a right-handed circular polarization structure, and the function of the reflected wave is also suppressed, so the reflected wave signal intensity is generally reduced in addition to the phase delay.

(2) Multi-path error in the carrier phase measurement

Let the direct-wave signal be

$$S_d = U\cos wt \tag{2-34}$$

where, U is the signal voltage; w is the angular frequency of the carrier. Digital expressions for the reflected signals are:

$$S_r = aU\cos(wt+\theta) \tag{2-35}$$

The reflected signal and the direct signal are "superimposed" and received by the receiving antenna, so the actual signal received by the antenna is:

$$S = \beta U\cos(wt+\varphi) \tag{2-36}$$

where, $\beta = (1+2a\cos\theta+a^2)^{1/2}$, $\varphi = \arctan[a\sin\theta/(1+a\cos\theta)]$.

φ is the multipath error in the carrier phase measurement. Equation (2-36) counts and makes it equal to zero:

$$\begin{aligned}\frac{d\varphi}{d\theta} &= \frac{1}{1+\left(\frac{a\sin\theta}{1+a\cos\theta}\right)}\cdot\frac{(1+a\cos\theta)\cdot a\cos\theta+a^2\sin^2\theta}{(1+a\cos\theta)^2} \\ &= \frac{a\cos\theta+a^2}{(1+a\cos\theta)(1+a\cos\theta+a\sin\theta)} = 0\end{aligned} \tag{2-37}$$

$\theta = \pm\arccos(-a)$ At that time, the multipath error had maxima:

$$\varphi_{max} = \pm\arcsin a \tag{2-38}$$

In fact, multiple reflected signals may enter the receiving antenna at the same time. The multipath error is:

$$\varphi = \arctan\left(\frac{\sum_{i=1}^{n} a_i \sin\theta_i}{1+\sum_{i=1}^{n} a_i \cos\theta_i}\right) \quad (2\text{-}39)$$

It is seen that multipath effects are far more severe on pseudodistance measurements than carrier phase measurements.

2.5.3. RECEIVER RELATED ERROR

(1) Receiver clock error

Similar to the satellite clock, the clock in the receiver gives a deviation between the moment when the receiver receives the satellite signal and the standard satellite navigation system, namely the receiver clock error. Moreover, most receiver clocks use quartz clocks, and the accuracy and stability of the quartz clocks are less than the atomic clocks used by the satellite clock, so the error of the receiver clock is often more obvious than that of the satellite clock.

In relative positioning, the double difference observation amount can be used to eliminate or weaken the influence of the receiver clock difference; in a single point positioning, the receiver clock difference is generally solved as the 3D position of the user, but this will increase the number of unknowns to be estimated and increase the calculation time of the satellite clock difference. The polynomial can be expressed as follows:

$$\delta t_k = b_0 + b_1(t_k - t_0) + b_2(t_k - t_0)^2 + \cdots\cdots \quad (2\text{-}40)$$

where, t_0 is the selected reference moment, b_0, b_1 and b_2 is the pending coefficient, representing the clock deviation, the relative frequency deviation, and the clock acceleration, respectively.

The order of the equation (2-40) is related to the length of the observation time period and the stability of the frequency standard used by the receiver. For example, if the receiver uses the cesium frequency standard, it can generally take the first order term of the equation; if the quartz crystal frequency standard is used, it must be taken above the second order term of the equation.

(2) Receiver position error

During time service and orbit determination, the position of the receiver is usually considered to be known, and its error will cause systematic error in the results of time service and orbit determination. This error has the same effect on the code pseudo range observation and carrier phase observation.

1) Receiver antenna phase center deviation

When the receiver antenna is aligned and the antenna height is measured, the antenna reference point ARP is used as the reference. During alignment, the center of ARP and markstone is directly located on the same plumb line, so that their plane positions are the same (otherwise, centering correction is required); The antenna height is the vertical distance from the center of the markstone to the ARP, according to which the elevation of the ARP can be reduced to the center of the markstone. However, GNSS measures the position of the antenna phase center. The difference between the receiver antenna phase center and the ARP is called the receiver antenna phase center deviation. At present, IGS and other organizations have measured and published the antenna phase center deviation of various commonly used receivers. Users can make corrections accordingly.

2.5.4. OTHER ERRORS

EARTH TIDE ERROR

The gravity of the sun and the moon on the earth causes tidal deformation of the ocean, causing periodic fluctuations in the actual sea level, resulting in the redistribution of the global mass of seawater. This seawater flow causes elastic deformation of the solid earth, which is called Ocean Tide Loading, or OTL for short.In 1972, Farrell put forward the method of load Green function and the convolution integral of ocean tide height to calculate the influence of ocean tide load. Among them, the load Green function is related to the earth model adopted, and the tide height is provided by the ocean tide model. Since Schwiderski constructed the first global ocean tide model, with the accumulation of satellite altimetry data and the development of numerical calculation technology, more and more ocean tide models have been applied to the study of ocean tide load, and the accuracy is getting higher and higher, such as CSR 4.0, NA099, FES2004, GOT00, TPXO7.0, etc.

The influence of the sea tide load on the displacement of the measuring station is generally on the millimeter scale, and even on the centimeter scale in coastal areas, so the influence on precision positioning cannot be ignored.According to the load theory proposed by Farrell, the vertical and horizontal tidal load effects of the station displacement can be attributed to the load Green function and the convolution integral of the tidal height, such as the formula:

$$\mathrm{L}(\varphi,\lambda,\mathrm{t})=\rho_{\omega}\mathrm{R}_{\mathrm{e}}^{2}\iint_{\mathrm{S}_{z}}\mathrm{H}\left(\varphi^{'},\lambda^{\mathrm{t}},\mathrm{t}\right)\mathrm{G}(\theta,\mathrm{A})\sin\varphi\mathrm{d}\varphi^{'}\mathrm{d}\lambda^{\mathrm{r}} \quad \textbf{(2-41)}$$

Where, φ and λ are the complementary latitude and longitude of the calculation point respectively; $\varphi^{'}$ and R_{e} $\lambda^{'}$ are the complementary latitude and longitude of the load point respectively; R_{e} is the radius of the earth; ρ_{ω} is seawater density; $\mathrm{H}\left(\varphi^{'},\lambda^{'},\mathrm{t}\right)$ is the tide height of the load point in the global regional S_{G}; A is the azimuth angle from the calculation point(φ , λ)to($\varphi^{'}$, $\lambda^{'}$) the load point; θ θ is the spherical angle from the calculation point(φ , λ)to the load point($\varphi^{'}$, $\lambda^{'}$); $\mathrm{G}(\theta,\mathrm{A})$ is the load Green function, which is calculated from the load loff number. The load factor is related to the selected earth model $\mathrm{L}(\varphi,\lambda,\mathrm{t})$ .is the tidal load in U, E and N directions at time t respectively, and the corresponding $\mathrm{G}(\theta,\mathrm{A})$ also uses vertical and horizontal Green's functions, respectively. After the global integration obtains the influence of the tidal load on the station displacement, the amplitude and phase of the tidal wave displacement correction can be obtained in the frequency domain. With the amplitude and phase of the tidal wave, the load deformation of the station displacement can be obtained by adding some tidal wave components, such as the formula:

$$\Delta_{\mathrm{j}}=\sum_{\mathrm{i}=1}^{\mathrm{n}}\mathrm{f}_{\mathrm{i}}\mathrm{A}_{\mathrm{j}}\cos\left(\omega_{\mathrm{i}}\mathrm{t}+\chi_{\mathrm{i}}+\mu_{\mathrm{i}}-\phi_{\mathrm{j}}\right) \quad \textbf{(2-42)}$$

Where, Δ_{j} (j=1, 2, 3) is the tidal load deformation in N, E and U directions of the station respectively; n is the total number of tidal waves considered; f_{i} is the coefficient related to the longitude of the lunar ascending node; A_{j} and ϕ_{j} are respectively the amplitude and Greenwich phase of the ith tidal component corresponding to the jth displacement component of the station; $\omega_{\mathrm{i}}\mathrm{t}+\chi_{\mathrm{i}}+\mu_{\mathrm{i}}$ is the phase delay caused by the earth's solid tide at time t of the i-th tidal component wave, in which $\omega_{\mathrm{i}}\mathrm{t}$ is the angular frequency of the ith tidal component wave, χ_{i} is its astronomical argument number, and μ_{i} is the parameter related to the longitude of the lunar ascending node.

EARTH ROTATION CORRECTION

GPS data processing is generally carried out in the conventional terrestrial system, that is, ground stations and satellites are represented by ground fixed coordinates. If the position of the satellite in space is calculated according to the transmission time of t_1, then the position of the satellite $\left(x_1^s, y_1^s, z_1^s\right)^T$ in the conventional terrestrial system at the time of t_1 is obtained. When the signal arrives at the receiver at t_2, the conventional terrestrial system will rotate around the earth's rotation axis (z axis) by an angle $\Delta\alpha$:

$$\Delta\alpha = \omega\left(t_2 - t_1\right) \tag{2-43}$$

where, ω is the angular velocity of the earth. At this time, the satellite coordinates will have the following changes:

$$\begin{pmatrix}\delta x_s\\ \delta y_s\\ \delta z_s\end{pmatrix} = \begin{pmatrix}0 & \sin\Delta\alpha & 0\\ -\sin\Delta\alpha & 0 & 0\\ 0 & 0 & 0\end{pmatrix}\begin{pmatrix}x_1^s\\ y_1^s\\ z_1^s\end{pmatrix} \approx \begin{pmatrix}0 & \Delta\alpha & 0\\ \Delta\alpha & 0 & 0\\ 0 & 0 & 0\end{pmatrix}\begin{pmatrix}x_1^s\\ y_1^s\\ z_1^s\end{pmatrix} = \begin{pmatrix}\omega\left(t_2 - t_1\right)y_1^s\\ -\omega\left(t_2 - t_1\right)x_1^s\\ 0\end{pmatrix} \tag{2-44}$$

After the above correction is added to $\left(x_1^s, y_1^s, z_1^s\right)^T$, the coordinates of the satellite in the conventional terrestrial system at t_2 can be obtained, because all calculations are performed in the conventional terrestrial system at t_2 . (δx_s, δy_s, δz_s) is the earth rotation correction of the satellite position.

After the satellite position has changed (δx_1^s, δy_1^s, δz_1^s),The distance between the satellite and the receiver $\rho = \left[\left(x_1^s - X\right)^2 + \left(y_1^s - Y\right)^2 + \left(z_1^s - Z\right)^2\right]^{1/2}$ will change $\delta\rho$ accordingly.

$$\begin{aligned}\delta\rho &= \frac{\partial\rho}{\partial x_1^s}\delta x_1^s + \frac{\partial\rho}{\partial y_1^s}\delta y_1^s = \frac{x_1^s - X}{\rho}\omega\left(t_2 - t_1\right)y_1^s - \frac{y_1^s - Y}{\rho}\omega\left(t_2 - t_1\right)x_1^s\\ &= \frac{\omega\left(t_2 - t_1\right)}{\rho}\left[\left(x_1^s - X\right)y_1^s - \left(y_1^s - Y\right)x_1^s\right]\\ &= \frac{\omega}{c}\left[\left(x_1^s - X\right)y_1^s - \left(y_1^s - Y\right)x_1^s\right]\end{aligned} \tag{2-45}$$

The above formula directly gives the influence of the earth's rotation on the distance ρ between the earth and the earth.

When the cut-off altitude angle of the satellite is 15 °, for the station on the equator, the value of $\delta\rho$ can reach 36m. When the distance between the two stations is 10km, the influence of the earth rotation correction on the baseline component can be greater than 1cm.

2.6. GNSS OBSERVATION AND POSITIONING PRINCIPLE

GNSS uses space satellites as base stations and adopts resection to achieve positioning. The GNSS constellation contains more than 100 navigation satellites, which broadcast satellite signals to Earth users, and the satellite position information is written in the satellite ephemeris and broadcast to users along with the satellite signals; Users on the earth surface receive satellite signals using receivers, indirectly measure the distance between satellites and users, and obtain the spatial position information of satellites visible

to users at the moment of observation by analyzing ephemeris. The location of the user is the intersection point with these visible satellites as the center of the sphere and the distance from the satellite to the point as the radius. According to geometric knowledge, at least three such satellites are required. Three spheres intersect at two points, one of which is closer to the earth's surface and the other is often too far away from the earth's surface, which is not the required point. However, as the receiver clock error when receiving satellite signals is an unknown quantity that cannot be ignored, it is the same as the user's three-dimensional coordinate component as the undetermined parameter, so it is necessary to observe one more satellite, so at least four satellites need to be observed to determine the three-dimensional space position of a point on the earth surface. In practical applications, in order to improve the positioning accuracy, more than 4 satellites are often observed as redundant observations. For GNSS observation, we can mainly obtain pseudo range and carrier phase observation data, which correspond to the observation data type. In GNSS, we can generally use range code or carrier phase ranging to indirectly determine the satellite earth distance.

2.6.1. PSEUDO-RANGE OBSERVATION AND POSITIONING PRINCIPLE

Pseudo range observation value is the product of the time and the speed of light of the satellite signal measured by the ranging code from being broadcast by the satellite to being received by the receiver. Because the measured value contains various errors, it is not equal to the real distance between the satellite and the user, so it is called pseudo range. While receiving the satellite signal and demodulating the ranging code, the receiver generates the duplicate code that is synchronous with and identical to the range code broadcast by satellite. Considering the strong autocorrelation of the range code, the delayer can align the duplicate code with the received range code after the delay time Δt, which is the propagation time of the satellite signal, and then multiply it by the speed of light to obtain the satellite earth distance measured by the ranging code, that is, pseudo range. GNSS pseudo range observation equation can be expressed as:

$$P_i^k = \rho_i^k + c\left(\Delta t_i - \Delta t^k\right) + \Delta\rho_{i,trop}^k + \Delta\rho_{i,ion}^k + \varepsilon \tag{2-46}$$

where, P_i^k represents the pseudo range observation value of k satellite at frequency i; ρ_i^k represents the geometric distance from the receiver to satellite k; c is the propagation speed of light in vacuum; Δt_i , Δt^k are receiver clock error and satellite clock error respectively; $\Delta\rho_{i,trop}^k$, $\Delta\rho_{i,ion}^k$ are the tropospheric and ionospheric delay of satellite k at frequency i; ε represents the observation noise of the receiver.

According to the satellite ephemeris file, the coordinates of satellite k can be obtained as $\left(X^k, Y^k, Z^k\right)^T$ and the receiver coordinates at this time are set as $(X, Y, Z)^T$, then the geometric distance ρ_i^k in the formula can be expressed as:

$$\rho_i^k = \sqrt{\left(X^k - X\right)^2 + \left(Y^k - Y\right)^2 + \left(Z^k - Z\right)^2} \tag{2-47}$$

Substitute equation (4-26) into equation (4-25) and expand Taylor series to obtain:

$$\begin{cases} l^k = \dfrac{\left(X^k - X\right)}{\rho_i^k} \\ m^k = \dfrac{\left(Y^k - Y\right)}{\rho_i^k} \\ n^k = \dfrac{\left(Z^k - Z\right)}{\rho_i^k} \end{cases} \tag{2-48}$$

Ignoring the influence of the second-order term, the linearized pseudo-range observation equation is as follows:

$$P_i^k - \rho_i^k = -\left(l^k, m^k, n^k\right)\begin{bmatrix}\delta x\\ \delta y\\ \delta z\end{bmatrix} + \delta T + \varepsilon \tag{2-49}$$

where, δx, δy and δz are the coordinates of the receiver, and δT is the equivalent distance error of the receiver clock error. When more than 4 satellites are observed, $n(n \geq 4)$ equations can be written:

$$\begin{bmatrix}P_i^1 - \rho_i^1\\ \vdots\\ P_i^n - \rho_i^n\end{bmatrix} = \begin{bmatrix}l^1 & -m^1 & -n^1 & 1\\ \vdots & \vdots & \vdots & 1\\ -l^n & -m^n & n^n & 1\end{bmatrix}\begin{bmatrix}\delta x\\ \delta y\\ \delta z\\ \delta T\end{bmatrix} + \begin{bmatrix}\varepsilon^1\\ \vdots\\ \varepsilon^n\end{bmatrix} \tag{2-50}$$

Thus, the error equation of GNSS pseudo range single point positioning is:

$$v = A\delta\hat{X} - L \tag{2-51}$$

$$L = \begin{bmatrix}P_i^1 - \rho_i^1\\ \vdots\\ P_i^n - \rho_i^n\end{bmatrix} \quad A = \begin{bmatrix}l^1 & -m^1 & -n^1 & 1\\ \vdots & \vdots & \vdots & 1\\ -l^n & -m^n & n^n & 1\end{bmatrix} \quad \delta\hat{X} = \begin{bmatrix}\delta x\\ \delta y\\ \delta z\\ \delta T\end{bmatrix} \tag{2-52}$$

When $n \geq 4$, the least square method can be used to solve, where

$$\delta\hat{X} = -\left(A^T A\right)^{-1}\left(A^T L\right) \tag{2-53}$$

2.6.2. CARRIER PHASE OBSERVATION AND POSITIONING PRINCIPLE

The carrier phase observation value is the phase difference between the satellite carrier signal phase received by the user receiver and the carrier signal phase broadcast by the satellite at the same time. In the carrier phase measurement, the wavelength λ of the radio wave sent by the satellite is taken as the length unit, and the satellite earth distance is obtained by measuring the wavelength λ of the carrier wave between the satellite and the receiver. However, because measuring the phase of satellite carrier at the time of broadcasting and receiving can only obtain the part of the wavelength λ number corresponding to the satellite to ground distance that is less than one cycle, the relevant method must also be used to determine the whole wavelength λ number in the satellite to ground distance, that is, to determine the ambiguity of the whole cycle. The GNSS carrier phase observation equation can be expressed as:

$$\begin{cases} P_i^k = \rho_i^k + c\left(\Delta t_i - \Delta t^k\right) + T_{DCB} + d_{orb} + \Delta\rho_{i,trop}^k + \Delta\rho_{i,ion}^k + d_{rel} + \varepsilon \\ L_i^k = \rho_i^k + c\left(\Delta t_i - \Delta t^k\right) + T_{DCB} + d_{orb} + \Delta\rho_{i,trop}^k - \Delta\rho_{i,ion}^k + d_{rel} + \lambda N^k + \varepsilon \end{cases} \tag{2-54}$$

where, P_i^k and L_i^k represent pseudo range observation value and carrier observation value of k satellite at frequency i point respectively;

ρ_i^k indicates the geometric distance from the receiver to satellite k;

c is the propagation speed of light in vacuum;

T_{DCB} represents the hardware delay of the receiver;

d_{orb} represents orbit error;

Δt_i , Δt^k are receiver clock error and satellite clock error respectively;

$\Delta\rho^k_{i,trop}$, $\Delta\rho^k_{i,ion}$ is the tropospheric and ionospheric delay of satellite k at frequency i;

d_{rel} represents the relativistic error;

λ is the carrier phase wavelength;

N^k is the ambiguity;

ε represents the observation noise of the receiver.

Through the precise orbit and precise ephemeris products provided by IGS (international GNSS service) or iGMAS (international GNSS Monitoring & Assessment System), the influence of Δt^k , d_{orb} can be corrected. In addition, IGS will also issue corresponding DCB (Differential Code Bias) files to correct the impact of T_{DCB} ; Relativistic errors are generally corrected by models; Tropospheric errors are generally treated by the combined method of model correction parameter estimation; The ionospheric error can be corrected by the combination of dual frequency de ionosphere or model. At the same time, the weight ratio of observations is generally determined based on satellite altitude angle and observation noise, and the coordinate vector is estimated as a Gaussian Markov model; The receiver clock error is treated as white noise; Tropospheric parameters are estimated according to random walk or piecewise constant. Ambiguity parameters are treated as constants when there is no cycle slip and re initialized when there is cycle slip.

The Kalman filter is used for parameter estimation, and the error model is:

$$V = H \times X - l \tag{2-55}$$

where, V is the observed residual vector, H is the coefficient matrix, l is the difference between the observed and calculated quantities, and X is the state vector, including receiver position increment, receiver clock error, zenith tropospheric wet delay, DCB, ambiguity, etc. The observation noise matrix R is a diagonal matrix, which is generally determined by the satellite altitude angle, the state transition matrix F is the unit matrix, and the system noise matrix Q is determined by experience.

In addition, in the carrier phase observation and positioning, the original data should be preprocessed to obtain a clean observation value without gross error and anomaly, and then error correction and positioning solution should be carried out.

3. NAVIGATION PERFORMANCE REQUIREMENTS OF G-ATM

This chapter introduces integrity and related civil aviation concepts, as well as performance requirements and integrity monitoring indicators and methods for civil aviation navigation systems. Integrity focuses on the reliability of positioning results, which is particularly important in satellite navigation.

3.1. GNSS NAVIGATION PERFORMANCES

The four navigation service performances of GNSS refer to integrity, continuity, accuracy and availability (ICAA) [Ilcev 2011], which is referred to as the four navigation properties in this report. ICAA originated from the quantitative requirements of aircraft precision landing for required navigation performance in aviation applications [Enge 1996]. International standards and recommended measures for radio navigation equipment in ICAO Aeronautical Telecommunications Annex 10[NSP 2006] give a detailed description of ICAA for GNSS aviation applications. The integrity of GNSS has also been extended to other industries along with ICAA. FRP2010[Gates 2011] introduced the ICAA of GNSS in aviation and other more industries.

The four ICAA parameters respectively correspond to a risk (probability) of AL that the error of PVTA navigation solution results exceeds the maximum allowable limit: integrity corresponds to a potential (not yet occurred) risk of PVTA navigation solution errors; The continuity corresponds to the risk of navigation interruption caused by unexpected PVTA navigation solution errors (errors have been determined); The accuracy corresponds to the risk of errors in the actual PVTA navigation solution; The availability corresponds to the risk of any failure to meet the above three service performance indicators during the entire navigation process. Ober has a more detailed discussion on integrity and the meaning of the other three parameters in ICAA in his doctoral thesis [Ober 2004].

1) Accuracy

Accuracy is a statistical concept, which includes measurement of precision (variance, repeatability) of measurement range and accuracy (mean, centrality) of relative true value. It is usually expressed by the corresponding value of accuracy error. There are three methods to express precision by error: relative method (the percentage of the maximum error in the true value), absolute method (the absolute value of the maximum error) and statistical method (the probability is used to express the error distribution). In the navigation discipline, two statistical methods are commonly used to characterize accuracy: one is root mean square (RMS) error, also known as "mean square error" or "standard deviation". The standard deviation of the two-dimensional position coordinate component is represented by the long and short semi axes of the confidence ellipse. One time standard deviation (1σ) The probability value of is 68.3%, and the probability values of two times and three times standard deviation are 95.5% and 99.7% respectively. Many literatures use distance root mean square (DRMS) difference to express two-dimensional positioning accuracy, which is actually 1σ .Second, circular error probability (CEP) and spherical error probability (SEP) discrete distribution measurement of point locations whose real location is the centre of a circle or sphere and whose deviation probability is 50%. In addition, there is a point accuracy distribution metric with a deviation probability of 95%.

In order to avoid ambiguity in the representation accuracy, the confidence probability should be attached to the representation accuracy. The GNSS accuracy mentioned in this report refers to the degree to which the PVTA navigation solution value of the navigation

system is kept correct at the 95% confidence level. GNSS precision reflects the ability of the whole navigation system to control navigation error within the specified range.

2) Integrity

GNSS integrity is a measure of confidence in the correct navigation information provided by the entire navigation system. Integrity includes the ability of the system to send timely and effective warnings (called alerts) to users when it cannot be used for certain scheduled operations [Kaplan 2017], that is, the ability of the system to warn navigation users when it does not trust the navigation results. GNSSIR refers to the probability (potential risk) that the GNSS system does not reach the specified navigation accuracy but is not detected. It should be noted that IR does not refer to the probability of not reaching the specified navigation accuracy, but refers to the probability that overrun errors occur but are not detected. Therefore, when GNSS is used as a non-primary navigation system, its insufficient accuracy will not cause serious security problems (there are also other navigation systems with higher reliability that can provide more reliable results). It is terrible that users are not notified within a specified short time when the accuracy is insufficient, which directly leads to users believing in the wrong navigation results and may lead to security accidents. In this sense, the integrity monitoring of GNSS is more important than the accuracy of GNSS itself, and more concerned by the industry. This is the first primary performance reason why the integrity of GNSS is ranked first in ICAA.

3) Continuity

Continuity refers to the ability of the entire navigation system to continuously provide the navigation accuracy and integrity service performance required by users within a period of time. Software and hardware failures of the navigation system and alarms due to lack of integrity will cause interruption of system continuity. Continuity is an index to measure the accuracy and integrity robustness over a period of time. However, the duration of this period is related to the user's task execution. Even different phases of the same task may require different requirements. For example, each approach of aircraft landing will last for at most 2 minutes. This short-term continuity can be evaluated by the navigation system's uninterrupted service during each approach, while the hourly alarm ratio can be used to evaluate the route that usually lasts for 1 hour to several hours. Alarms generated by FDs in integrity services will reduce the continuous performance of the system. If FDEs are further used to eliminate errors, the continuous service performance can be improved.

4) Availability

Availability refers to the proportion of time or space that the navigation system provides the required accuracy, integrity and continuity of the three navigation service performance requirements for the entire operation process. Availability in the time dimension is usually aimed at a specific navigation task during the entire task execution period. Spatial availability can be used to evaluate the coverage of a GNSS (one or more GNSS, a local navigation system, an enhanced system) in geospatial service performance.

Four logical relationships of GNSS navigation: this report summarizes the functions of four ICAA navigation services as follows: accuracy is the most basic and minimum requirement of the navigation system; integrity is the most important and critical requirement; continuity is the most robust and robust requirement; availability is the most comprehensive and advanced requirement (including the other three aspects). Among them, continuity and availability are performance indicators related to time duration.

3.2. GNSS INTEGRITY

3.2.1. GNSS INTEGRITY CONCEPT

In the field of GNSS, integrity is defined as the measurement of the confidence in the correctness of the information provided by the navigation system, and also includes the ability of the system to send an alarm to the user when it cannot be used for navigation[Zhu 2018]. In other words, the purpose of the integrity assessment process is related to the reliability of the positioning system. GNSS itself has a certain embedded integrity monitoring capability, but this cannot meet the needs of many GNSS users. The integrity problem of GNSS is a service performance problem raised against GNSS vulnerabilities. GNSS integrity monitoring and service performance enhancement are actually the process of real-time leak detection and patching up of GNSS, that is, quickly find out GNSS vulnerabilities, timely notify GNSS users, and try to remedy these vulnerabilities if possible. The concept of integrity originated in the early days of civil GPS system and was defined in the requirements and specifications of the International Civil Aviation Organization (ICAO) to use GNSS in CNS (Communications, Navigation and Surveillance) and ATM (AirTraffic Management) systems. It is necessary to propose the concept of integrity for the following reasons:

1) The user location calculation process is actually an approximation process. Since there are always errors from various sources, it is impossible to calculate the exact real position, but only to approximate it with a certain accuracy level. Integrity monitoring provides a method to monitor the positioning error to ensure the reliability of the results.
2) Unexpected failures may occur on the GNSS system, such as satellite clock errors and ephemeris errors, which will lead to excessive positioning errors. Such an unexpected failure may affect a limited number of satellites or affect the entire constellation with the least possibility. The traditional integrity monitoring method has allowed users to detect satellite fault errors, but the recent integrity monitoring algorithm also takes into account the constellation failure, that is, the satellite failure of the whole satellite constellation at the same time.
3) Since applications such as general aviation involve life safety, especially in some flight stages (such as landing or takeoff), the reliability of positioning system is the main tool for pilots to make decisions. Therefore, integrity monitoring is essential to ensure the reliability and safety of flight.

In order to implement the integrity assessment process, some concepts have been defined:

Protection level: protection level PL is the real-time positioning error protection value calculated according to the alarm rate requirements of GNSS applications and the actual measurement state. The physical meaning of PL refers to the minimum detectable error that can be achieved in the current GNSS state under the premise of meeting the alarm rate requirements of specific GNSS applications. The error below PL is the maximum value that GNSS can achieve under the alarm rate required by users. If this value exceeds the alarm limit (AL) required by users, the system does not meet the integrity. When calculating PL, it is usually divided into horizontal and vertical aspects, that is, horizontal protection level (HPL) and vertical protection level (VPL).

Alarm limit: The alarm limit refers to the maximum critical standard deviation that the system can tolerate. When the user's positioning error exceeds the limit specified by the system, the system will send an alarm to the user. The event that the actual position error exceeds the alarm threshold is called Hazardous Misleading Information (HMI), and the probability of such event is called Probability of Hazardous Misleading Information (PHMI). If the position error is detected to exceed the alarm limit, the system shall be marked as unavailable. Similar to the protection level, the alarm limit is also defined along the horizontal and vertical directions, which are called horizontal alarm limit (HAL) and vertical alarm limit (VAL) respectively. Alarm limits are usually defined according to the

requirements of the intended application, and then the availability of the positioning system for such applications is determined.

Integrity risk: Integrity risk (IR) refers to the probability (potential risk) that the GNSS system fails to achieve the specified navigation accuracy but is not detected. In other words, the required integrity risk is the upper limit of the probability of dangerous misleading information, that is, the possibility that the position error exceeds the protection level but is not detected.

Alarm time: Time to Alert (TTA) refers to the longest alarm time that can be tolerated, that is, the time difference between the time when the user's position error exceeds the alarm limit and the time when the system displays this alarm to the user. Some are also called "alarm time consuming".

The concept of integrity may sometimes be mistaken for accuracy, because both concepts involve the statistical distribution of position errors, especially in the field of civil aviation. In fact, integrity and accuracy are two of the four parameters defined for the required navigation performance to evaluate the GNSS system performance, and the other parameters are availability and continuity. There are several significant differences in the concepts of integrity and precision:

The most important difference is that integrity includes alerts. Although accuracy is mainly related to the correctness of positioning solutions, and no alarm is required, integrity also evaluates the consistency and reliability of such solutions, so when the poor performance of the system may lead to a dangerous situation, an alarm will be issued. Mathematically, the two concepts use different percentiles for their respective requirements. In the aviation field, the accuracy specification requires that the accuracy level be measured at 95% percentile, while the percentile required for integrity must be higher than 99% (according to different operations, the integrity risk range is 10-7 to 10-4).

3.2.2. CRITICAL STATISTICS OF GNSS INTEGRITY

This section attempts to explain the statistical significance of GNSS integrity and the ways to enhance integrity service performance from the perspective of probability, and define the relationship between GNSS integrity and precision, reliability and vulnerability.

1) Probability characteristics of GNSS integrity

In particular, this report has drawn a GNSS integrity diagram Figure 3-1, which represents the integrity of GNSS and its related precision, as well as the quantitative relationship of navigation error probability density function (PDF) from the perspective of probability density. The abscissa in the figure represents PVTA deviation (PVTA-D) of navigation solution value of any GNSS application, which is represented by Δx. The alarm limit given on the abscissa corresponding to the specific GNSS application (indicated by the yellow vertical line $\pm AL$ in the figure).

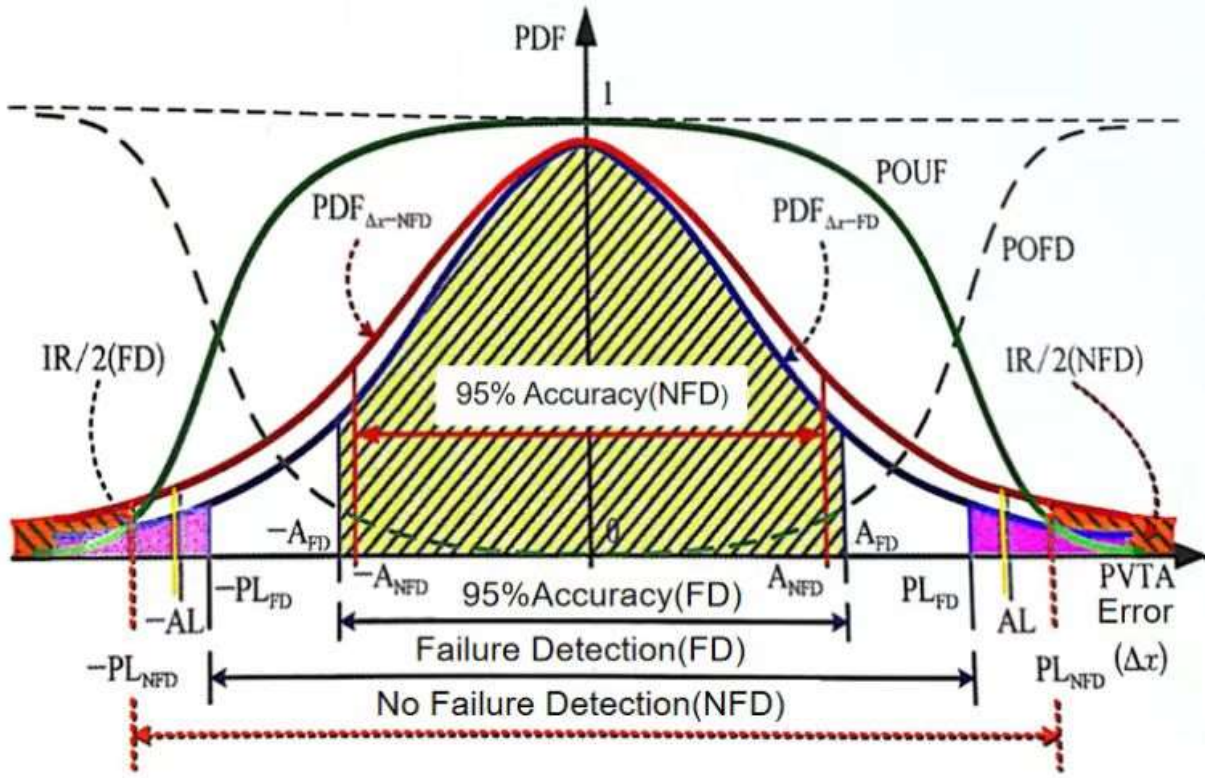

Figure 3-1: Schematic Diagram of GNSS Integrity.

There are four main curves in Figure 3-1. The green long dash curve in the shape of the bottom pan represents the probability of failure detection (POFD) of GNSS navigation system's corresponding error Δx, which reflects the GNSS system's ability to detect navigation errors; The top bell shaped green solid line curve represents the probability of undetected failure, The bell shaped green solid curve at the top indicates the probability of undetected failure (POUF) of GNSS navigation system corresponding to the error Δx. The error Δx near the zero point of the horizontal axis is very small. At this time, it is difficult to detect the error. Therefore, $POUF(0) \approx 1$ $POFD \approx 1$. As the absolute value of error increases, POUF continues to decrease until it is close to the zero position. At this time, $POFD \approx 1$. The two green probability curves above and below the branch are complementary:

$$POFD + POUD = 1 \quad \textbf{(3-1)}$$

In Figure 3-1, the middle red solid line (below the bell-shaped solid line) represents the probability density function ($PDF_{\Delta x-NFD}$) of Δx when no failure detection (NFD) is performed during navigation. The main body part enclosed by the vertical line and horizontal axis of the red size mark accounts for 95% of the $PDF_{\Delta x-NFD}$ area, thus giving the 95% accuracy range value $\pm A_{NFD}$ of the navigation system when NFD is performed. For a specific GNSS navigation application, the respective integrity risk indicator (IR) is specified, and the corresponding IR in NFD is the area of the two ends of the $PDF_{\Delta x-NFD}$ curve (the brown shaded area of the two left diagonal lines in Figure 3-1), and thus the protection level (PL) in NFD is determined, as shown in the two brown endpoint lines $\pm PL_{NFD}$ of the NFD protection range marked by the brown dotted line size in Figure 3-1 (outside AL, the integrity is lost).

The solid blue line in the middle of Figure 3-1 represents the probability density function($PDF_{\Delta x-FD}$) of Δx when FD is performed in navigation, which is the product of the red $PDF_{\Delta x-NFD}$ curve above and the green $POUF$ probability curve:

$$PDF_{\Delta A-FD} = PDF_{\Delta x-NFD} - POUF = PDF_{\Delta x-FD} - (1 - POFD) \quad \textbf{(3-2)}$$

GNSS integrity monitoring is actually an error detection mechanism introduced in the GNSS navigation process. Multiplying the bell-shaped POUF probability curve in Figure 3-1 represents the integrity monitoring process. It can be seen from Figure 3-1 that the probability density function $PDF_{\Delta x-FD}$ of Δx after FD is compressed downward compared with $PDF_{\Delta x-NFD}$ in NFD, which is the result of introducing integrity monitoring. The advantage is that for the same integrity risk indicator IR, the two end parts of $PDF_{\Delta x-FD}$ curve (the purple shaded area of two sand points in the figure) corresponding to the two blue endpoint lines ± FDPL approach 0, that is, the value of PL decreases, After the $\pm PL_{NFD}$ previously outside AL passes through FD, the $\pm PL_{FD}$ and their determined protection area (the FD protection area marked by the blue size) are lower than AL, and the integrity is guaranteed. However, the enhancement of integrity also comes at a cost: the 95% accuracy range value $\pm A_{NFD}$ determined by the 95% accuracy $PDF_{\Delta x-FD}$ corresponding to the depressed Δx probability density function $PDF_{\Delta x-FD}$ (the light green shaded area of the right diagonal line in the figure) also has a small increase compared with the previous $\pm A_{NFD}$ (the accuracy performance has slightly decreased). At the same time, the number of errors detected and alarms will inevitably increase after the increase of FD, which increases the risk of the interruption of the navigation system service performance. This means that the integrity enhancement is at the cost of the loss of accuracy and continuity (cost analysis of GNSS integrity enhancement). Therefore, the four features of ICAA's navigation are a set of service performances that restrict each other and eliminate each other, and need to be balanced and coordinated in navigation.

2) Relationship between integrity and accuracy

Integrity and precision are closely related, but they are also very different, and sometimes they are easy to be confused. The following is a special discussion on the relationship between them. GNSS navigation accuracy is the basis of ICAA service performance of four navigation properties, including integrity. Integrity monitoring and evaluation are also carried out based on the PVTA error of navigation solution. In addition, according to the cost analysis of GNSS integrity enhancement, the enhanced integrity service performance will also reduce the navigation accuracy performance by a small margin of 95%, so integrity and accuracy are highly correlated. However, integrity and accuracy are also different in three aspects: first, the range of errors concerned is different and the magnitude difference is large, With reference to the probability density function $PDF_{\Delta x-FD}$ (solid blue line in the middle) of navigation solution value error Δx in Figure 3-1, it can be seen that the determination area of accuracy and integrity is far from each other: the accuracy is determined by the navigation solution value error Δx interval $\pm A_{FD}$ determined by circling 95% of the longitudinal section area (as shown in the light green shadow protection area of the right diagonal line in the figure) with zero error as the center, The integrity is determined by the navigation solution value error Δx interval $\pm PL_{FD}$ determined by symmetrically circling the integrity risk IR corresponding longitudinal section area from the far end of the two ends of the $PDF_{\Delta x-FD}$ curve (as shown in the two purple shaded areas of sand points in the figure), and generally this area is very small (the magnitude can be as small as 0.1μ for aerospace applications); Second, they have different positions. Accuracy is evaluated from the perspective of GNSS meeting the required navigation performance, while integrity is defined from the perspective of not meeting the required navigation performance; Third, time requirements and representations are different. Accuracy is a statistical concept and does not need alarm, while integrity has real-time and time independence (integrity of the front and back time is independent of each other). Users should be notified in time when errors occur.

3) Relationship between integrity and reliability

System reliability has different meanings in two fields. One definition field is used for time related product quality assessment, which represents the ability of the system to complete specified functions under specified conditions and within specified time. It is usually used

to measure the stability of machinery, equipment and product functions in terms of time, and commonly used indicators such as mean time between failures (MTBF), mean time to repair (MTTR), and mean time to failure (MTTF) to measure reliability, such as vehicle mileage, lamp service life, etc. This meaning is most widely used, but it is far from the integrity research theme of this book. Another definition field of reliability is the evaluation of the measurement quality of surveying systems such as geodetic surveying. This concept was proposed by Willem Baarda, a Dutch professor, in 1968, and carried forward by the Delft Geodetic Computing Center (LGR), which was founded and led by him [Qu 1999]. The reliability in surveying and mapping can be divided into two categories: under the given hypothesis test conditions, the ability of the system to find model errors including gross errors and systematic errors is called internal reliability (IR), and the impact of model errors on results is called external reliability (ER). This layer means that both GNSS integrity and GNSS integrity are error detection, which is a good reference for integrity. However, in comparison, the integrity of GNSS also needs to consider that the system will send an alarm to the user in time when it is unable to be used for some scheduled operations.

4) Relationship between integrity and vulnerability

Vulnerability refers to the characteristics (vulnerability) of things or systems that are vulnerable to damage or failure, and GNSS vulnerability refers to the inherent vulnerability of GNSS systems. Specifically, vulnerability refers to the degree to which GNSS maintains normal and stable operation at the system end and normal service quality at the user end under the influence of various factors. Vulnerability and integrity are interrelated. Vulnerability is a vulnerability of GNSS, while integrity of GNSS is actually a lack of navigation service performance due to the inherent vulnerability of GNSS, which is a causal relationship. There are also differences between vulnerability and integrity. The vulnerability study on the inherent vulnerability of GNSS and its mitigation methods is to study how to deal with the damage or failure of GNSS. Integrity, like other ICAA indicators, refers to the service performance of GNSS. The focus is to find the existing vulnerabilities and give an alarm in time. There are few mitigation methods, but the two also tend to converge.

3.3. INTEGRITY MONITORING METHODS

Integrity monitoring method is an algorithm designed to protect users and ensure integrity throughout the operation. There are mainly three methods: SBAS, GBAS and ABAS.

3.3.1. GROUND BASED AUGMENTATION SYSTEM

The ground improvement system (GBAS) defined by the International Civil Aviation Organization (ICAO) is a location service enhancement system [Wang 2016]. The enhanced data provided by GBAS include difference correction data to improve positioning accuracy and data related to integrity monitoring services[Yu 2017]. GBAS is usually installed in the airport to provide assistance for aircraft during takeoff or landing, and can provide services to the area within a radius of 23 nautical miles (about 42 kilometers) of the airport. GBAS broadcasts enhanced data in the VHF band (108-118MHz). For calibration service, GBAS adopts a positioning technology called local differential GPS (LADGPS). In principle, GBAS (or any usual DGPS system) monitors the quality of navigation signals by using ground monitoring and control stations (referred to as reference stations in DGPS terminology). Knowing the exact position of the radio station, it can accurately measure the ranging error and transmit it to the user. Using the correction provided by the ground monitoring station, the receiver (referred to as the mobile station in DGPS terminology) can reduce the potential positioning error, thus improving the overall accuracy [Yang 2010] [Zhu 2015]. According to this method, GBAS can correct the common errors of ground station and receiver, including ionospheric error, tropospheric error, satellite clock error and ephemeris

error. However, GBAS cannot eliminate other local sources of error for each receiver, namely multipath effect interference and receiver noise.

For integrity monitoring services, GBAS also works with ground stations to monitor the quality of navigation signals and provide real-time instructions to ensure that signal integrity is guaranteed. GBAS also calculates PL on the ground and sends it to users based on the following assumptions:

1) Airborne receiver is fault-free
2) After using GBAS to enhance data correction, the pseudo range of airborne receiver is only affected by noise, that is, other errors have been mitigated.
3) One of the reference receivers may be malfunctioning.
4) Both ground stations and airborne receiver use the same satellite constellation.

At present, GBAS can provide services for APV level I and II, and CAT I in PA, and it is also recommended that GBAS be used to override CAT II / III in PA. However, there are also some error problems in GBAS: first, ionospheric anomaly monitoring. The ionospheric anomaly was first discovered in the United States in 2000. After years of observation and research, a partial ionospheric anomaly model is proposed. However, these models are based on the ionospheric anomaly data of North America in the middle latitudes and may not be suitable for other latitudes or regions of different longitudes at the same latitude. The second is radio frequency interference suppression. Radio frequency interference is another important error problem faced by GBAS. The GBAS equipment installed and tested at Newark International Airport in the United States on November 23, 2009 was interfered by interference sources, resulting in satellite tracking interruption of the reference receiver, and similar radio frequency interference incidents occur from time to time. Therefore, in civil aviation applications, GBAS needs to have high-performance anti-interference ability to ensure safe operation.

3.3.2. SATELLITE BASED AUGMENTATION SYSTEM

A satellite-based enhancement system (SBAS) is defined as a wide area enhancement system in which users receive enhancement information from a satellite-based transmitter [Gan 2008]. SBAS is a position enhancement technology based on wide area differential GPS (WADGPS). LADGPS and GBAS systems can only provide corrections that are common to ground stations and airborne receivers and are limited to the area near the airport, but WADGPS can generate and broadcast correction data for users covering large areas or even the whole continent. The WADGPS correction is generated by a network of monitoring stations running in the coverage area. In fact, there are several obvious differences between SBAS and GBAS：

SBAS broadcast band can be the same as GPS signal, while GBAS can only use VHF band.

SBAS uses geostationary satellites covering specific service areas which enables the system to provide a wider range of services than GBAS. In fact, SBAS satellites can also provide ranging measurement similar to GNSS satellites, thereby improving the geometry and redundancy of positioning solution.

SBAS uses a network of monitoring stations in the service area to generate calibration data, rather than installing several stations in the airport as GBAS does.

SBAS provides vector correction, that is, individual correction for each type of error (clock, ionosphere, ephemeris), while GBAS packages all errors as pseudo-range correction.

For integrity monitoring services, SBAS provides the health status of all satellites in the monitored constellation. If a satellite signal is not received from the ground station, it can be declared "unmonitored", and if an integrity failure occurs, it can be declared "not used". On the other hand, SBAS also provides users with a set of parameters for PL calculation. These parameters include:

User Differential Range Error (UDRE): the estimated range of pseudo-range residual error after ephemeris/clock correction is applied to each satellite.

Grid Ionospheric Vertical Error (GIVE): the estimated range of pseudo-range residual error after ionospheric correction is applied to each satellite.

In each period, the PL is calculated by the parameters provided by the user's receiver with SBAS and airborne parameters, following the SBAS integrity monitoring algorithm. If the calculated PL exceeds the corresponding AL, the SBAS service is declared unavailable for the expected operation.

Currently, there are several operational SBAS systems (WAAS,EGNOS,MSAS and GAGAN) in the world, and others are in the implementation or research stage [Li 2012]. WAAS is jointly developed by the U.S. Department of Transportation and FAA. The development began in 1994 and was launched for general aviation in 2003. WAAS now mainly covers North America, including the United States (up to Alaska), Canada and Mexico. On the other hand, the Multi-function Satellite Enhancement system (MSAS) provides SBAS service in the Japanese region, including two geostationary satellites and a small network of monitoring stations and control centers. In India, a GPS-assisted GEO enhanced Navigation (GAGAN) system has been developed to improve the accuracy of GNSS receivers and to modernize CNS/ATM systems. The GPS-assisted GEO enhanced Navigation (GAGAN) has 15 reference stations, 3 control centers and 3 satellites (one of which is geostationary). In Europe, the European Geosynchronous Navigation coverage Service (EGNOS) is the latest system developed by the European Space Agency (ESA) and EUROCONTROL. The system uses a network of three GEO satellites and 40 ground stations to cover the entire European region. EGNOS provides three basic services:

Open service: suitable for any EGNOS-compatible GNSS receiver.

EGNOS Data Access Service (EDAS): provides services to professional users through a terrestrial transmission system. The data provided include EGNOS enhanced data (also sent by EGNOS satellite) and GPS raw data collected by EGNOS monitoring stations.

SOL services: mainly used for security-critical applications, such as civil aviation. The service has enhanced and guaranteed performance, as well as integrity monitoring capabilities. This service has been available since March 2012.

All countries and regions which have big aviation network are upgrading and building SBAS, but for the system operator, how to achieve the compatibility and interoperation between multiple SBAS; for airborne users, how to select the SBAS information broadcast by GEO satellite and how to use the information fusion of multiple SBAS to achieve seamless high-precision navigation is a possible problem in the future SBAS application.

3.3.3. AIRBORNE BASED AUGMENTATION SYSTEM

GBAS and SBAS provide integrity monitoring at the system level, while the airborne enhancement system ABAS aims to provide integrity monitoring at the sensor/receiver level. Different from the other two, ABAS can make use of a set of integrity evaluation algorithms that run completely independently, which only rely on the measurement data of the airborne receiver. As a result, ABAS enhancements allow integrity monitoring services to be available even outside the coverage of SBAS/GBAS, or can be seen as redundancy in the presence of other enhanced systems. The ABAS integrity monitoring service relies on an algorithm called receiver autonomous integrity monitoring (RAIM). In principle, the process of integrity assessment using the ABAS algorithm usually consists of two main steps. The first step is called fault detection and exclusion (FDE). ABAS uses the observed redundant data to perform a consistency check to check the fault in the input data, and if a fault is detected, it may try to exclusion the input. If the conformance check passes, ABAS proceeds to the next step to calculate the PL. In short, the goal of the integrity assessment process is to protect users from excessive positioning errors through

detection and exclusion, and to warn users when in the worst case. Traditionally, ABAS integrity monitoring algorithms run under the following assumptions:

Use only one constellation (although the algorithm can be extended to multiple constellations);

(1) There is at most one satellite failure at a time;

(2) PL mainly depends on the geometry of the satellite;

(3) PL mainly depends on the geometry of the satellite;

PL mainly depends on the geometry of the satellite;

The measured pseudo-range may be affected by errors from multiple sources (atmospheric error, satellite clock error, multipath, etc.). However, the error component is independent, and the pseudo-range error is zero mean and obeys normal distribution.

There are two main methods of ABAS method: the residual-based method in the measurement domain and the separation-based method in the location domain. Although residual-based ABAS is simple and fast, ABAS based on de-separation can have better performance.

RAIM determines the integrity of the GNSS solution from the user receiver itself, and the RAIM algorithm compares the multiple navigation solutions of all measurements or partial solutions to ensure their consistency. Usually the RAIM algorithm detects the relative consistency of measurements through redundant measurements (using residual vectors), so as to determine the channel (satellite) that is most likely to fail. Assuming that measurement errors obey independent Gaussian distribution, conventional RAIM algorithm includes measurement solution integrity monitoring [Brown 1992], mainly SRAIM and MRAIM. The MSS method in SRAIM was first proposed [Brown 1988], and recently there has been a SRAIM method for integrity monitoring using the parameter estimation method of RANSAC model widely used in computer vision. MRAIM is represented by the measured residual vector integrity monitoring method, including PRAIM and FRAIM, and the most commonly sed PRAIM is divided into pseudo-range comparison method [Lee 1986], least square residual method [Parkinson 1988] and parity method [Sturza 1988]. Other RAIM algorithms include the RAIM algorithm based on Kalman filter (Kalman filtering, KF) proposed by Brown in 1986, which uses historical observations to improve the effect, this method must first give a priori error characteristics, but the actual error characteristics are difficult to accurately predict, if the prediction is not accurate, it will reduce the effect, so it is not widely used.

3.4. INTEGRITY MONITORING INDICATOR

GNSS integrity monitoring service indicators are numerous, some indicators have different names, different industries also have their own focus of attention, but also lead to indicators are not unified, this section attempts to summarize and standardize the existing integrity index system. All integrity monitoring is finally reflected in notifying users, so as shown in Figure 3-2, GNSS integrity monitoring indicators are divided into three parts: The user integrity monitoring centered on the input indicator, user integrity monitoring indicator and integrity monitoring output indicator.

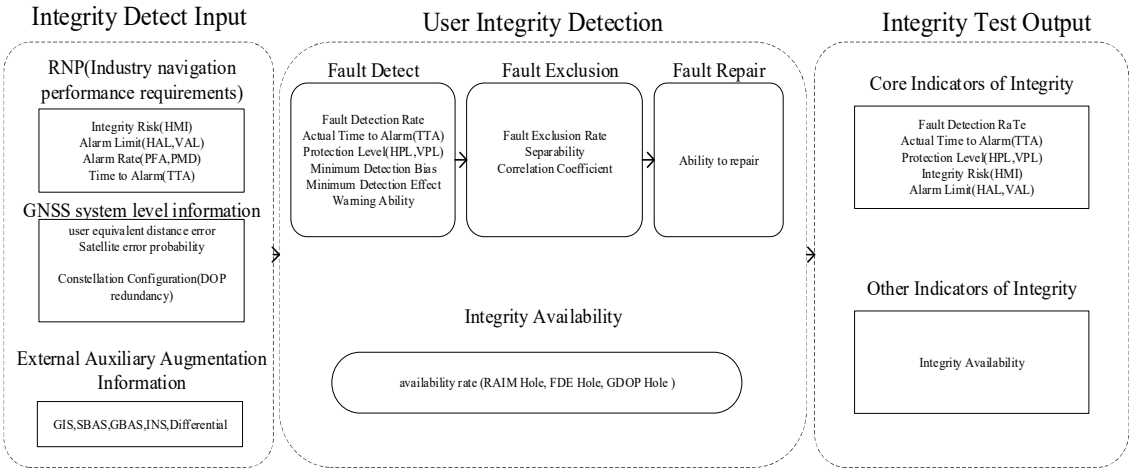

Figure 3-2: GNSS integrity monitoring index relationship graph

3.4.1. INPUT OF INTEGRITY MONITORING

Integrity monitoring input indicators include industry-specific RNP indicators, real-time and empirical system information obtained by GNSS, external enhanced navigation system information and auxiliary navigation information available to users.

(1) Navigation performance indicators required by industry applications

The required navigation performance RNP indicators for industry-specific applications include integrity risk (IR). Maximum allowable alarm rate: including false alarm rate (probability of false alarm, PFA), missed detection rate (probability of missed detection, PMD), AL and TTA.

1) Integrity Risk
   Integrity risk (IR), such as the probability that the GNSS system does not achieve the required navigation accuracy but is not detected (potential risk). IR is called HMI in some literature, or it is called integrity in some literatures.
2) Maximum allowable alarm rate
   a) False alarm rate
      The false alarm probability is the false alarm rate, which is sometimes called "false alarm rate" or "significance level". It is the "abandoning true error" of the two types of errors, which refers to the integrity alarm rate allowed to be caused when there is no fault in the system, which is often expressed by α .
   b) Miss detect rate
      The probability of missing detection is PMD, sometimes also known as the integrity level, allowable IR, 1-minimum detection probability, is the "false error" of the two types of errors. indicating that the user PVTA error within the alarm capacity exceeds AL and the prescribed warning time, the system does not issue the alarm probability, commonly expressed by β. PMD(β) and a complementary concept is the detection rate (detection efficiency), commonly used to indicate γ : γ= 1-β. PMD of WAAS is less than 1.61×10^{-6}/day [Kaplan 2017].
3) Alarm Limit
   The alarm limit value AL refers to the maximum critical standard deviation that can be tolerated by the system. When the user's PVTA error exceeds this limit, the system issues an alarm to the user. AL is usually decomposed into two values in the vertical direction of the horizontal plane, which are the horizontal alarm limit and the vertical alarm (vertical alarm limit, VAL).
4) Time to Alarm
   Time to alarm TTA refers to the maximum tolerable alarm time, that is, the time when the user's PVTA error exceeds AL and the system displays this to the user-the time

difference of the alarm time, some also known as "alarm time" The TTA of WAAS should generally be less than 2s and the maximum should not exceed 6s.

(2) GNSS system-level information

The real-time and empirical system information obtained by GNSS includes user equivalent distance error (UERE), satellite error probability (probability of a satellite failure, PS) and constellation configuration (constellation configuration).

1) User Equivalent Range Error
   UERE means that all kinds of errors introduced by the GNSS system are equivalent to a total error on the pseudo range. Analyzing the influence of various errors on the positioning accuracy can be regarded as only this error on the pseudo range, which is more convenient to deal with.
   UERE is commonly represented by a(σ), which is the square root result of statistical variance D(ε) of GNSS pseudo-distance measurement error ε. Based on probabilistic statistical knowledge, UERE can be obtained by the following formula:

$$\mathrm{UERE} = \sigma = \sqrt{\mathrm{D}(\varepsilon)} = \sqrt{\mathrm{E}[(\varepsilon - \mathrm{E}(\varepsilon))^2]} \quad \textbf{(3-3)}$$

   where, E(ε) represents the statistical mean of GNSS pseudo-distance measurement error ε.
2) Probability of Satellite Error
   Satellite error probability (PS) is the error probability of GNSS satellite in a statistical period of time (usually one year). This is a statistical empirical value and is the error probability of GNSS measurement source.
3) Constellation Configuration
   Constellation configuration refers to the spatial layout of GNSS satellites. Constellation configuration is a real-time satellite measurement geometric distribution, which is usually characterized by Dilution of Precision (dilution of precision, DOP) and satellite visibility (redundancy).
   a) Dilution of Precision
      Dilution of Precision is one of the important standards to measure the positioning accuracy. It represents the distance vector amplification factor between the receiver and the space satellite caused by the GNSS ranging error. The ranging error of the satellite signal multiplied by the appropriate DOP value can roughly estimate the position or time error. There are many kinds of DOP, including all factors called GDOP,GDOP, which has four components in all directions and time: three-dimensional position Dilution of Precision(PDOP), horizontal Dilution of Precision(HDOP), vertical Dilution of Precision(VDOP) (sometimes called height Dilution of Precision), time Dilution of Precision (TDOP).
   b) Satellite Visibility
      Users in different locations see different geometric layout of GNSS satellites, and the number of satellites they can see is also different. Satellite visibility refers to the number of satellites that users can see at a specified elevation, which is usually measured by NVS.
4) External auxiliary Augmentation information

External auxiliary Augmentation information refers to external enhanced navigation system information (such as GIC, SBAS, GBAS) and auxiliary navigation information available to users (such as differential, etc.).

3.4.2. USER INTEGRITY MONITORING INDICATORS

All integrity monitoring is designed to inform users ultimately, and the metrics are divided into four categories: fault detection (FD), fault exclusion (FE), fault remedy (FR), and integrity availability. Fault detection improves the alarm rate. If the fault can be removed, the availability and continuity of the integrity can be indirectly improved under the condition of signal redundancy. If the fault can be repaired, the availability and continuity

of the integrity can be indirectly improved without reducing the redundancy. FR is an important consideration for GNSS as a unique navigation.

(1) Fault Detection

Fault detection (FD) is expressed by fault detection rate, alarm time, protection level, reliability index (including MDB and MDE) and alarm capability.

1) Fault Detection Rate
   The fault detection rate is expressed by the ratio between the number of sampled points detected and the number of sampled points with actual faults, which is one of the important indicators to measure the integrity monitoring.
2) Time to Alarm
   Time to alarm (TTA) is very important for GNSS applications with strong real-time requirements, which refers to the actual alarm time that can be achieved. TTA is also an important indicator of integrity.
3) Protection Level
   The protection level PL is the real-time positioning error protection threshold calculated according to the alarm rate requirements of GNSS applications and the actual measurement state. The physical meaning of PL refers to the minimum detectable error that can be achieved in the current GNSS state (similar to the concept of MDE) under the premise of meeting the alarm rate requirements of specific GNSS applications. The error below PL is the maximum value that GNSS can achieve under the alarm rate required by users. If this value exceeds the alarm limit required by users (PL > AL), the system does not meet the integrity. When calculating PL, it is usually decomposed into horizontal and vertical aspects, that is, horizontal protection level (horizontal protection level, HP) and VPL.
4) Minimum Detection Bias
   The minimum detection bias (MDB) refers to the lower limit of the GNSS bias.[Hewitson 2006] That can be found MDB is used to measure the internal reliability of the system, that is, the size of measurement bias can be found with a certain detection probability in statistical detection, which characterizes the ability of fault detection algorithm to detect location bias.
5) Minimum Detection effect
   Minimum detection effect (MDE) is also described as "edge detection error (marginally detectable error)" in some literature [Ochieng 2002], which refers to the influence of undetectable GNSS errors on the detection results, indicating the impact of pseudo-range errors on location results[Su 2010], similar to the concept of HPL/VPL. MDE characterizes the external reliability of the system, which is somewhat similar to the previous concept of DOP, which transforms the minimum ranging error in the pseudo-range domain into the location domain.
6) Alarm Capability
   Alarm capability refers to the percentage of area (or a period of time) in which the system cannot alert users within the coverage area of the system. The value of WAAS within the scope of each regional base station should be less than 0.5 per cent.

(2) Fault Exclusion

Fault exclusion (FE) is an extension on the basis of RAIM. When the minimum NVS is greater than 6, the navigation system can not only detect but also eliminate the wrong satellites from the navigation solution, so that the navigation system can run continuously without interruption[Kaplan 2017]. FDE also includes two parts: satellite error and satellite bad geometry detection and exclusion[Su 2010], in which exclusion includes two meanings: identification and isolation. Fault exclusion was evaluated by fault recognition rate, separability (separability) and correlation coefficient (correlation coefficient).

1) Fault Exclusion Rate
   The fault exclusion rate is the ratio of the number of sample points of the eliminated fault to the number of sample points with the fault.
2) Separability

Separability, also sometimes referred to as "localizability"[Hewitson 2003], is applicable to multi-dimensional (multi-error) situations and represents the ability to distinguish or identify a measurement error from other measurement errors. When a faulty measurement has an adverse impact on the reliability of navigation solutions, but the error is incorrectly identified as "good" measurement, The degree of separability is very important. Separability is measured as minimal separable bias (MSB).

3) Correlation Coefficient

The correlation coefficient is also the measurement of the correlation between the detection statistics under multi-dimensional (multi-error). The correlation coefficient is not only related to the geometric distribution of the satellite, but also related to the redundancy of the measurement. The larger the correlation coefficient of any two detection statistics is, the more difficult it is to separate. The correlation of any two detection statistics can be used to judge the separability. In practice, maximum correlation coefficient is commonly used to judge the separability[Hewitson 2004]

(3) Fault Repair

Failure repair (FR) can indirectly improve the availability and continuity of integrity without reducing redundancy. At present, due to the lack of integrity in aviation applications, GNSS can only be used as standby navigation. In general, GNSS has more than 6 NVS, which usually only requires simple troubleshooting of faulty satellites. Therefore, FR rarely sees relevant research reports on GNSS integrity. But when GNSS is used as a primary navigation application and multi-fault and NVS are not rich, FR should be given a higher priority. The index of FR is the repairable rate, which is the ratio of the number of sample points of the repaired faults to the number of sample points with faults.

(4) Integrity Availability

Before integrity monitoring, it is necessary to conduct integrity availability testing, that is, to see whether NVS and constellation geometry meet the basic requirements of integrity monitoring. integrity availability can be evaluated by the availability rate, which refers to the ability of FDE in positive terms, but in practice, it often refers to the contrary side with holes to indicate the percentage of FDE that is not successfully achieved. For fault detection and exclusion, RAIM holes (RAIM holes), FDE holes (FDE holes) and GDOP holes (GDOP holes) are used to evaluate their availability, respectively.

1) RAIM Holes

RAIM holes are also called "fault detection holes (FD Holes)". The concept of RAIM holes was first proposed by AFSPC in CRD document 00[AFSC. 1997]: The masking angle (MA) in which less than 5 satellites are visible is regarded as an RAIM hole. In this case, RAIM calculation and fault detection cannot be performed due to insufficient number of satellites. The appearance of RAIM hole is related to time, space location, sampling density and constellation conditions.

2) FDE Holes

FDE holes (FDE holes), also known as "fault exclusion holes (FE Holes)", are the cases where there are less than 6 visible satellites under MA, and NVS is insufficient for fault exclusion.

3) GDOP Holes

GDOP holes, also known as "geometric dilution of precision holes", refer to the bad GDOP situations formed by satellite constellation geometry and GNSS state. According to the "Global Positioning System Standard Positioning Service Performance Standard (Fourth Edition)" released by the US Department of Defense in 2008[DOD. 2008], it is pointed out that in the nominal 24 satellite GPS constellation, the maximum acceptable threshold of position accuracy factor PDOP in the positioning domain is no more than 6(≥98% under the global PDOP available standard). Considering the demand of timing integrity, analogies are used to set the state of GDOP>6 as GDOP black hole. GNSS navigation results in this state are also untrustworthy.

3.4.3. OUTPUT OF INTEGRITY MONITORING

As shown in Figure 3-3, the right part of the integrity monitoring output indicator is the five core indicators extracted from the previous two input indicators and three user integrity monitoring indicators, as well as the availability of integrity and other related indicators. Core indicators of integrity include the following 5 indicators: fault detection rate, TTA, PL, HMI and AL. The latter 4 indicators are specifically emphasized by ICAO in the International Standards and Recommended Measures for radio navigation equipment in Aviation Telecommunications Annex 10 [ICAO 2006].

3.5. THE NAVIGATION PERFORMANCE REQUIREMENTS

The concept of integrity originated from civil aviation, so most of the existing integrity monitoring methods and their inherent performance specifications have been defined for civil aviation. Therefore, it is necessary to briefly introduce related terms and basic concepts in order to correctly understand the integrity requirements of civil aviation. In civil aviation, a flight consists of multiple stages as an aircraft travels from its origin to its destination. The main stages include:

Departure: Transition from takeoff (end of runway, followed by other ground operations such as standing, taxiing, etc.) to the first cruising altitude.

En-route: The second major stage, the flight from origin to destination airport

Approach: The stage in which an aircraft attempts to land, consisting of two sub-stages. The Initial Approach segment is from the Initial Approach Fix (IAF) to the Final Approach Fix (FAF), and the last approach segment is the stage where the alignment of the landing track is completed and the landing is carried out. It started at the last Approach Point and ended at the Missed Approach Point (MAP). On the other hand, if a safe landing is not possible due to instrument errors on the aircraft, weather reasons, etc., the go-around must be performed at the go-around point, and the pilot will abort the landing operation and follow other instructions of the Air Traffic Control (ATC) to climb.

The pilot's operations during the Approach phase are defined in the Instrument Approach Procedure (IAP), which is a series of scheduled actions in which the aircraft moves in an orderly manner from the initial approach anchor point to the landing or visual landing site.

Instrument approach program is divided into three categories:

Non Precision Approach (NPA) - Only horizontal guidance, no vertical guidance approach

Approach with Vertical guidance (APV) - Vertical guided approach refers to the instrument approach with both horizontal and vertical guidance in the final approach segment, but the guidance accuracy is not sufficient to meet the requirements of precision approach and landing operation. The vertical guided approach is divided into two performance classes: APV-I and APV-II.

Precision Approach (PA) - An instrument approach that provides precise azimuthal and glide guidance from an instrument landing system or precision approach radar. It is classified into three performance levels: CAT-I, CAT-II, and CAT-III. The specific classification criteria are as follows [FAA 1984] [FAA 2002]:

(1) CAT-I: Decision Hight (DH) not less than 200 feet (60 meters), visibility not less than 800 meters or Runway Visual Range (RVR) not less than 550 meters.

(2) CAT-II: Determination altitude shall not be less than 100 feet, not more than 200 feet, and runway apparent range shall not be less than 350 meters.

(3) CAT-IIIa: Decision height is less than 100 feet or no decision height, and the runway apparent range is not less than 200 meters.

(4) CAT-IIIb: Decision height of less than 50 feet or no decision height, and runway apparent range of less than 200 meters but not less than 50 meters.

(5) CAT-IIIc: No decision altitude, no runway visual range requirement (automatic landing, Instrument Landing)

On the other hand, Localizer Performance with Vertical guidance (LPV) is another form of approach, It relies on U.S. GPS and Wide-Area Augmentation System (WAAS). Although an LPV is by definition considered an APV, it provides a performance level equivalent to the CAT-I performance level in a precision approach PA.

The ICAO requirements for civil aviation navigation systems are defined by four parameters: accuracy (95%), integrity, availability and continuity. Although the concepts of precision and completeness have been discussed above, two other concepts are also related to completeness. Availability is the proportion of time or space occupied by the navigation system to simultaneously provide the required accuracy, integrity and continuity of the navigation service performance requirements in the whole operation process. The availability in the time dimension is usually based on the whole execution period of a specific navigation task. The availability in the space dimension can be used to evaluate the coverage degree of a GNSS (one or more GNSS, a local navigation system, or an enhanced system) in the geographic space. On the other hand, the continuity of navigation system refers to the ability of the whole navigation system to provide navigation accuracy and perfect service performance required by users continuously and without interruption in the same period of time. Continuity is a measure of accuracy and integrity robustness over time. Even different stages of the same task may have different requirements. For example, each approach of an aircraft landing can only last for 2 minutes at most. This short-term continuity can be evaluated by the uninterrupted service of the navigation system during each approach. On routes that typically last from one hour to several hours, the hourly alarm ratio can be evaluated.

ICAO has developed various flight concepts in accordance with the navigation performance required by aviation. With the addition of GNSS and other navigation equipment and the continuous development of avionics and airborne equipment, ICAO puts forward the method of area navigation (RNAV), which enables pilots to automatically determine aircraft position from ground navigation signals or airborne navigation equipment or a combination of both. In order to achieve the goal of direct flight from any two points after the performance of airborne navigation equipment is gradually improved and no longer dependent on ground navigation equipment. However, the management, approval and selection of airborne navigation equipment are too heavy. In 1994, ICAO put forward the required navigation performance(RNP), The concept of RNP defines the navigation accuracy that aircraft in each air route or airspace must possess to match the corresponding airspace capability and make effective use of the airspace, as shown in Figure 3-3 [Feng 2012].

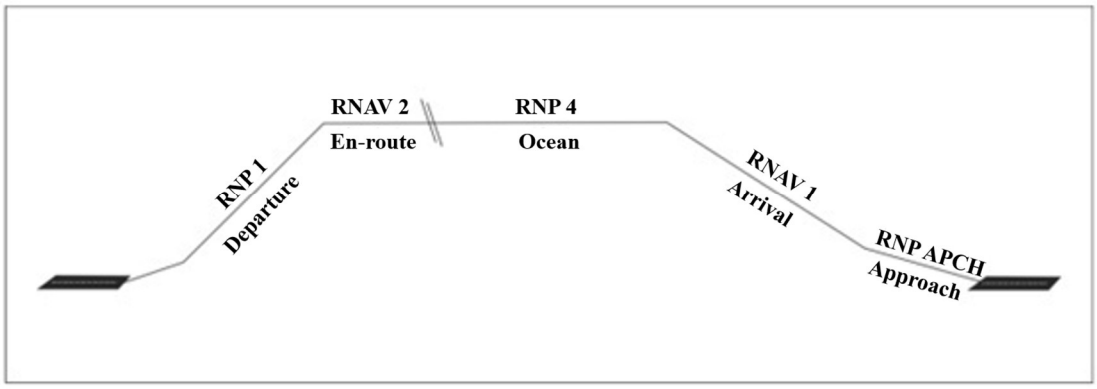

Figure 3-3: Navigation specifications that support specific airspace concepts

RNP is a concept of precision, but also includes performance requirements for airborne equipment monitoring and alerting that are not specified by RNAV.Table 3-1 lists the types,

positioning accuracy and applications of various RNPS. RNAV and RNP exist in parallel and develop separately. ICAO has launched a new navigation system concept, namely performance based navigation (PBN), on the basis of integrating the operational practices and technical standards of RNAV and RNP of various countries [Jin 2011] PBN refers to the performance requirements on ICAA and functions of the system when an aircraft flies in the designated airspace or along the air route and instrument flight procedures under the conditions of corresponding navigation infrastructure [RNPSORSG 2007]. The introduction of PBN reflects the transformation of navigation mode from sensor-based navigation to performance-based navigation [Wang 2013]. The operation of PBN mainly relies on GNSS, but considering the stability of operation, some ground-based navigation facilities are still retained to run mixed with GNSS or as backup navigation mode in a certain period of time [CAAC 2009].

Table 3-1: The types, positioning accuracy and application of various RNPS

Navigation Specification	95% Accuracy of positioning（NM）	Application	Airspace
RNP 0.3	±0.3	Precision RNAV（PRNAV）	Terminal Area
RNP 1	±1.0	Allow for flexible navigation	Terminal to En-route
RNP 4	±4.0	Establish navigation routes between navigation stations and airspace	Continental Airspace
RNP 5	±5.0	Basic RNAV	European Airspace
RNP 10	±10	Remote airspace lacking navigation stations	Oceanic En-route
-RNP 12.6	±12.6	Lack of navigation station airspace optimization route	（Rarely used）
RNP 20	±20	Increased ATS for minimum air freight	（Rarely used）

The airspace stage of aviation can be divided into oceanic en-route, continental en-route, terminal and approach. The performance requirements of the navigation system are determined according to different flight segments, and the integrity requirements are defined in Table 3-2. APV-I (Approach operations with vertical guidance-I) and APV-II (Approach operations with vertical) guidance-II) is a type I approach with vertical guidance and a Type II approach with vertical guidance. The Non-precision approach (NPA) means the non-precision approach, which does not require the navigation system to provide vertical guidance. Another standard that is often used in relation to GNSS navigation systems is the LPV 200, It was the standard for the CAT-I approach using the navigation System of GNSS/SBAS (Satellite Based Augmentation System) (decision height, visibility and RVR were in line with CAT-I). The LPV-200 is the only precision approach among all GNSS/SBAS based approaches that does not require specialized crew training. The LVV-200 is similar to the CAT-I, except that the Vertical Alert Limit (VAL) of the LVV-200 is 35 meters, which is slightly higher than the 10-15 meters of the CAT-I. ICAO is currently revising the CAT-I definition criteria to include LPV-200 in CAT I [DOD 2019].

Table 3-2: Integrity requirements for aviation applications

Operations	Integrity	TTA	HAL	VAL
En-Route(Ocean)	1×10^{-7}/h	10min	7.4km	N/A
En-Route(Continental)	1×10^{-7}/h	5min	3.7km	N/A
Terminal	1×10^{-7}/h	15s	1.85km	N/A
Initial approach, Intermediate approach, NPA, Departure	1×10^{-7}/h	10s	556m	N/A
APV-I	2×10^{-7}/approach	10s	40m	50m
APV-I	2×10^{-7}/ approach	6s	40m	20m
PA CAT-I	1×10^{-7}/ approach	6s	40m	35m-10m
PA CAT-II/ CAT-III	1×10^{-7}/ approach	6s	20m	10m
LPV 200	2×10^{-7}/ approach	6.2s	40m	35m

Table 3-3 details the requirements for continuity, availability and Accuracy, including Horizontal Accuracy (HA) and Vertical Accuracy (VA). Similar to the completeness requirement, there is no vertical accuracy VA requirement for non-precision approach NPA, and the other requirements are significantly more relaxed than for other approaches (except for availability). The LPV 200 and CAT-I have nearly the same requirements and are more stringent than the vertically guided approach APV.

Table 3-3: Integrity requirements for aviation applications

Operations	HA(95%)	VA(95 %)	Continuity	Avalability
En-Route(Ocean)	3.7km	N/A	10^{-8}-10^{-4}/h	10^{-5}-10^{-2}
En-Route(Continental)	0.74km	N/A	10^{-8}-10^{-4}/h	10^{-5}-10^{-2}
Terminal	0.74km	N/A	10^{-8}-10^{-4}/h	10^{-5}-10^{-2}
Initial approach, Intermediate approach, NPA, Departure	220m	N/A	10^{-8}-10^{-4}/h	10^{-5}-10^{-2}
APV-I	16m	20m	8×10^{-6}/15s	10^{-5}-10^{-2}
APV-I	16m	8m	8×10^{-6}/15s	10^{-5}-10^{-2}
PA CAT-I	16m	6m-4m	8×10^{-6}/15s	10^{-5}-10^{-2}
PA CAT-II/ CAT-III	16m	2m	8×10^{-6}/15s	10^{-5}-10^{-2}
LPV 200	16m	4m	8×10^{-6}/15s	10^{-5}-10^{-2}

4. MULTI-CONSTELLATION GNSS ERROR MODEL FOR G-ATM

4.1. RESEARCH STATUS OF GNSS ERROR MODEL

4.1.1. RESEARCH STATUS OF IONOSPHERIC ERROR MODEL

As an electromagnetic wave, when GNSS signals pass through the ionosphere, its propagation path will be deflected, and the propagation speed of the signal will also be influenced, resulting in the deviation of the final positioning result. Therefore, ionospheric errors must be corrected in order to obtain high-precision navigation and positioning information. Common solutions to ionospheric errors are: using the ionospheric error model and dual frequency GNSS to eliminate ionospheric errors. Among them, the ionospheric error model is the most widely used method, and its core is to determine the total electron content (TEC) of the ionosphere. Through in-depth study of the characteristics of TEC changes with time and space, we can fully understand the internal changes of the ionosphere of abnormal disturbances, stratospheric storms, etc., which can help to weaken the ionospheric error and improve the accuracy of navigation and positioning.

At present, methods based on empirical prediction models for the ionosphere include Klobuchar model, Bent model and IRI model,etc. They are mainly empirical models fitted by ionospheric observatories around the world through a large number of observation data. They are simple and useful, but their accuracy is limited. Among them, Klobuchar model can only achieve 50%-60% accuracy [WANG 2016], which can not meet the needs of high-precision navigation and positioning services. Another method is to use the measured data to establish a model, represented by the Global Ionosphere Map (GIM) provided by the International GNSS Service (IGS) and the spherical harmonic function model published by the Center for Orbit Determination in Europe (CODE). Such products are obtained from the actual dual frequency observation data of GNSS on the ground tracking station and can be used for the ionospheric error correction of GNSS worldwidely. On this basis, Zhang Xiaohong et al. used GPS dual frequency observation data to model the small area ionosphere, which can provide single frequency users with ionospheric error correction with zenith direction better than 0.4m [Zhang 2001]. Wei Chuanjun et al. used spherical harmonics to model the global ionosphere, and the experimental results show that the model has high accuracy [Wei 2014]. Li Yongtao et al. established a single station TEC model for 16 stations in Europe based on the 2~15 order spherical harmonic function model, and generated a regional grid TEC model. The experimental results show that the accuracy of the model is equivalent to the product accuracy provided by IGS and CODE within the radius of less than 600km [Li 2021]. However, such models are usually complex and difficult to calculate, and their accuracy is usually affected by many factors and hard to operate. In addition, in order to ensure real-time ionospheric error correction, TEC values are often required to be predicted during navigation. In addition to traditional models, some scholars proposed to use the time characteristics of ionospheric TEC to model and predict TEC based on measured TEC data using time series models. Zhang Xiaohong et al. used ARIMA model to forecast the ionospheric TEC. The experimental results show that: in terms of prediction accuracy, the average relative accuracy of ionospheric calm period and active period for 6 days can reach 83.3% and 86.6% [Zhang 2014]. Tang Hong et al. used 15-day TEC data released by IGS as samples, and Holt Winters and ARIMA models to make 5-day TEC prediction. They analyzed the effects of solar activity, latitude, and prediction duration on the prediction accuracy of the model. The experimental results show that the prediction accuracy of model declines with the decrease of latitude and the increase of forecast duration [Tang 2019]. Zhang Lu studied the ionospheric TEC prediction using

ARIMA model and proved the accuracy and reliability of ARIMA model for TEC short-term prediction [Zhang 2012]. Xie Shaofeng et al. used the addition and multiplication theory of Holt Winters time series model to make a short-term prediction of ionospheric TEC. The experimental results show that the accuracy can reach 80% [Xie 2017]. Chen Peng et al. used the TEC data released by IGS as the sample, making predictions using time series analysis. The experimental results show that the average relative accuracy of the 7-day prediction can reach 87.75% [CHEN 2011]. However, due to the limited nonlinear mapping ability of time series model, its prediction effect decreases with the increase of time, which cannot accurately reflect the change of TEC value with time.

In view of the problems in the existing models, neural networks are used to predict TEC with their excellent learning ability, strong nonlinear mapping ability and the ability to process massive data in large scale at the same time. Relevant researches have also made some achievements. Liu Xiandong et al. used wavelet neural network to make short-term ionospheric prediction, and the experiment achieved good accuracy [Liu 2010]. Li Shuhui proposed a multi-factor chaotic neural network prediction model, which improved the accuracy of short-term prediction [Li 2010]. Zhang Fubin et al. used the encoder decoder structure combined with the short-term memory artificial neural network to achieve the global space and time prediction of TEC. The experimental results of the model within one week show that the root mean square error of the model prediction one day in advance is less than 1.5 TECU, and the root mean square error within one week is less than 2 TECU [Zhang 2021]. Yuan Tianjiao used the TEC, F10.7 index, ap index and solar wind parameters of the first five days to predict the 24-hour TEC value of the sixth day through the cyclic neural network, and proved that the prediction error of the model was 0.49~1.46 TECU lower than that of the back-propagation neural network, the root mean square error of predicting strong ionospheric storms was 0.2 TECU lower than that of the back-propagation neural network, the average prediction error was 0.36~0.47 TECU lower, and the accuracy of predicting ionospheric normal storms was 16.8% [Yuan 2018]. Li Shuhui used the data of ($40°N,115°E$) grid points provided by the neural network through IGS to construct a prediction model at this point one day in advance. The experimental results show that the trained model can reflect the changes and characteristics of TEC in different seasons and states [Li 2013]. A lot of research shows that the neural network has a remarkable effect on TEC prediction. However, the traditional neural network model is prone to fall into the local minimum, slow convergence speed and it is difficult to determine the network structure. Therefore, it is necessary to improve the availability of the traditional neural network. In addition, the current research mainly focuses on the short-term prediction of TEC, while the research on the long-term prediction of TEC change is less.

4.1.2. RESEARCH STATUS OF TROPOSPHERIC ERROR MODEL

Tropospheric error is caused by the refraction of satellite signal by non-ionized atmosphere. The non-ionized atmosphere includes the troposphere and the stratosphere, which are about 60km from the ground. Because the main satellite signal refraction occurs in the troposphere, the tropospheric delay is usually called tropospheric refraction. Tropospheric error is closely related to the changes of surface climate, atmospheric pressure, temperature and humidity, which also make tropospheric error more complex than ionospheric error. In the process of satellite signal passing through the troposphere, not only the speed but the propagation direction changes, and the path also presents a curve. The magnitude of tropospheric error is related to the altitude angle of the signal. When the satellite is in the zenith direction (the elevation angle of the satellite is 90°), its influence can reach 2-3m; When it is in the ground direction (the height angle is 10°), its influence can reach 20m.

Since the distribution of water and gas in the atmosphere varies greatly in time and space, the tropospheric delay is difficult to predict accurately, so empirical models can only be used to correct tropospheric errors. Tropospheric error models generally establish the Zenith Tropospheric Delay (ZTD) model in the zenith direction, and then project it to the

propagation direction of satellite signals. The relationship between ZTD and Signal Tropospheric Delay (STD) on the signal propagation path is:

$$\mathrm{STD} = \mathrm{M} \times \mathrm{ZTD} \quad \textbf{(4-1)}$$

Where, M is the projection function, which is the function of satellite altitude angle and other factors.

Tropospheric error model is to establish a priori model that can describe the change rule of tropospheric delay in time domain and space domain by analyzing the factors that affect tropospheric delay and according to the temporal and spatial change rule of the influencing factors, including models that rely on measured meteorological parameters and models that do not rely on them. Although the accuracy of the empirical model can only reach the centimeter level at present, this method is the most widely used tropospheric delay correction method due to its simplicity and low cost. At present, the tropospheric error models with high accuracy are generally global tropospheric models based on global meteorological data. Such models usually have good accuracy in the global scope. However, due to the large differences in the climate characteristics of different regions of the world, and the large impact of climate change on the convective layer delay, the global tropospheric models may have systematic deviations in local areas. It is difficult to provide high-precision tropospheric delay estimation for local areas, so some scholars also studied high-precision tropospheric empirical models applicable to specific areas. In the 1960s and 1970s, there were few meteorological observation data. The empirical tropospheric model initially established depended on the measured meteorological parameters. This type of model expressed the relationship between the measured meteorological parameters at the stations and the tropospheric delay. It was necessary to obtain the meteorological parameters at the stations to obtain the tropospheric delay with high accuracy. The representative ones were the Hopfield model [Hopfield 1969] [Hopfield 1971] and the Saastamoinen model [Saastamoinen 1972]. In recent years, thanks to the steady improvement of the accuracy and spatial resolution of the Numerical Weather Model (NWM), scholars at home and abroad have begun to establish a high spatial and temporal resolution zenith tropospheric delay model based on the NWM model, such as the GPT2 series model [Lagler 2013] [Böhm 2015], TropGrid2 model [Schuler 2013], IGGTrop model [Li 2012] [Li 2015] SHAO series model [Li 2015] [Song 2011], GZTD series model [Zhao 2015] [Yao 2015], etc, NWM data has become one of the important means to study and construct tropospheric correction model.

4.1.3. RESEARCH STATUS OF MULTIPATH ERROR MODEL

GNSS signals can be divided into the following two types due to multipath effects: non-light-of-sight (NLOS) reception and multipath interference (MI). The "clean" signals that are not affected are called light-of-sight (LOS) reception. Among them, LOS are direct signals that are not shielded by obstacles or reflected or diffracted; NLOS are the reflected signals that arrive at the receiver after reflection; MI refers to the mixed signal of NLOS and LOS. Although the ranging errors generated by NLOS and MI are different and the targeted processing methods are also different, they are usually classified into one category, namely "multipath effect", for discussion. At present, the methods for multipath error elimination can be divided into three categories: antenna based design, signal processing based and observation based modeling.

Antenna-based design methods include the use of antenna arrays, choke antennas, and other types of antennas to directly mitigate multipath effects at low elevations. Thornberg et al. combined the multi-channel restricted antenna with the high zenith antenna, and improved the suppression of ground multi-channel in dense urban areas through the proposed antenna array system [Thornberg 2003]. The choke antenna uses its special structure, that is, a group of concentric choke rings around the antenna element, which can attenuate the influence of multipath signals, but is not suitable for the processing of high elevation multipath signals [Groves 2013]. The method based on signal processing is

mainly based on the design and implementation of correlator. Correlators are used to estimate the best approximation of signal amplitude [Heinrichs 2004]. Some correlators and delay locked loop (DLL) technologies, such as narrow correlators, multipath estimation delay locked loop (MEDLL), shaping correlators and other signal processing methods [Van Dierendonck 1992] [Townsend 1994] [McGraw 1999] [Townsend 1995] [Weill 2002] can mitigate the multipath effect, but can not mitigate the impact on positioning accuracy when NLOS is only available. The method based on observation modeling integrates GNSS observations with other information sources, or performs mathematical statistics and modeling on observations to improve positioning accuracy. Soloviev et al. proposed an algorithm of integrated inertial measurement unit (IMU), laser scanner and GPS to identify GPS signals affected by multipath in urban environment [Soloviev 2008]. Meguro et al. used panoramic infrared cameras to detect the environment, and eliminated invisible satellites captured by GNSS receivers [Meguro 2009]. However, vision sensor is vulnerable to the impact of urban landscape obstacles and weather, which leads to the decline of image recognition ability and ultimately affects the positioning performance. However, although the information fusion method based on multi-sensor can make use of the complementary advantages of various systems to improve the positioning accuracy, the accompanying high cost and volume problems should not be underestimated. In addition to multi-sensor fusion, recent research also uses spatial geographic information (such as 3D city models) to mitigate the impact of NLOS and Multipath. For example, Groves et al. developed a shadow matching algorithm to detect NLOS with the aid of 3D urban model, thus improving the positioning accuracy [Groves P D 2011]. Shadow matching technology can avoid the problem of insufficient available satellites due to NLOS signal elimination, so as to simulate the visibility of each satellite and match the best candidate position [Wang 2013]. Although these methods can reduce the error caused by NLOS to a certain extent, and thus improve the positioning accuracy, the determination of satellite reception type is very dependent on the accuracy of the city model used. The use of high-precision complex models will inevitably lead to poor computational efficiency. In addition, the method based on 3D city model cannot deal with the multi-path effect caused by dynamic occlusion, And the universality and portability of its model construction still need to be verified.

With the development of artificial intelligence technology, machine learning, through a large number of data training, learns and excavates the potential relationship between data, and enables AI to determine the type of satellite signal reception in cities. The development of cloud computing and communication technology also provides technical support for users to call public models online to correct pseudo range errors. In recent years, research on the application of machine learning in the field of navigation and positioning has emerged endlessly. Hsu Li-Ta and others used machine learning to classify the received satellite signals, and learned the characteristics of GPS observation variables in urban canyons through support vector machine algorithm to predict the type of satellite signal reception, with a classification accuracy of about 75% [Hsu 2017]. Monsak proposed a vehicle cooperative navigation algorithm [Socharoentum 2016], which uses machine learning and pseudo range correction to detect NLOS, and the detection accuracy is better than 90%. However, classifying the signals and eliminating NLOS signals will make the number of available satellites in the urban canyon environment, where the lack of satellites is already very serious, more precarious.

4.2. THE GA-BP BASED IONOSPHERIC ERROR MODEL

4.2.1. MODEL DESIGN

Aiming at the ionospheric error of BDS/GALILEO multi constellation system, this project has established an ionospheric error model based on GA-BP (Genetic Algorithm – Back Propagation Neural Network).

MODEL FRAMEWORK

The process of GNSS ionospheric error modeling method based on GA-BP is shown in Figure 4-1:

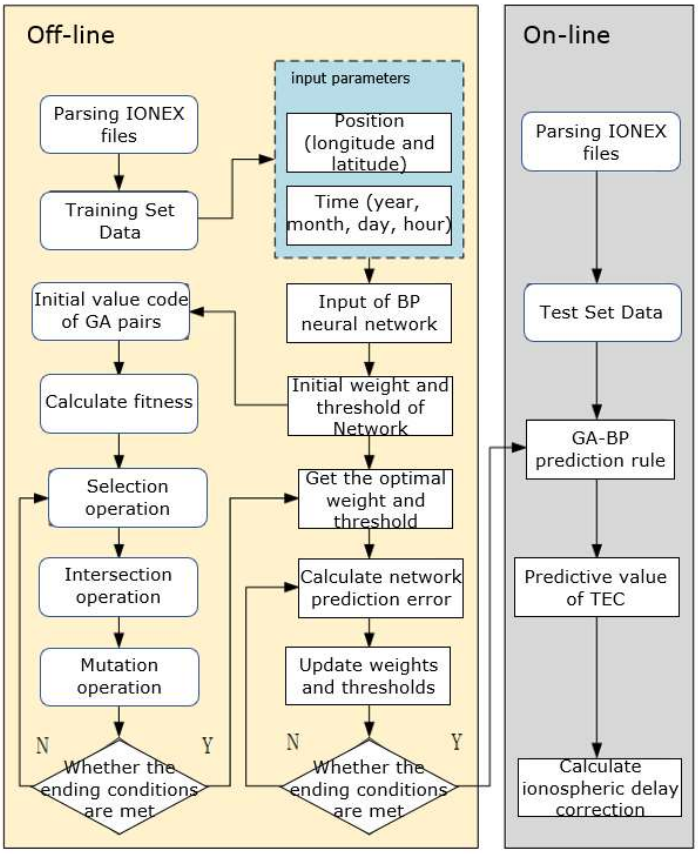

Figure 4-1: Flow Chart of GNSS Ionosphere Error Modeling Based on GA-BP

First, analyze the ionospheric file in IONEX format provided by IGS, extract and save the TEC data corresponding to GIM grid points. The model has 6 input variables, which are selected as: 1)year, 2)month, 3)date, 4)hour, 5)longitude, 6)latitude; one output variable, i.e. TEC value at corresponding position time. Each input variable is input into the model through the input node, and compared with the node threshold value after the linear weighted sum. After exceeding the threshold value, the output is activated by the sigmoid function, which is the output result of the model. After determining the structure of BP neural network according to prior information, the difference between the predicted value of BP neural network and the reference value is taken as the fitness value of genetic algorithm; the genetic algorithm iteratively obtains the individual corresponding to the optimal fitness value according to the selection, crossover and mutation operations, and assigns the weight value and threshold value corresponding to the optimal individual to the BP neural network; after training, BP neural network can predict TEC value in the region; finally, the TEC value predicted by the GA-BP model can be combined with the

ionospheric error correction formula to calculate the ionospheric error correction value at the corresponding position time.

CHARACTERISTIC VARIABLE SELECTION

A large number of studies and actual observations show that TEC is related to time, position, solar activity, ionospheric activity and other factors [Li 2013]. This project mainly focuses on the prediction and research of the ionospheric TEC changes in a solar activity cycle when the solar activity is relatively gentle, so the influence of solar activity factors is not considered in this study. In addition, since the comprehensive influencing factors of ionospheric activities are relatively complex, further analysis and research are still needed, and more input characteristics will also increase the difficulty of calculation. In order to give consideration to the practical application and calculation efficiency of the model, a total of 6 input variables are selected for this project, as follows:

1) Longitude and Latitude. The research shows that the change of TEC is affected by the change of longitude and latitude. In low latitude and other areas with strong solar radiation, the change of TEC is more obvious than other areas. However, in the middle and high latitudes and some areas with weak solar radiation, the change of TEC tends to be gentle as a whole, with a small change range. However, it is not enough to use only longitude and latitude to predict the change of TEC, and other features are also needed.
2) Year, month, date, hour. According to the actual observation of the ionosphere, the change of the ionospheric TEC is related to the specific local time in a certain year. In the daytime, the ionospheric TEC increases with the gradual increase of solar radiation, reaches the maximum value at about 14:00 local time, then decreases with the gradual decrease of solar radiation, and drops to the minimum value at night. Day after day, there are periodic changes.

Since the intensity of solar radiation varies from year to year, the TEC value changes seasonally. In addition, at the same time, the TEC values at different geographical locations are different, but they can be expressed by longitude, latitude and specific time variables. Therefore, the above six variables are selected as input variables in this project, and the output variables are the TEC values at the corresponding Longitude, latitude and time.

IONOSPHERIC ERROR MODEL CONSTRUCTION

BP neural network is a supervised learning algorithm for nonlinear and adaptive information processing, which is composed of multiple artificial neurons. Its characteristics are signal forward transmission and error back transmission. It adjusts the weight and threshold of BP neural network through the error between the predicted output and the ideal output calculated in each iteration, so that the predicted output approximates the ideal output [Zhu 2015]. However, due to the serial search mechanism of BP neural network, when it faces a large number of data, the search speed will be reduced and may converge to the local minimum. Genetic algorithm is a parallel random search optimization algorithm formed by simulating natural genetic mechanism and biological evolution theory [Gan X L 2008]. Compared with BP neural network, the parallel search mechanism of genetic algorithm makes it easier to converge to the global optimum. Therefore, this project combines BP neural network and genetic algorithm to build a GA-BP combination model. Genetic algorithm is used to optimize the initial weight and threshold of BP neural network to improve the operation speed of the model and avoid falling into local extreme value. The calculation steps of the constructed GA-BP model are as follows:

1) Initialize BP neural network and genetic algorithm parameters
   The number of input nodes of the initialized BP neural network is 6, corresponding to the six input variables of the model: year, month, date, hour, longitude and latitude; the number of output nodes is set to 1, which is the TEC value corresponding to this

position and time. Reference formula for selecting the number of nodes in the initial hidden layer:

$$l < \sqrt{(m+n)} + a \tag{4-2}$$

Where, n is the number of nodes in the input layer; l is the number of hidden layer nodes; m is the number of output layer nodes; a is a constant between 0 and 10. Subsequently, the best number of nodes is determined by trial and error method.
The output calculation formula of initialized BP neural network neuron is as follows:

$$I = \sum w_{ij} x_i \tag{4-3}$$

Where, x_i is the ith input variable, w_{ij} is the weight between the ith input variable and the jth neuron, and I is the neuron output.
The activation function f of the initialized BP neural network is a hyperbolic tangent S-type function. The calculation formula of the activation function output corresponding to the input variable x is as follows:

$$f(x) = \frac{1 - e^{-x}}{1 + e^{-x}} \tag{4-4}$$

The number of initialization network iterations is 100, the learning rate is 0.005, and the learning goal is 0.00001.
The initial population size of genetic algorithm is 25; The number of evolutions is 150; The crossing probability is 0.3; The probability of variation is 0.2.

2) GA-BP Model Training and Prediction
First, the input variables are input into the BP neural network through the input nodes, and the genetic algorithm encodes the initial weights and thresholds of the BP neural network. Then calculate the length of each individual of the genetic algorithm. Each individual contains all the weights and thresholds in the BP neural network. The calculation formula of individual length is:

$$T = 4 \times c + c \times 1 + c + 1 = 6c + 1 \tag{4-5}$$

Where, c is the number of nodes in the hidden layer of the network, and T is the length of the individual of the genetic algorithm.

Secondly, the genetic algorithm is used to calculate the fitness value, and the absolute value F of the error between the predicted output and the ideal output of the BP neural network is taken as the individual fitness value. F is calculated as follows:

$$F = \sum_{i=1}^{n} |y_i - o_i| \tag{4-6}$$

Where, n is the number of network output nodes; y_i and o_i are the expected output and predicted output of the BP neural network respectively.

Then, genetic algorithm finds the optimal fitness value and its corresponding individuals through selection, crossover and mutation operations. This project constructs a selection operation method based on fitness ratio. The calculation method of selection probability of individual i is as follows:

$$f_i = \frac{k}{F_i} \tag{4-7}$$

$$p_i = \frac{f_i}{\sum_{j=1}^{N} f_j} \tag{4-8}$$

Where, F_i is the fitness value corresponding to the individual i; k is the coefficient, set to 10; N is the number of individuals in the population. This project also constructs a cross operation method based on real number cross. The cross calculation formula of the kth chromosome a_k and the first chromosome a_l at position j is as follows:

$$\left.\begin{aligned} a_{kj} &= a_{kj}(1-b)+a_{lj}b \\ a_{lj} &= a_{lj}(1-b)+a_{kj}b \end{aligned}\right\} \quad (4\text{-}9)$$

Where, b is a random number between [0,1]. Select the m-th gene of the nth individual a_{mn} for variation, and the formula for variation is as follows:

$$a_{mn} = \begin{cases} a_{mn}+(a_{mn}-a_{max})\times r_2\left(\dfrac{1-g}{G_{max}}\right)^2 & r > 0.5 \\ a_{mn}+(a_{min}-a_{mn})\times r_2\left(\dfrac{1-g}{G_{max}}\right)^2 & r \le 0.5 \end{cases} \quad (4\text{-}10)$$

Where, a_{max} and a_{min} are the upper and lower bounds of gene a_{mn} respectively; r_2 is a random number, g is the current iteration number; G_{max} is the maximum number of evolutions, set to 100; r is a random number between [0,1].

Finally, the weight and threshold corresponding to the optimal individual are assigned to the BP neural network, and the BP neural network continues to adjust the weight and threshold to the optimal value according to the error between the calculated prediction result and the ideal result, and the GA-BP model is trained. After model training, TEC value can be calculated according to the information of input variables and prediction rules:

$$TEC = f(H_j-\theta_j) = \frac{1-e^{-(H_j-\theta_j)}}{1+e^{-(H_j-\theta_j)}} \quad (4\text{-}11)$$

Where, H_j is the output result of hidden layer; θ is the threshold of the output layer.

3) Calculation of GNSS ionospheric error correction
The equation of ionospheric error correction that should be applied when satellite signal uses range code and carrier phase for positioning [Li 2012] is as follows:

$$V_{ion} = \pm\frac{40.3}{f^2}TEC \quad (4\text{-}12)$$

Where, V_{ion} represents the ionospheric error correction; f is the frequency of the GNSS signal passing through the ionosphere. Substitute the TEC value predicted by GA-BP model into equation (4-11) to obtain the GNSS ionospheric error correction result at the corresponding position time.

4.2.2. MODEL VALIDATION

EXPERIMENT DESIGN

In this project, Klobuchar model, ARIMA model and the proposed GA-BP model are selected for precision comparison. Based on the ionospheric IONEX file published by IGS from 2011 to 2017, TEC data at GIM grid points in Central Europe $-20°E \sim 140°E$, $10°N \sim 80°N$ are extracted every $5°N \times 10°E$, with a time resolution of 2h. The specific sample number of each data set is shown in Table 4-1. Since the variation range of TEC varies greatly with latitude, in order to better test the working conditions of the model in different regions with different variation ranges of TEC, this project has selected three locations (low latitude

($10°N,120°E$), middle latitude ($45°N,120°E$) and high latitude ($80°N,120°E$)) as the experimental objects at the same time. A total of 99723 groups of samples were obtained, and the extracted data were classified into training sets and test sets. The training set includes TEC data of three locations from 2011 to 2016; The test set contains the data of three locations in 2017.

Table 4-1: Number of samples in each data set (Unit: piece)

Data set	Low latitude sample quantity	Mid latitude sample quantity	High latitude sample quantity	Total number of samples
Trainning set	28496	28496	28496	85488
Test set	4745	4745	4745	14235

On the basis of the short-term TEC prediction experiment, the project continues to further evaluate the prediction effect of the proposed algorithm model in the medium and long-term TEC prediction, that is, predict the short-term (1 week), medium-term (January) and long-term (1 year) TEC changes at three different locations, and compare with the prediction results of Klobuchar model and ARIMA model to analyze the prediction effect of the model. The specific experimental settings are shown in Table 4-2.

Table 4-2: Experiment design (no units)

Experiment model	Experiment 1	Experiment 2	Experiment 3
Klobuchar ARIMA GA-BP	Predict TEC changes in the next week at three different latitudes using each model	Predict TEC changes in the next January at three different latitude points using each model	Predict TEC changes in the next year at three different latitude points using various models

In the experiment, TEC data extracted from the 2017 IONEX file released by IGS is used as the reference true value, and deviation () and root mean square error (RMSE) are used as the precision evaluation indicators of the model. The calculation formula of and is as follows:

$$\mathrm{BIAS} = \left|\mathrm{TEC}_{\mathrm{pre}} - \mathrm{TEC}_{\mathrm{ref}}\right| \quad \textbf{(4-13)}$$

$$\mathrm{RMSE} = \sqrt{\frac{1}{N_p}\sum_{i}\left(\mathrm{TEC}_{\mathrm{pre}}(i) - \mathrm{TEC}_{\mathrm{ref}}(i)\right)^2} \quad \textbf{(4-14)}$$

Where, $\mathrm{TEC}_{\mathrm{pre}}$ represents the TEC value predicted by the model; $\mathrm{TEC}_{\mathrm{ref}}$ indicates the true value of TEC; N_p indicates the number of predictions.

RESULTS ANALYSIS

The precision of the GA-BP based Central European GNSS ionospheric error model proposed in this project is compared with the short-term predictions of Klobuchar model and ARIMA model, as shown in Figure 4-2 and Table 4-3.

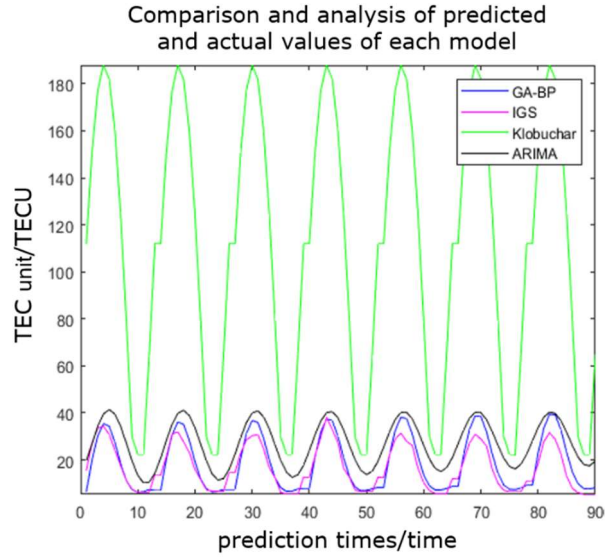

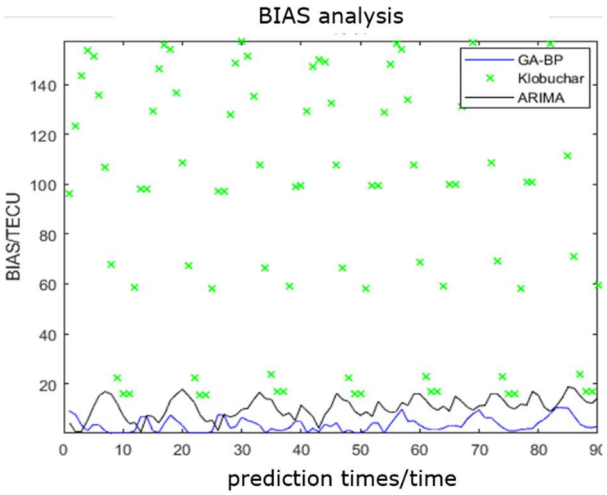

(a) Comparison of low latitude prediction results

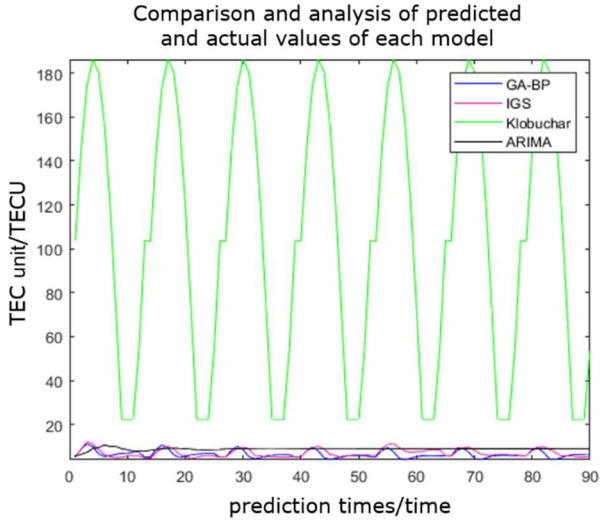

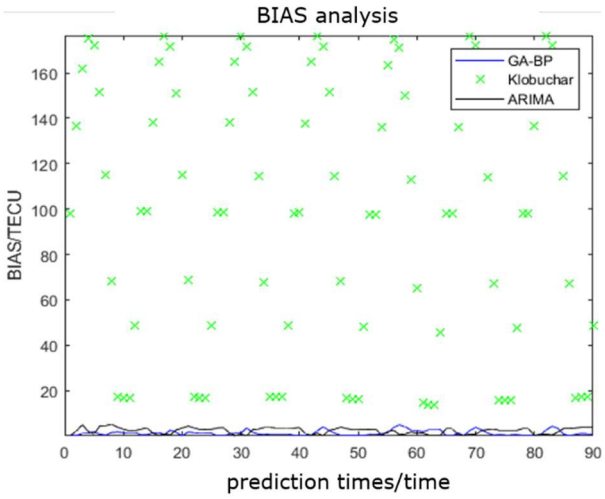

(b) Comparison of mid latitude prediction results

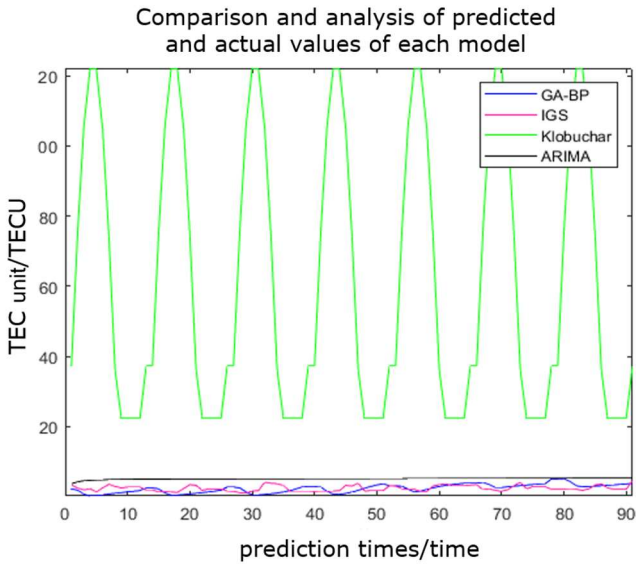

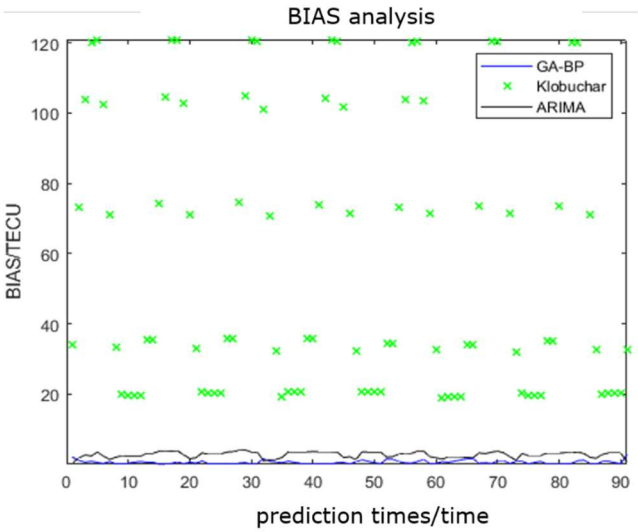

(c) Comparison of high latitude prediction results

Figure 4-2: Comparison chart of short term (1 week) forecast results based on various models

Table 4-3: Comparison of short-term (one week) prediction accuracy based on various models (unit: TECU)

Error type	prediction model	Low latitude	Mid latitude	High latitude
accuracy（RMSE）	Klobuchar	105.48	114.19	71.21
	ARIMA	11.30	2.67	2.85
	GA-BP	3.66	1.70	0.75

It can be seen from the sub maps in Figure 4-2 that the changes of ionospheric TEC are more active in low latitude regions, while the changes in mid latitude and high latitude regions are more gentle. From the comparison between the predicted values and actual values of each model in Figure 4-2, combined with the comparison results of short-term prediction accuracy of each model in Table 4-3, it can be seen that the RMSE of the GA-BP model built in this project at low, middle and high latitudes is 3.66 TECU, 1.70 TECU and 0.75 TECU respectively, which is lower than 11.30 TECU, 2.67 TECU and 2.85 TECU of ARIMA model; It is much lower than 105.48 TECU, 114.19 TECU and 71.21 TECU of Klobuchar model.

Table 4-4 reflects the accuracy improvement rate of GA-BP model compared with the other two models. Among them, compared with Klobuchar model, the prediction accuracy of the GA-BP model built in this project has increased by 96.53%, 98.51% and 98.95% in low latitude, middle latitude and high latitude respectively. In the mid latitude region, the prediction accuracy of the GA-BP model built by this project has increased by 36.33% compared with ARIMA model. In the low latitude and high latitude areas, the model accuracy improved by 67.61% and 73.68% respectively. It can be seen from the BIAS curves of each model in Figure 4-2 that the BIAS of the GA-BP model built in this project is lower than ARIMA model and Klobuchar model in the short-term prediction process. These fully reflect the accuracy advantage of the GA-BP model built in this project in short-term prediction of TEC changes.

Table 4-4: Improvement rate of short-term prediction accuracy (RMSE) of GA-BP model (unit:%)

type	Low latitude	Mid latitude	High latitude
Lifting rate compared with Klobuchar model	96.53	98.51	98.95
Improvement rate compared with ARIMA model	67.61	36.33	73.68

It can be seen from the comparison chart of predicted values and actual values of each model in Figure 4-2 that the GA-BP model built in this project can well fit the changes of TEC in different latitudes in terms of fitting the changes of TEC; ARIMA model can better fit the changes of TEC in the regions with active changes of TEC in low latitudes, but the fitting effect decreases significantly in the middle and high latitudes, and the whole fitting curve tends to a straight line, which can not fit the changes of TEC well; The fitting ability of Klobuchar model is the worst among the three models. The above shows that the GA-BP model built in this project is superior to the other two models in terms of prediction accuracy and ability to fit TEC changes.

Experiment 2 shows the prediction of TEC change in one month at three locations of each model. The experimental results are shown in Figure 4-3 and Table 4-5.

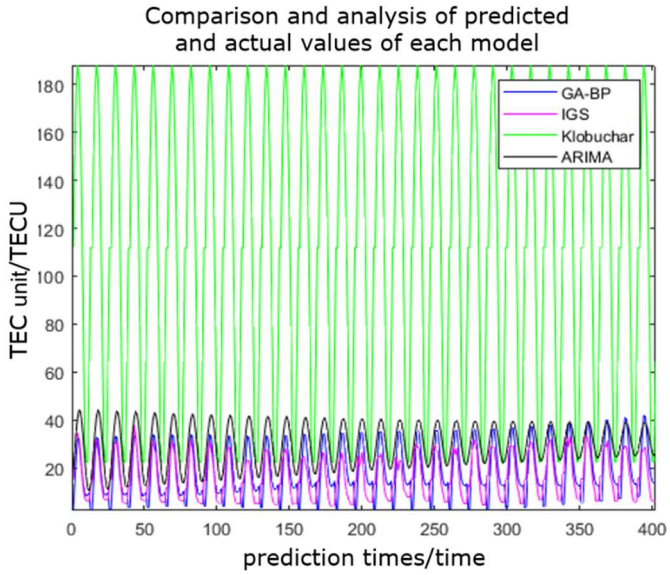

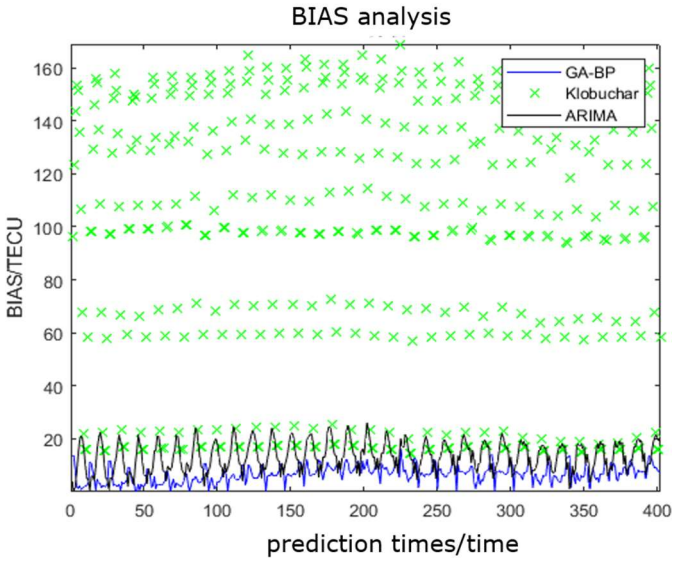

(a) Comparison of low latitude prediction results

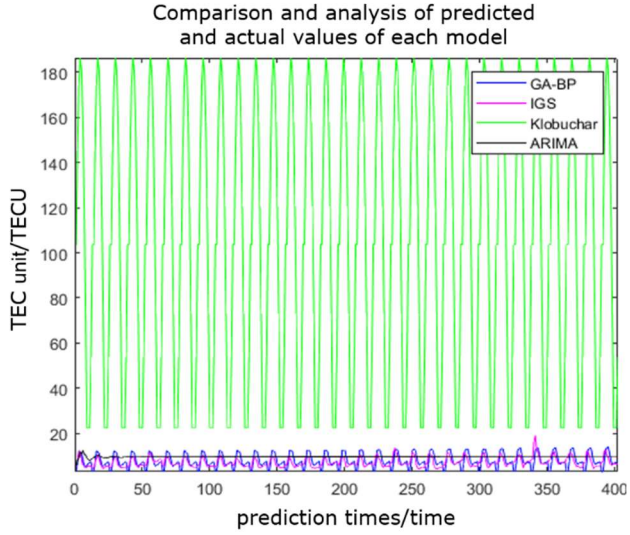

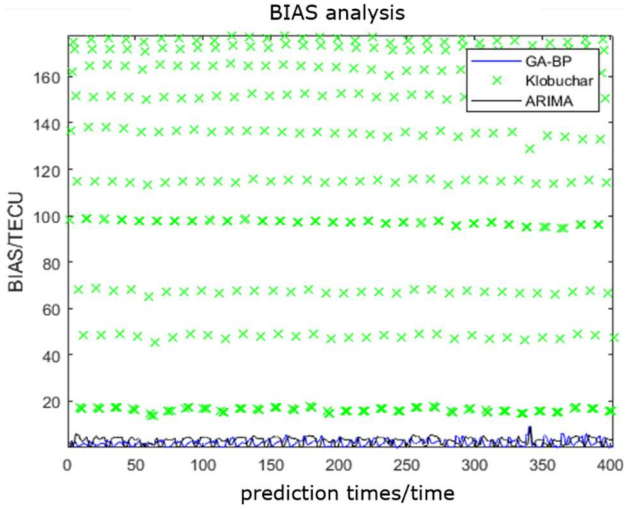

(b) Comparison of low latitude prediction results

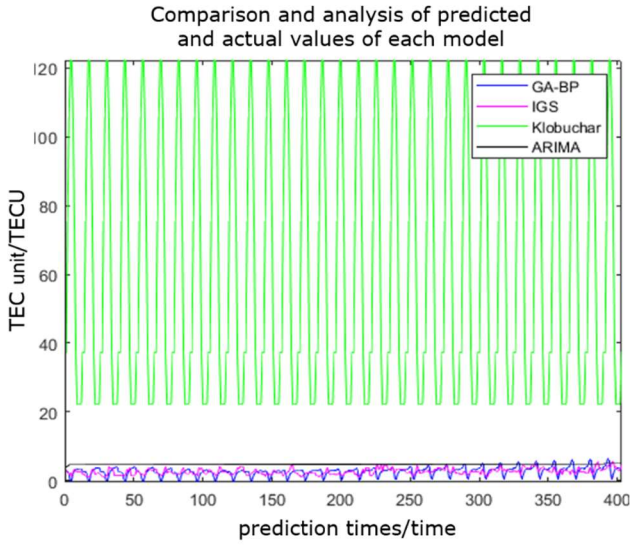

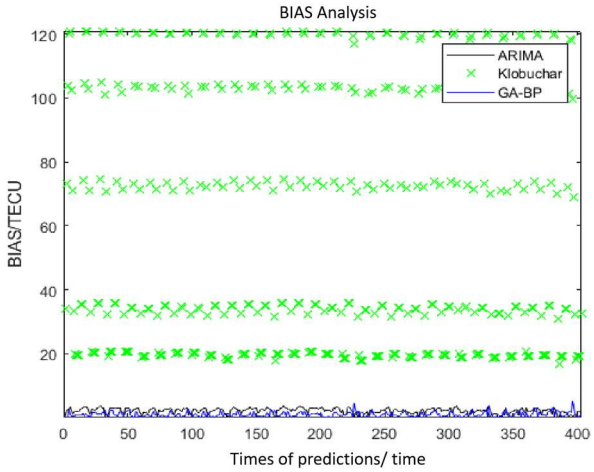

(c) Comparison of high latitude forecast results

Figure 4-3: Comparison of medium-term (January) prediction results based on various models

As can be seen from the comparison between the prediction of each model and the actual value in Figure 4-3, the GA-BP model constructed in this project performs well in the

nonlinear fitting ability of TEC in the interim prediction process, and could better reflect the change of TEC over time.

Table 4-5: Comparison of medium-term (January) prediction accuracy based on various models (unit TECU)

Error type	Prediction Model	Low latitude	Middlelatitude	Highlatitude
Precision（RMSE）	Klobuchar	105.07	113.76	70.92
	ARIMA	14.50	3.31	3.95
	GA-BP	6.66	2.57	0.85

Table 4-5 shows the prediction accuracy of the three models. The RMSE of the GA-BP model constructed in this project at low, middle and high latitudes are 6.66 TECU, 2.57 TECU and 0.85 TECU, respectively. Lower than 14.50 TECU, 3.31 TECU and 3.95 TECU in ARIMA model; It is much lower than the 105.07 TECU, 113.76 TECU and 70.92 TECU of Klobuchar model.

Table 4-6: Medium-term prediction accuracy (RMSE) improvement rate of GA-BP model (unit: %)

Type	Low latitude	Middle latitude	High latitude
Rate of increase relative to Klobuchar Model	93.66	97.74	98.80
Rate of increase relative to ARIMA Model	54.07	22.35	78.48

Table 4-6 shows the increase ratio predicted by GA-BP model compared with other models. As can be seen from Table 4-6, compared with Klobuchar model, the accuracy of the GA-BP model constructed in this project reaches 93.66%, 97.74% and 98.80% respectively at different latitudinal positions. Compared with ARIMA model, the precision improvement ratio also reached 54.04%, 22.35% and 78.48%, respectively.

As can be seen from the BIAS curve of the medium-term prediction of each model in Figure 4-3, the BIAS of the GA-BP model constructed in this project is basically lower than that of the ARIMA model and much lower than that of the Klobuchar model. This indicates that the GA-BP algorithm model proposed in this project still shows good fitting ability and prediction accuracy in the medium-term prediction of TEC, both of which are superior to the other two models. The fitting effect of ARIMA model was better in the first few days at low latitude, and then gradually decreased with the increase of time, which could not well reflect the change of TEC over time. In addition, in the middle and high latitudes, although the prediction accuracy of ARIMA model has been greatly improved compared with that of low latitudes, its fitting curve still cannot effectively fit the change of TEC over time. Finally, compared with the other two models, the prediction accuracy of Klobuchar model and the fitting ability of TEC were still poor.

To sum up, experiment 2 proves that in the process of predicting the mid-term changes of TEC, the GA-BP model constructed in this project still performs well, and its prediction accuracy and fitting ability of TEC changes are superior to other models.

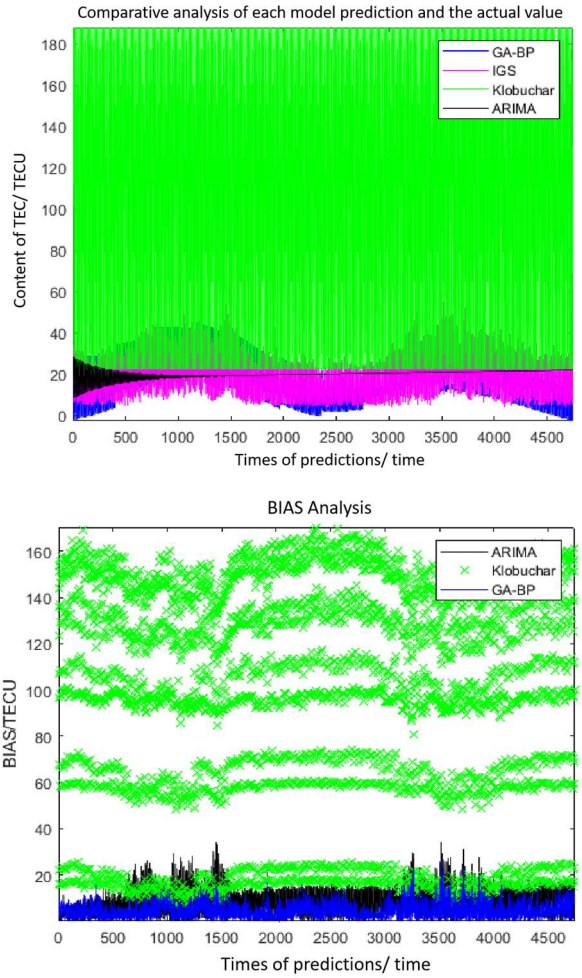

(a) Comparison of low-latitude forecast results

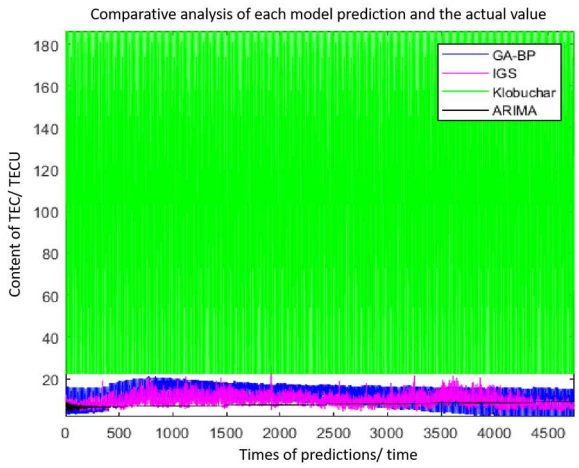

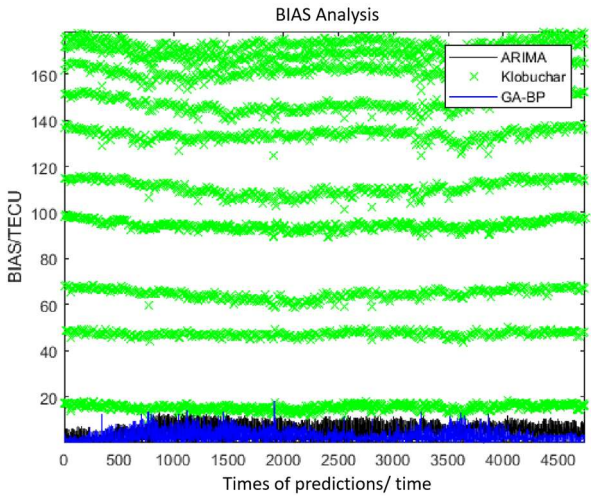

(b) Comparison of mid-latitude forecast results

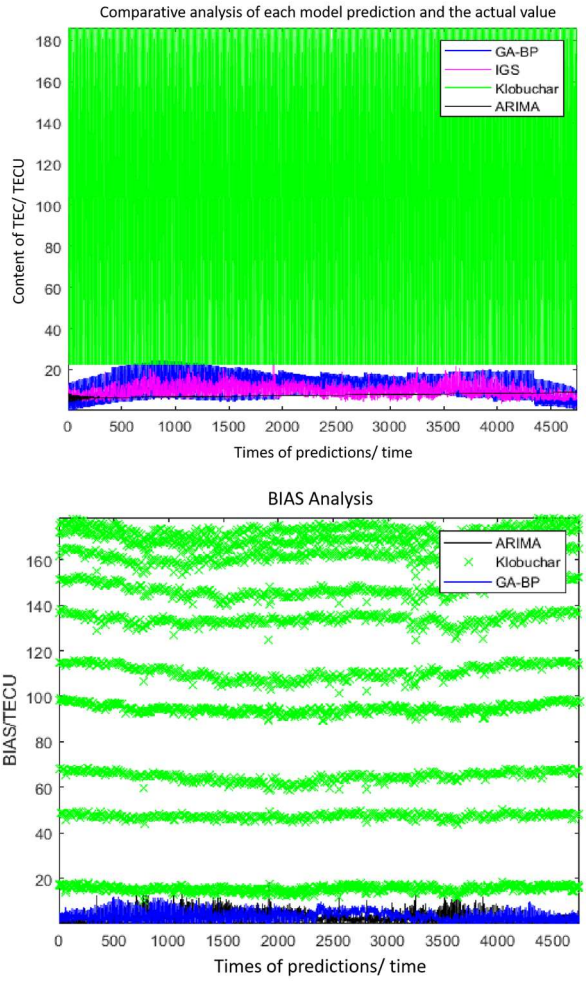

(c) Comparison of high latitude forecast results

Figure 4-4: Comparison of long-term (1 year) prediction results based on various models

Table 4-7: Comparison of long-term (1 year) prediction accuracy based on various models (unit TECU)

Error type	Prediction Model	Low latitude	Middle latitude	High latitude
	Klobuchar	103.53	98.23	67.95

Precision（RMSE）	ARIMA	10.52	6.67	4.33
	GA-BP	5.73	3.75	2.23

Experiment 1 and experiment 2 respectively prove that the GA-BP model constructed in this project shows good accuracy and fitting effect in short-term and medium-term TEC prediction. The project then studies the long-term prediction effect of this model. Figure 4-4 and Table 4-7 show the results of experiment 3. Table 4-7 shows the accuracy comparison of different models in the process of long-term prediction. The RMSE of the GA-BP model constructed in this project at low, middle and high latitudes are 5.73 TECU, 3.75 TECU and 2.23 TECU, respectively. Still lower than the ARIMA model of 10.52 TECU, 6.67 TECU and 4.33 TECU; It is much lower than the 103.53 TECU, 98.23 TECU and 67.95 TECU of Klobuchar model. It can be seen that among the three models, the GA-BP model constructed in this project still has the highest accuracy.

Table 4-8: Long-term prediction accuracy (RMSE) improvement rate of GA-BP model (unit: %)

Type	Low latitude	Middle latitude	High latitude
Rate of increase relative to Klobuchar Model	94.47	96.18	96.72
Rate of increase relative to ARIMA Model	45.53	43.78	48.50

Table 4-8 shows the accuracy improvement rate of GA-BP model compared with other models in long-term prediction. Among them, compared with Klobuchar model, the accuracy of GA-BP model constructed in this project reaches 94.47%, 96.18% and 96.72% respectively in each position. Compared with ARIMA model, the improvement ratio reaches 45.53%, 43.78% and 48.50%, respectively. Combined with the BIAS analysis diagram of each model in Figure 4-4, it can be seen that in the process of predicting the one-year change of TEC, the GA-BP model constructed in this project can still effectively fit the change of TEC and maintain a good accuracy, while the accuracy of ARIMA model is slightly lower. The Klobuchar model has the worst accuracy. Compared with the accuracy of short-term and medium-term prediction, the accuracy of long-term prediction of the GA-BP model constructed in this project is slightly lower, but its overall prediction accuracy is still higher than that of the other two models. As can be seen from the comparison of prediction results of various models in Figure 4-4, in the process of long-term prediction of TEC changes, the fitting ability of GA-BP model constructed in this project to TEC at various latitude locations also declines compared with short and medium term prediction, but the overall fitting effect is still better than the other two models. The fitting ability of ARIMA model is not good in long-term prediction. With the increase of prediction time, the fitting curve of ARIMA model tends to be a straight line, and the fitting effect of TEC over time is poor. However, the fitting effect of Klobuchar model is still inferior to the other two models.

To sum up, in the long-term prediction process of TEC changes, the GA-BP model constructed in this project is still superior to the traditional Klobuchar model and ARIMA sequence model in terms of fitting ability and prediction accuracy.

4.3. THE GMDH BASED TROPOSPHERIC ERROR MODEL

4.3.1. MODEL DESIGN

Aiming at the tropospheric error of BDS/GALILEO multi-system system, this project establishes a tropospheric error model based on GMDH (Group Method of Data Handling).

GMDH

GMDH is a heuristic self-organization modeling method proposed and developed by academician Ivakhnenko of Ukrainian Academy of Sciences in 1967. This method can effectively identify complex multivariable systems and give good prediction results. Its main idea is to simulate the evolutionary process of "heredity, variation, selection and evolution" of organisms: starting from a simple initial model set (initial organization), the elements in the model set are combined with each other according to certain rules to generate a new intermediate candidate model (heredity, variation), and then through some strategy or scheme to screen the intermediate candidate model (selection). This process of heredity, variation, selection and evolution is repeated constantly, so that the complexity of the generated intermediate model is continuously increased until the complexity of the newly generated model is no longer increased and the optimal complexity model is obtained. It is very suitable for the modeling of complex systems with high prediction accuracy and optimal complexity. GMDH can make decisions from the approximate, uncertain and even contradictory knowledge environment, avoiding the overfitting or under-fitting of the model structure.

GMDH neural network can be expressed as a set of neuron model, in which different pairs of neurons in each layer are connected by quadratic polynomial, and new neurons are formed in the next layer. For a given input vector $X=\{x_1,x_2,\ldots,x_n\}$, the result is as close to the actual output value y as possible by searching for a function $\hat{f}$. For a complex nonlinear system, the function form of multi-input and single-output data pairs is:

$$y_i = f(x_{i1},x_{i2},\ldots,x_{in}) \quad \textbf{(4-15)}$$

Where, y_i is the actual output; $x_{i1},x_{i2},\ldots,x_{in}$ is the input; N is the number of input variables.

The output value given by GMDH neural network training is

$$\hat{y}_i = \hat{f}(x_{i1},x_{i2},\ldots,x_{in}) \quad \textbf{(4-16)}$$

There is often a deviation from $\hat{y}_i$ to the actual output y_i, and its residual sum of squares is

$$e=\sum_{i=1}^{N}[\hat{f}(x_{i1},x_{i2},\ldots,x_{in})-y_i]^2 \quad \textbf{(4-17)}$$

GMDH neural network can be obtained by minimizing e.

TROPOSPHERIC ERROR MODEL CONSTRUSTION

The technical roadmap of GNSS tropospheric error modeling method based on GMDH is shown in Figure 4-5.

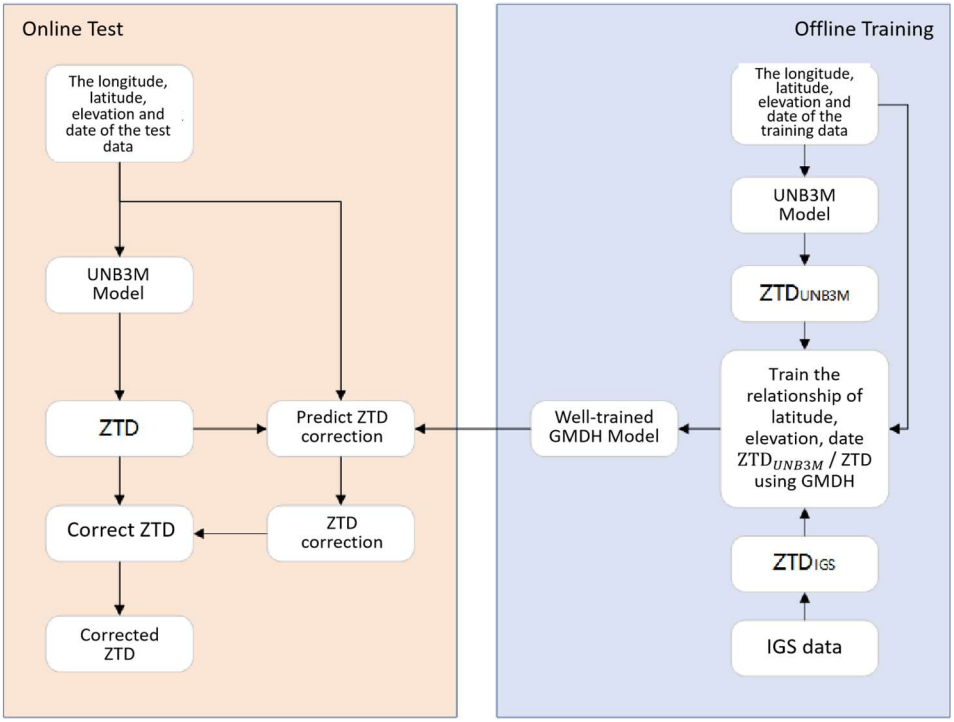

Figure 4-5: GMDH-based GNSS tropospheric error modeling roadmap for China-Europe

The method is mainly divided into two parts: offline training and online correction. In the offline training, firstly, the reference ZTD_{IGS} is solved through the files provided by International GNSS Service (IGS). Then, the ZTD_{UNB3M} estimated by the UNB3M model can be calculated according to the longitude and latitude, elevation and annual product day of the training data used. The ZTD error estimated by the UNB3M model can be calculated by subdividing the two. Then, ZTD_{UNB3M} calculated by longitude and latitude, elevation, annual product and UNB3M model is Grouped as inputs to the Grouped Method of Data Handling (GMDH). The ZTD calculated by the UNB3M model relative to the ZTD error correction provided by IGS will be used as the output of GMDH to train the GMDH model, and a well-trained GMDH model can be obtained. In the part of online correction, the longitude and latitude, elevation and annual product day of the test data are first input into the UNM3M model to obtain the ZTD estimated by the UNM3M model, and then the longitude and latitude, elevation, annual product day of the test data and ZTD estimated by the UNM3M model are input into the offline trained GMDH model. The ZTD error correction of GMDH model for UMB3M model can be obtained, and finally the ZTD estimated by UNB3M model can be modified to obtain the modified ZTD.

4.3.2. MODEL VALIDATION

In this project, Saastamoinen model (briefly referred to as SAAS in the figure and table), EGNOS model, UNB3M model and the proposed GNSS Tropospheric delay model based on GMDH are selected for comparison, and ZTD obtained from IGS is used as reference. In this project, mean deviation (BIAS) and root mean square error (RMSE) commonly used in tropospheric studies are selected as the accuracy evaluation indexes of the model. BIAS is used to measure the mean deviation degree of the model, and RMSE is used to measure the accuracy of the model. The calculation formula of BIAS and RMSE is as follows:

$$BIAS = \frac{1}{D}\sum_{d=1}^{D}(ZTD_{IGS} - ZTD_{Model}) \quad (4\text{-}18)$$

$$RMSE = \sqrt{\frac{1}{D}\prod_{d=1}^{D}(ZTD_{IGS} - ZTD_{Model})} \quad (4\text{-}19)$$

Where, D is the zenith tropospheric delay data sample, ZTD_{IGS} is the zenith tropospheric delay obtained by solving IGS files, ZTD_{Model} is the zenith tropospheric delay predicted by the model.

EXPERIMENT 1

Twenty-eight IGS stations uniformly distributed in the China-Europe route region are randomly selected as research objects. The 2018 data of these 28 IGS stations are used to train the GMDH model, and the 2019 data of these 28 IGS stations are used to test the reliability and accuracy of the GMDH model. The information of each IGS station is shown in Table 4-9. The location distribution of the station is shown in Figure 4-6.

Table 4-9: Information of each station in Experiment 1

No.	Site	Latitude	Longitud-e	Elevatio-n	No.	Site	Latitude	Longitu-de	Elevati-on
1	ankr	39.888	32.759	974.8	15	not1	36.876	14.99	126.2
2	artu	56.43	58.56	247.511	16	nril	69.362	88.36	47.894
3	badg	51.77	102.235	811.4	17	nvsk	54.841	83.236	123.643
4	bhr4	26.209	50.608	-13.9	18	nya2	78.930	11.859	81.5
5	chan	43.791	125.443	268.3	19	opmt	48.836	2.335	124.2
6	hksl	22.372	113.928	95.303	20	penc	47.79	19.282	291.7
7	hyde	17.417	78.551	441.68	21	pol2	42.68	74.694	1714.2
8	jfng	30.516	114.491	71.324	22	reyk	64.139	-21.955	93.1
9	joze	52.097	21.032	141.4	23	shao	31.1	121.2	22.09
10	kiru	67.857	20.968	390.9	24	svtl	60.533	29.781	76.8
11	kit3	39.135	66.885	622.6	25	tehn	35.697	51.334	1194.57
12	lhaz	29.657	91.104	3622	26	urum	43.808	87.601	858.9
13	madr	40.429	-4.25	829.5	27	yibl	22.186	56.112	95.1
14	meli	35.281	-2.952	93.5	28	zeck	43.788	41.565	1167

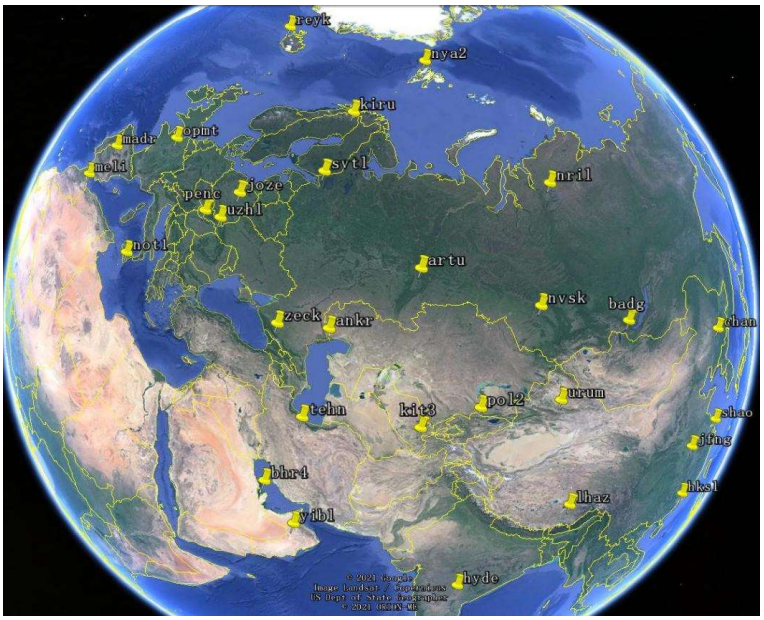

Figure 4-6: Position distribution of IGS stations in Experiment 1

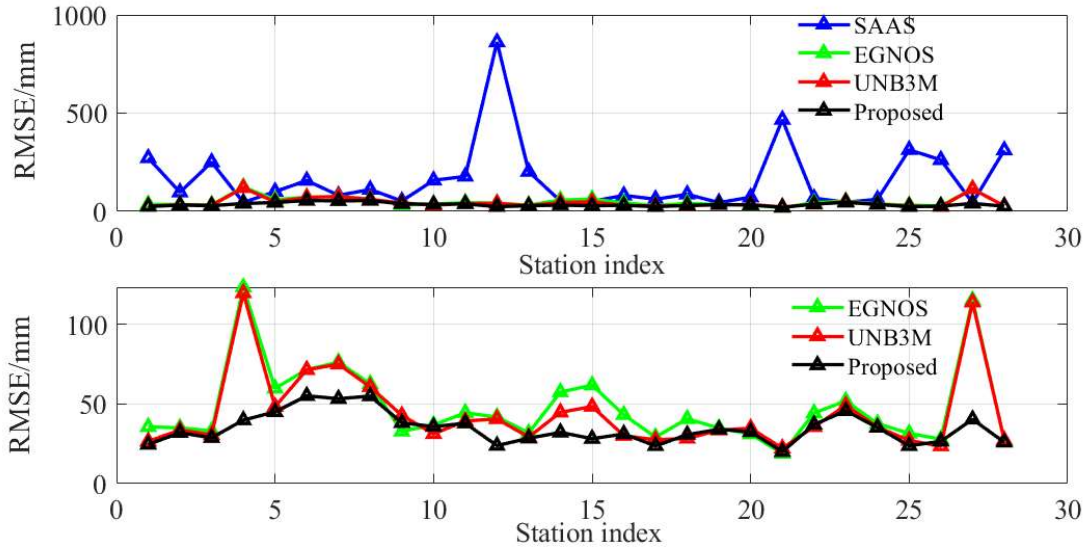

Figure 4-7: RMSE of various models in Experiment 1 in the China-Europe route region

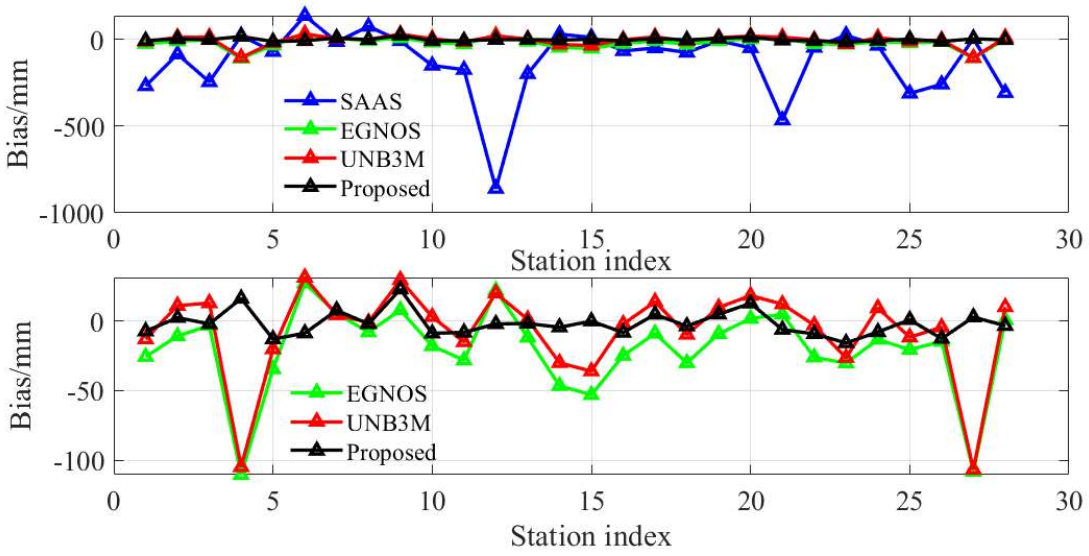

Figure 4-8: BIAS of various models in the China-Europe route region in Experiment 1

Table 4-10: RMSE of various models in the China-Europe route region in Experiment 1

RMSE	SAAS /mm	EGNOS /mm	UNB3M /mm	Proposed /mm
Mean	163.85	47.77	43.94	34.46
Max	861.66	123.31	119.67	55.12
Min	43.33	18.92	22.19	19.99

Table 4-11: BIAS of various models in the China-Europe route region in Experiment 1

BIAS	SAAS /mm	EGNOS /mm	UNB3M /mm	Proposed /mm
Mean	-123.61	-20.25	-7.11	-1.88
Max	135.92	27.01	31.10	22.64
Min	-860.41	-110.21	-106.55	-15.79

It can be seen from Figure 4-7, Figure 4-8 and Table 4-10 and Table 4-11 that in experiment 1, the Saastamoinen model without measured meteorological parameters as input has the worst accuracy. RMSE and BIAS of Saastamoinen model are far greater than those of EGNOS, UNB3M and the algorithm proposed by this project. The Saastamoinen model estimated that the mean, maximum and minimum zenith tropospheric delay errors of 28 IGS stations in 2019 were 163.85mm, 861.66mm and 43.33mm, respectively. The mean BIAS, maximum BIAS and minimum BIAS were -123.61mm, 860.41mm and 4.86mm, respectively. Compared with the algorithms proposed by EGNOS,UNB3M and this project, the accuracy of the UNB3M model is higher than that of the EGNOS model, while the algorithm proposed by this project has the highest accuracy, whose average RMSE, maximum RMSE and minimum RMSE are 34.46mm, 55.12mm and 19.99mm, respectively. The mean BIAS, maximum BIAS and minimum BIAS were -1.88mm, 22.64mm and -15.79mm, respectively.

EXPERIMENT 2

In order to further verify the effectiveness of the proposed model, experiment 2 has been designed in this project. The 28 stations selected in Experiment 1 in 2018 are used as

training data to train the GMDH model, and the new 18 stations which were not used as training data in 2019 are used as test data to verify the effectiveness of the model. The information of 18 new IGS stations is shown in Table 4-12. The distribution of trained IGS stations and tested IGS stations is shown in Figure 4-9, where the yellow icon is the training station and the red icon is the test station.

Table 4-12: Information table of IGS station added in Experiment 2

No.	Site	Latitude	Longitu-de	Elevatio-n	No.	Site	Latitud-e	Longitu-de	Elevati-on
1	aruc	42.286	44.086	1222	10	novm	55.031	82.909	149.98
2	bjfs	39.609	115.892	87.413	11	osn4	37.083	127.034	64.4
3	ebre	40.821	0.492	107.3	12	ramo	30.598	34.763	893.1
4	hkws	22.434	114.335	63.789	13	riga	56.949	24.059	34.7
5	hofn	64.267	-15.198	82.3	14	sofi	42.556	23.395	1119.6
6	isba	33.341	44.438	72.4	15	tash	41.328	69.296	439.7
7	kznz	55.791	49.119	94.6	16	ulab	47.865	107.052	1575.7
8	lck4	26.912	80.956	64.182	17	wroc	51.113	17.062	180.3
9	mikl	46.973	31.973	94.7	18	wtzz	49.144	12.879	665.9

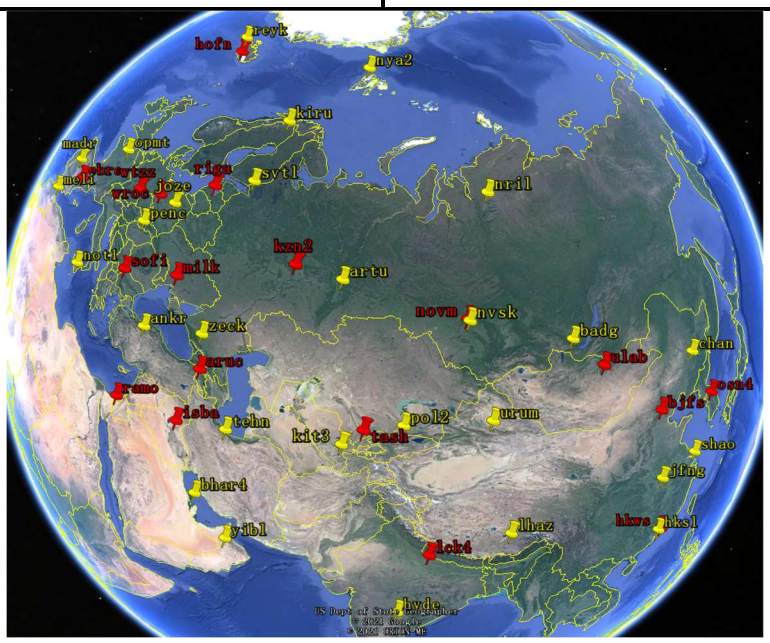

Figure 4-9: Location distribution of training station (yellow) and test station (red) in Experiment 2

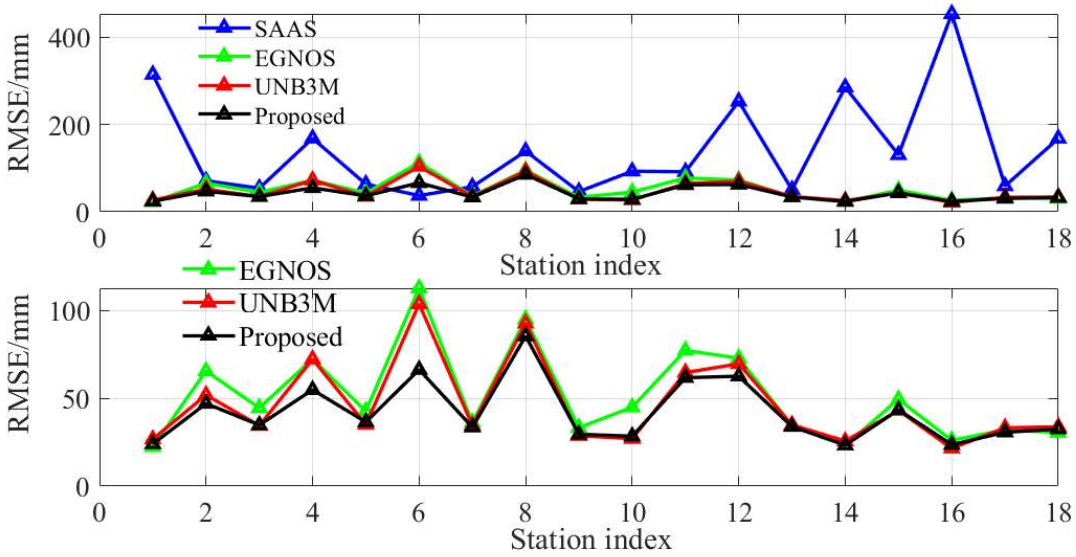

Figure 4-10: RMSE of various models in the China-Europe route region in Experiment 2

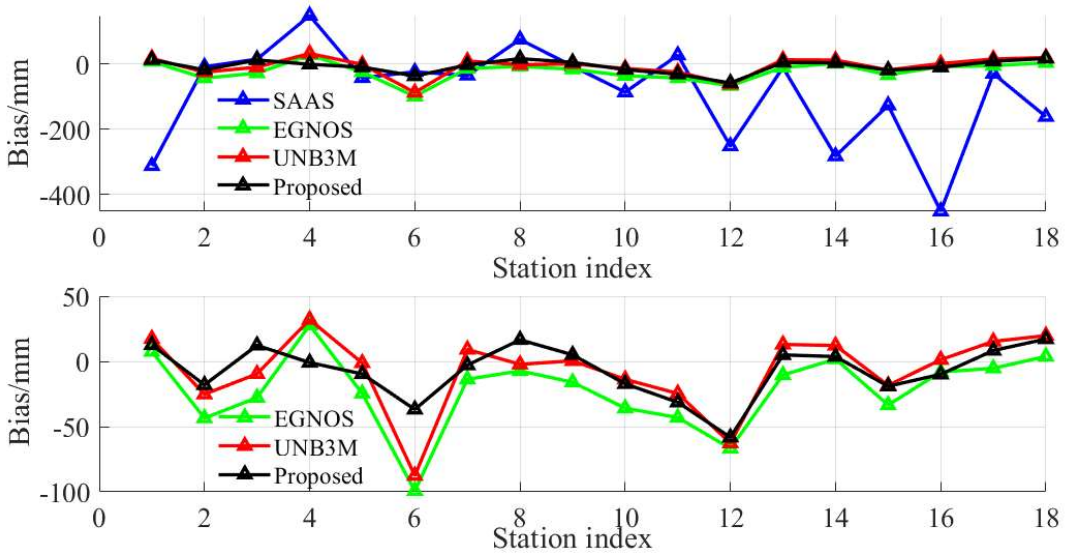

Figure 4-11: BIAS of various models in the China-Europe route region in Experiment 2

Table 4-13: RMSE of various models in the China-Europe route area in Experiment 2

RMSE	SAAS /mm	EGNOS /mm	UNB3M /mm	Proposed /mm
Mean	140.99	50.91	46.36	41.82
Max	453.71	112.81	103.87	85.51
Min	37.23	22.38	21.54	23.35

Table 4-14: BIAS of various models in the China-Europe route region in Experiment 2

BIAS	SAAS /mm	EGNOS /mm	UNB3M /mm	Proposed /mm
Mean	-86.96	-21.89	-6.93	-6.85
Max	148.59	27.78	32.02	17.15

Min	-452.02	-99.21	-87.58	-58.25

From Figure 4-10, Figure 4-11, Table 4-13 and Table 4-14, it can be seen that in Experiment 2, the Saastamoinen model without measured meteorological parameters as input still has the worst accuracy, and RMSE and BIAS are far greater than other models. The Saastamoinen model estimates that the mean, maximum and minimum zenith tropospheric delay errors of 18 IGS stations in 2019 were 140.99mm, 453.71mm and 37.23mm, respectively. The mean BIAS, maximum BIAS and minimum BIAS are -86.96mm, 148.59mm and -452.02mm, respectively. Compared with the algorithms proposed by EGNOS,UNB3M and this project, the accuracy of the UNB3M model is higher than that of the EGNOS model, while the algorithm proposed by this project is still the highest, with the average RMSE, maximum RMSE and minimum RMSE being 41.82mm, 85.51mm and 23.35mm, respectively. The mean BIAS, maximum BIAS and minimum BIAS are -6.85mm, 17.15mm and -58.25mm, respectively.

4.4. THE GBDT BASED MULTIPATH ERROR MODEL

Although multipath signals can be detected by certain methods, it is difficult to eliminate its influence in data processing by establishing a model. Based on this, this project builds a multipath error prediction model based on GBDT (Gradient Boosting Decision Tree).

4.4.1. MODEL DESIGN

The flowchart of GBDT-based multipath error model established by this project is shown in Figure 4-12.

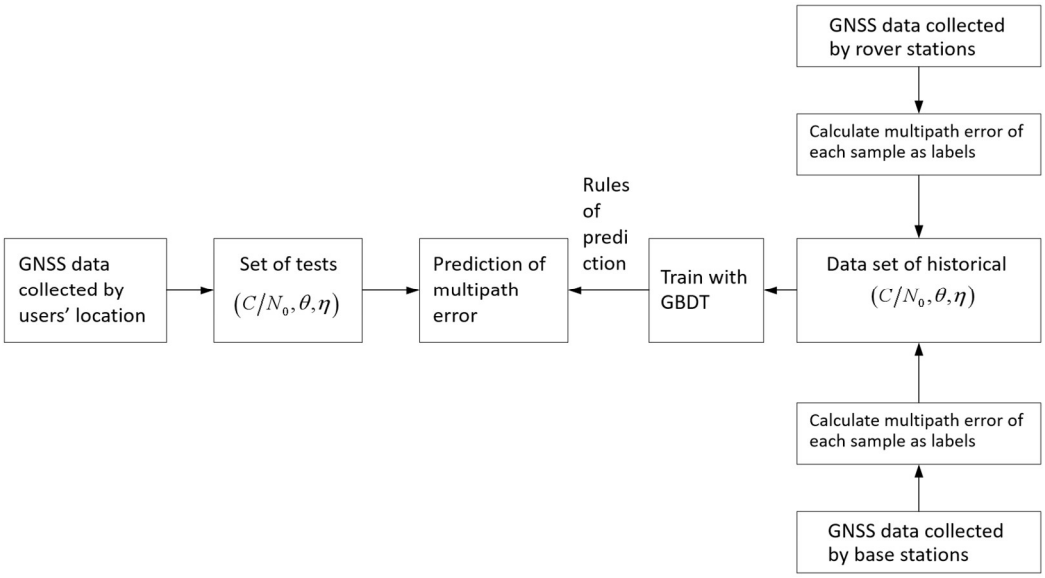

Figure 4-12: Multipath error prediction model based on gradient decision tree

Figure 4-12 shows the GBDT-based multipath error prediction model framework proposed by this project. GBDT (Gradient Boosting Decision Tree) is a supervised machine learning algorithm, which is based on gradient boosting idea and composed of several decision trees. This project uses GBDT to mine the relationship between input characteristic signal strength C/N_0, pseudo-distance residual η, satellite altitude Angle θ and output variable multipath error $\Delta\rho$, so as to build the multipath error $\Delta\rho$ prediction law.

The input of GBDT algorithm is $\boldsymbol{T}=\{(\boldsymbol{x}_1,\Delta\rho_1),(\boldsymbol{x}_2,\Delta\rho_2),(\boldsymbol{x}_3,\Delta\rho_3),\cdots(\boldsymbol{x}_N,\Delta\rho_N)\}$, namely, the historical training data set constructed. Each sample x contains three input features,

namely signal strength C/N_0, pseudo-distance residual η and satellite altitude Angle θ, as well as the multipath error $\Delta\rho$ obtained after pseudo-distance correction through the ionosphere and troposphere, as its label. That is, the n sample can be expressed as $x_n=(C/N_{0n},\eta_n,\theta_n)$: and its label is $\Delta\rho$. The squared loss function is used to evaluate the similarity between the predicted result of the learner $f(x_n)$ and the true value:

$$L\left(\Delta\rho_n,f\left(\boldsymbol{x}_n\right)\right)=\frac{1}{2}\left(\Delta\rho_n-f\left(\boldsymbol{x}_n\right)\right)^2 \quad (4\text{-}20)$$

GBDT algorithm uses iteration. Each iteration generates a new learner, namely the decision tree, along the direction of the fastest decline, namely the direction of negative gradient, to make up for the residual of the previous learner, making the loss function gradually smaller, that is to say, making the prediction more accurate. Then the addition model is used to weight the weak learner generated by each step iteration by setting the learning rate, and superposition them to generate the final strong learner. Let the number of iterations be M, and GBDT algorithm training process is as follows:

1) Initialize the weak learner:

$$f_0(\mathbf{x}_n)=\arg\min_{\gamma}\prod_{n=1}^{N}L(\Delta\rho_n,\gamma) \quad (4\text{-}21)$$

Where, $f_0(\mathbf{x}_n)$ is the weak learner initially constructed, is a decision tree containing only one root node, γ is its output, and is a constant. Then the iterative process begins:

2) For the m iteration $m=1,2,\ldots,M$

① Calculate the negative gradient as

$$\tilde{y}_n=-\left[\frac{\partial L(\Delta\rho_n,f(\mathbf{x}_n))}{\partial f(\mathbf{x}_n)}\right]_{f(\mathbf{x})=f_{m-1}(\mathbf{x})} \quad (4\text{-}22)$$

Where, $\tilde{y}_n$ represents the n negative gradient of the fourth sample, $f_{m-1}(\mathbf{x})$ is the learner built in the last iteration.

② Replace the labels $\Delta\rho_n$ of the samples in the original historical training data set with negative gradients $\tilde{y}_n$ to get a new data set $T_m=\{(\mathbf{x}_1,\tilde{y}_1),(\mathbf{x}_2,\tilde{y}_2),(\mathbf{x}_3,\tilde{y}_3),\ldots,(\mathbf{x}_N,\tilde{y}_N)\}$, and train it to get a new regression tree. The training process is shown as follows:

$$\mathbf{a}_m=\arg\min_{\mathbf{a}}\sum_{n=1}^{N}(\tilde{y}_n-h_m(\mathbf{x}_n;\mathbf{a})) \quad (4\text{-}23)$$

Where, $h_m(\mathbf{x};\mathbf{a}_m)$ represents the new regression tree generated by the m iteration. The parameters $\mathbf{a}_m$ of the regression tree include the split feature of each node, the optimal segmentation point and the predicted value of the node.

③ Accumulation to obtain a strong learner:

$$f_m(\mathbf{x})=f_{m-1}(\mathbf{x})+\beta h_m(\mathbf{x}_n;\mathbf{a}_m) \quad (4\text{-}24)$$

Where, $f_m(\mathbf{x})$ represents the strong learner obtained in the m iteration and β represents the learning rate. In order to prevent overfitting, it is usually selected between 0 and 1.

3) After the iteration, the final strong learner $f_M(\mathbf{x})$ is obtained:

$$f_M(\mathbf{x}) = f_0(\mathbf{x}) + \prod_{m=1}^{M} \beta h_m(\mathbf{x}; \mathbf{a}_m) \quad (4\text{-}25)$$

$f_M(\mathbf{x})$ represents the finally obtained strong learner, which is obtained by the weighted accumulation of the regression tree generated by successive iterations. As the multipath error prediction rule of GBDT output, $f_M(\mathbf{x})$ can be used to predict the corresponding multipath error of newly acquired variables $\mathbf{x} = (C/N_0, \eta, \theta)$ in the online part of the algorithm.

4.4.2. MODEL VALIDATION

In order to verify the accuracy of the multipath error model constructed in this project, the established model was used to calculate the observation data from the Mu Lway station at 10:00:00 on December 29, 2019. The estimated value of the multipath error was obtained and then compared with the multipath error obtained after correction of other errors. As can be seen from Figure 4-13, the multipath error predicted based on GBDT is within 5% of the error of the reference algorithm.

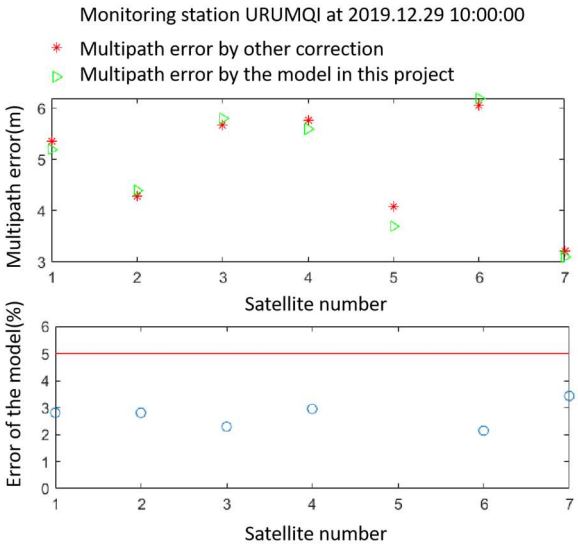

Figure 4-13: Predicted multipath error and true multipath error

4.5. SUMMARY OF THIS CHAPTER

In order to realize high-performance multi-system GNSS navigation for green air traffic, this project studies the mechanism of GNSS positioning error sources, and uses mathematical statistics and machine learning algorithms to realize the modeling of main GNSS error sources.

Aiming at the ionospheric error of BDS/GALILEO multi-system system, this project proposes an ionospheric error model based on GA-BP. The experimental results of short-, medium- and long-term prediction based on IGS data show that the GA-BP model constructed in this project has good prediction accuracy, and the average RMSE of short-, medium- and long-term prediction is 5.35 TECU, 2.67 TECU and 1.28 TECU, respectively. Compared with Klobuchar model, the accuracy of GA-BP model constructed in this project is improved by more than 90% in each latitude on average. Compared with the ARIMA model, the accuracy in each latitude is improved by more than 50% on average. The GA-BP model constructed in this project shows good TEC fitting ability both in low latitudes with drastic TEC changes and in middle and high latitudes with gentle TEC changes.

Aiming at the tropospheric error of BDS/GALILEO multi-system system, this project proposes a tropospheric error model based on GMDH. Two groups of experiments based on IGS data have proved that the tropospheric error model built in this project has better accuracy than the Saastamoinen model, EGNOS model and UNB3M model under standard atmospheric parameters. In experiment 1, the proposed GMDH tropospheric error model increased by 78.97%, 27.87% and 21.60% compared with Saastamoinen model, EGNOS model and UNB3M model, respectively. In experiment 2, the average RMSE based on GMDH tropospheric error model was increased by 70.34%, 17.85% and 9.8% compared with that of Saastamoinen model, EGNOS model and UNB3M model, respectively.

Aiming at the multipath error of the multi-system system of BDS/GALILEO, this project constructs a multipath error prediction model based on GBDT. The experimental results based on IGS observatory data show that the difference between the error predicted by the GBDT-based multipath error model and the error value of the reference algorithm is within 5%.

In general, the multi-system error model of BDS/GALILEO built by this project can provide real-time and high-precision correction parameters of GNSS ionospheric errors, tropospheric errors and multipath errors for civil aviation users within the China-Europe route with fewer input features and higher operation speed. It can effectively improve the accuracy and reliability of positioning results of BDS/GALILEO multi-system system, and has certain significance for the realization of green air traffic operation technology based on four-dimensional track.

5. MULTI-CONSTELLATION GNSS FAULT DETECTION AND EXCLUSION MODEL FOR G-ATM

5.1. RESEARCH STATUS OF GNSS FAULT DETECTION AND EXCLUSION

The accuracy and reliability of GNSS positioning is always affected by a variety issues in urban areas. The increased positioning uncertainty arising from the mixture of faulty signals is a result of the signal challenges posed by urban areas, mainly due to the NLOS/multipath effects from the surrounding environments (e.g., skylines, canyons, tunnels, etc.). In addition, malfunctions in the satellite clock, incorrect modelling of orbits, ionization of satellite payload silicon material, and inter-channel bias could also contribute to the excessive positioning errors [Bhatti 2007]. It is therefore very important to guarantee that the GNSS signals received from different satellites are correct and accurate, since these are related to GNSS positioning performance and integrity evaluation. In order to deal with this issue, a satellite navigation integrity monitoring scheme is proposed within the receiver, i.e. a Receiver Autonomous Integrity Monitoring (RAIM) system. This seeks to detect significant measurement errors arising from satellite malfunctions, the propagation environment, and others by the use of information including redundant measurements, the geometrical configuration of satellites relative to the users, and knowledge of nominal error behavior [Bhatti 2007].

Domestic and foreign scholars have done a lot of research on RAIM and similar GNSS quality control. One commonly-used technique, for example, is the signal weighting-based method [Wieser 2000]. The key idea of this method is to use one or multiple variables (e.g. C/N0 or elevation angle or their combination, etc.) of the observed pseudorange to obtain proportional weights and thus better quality signals in the positioning calculation. Furthermore, a number of algorithms for NLOS/multipath classification and thereafter mitigation or exploitation have been developed in recent years for environments such as urban areas. These strategies mainly include signal processing, antenna design and measurement-based modelling. Signal processing strategies distinguish the multipath and LOS signals based on the different characteristics of correlation functions. Such correlation aims at optimal approximation of the signal range [Heinrichs 2004, Blanch 2012]and some correlator-related and Delay-Locked Loop (DLL) technologies have been proposed for error mitigation, including narrow correlators, high-resolution correlators, strobe correlators, shaping correlators and Multipath Estimating Delay Lock Loop (MEDLL), etc. [Blanch 2012, Townsend 1995]. Receiver signal processing techniques can help to separate out the components of a multipath contaminated signal, but they are use-less if there is no direct LOS component. Antenna design strategies, meanwhile, include the use of antenna arrays, choke-ring antennas and other types of antennas to mitigate multipath effects and then improve the positioning performance [Thornberg 2003, Groves 2013]. Measurement-based strategies include integrating GNSS observables, measurements, satellite and signal information with other information sources. For example, using the GNSS elevation angle, pseudorange rate, C/N0, Doppler, etc., with the data from external aids such as Inertial Measurement Units (IMU), map aiding, ray tracing, etc., to improve the positioning performance [Soloviev 2008, Meguro 2009, Wang 2015].

Fault Detection and Exclusion (FDE) algorithms are also widely used for RAIM, these include: (1) range and position comparison methods [Lee 2004]; (2) least squares

residuals methods (LSRM) [Parkinson 1988]; (3) parity space methods [Sturza 1988]; and (4) maximum slope (MS) methods [Brown 1988]. Various extensions have been further developed from these basic methods. For example, Brown applied an improved MS method, denoted as the slope-max-max method, by imposing a worst-case hypothetical two-failure requirement on RAIM to handle dual satellite failures [Brown 1997]. Since the traditional RAIM algorithms are designed only for horizontal position monitoring, advanced RAIM (ARAIM) has emerged and therein the prospect of handling any number of simultaneous significant measurement errors, as well as vertical integrity monitoring [Rippl 2011]. Usually, FDE schemes entail both global and local tests, where the global test is used to check for the presence of any fault (for which a minimum of five satellites is required) and then the local test is used to identify the precise (for which six satellites are needed). A common approach to performing the global test is to use a test statistic, based on the Normalized Sum of Squared Error (NSSE), checking whether or not this variable, multiplied by a variance factor and by the degrees of freedom (n-p), follows a centrally chi-squared distribution [KuusniemiH 2004]. Basic FDE algorithms are able to detect and exclude one fault in all measures, whereas more advanced recursive consistency-checking based methods are able to exclude multiple faults in the measures. Blanch et al. has pro-posed a greedy search and L1 norm minimisation combinatorial method for multiple fault detection and exclusion (FDE) with pseudorange errors above 20 m [Blanch 2015]. Similarly, Hsu et al. uses greedy and exhaustive methods to improve the consistency checking process of the FDE [Hsu 2017]. These consistency check-based FDE algorithms are only effective when at least six satellites can be observed, however. In addition, although optimisation algorithms are used for the subset search, calculation efficiency is still a major issue with increased satellite numbers. Kaddour et al. has proposed a multi-faults detection algorithm based on observation projection on the information space [Kaddour 2015]. The positioning estimation is then calculated by excluding pseudorange measurement faults from the in-formation filter process. In the designed Kalman Filter (KF) process, the state vector is based on the simple difference, with the satellite with the highest elevation angle being the reference at each epoch. In urban canyons, however, the rapid changes in reference satellites may lead to reduced performance of the algorithm.

For the weighting and FDE-based methods for RAIM discussed above, the current signal weighting-based methods can find it difficult to determine the weightings in urban areas. For example, satellites with a lower elevation angle along the street direction may suffer from less NLOS than satellites with higher elevation angles in the crossing street direction. The current FDE algorithms are also not robust enough in these kinds of situations. Some of the algorithms use the single fault assumption, which is not suitable for urban vehicles positioning because the environment is changing rapidly and individual satellites can therefore be associated with faulty signals at one instant and not at the next instant. This means that the fault associated with the current satellite may be gone in the next epoch but then it may reappear again with either the same or a new satellite in the next epoch. Thus, the single fault assumption is not realistic in urban areas.

In addition, most of the multiple fault detection algorithms require at least six satellites for the FDE, which is difficult to achieve in an urban context. Furthermore, the huge number of subsets in the consistency check reduce the calculation efficiency of these algorithms. These problems are difficult problems that restrict the engineering application of fault detection algorithm in urban environment. In practical navigation applications, navigation information needs to be solved in a short enough time, generally not exceeding an epoch period, especially for the applications of high dynamic targets. Therefore, the research on GNSS fault detection and exclusion algorithm in urban environment has considerable application prospects and research value.

5.2. DOUBLE DETECTION FACTORS BASED FAULT DETECTION AND EXCLUSION ALGORITHM

5.2.1. ALGORITHM DESIGN

This section describes the specific implementation process of the GNSS FDE algorithm based on double detection factor in detail. Firstly, the algorithm framework is introduced, and then the algorithm initialization, pseudo range rate transfer model, fault detection based on double detection factors and detection thresholds determination are described in detail.

SYSTEM FRAMEWORK

The flowchart for the proposed FDE-based positioning algorithm is presented in Figure 5-1. Before a mission is assigned, it is necessary to conduct initialization of the receiver, in a relative open sky area, which could be satisfied frequently in urban areas. The purpose of initialization is to use this method aimed at multi-fault as the reference to create the initial datasets, using the measurements from these satellites with both "normal" and "fault" measurements, identified and labelled from the onboard GNSS receiver (as described in Section 0, algorithm initialization).

As shown in Figure 5-1, the "normal" measurements are stored in dataset 'Set I' and the 'non-trustable' measurements are stored in dataset 'Set II' (this initially contains only satellites with faulty measurements, but during the operation it will contain 'new' satellites that do not exist at last epoch, which may or may not have faulty measurements). During operation, once a new observation (means the satellite observed at a specific epoch) is received, a judgement will be carried out to check whether this satellite has already been tracked in Set I, in which case the observed information will be added to Set I (contains tracked satellites), otherwise the observed measurements will be added in Set II (contains faulty satellites and newly observed satellites). In this way, satellites in Set I are ensured that there is no fault in the previous epoch observation, while the failed satellites in the previous epoch observation and the new satellite are in Set II. In the detection process, the fault detection of the two satellite sets does not interfere with each other, but the satellites of set I and set II in each epoch will be redistributed according to their detection results, so as to keep updating. The detector (D_1) of each satellite in set I is obtained based on the Kalman innovation constructed from the pseudoranges observed in set I. Section 0 details the generation process of D_1. Compare D_1 with the threshold T_1 to determine whether the satellite is faulty. If the absolute value $|D_1|$ of D_1 is less than T_1, then the satellite in set I remains unchanged and is considered as a normal satellite; Otherwise, it is necessary to consider the receiver clock drift change detection. For an epoch, if the number of satellites meeting $|D_1| < T_1$ is less than 4, and the number of satellites in set I no longer meets the positioning requirements, then the clock drift change detection is performed for the epoch; Otherwise, the clock drift change rate will not be detected, and the satellites larger than T_1 will be moved to Set II. The detector (D_2) of Set II is created based on the difference in the pseudoranges of the satellites in Set II and predicted pseudoranges, which is used to detect whether the satellites in Set II or new satellites are normal, so as to meet the positioning requirements. Section 0 details the construction process of D_2. Among them, the predicted pseudoranges is calculated based on the real-time position obtained from the positioning solutions of the satellites in Set I at current epoch and the measurement in-formation of the satellites in Set II. Compare D_2 with the threshold T_2 to judge whether the satellite observation value is fault or normal. If it is normal, move the satellite back to Set I.

Once the faulty satellite in Set II is excluded, the $|D_2|$, the absolute value of D_2, will immediately drop below the threshold T_2. If the $|D_2|$ value remains below the T_2 for two consecutive epochs, we will move the satellite back to Set I where it would be used at that epoch for the positioning calculation. The threshold determination for D_2 and D_1 is described in Section 0 as well. The final positioning will be output if the usable number of satellites in Set I is equal to or greater than four.

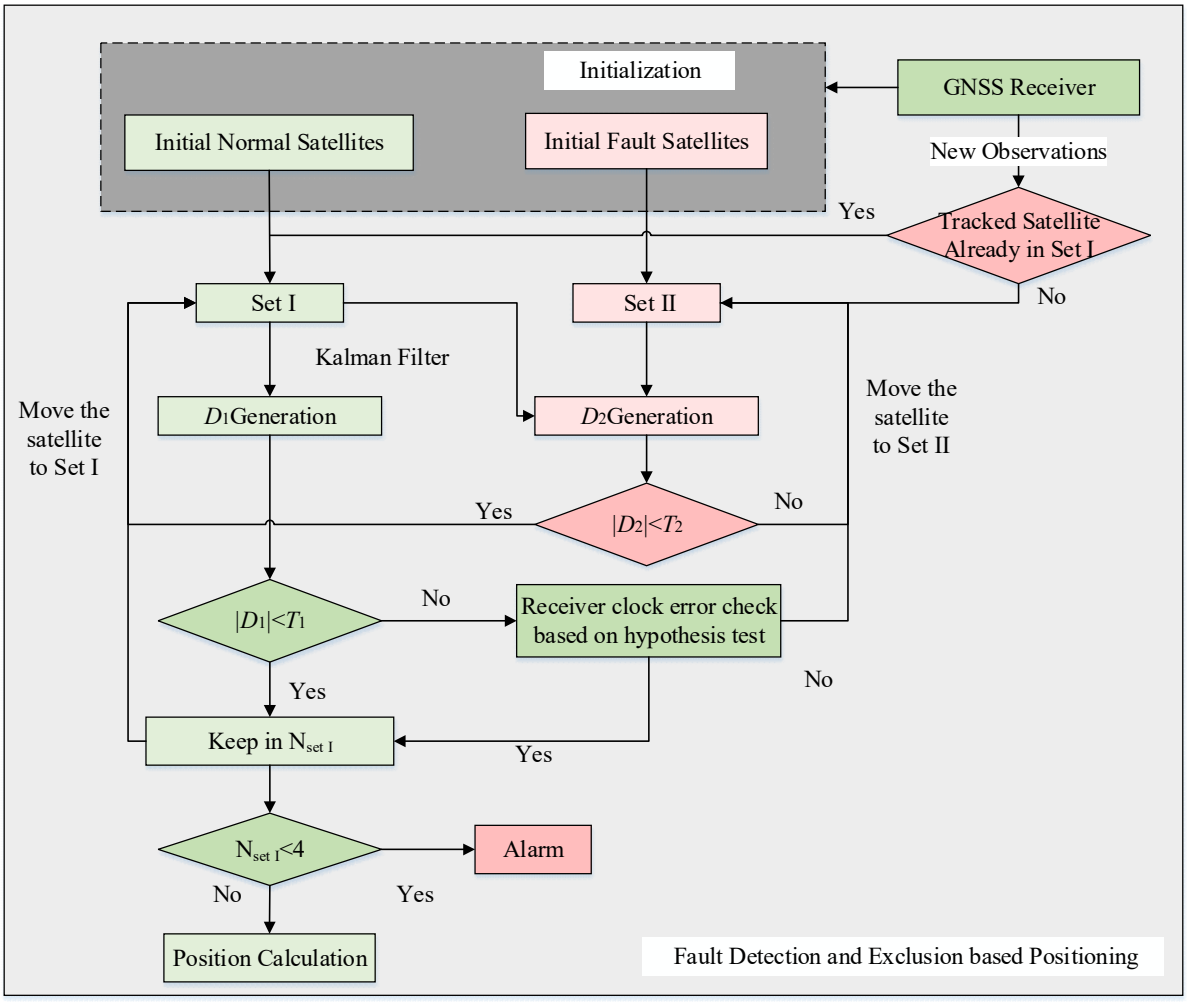

Figure 5-1:. System framework.

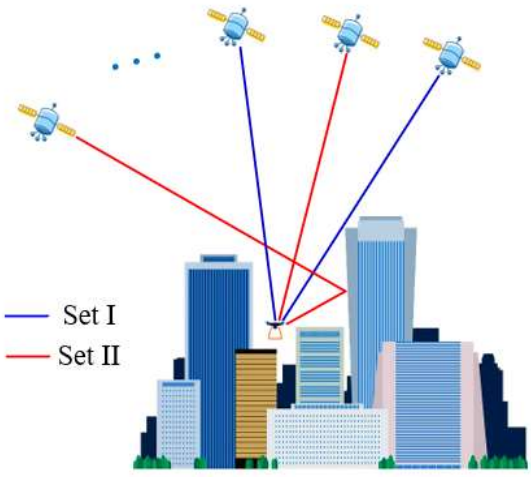

Figure 5-2: Normal satellite set (blue) and non-trustable satellite set (red).

ALGORITHM INITIALIZATION

As described in Section 0, the proposed process requires an initialization process in a relative open sky area. Since the position is known, we can use the known position and the observed satellite ephemeris to retrieve the pseudorange of each satellite, and then compare it with the observed pseudorange to judge which satellite is normal and which is faulty. Thus, the Initial Set I and II are represented as follows:

$$\text{Initial Set I} = \left\{ \text{SV}_1 \ \text{SV}_2 \ \cdots \ \text{SV}_n \right\} \tag{5-1}$$

$$\text{Initial Set II} = \left\{ \text{SV}_1^{'} \ \text{SV}_2^{'} \ \cdots \ \text{SV}_m^{'} \right\} \tag{5-2}$$

where, Initial Set I contains the set of satellites returning normal data during the initialization process, and SV_1 to SV_n represent the ID of these satellites, from 1 to n. Meanwhile, Initial Set II contains the set of satellites returning faulty measurements, and $\text{SV}_1^{'}$ to $\text{SV}_m^{'}$ represent the ID of these satellites, from 1 to m. All the historical measurements are included in the sets for the specific satellites, including the raw measurements of pseudoranges, satellite position, etc.

PSEUDORANGE RATE BASED TRANSITION MODEL

The pseudorange is one of the most important observations in GNSS, and the accuracy of the pseudorange contributes significantly to the accuracy of the positioning. In the case of the satellites returning faulty data, the associated NLOS, multipath and satellite clock errors are expressed in the form of pseudorange errors. Most errors with slow changes can be eliminated by using the time-difference model. Time-differenced pseudorange measurements can be expressed as:

$$\Delta\rho_k = \rho_k - \rho_{k-1} = \Delta r_k + c\Delta dt_{R_k} + \Delta\varepsilon_\rho \tag{5-3}$$

where, $\Delta\rho$ and Δr are the changes in pseudorange and geometric range between two measurement epochs; $c\Delta dt_{R_k}$ is the variation of receiver clock errors at two adjacent epochs. The remaining measurement error, which is not removed through calculating the time differences, is denoted with $\Delta\varepsilon_\rho$. These residual errors are considered to be negligible for the purposes of this process, however. The Δr_k can be represented as:

$$\begin{aligned} \Delta r_k &= r_k - r_{k-1} = \left| \mathbf{X}_k^S - \mathbf{X}_k^R \right| - \left| \mathbf{X}_{k-1}^S - \mathbf{X}_{k-1}^R \right| \\ &= \vec{\mathbf{r}}_k \cdot (\mathbf{X}_k^s - \mathbf{X}_k^R) - \vec{\mathbf{r}}_{k-1} \cdot (\mathbf{X}_{k-1}^S - \mathbf{X}_{k-1}^R) \end{aligned} \tag{5-4}$$

where, r_k and r_{k-1} are the geometric ranges between the receiver position and the satellite position at two epochs, k and $k-1$; X_k^S and X_{k-1}^S are the satellite position vectors at two epochs; X_k^R and X_{k-1}^R are the receiver position vectors. $\vec{r}_k$ and $\vec{r}_{k-1}$ are the unit vectors pointing to the satellite from the receiver position. We consider that $\vec{r}_k$ is approximately equal to $\vec{r}_{k-1}$ due to the remote distance between the satellite and the receiver. Therefore, when the two epochs are very close together in time, we can obtain:

$$\Delta r_k = \vec{\mathbf{r}}_k \cdot (\mathbf{X}_k^S - \mathbf{X}_k^R) - \vec{\mathbf{r}}_k \cdot (\mathbf{X}_{k-1}^S - \mathbf{X}_{k-1}^R) = \vec{\mathbf{r}}_k \cdot (\Delta\mathbf{X}^S - \Delta\mathbf{X}^R) \tag{5-5}$$

where, ΔX^S and ΔX^R are the change in geometric range of satellite and receiver between two epochs in an Earth Centered Earth Fixed coordinates frame. According to Eq.(5-4) and Eq. (5-5), we can obtain:

$$\Delta\rho_k = \vec{r}_k \cdot (\Delta \mathbf{X}^S - \Delta \mathbf{X}^R) + c\Delta dt_{R_k} + \Delta\varepsilon_\rho \quad (5\text{-}6)$$

If the acceleration of the vehicle is a in a specific direction, then the difference of position change between two adjacent epochs is $a\Delta t^2$, where Δt is the time interval. When Δt is 0.1s, taking $a = 10 m/s^2$ as an example, the corresponding value is 0.1 m, which is small enough and can be neglected within the fault detection algorithm. To be noted that the proposed algorithm is for civil applications in urban areas, these vehicles (e.g. UAVs) are with low accelerations (e.g. less than 10 m/s2). Here, the movement of the vehicle can be considered as a continuously linear motion at a constant speed in a very short time (e.g. within 1 second). Similarly, the movement of the satellites can be considered as a linear motion at a constant speed in a very short time (e.g. within 1 second), because of their stable circular motion. Therefore, our algorithm is applicable for the sharp turn of the vehicle in the urban areas, since it can be considered as an accelerated motion. In the algorithm, we use hypothesis testing to process the receiver clock drift rate $c\Delta dt_{R_{k\_k-1}}$.

H_0 means the receiver clock drift rate is 0, that is

$$\Delta\rho_k = \Delta\rho_{k-1} + \Delta\varepsilon \quad (5\text{-}7)$$

H_1 means that the receiver clock drift rate is not 0, that is

$$\Delta\rho_k - c\Delta dt_{R_{k\_k-1}} = \Delta\rho_{k-1} + \Delta\varepsilon \quad (5\text{-}8)$$

Wherein, $\Delta\varepsilon$ is random noise.

DETERMINATION OF DOUBLE DETECTORS

Kalman filtering is widely used in various fields because of its low computational complexity and optimal estimation accuracy. During the construction of D_1, the filter used is Kalman filter. Build the state vector $\mathbf{X}$ and observation vector $\mathbf{Z}_k$:

$$\mathbf{X} = [\Delta\rho] \quad (5\text{-}9)$$

$$H_0 : \mathbf{Z}_k = [\rho_k - \rho_{k-1}] \quad (5\text{-}10)$$

$$H_1 : \mathbf{Z}_k = [\rho_k - \rho_{k-1} - c\Delta dt_{R_k}] \quad (5\text{-}11)$$

The state transition equation and measurement equation are as follows:

$$\begin{aligned} \mathbf{X}_k &= \mathbf{\Phi}_{k,k-1}\mathbf{X}_{k-1} + \mathbf{w}_{k-1} \\ \mathbf{P}_{k,k-1} &= \mathbf{\Phi}_{k,k-1}\mathbf{P}_{k-1}\mathbf{\Phi}_{k,k-1}{}^T + \mathbf{Q}_{k-1} \\ \hat{\mathbf{X}}_k &= \hat{\mathbf{X}}_{k.k-1} + \mathbf{K}_k(\mathbf{Z}_k - \mathbf{H}_k\hat{\mathbf{X}}_{k,k-1}) \end{aligned} \quad (5\text{-}12)$$

$$\mathbf{Z}_k = \mathbf{H}\mathbf{X}_k + \mathbf{v}_k \mathbf{H} = 1 \quad (5\text{-}13)$$

Where, $\mathbf{X}_k$ and $\mathbf{X}_{k-1}$ are state vectors in the time epoch k and $k-1$ respectively, and $\mathbf{\Phi}_{k,k-1}$ is the transition matrix; $\mathbf{w}_{k-1}$ is the process noise in the time epoch $k-1$, with the covariance matrix $\mathbf{Q}$; $\mathbf{Z}_k$ is the measurement at the time epoch k, and $\mathbf{H} = 1$ is the measurement mapping matrix; $\mathbf{v}_k$ is the measurement noise in the time epoch k, with the covariance matrix $\mathbf{R}$.

The discrete form of Kalman filtering can be divided into two stages, as shown below:

Forecast stage:

$$\hat{\mathbf{X}}_{k.k-1} = \mathbf{\Phi}_{k,k-1}\hat{\mathbf{X}}_{k-1} \quad (5\text{-}14)$$

$$\mathbf{P}_{k,k-1} = \mathbf{\Phi}_{k,k-1}\mathbf{P}_{k-1}\mathbf{\Phi}_{k,k-1}^{T} + \mathbf{Q}_{k-1} \quad (5\text{-}15)$$

Update phase:

$$\mathbf{K}_k = \mathbf{P}_{k,k-1}\mathbf{H}_k^T(\mathbf{H}_k\mathbf{P}_{k,k-1}\mathbf{H}_k^T + \mathbf{R}_k)^{-1} \quad (5\text{-}16)$$

$$\mathbf{P}_k = (\mathbf{I} - \mathbf{K}_K\mathbf{H}_k)\mathbf{P}_{k,k-1} \quad (5\text{-}17)$$

$$\hat{\mathbf{X}}_k = \hat{\mathbf{X}}_{k.k-1} + \mathbf{K}_k(\mathbf{Z}_k - \mathbf{H}_k\hat{\mathbf{X}}_{k,k-1}) \quad (5\text{-}18)$$

Where, $\hat{\mathbf{X}}_k$ is the state estimation of the system in the time epoch k; $\mathbf{\Phi}_{k,k-1}$ and $\mathbf{H}_k$ are the transition matrix and measurement mapping matrix in the time epoch k respectively; $\mathbf{P}_k$, $\mathbf{Q}_k$ and $\mathbf{R}_k$ are the covariance matrix of state error, system noise and measurement noise in the time epoch k respectively; and $\mathbf{K}_k$ is the Kalman filter gain matrix in the time epoch k, $\hat{\mathbf{X}}_{k.k-1}$ is the propagation of vector $\hat{\mathbf{X}}_k$ from epoch k-1 to epoch k.

The innovation sequence, $\mathbf{e}_k$, which is the difference between the observed value and the KF predicted value, is generated in order to detect the faults in data from each satellite in Set I:

$$\mathbf{e}_k = \mathbf{Z}_k - \mathbf{H}_k\hat{\mathbf{X}}_{k,k-1} \quad (5\text{-}19)$$

$\mathbf{e}_k$ follows a white Gaussian sequence in a long time period. Over short timeframes, however, its mean and standard deviation vary according to the velocity, quality of receiver, elevation of satellites and the condition of the troposphere, ionosphere, etc. Therefore, it is necessary to standardize $\mathbf{e}_k$ by using the prior mean and standard deviation, so as to build the D_1 value of each satellite in set I. The prior data are shown in **Error! Reference source not found.** and the standardized formula is shown in Eq.(5-20):

$$D_1^i = \left(e_k^i - \mu_1\right)/\sigma_1 \quad (5\text{-}20)$$

Where, i is the satellite, μ_1 and σ_1 are the prior mean and standard deviation. Use D_1 to check satellites in set I: if $|D_1| > T_1$, the observations of these satellites will be considered as possible failures in this epoch, and further detection is required.

Table 5-1: Test Statistics of Algorithms in UAV Simulation

PRN	$\mu_1(10^{-3})$	σ_1	μ_2	σ_2
10	0.2911	0.0635	0.0322	0.4273
12	0.6345	0.0766	-0.0306	0.7815
15	0.1748	0.0741	-0.0283	0.4102
20	0.6105	0.0782	1.2450	0.6985
21	0.3870	0.0772	-0.022	0.5176
24	0.3142	0.0623	-0.4612	0.4867
25	0.4727	0.0876	-1.0124	0.5554
32	0.1305	0.0825	0.2647	0.3473

In the project, we first use transition model of the KF to predict the pseudorange change of the observed satellites. In this prediction step, we assume the Δdt_{R_k} is not changed initially, which means the hypothesis H_0 holds. At the same time, we will obtain the observed pseudorange change. With the difference between observed pseudorange and predicted pseudorange changes (i.e. the innovation e_k), we evaluate the results based on the proposed check algorithm. When the difference between the predicted pseudorange change and the observed pseudorange change is less than the threshold, the satellite is considered normal, H_0 is accepted, and the algorithm is executed to the next epoch. When the difference between the predicted change and observed pseudorange change is greater than the threshold, it is necessary to detect whether the receiver clock drift changes before determining the faulty satellite. Both the real faulty measurement of the satellite and $\Delta^2 dt_{R_k}$ will result in the changes of the observed $\Delta\rho$, and they have different characteristics for both cases. For example, the change of $\Delta\rho$ caused by NLOS is not equal for all satellites, because NLOS signals are received from different directions in urban areas. While the $\Delta^2 dt_{R_k}$ will cause an equal length to every satellite in the change of $\Delta\rho$, further resulting in the almost equal e_k. Therefore, we can use the variance S^2 of e_k to determine the case at that epoch. If the S^2 is less than a specific determined threshold, we can consider the changes of $\Delta\rho$ are caused by the receiver clock. Otherwise, we will consider the changes of $\Delta\rho$ are caused by real fault, such as NLOS. The S_k^2 can be expressed as follow:

$$S_k^2 = \frac{1}{n-1}\sum_{i=1}^{n}(e_k^i - \bar{e}_k)^2 \qquad \textbf{(5-21)}$$

Here, n is the number of satellites; e_k^i is the KF innovation of each satellite at k epoch; $\bar{e}_k$ is the mean of all KF innovations detected at k epoch, and S_k^2 is the variance. The distribution of the S_k^2 value is in Figure 5-3. Since the variance is small, we set the threshold to 8. When the value of S_k^2 is smaller than 8, we can consider that these measurements of satellites are not faulty. However, when non-zero $\Delta^2 dt_{R_k}$ and real fault occur simultaneously, the S_k^2 will become much bigger than the threshold too. If we consider all satellites are faulty, it will reduce the satellite availability in a real-world situation. In order to solve this problem, assuming that N satellites are received by the receiver at epoch k, to find the satellite which includes both non-zero $\Delta^2 dt_{R_k}$ and real faults from these only containing non-zero $\Delta^2 dt_{R_k}$, an adaptive sliding window is designed as follows.

(1) Sort all of the e_k^i (i=1, 2 … N) of satellites in Set I at epoch k from the smallest to the largest.

(2) Use sliding window for the smallest four e_k^i and then calculate the S_k^2 of the current window.

(3) If $S_k^2 > 8$, we will discard the first e_k^i in window (flagged as the fault satellite) and move one step of the window to the right side with the window size unchanged. Then the new S_k^2 will be further check with the threshold. This process will be stopped until all e_k^i being checked or S_k^2 less than the threshold. For the former, we consider that there is no satellite can be used to calculate the position of the receiver at this epoch, and all of the satellites at this epoch will be moved to Set II. For the latter, go to the next step.

(4) If $S_k^2 < 8$, these satellites in the window can be used for positioning. Therefore, we consider them as satellites only containing non-zero $\Delta^2 dt_{R_k}$. In order to improve the positioning performance, it is preferable to use as many satellites as possible. Then the

window size will be extended to the right side with one more e_k^i, which means the next innovation will be included in the window. Then S_k^2 of this new window will be checked with the threshold again. If $S_k^2 < 8$, we will repeat the process of step (4). If the $S_k^2 > 8$, as the newly added e_k^i results in the big deviation of the S_k^2, then all of the e_k^i on the right side of this one will be flagged as faulty satellites. The process will be turned to step (5).

(5) Finally, the satellites inside of the window will be considered as normal satellites and those outside of the window are flagged as faulty satellites. The faulty satellites will then be put into Set II and the normal satellites will be put into Set I. The mean value of innovations for all normal satellites, $\bar{e}_k$, can be regarded as the value of $c\Delta^2 dt_{R_k}$ at this epoch. Once a non-zero $\Delta^2 dt_{R_k}$ is confirmed, we substitute $\mathbf{Z}_k = [\rho_k - \rho_{k-1} - \bar{e}_k]$ for Z_k for this epoch and the filtering process will be redone. But for the next epoch, the $\Delta^2 dt_{R_k}$ in Z_k will still be set as zero initially for the filtering process until a non-zero $\Delta^2 dt_{R_k}$ is detected again.

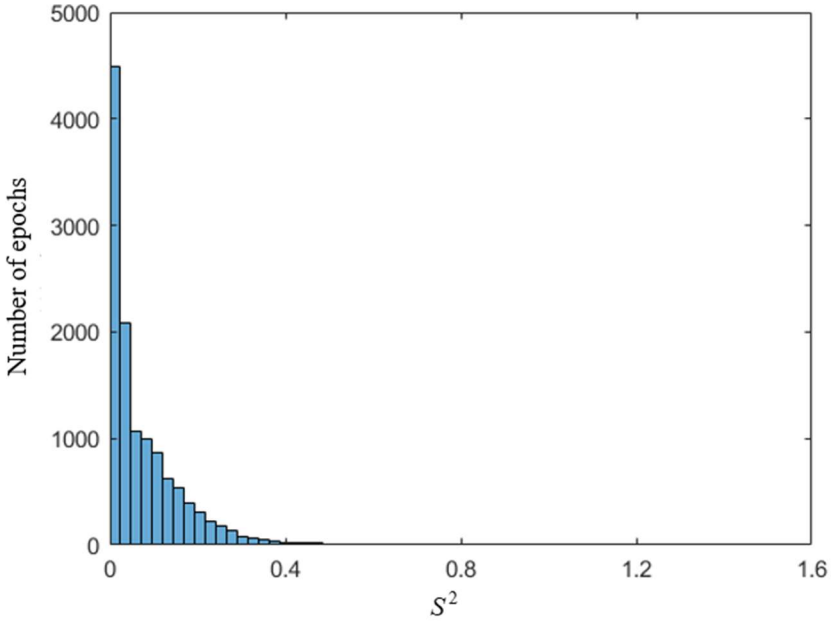

Figure 5-3: The distribution of S^2.

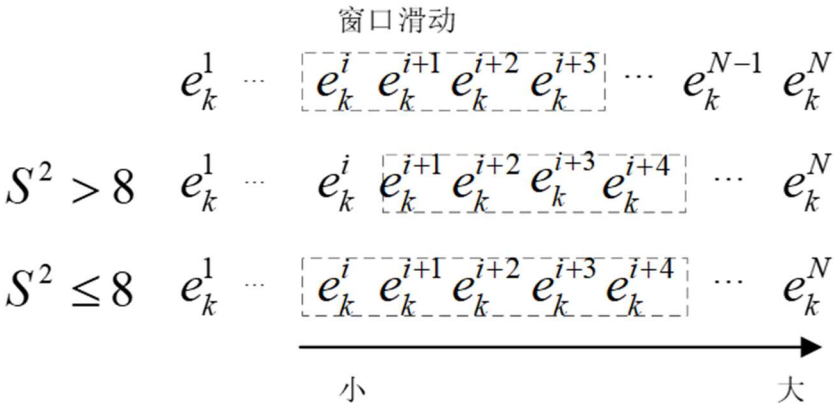

Figure 5-4: Windowing process for fault detection based on Set I.

Because the vehicle is moving relatively fast in the NLOS/multipath-affected urban environments, the visibility of satellites changes frequently. This means that newly-

observed satellites may suffer from NLOS or multipath, while the satellites originally in Set II may return to normal. Detector D_2 is therefore created for real-time fault status monitoring. Specifically, the satellites in Set I for a given epoch are used to calculate the position and receiver clock error. We then combine them with modelled ionospheric, tropospheric errors, Klobuchar model and Saastamoinen model respectively with parameters from the ephemeris data, and positions and clock errors of the satellites in Set II to predict the pseudoranges of these satellites, respectively. The predicted pseudorange and the observed pseudorange are then compared. The pseudorange prediction equation is:

$$\tilde{\rho}_{t_k} = \tilde{r} + c\left(\tilde{dt}_R - dt^S\right) + \tilde{I}_\rho + \tilde{T}_\rho \quad \textbf{(5-22)}$$

where, $\tilde{\rho}_{t_k}$ is the predicted pseudorange, and $\tilde{r}$ is the distance between the satellite position and the vehicle position calculated by the satellites of Set I. $\tilde{dt}_R$ is the estimated receiver clock error. $\tilde{I}_\rho$ and $\tilde{T}_\rho$ are the ionospheric and tropospheric errors estimated by models. By subtracting the observed pseudorange ρ_{t_k} from the predicted pseudorange $\tilde{\rho}_{t_k}$, we obtain:

$$R_k = \rho_{t_k} - \tilde{\rho}_{t_k} \quad \textbf{(5-23)}$$

Then we define the detector D_2 for each faulty or newly observed satellite as follows:

$$D_2^j = \left(R_k^j - \mu_2\right)/\sigma_2 \quad \textbf{(5-24)}$$

where, j is the satellite number; μ_2 and σ_2 are a priori mean and standard deviation of R_k^j (Table 5-1). The $|D_2|$ is then compared with the threshold T_2 to determine whether the satellite is still with faulty measurement or has recovered to normal. The faulty satellites will remain in Set II while the normal ones will be moved to Set I. Table 5-1 shows the prior data of UAV simulation experiment of this project. Specifically, μ_1 and σ_1 is the mean and standard deviation of e_k, μ_2 and σ_2 is the mean value and standard deviation of R_k, which change with the satellite elevation and the environment around the receiver, so it needs to be adjusted according to the satellite conditions. Because of the short duration of the experiment, we believe that these parameters remain unchanged.

DETERMINATION OF DETECTION THRESHOLDS

The distribution of the double detectors D_1 and D_2 both can be considered to follow a standard normal distribution. The following is an example of UAV simulation experiment, and the corresponding distribution is shown in Figure 5-5. The corresponding detection threshold T can be determined according to characteristics of standard normal distribution, positioning requirements for UAV Tasks and mathematical rules. The correlation can be given by the following formula:

$$P_{FA} = 1 - \int_{-T_D}^{T_D} \frac{1}{\sqrt{2\pi}} e^{-\frac{x^2}{2}dx} \quad \textbf{(5-25)}$$

Where, the detection threshold T is determined according to the 3σ principle. Theoretically, when the detected value exceeds this threshold, it is considered that the satellite fails at these times. However, the minimum value of T should be no less than the 3σ value. By using this strategy, some minor errors are inevitable in the pseudorange measurements. Nevertheless, it is not necessary to remove all errors completely since, where errors are small enough not to affect our positioning results, removing those satellites so as to rely on a smaller number of satellites with poor geometries for positioning

would risk enlarging positioning errors. For this reason, it is critical to get a trade-off between accuracy and integrity in determination of the threshold which is bigger than 3σ value.

Therefore, we set the thresholds of D_1 and D_2 to 15 and 10 respectively. It is worth noting that for same pseudorange errors, the denominator in the standardization process is the standard deviation σ_1 and σ_2, so the value of D_1 is greater than D_2 after standardization.

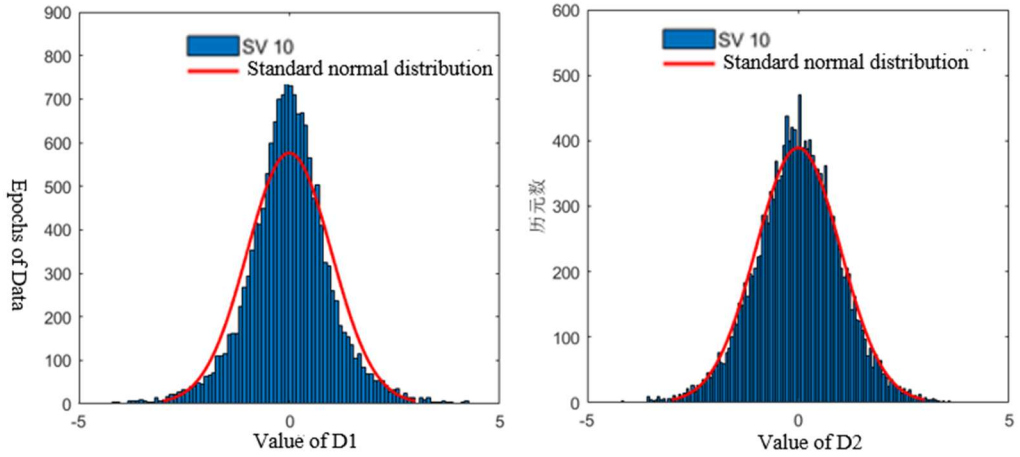

Figure 5-5: Distribution of the values of D_1 and D_2 for the UAV test.

5.2.2. ALGORITHM VERIFICATION

The simulation of faulty measurements scenarios in the UAV flight data is to test the proposed fault detection and exclusion algorithm. The UAV flight test data was collected in Nantou City, Taiwan, with the flight route shown in Figure 5-6. The raw pseudorange measurements were collected from a dual-frequency GNSS receiver, Trimble BD 982, with a sampling rate of 10 Hz. The UAV used in the test is AXH-E230 from AVIX Technology and was flown semi-automatic. It is equipped with intelligent autopilot system AJC and a smart power control module system to perform autonomous intelligent navigation flight mission. The speed of UAV was less than 10 m/s during the flight and the height was about 60m. The reference trajectory used in the experiment was obtained from close range photogrammetry providing centimeter-level positioning accuracy using the on-board VLP-16 Velodyne Lidar. Four defined fault scenarios were added to the real trajectory: single step error for scenario 1 and multiple step errors for scenario 2, 3 and 4. The details for the four scenarios are described in Table 5-2.

Figure 5-6: Flight trajectory.

Table 5-2: The defined scenarios.

Scenarios	Fault satellites numbers	Duration Time (s)	Number of Test	Error Sources
1	Single- fault	10	100	10~50 m range error added to one satellite with an interval of 10 m
2	dual-fault	10	100	10~50 m range error added to two satellites with an interval of 10 m respectively
3	dual-fault	0.1	100	20m and 50m errors added to two satellites respectively and 100 m $c\Delta^2 dt_{R_k}$ added to all satellites at one epoch
4	multi-fault	0.1	1	-60m, -40m, 20m, 30m and 60m errors added to 5 satellites respectively and 100 m $c\Delta^2 dt_{R_k}$ added to all satellites at one epoch

In Scenario 1, we conducted one hundred durations of the experiment for each value of range error added in the observed satellites. For every randomly chosen satellite at each time, pseudorange errors of between 10 and 50 meters were added in a specific time duration of 10s. The reason for not considering errors less than 10m is that these would not contribute significant positioning errors in the pseudorange-based positioning calculation. The proposed algorithm can be used for satellite quality control if less than five satellites are observed at one epoch. Nevertheless, for the purposes of this experiment, we only chose epochs with more than six satellites observed so as to ensure sufficient satellites for calculating the positioning solution.

Considering the characteristics of UAV in low altitude area, a 10-50m step error with a duration of 10 seconds is added to the observation pseudorange. This is because such errors often occur when UAVs receive NLOS/multipath signals when flying in low altitude areas. Take SV10 as an example. A sudden fault was added in SV10 during epoch 4000-4100. As shown in Figure 5-7, the fault could be detected by detector D_1 immediately. After a fault is detected, SV10 is moved to Satellite Set II. This would move SV10 to Set II and then the detector D_2 would be applied to monitor the ongoing quality of SV10 in Set II. Once the faulty satellite SV10 is excluded, the value of D_2 will immediately drop below the threshold. If the value of D_2 in two consecutive epochs remains below the threshold, we move the SV10 back to Set I, in which the pseudorange measurements are used for the positioning calculation at that epoch. It is indicated from the results in Table 5-3 that the designed algorithm in this project could achieve 100% correct detection for pseudorange errors above 10m. However, the traditional fault detection based on algorithm least squares has detection rates of 64% for 30m pseudorange error, 72% for more than 30m errors and 81% for 10m error, which is not sensitive to minor error, i.e. 20m.

In scenario 2, we again conducted one hundred iterations of the experiment for each defined fault case. For every randomly chosen two satellites, 10m, 20m, 30m, 40m or 50m pseudorange errors were added in specific time epoch durations. The errors can start from any epoch and lasts for 10s during the test. Because in this scenario, there are two satellites with errors in a given epoch, we chose those time epochs where more than six satellites were observable. The proposed algorithm is based on every single satellite, and is therefore very effective in detecting simultaneous errors in two satellites. Here we have defined a valid successful detection as occurring only when the faults in each of the two satellites are detected. From

Table 5-4, it is shown that the proposed algorithm achieved 100% correct detection for the case of two satellites with simultaneously errors, while the traditional fault detection based

on least squares algorithm could not be used for multi-fault satellites detection. The detailed comparisons is showed in

Table 5-6. The designed algorithm in the project also has the advantage of being able to detect faults even when only four satellite is available, and is also very sensitive to small faults, neither of which is the case with traditional fault detection based on least squares algorithm. The only disadvantage of the designed algorithm is that it requires historical information or initialization process and data cannot be interrupted.

In scenario 3, in order to test the performance of designed algorithm under the condition, where various multipath/NLOS errors mixed with non-zero $\Delta^2 dt_{R_k}$. The 20m and 50m errors were added to every randomly chosen two satellites, while 100 m $c\Delta^2 dt_{R_k}$ was added to all available satellites at a specific epoch. We conducted one hundred iterations of this experiment for defined fault case at epochs, where more than six satellites were observable. The valid successful detection is the same as scenario 2. From

Table 5-5, it is presented that the proposed algorithm achieved 100% correct detection for this case of two satellites with simultaneously errors and non-zero $\Delta^2 dt_{R_k}$. And

Table 5-7 shows the details how the sliding window worked at an experiment. The value of S_k^2 is very small when the window does not contain the e_k^i with both error and non-zero $\Delta^2 dt_{R_k}$, but it would increase hundreds of folds when the window includes a e_k^i of a faulty satellite. Therefore, the proposed algorithm is able to detect the satellite with only non-zero $\Delta^2 dt_{R_k}$ and the satellite with fault and non-zero $\Delta^2 dt_{R_k}$ mixed.

Scenario 4 is designed to evaluate the proposed algorithm in the condition that the normal satellites are less than 4. -60m, -40m, 20m, 30m and 60m errors were added to 5 satellites respectively as well as a 100 m $c\Delta^2 dt_{R_k}$ was added in all satellites received at this epoch.

Table 5-8 depicts an example of the windowing process. It is clear that the S^2 of every four satellite is above the threshold, and thus cannot be used for positioning. In this scenario, the designed algorithm can still be effective but the positioning cannot be calculated due to insufficient normal satellites at the epoch.

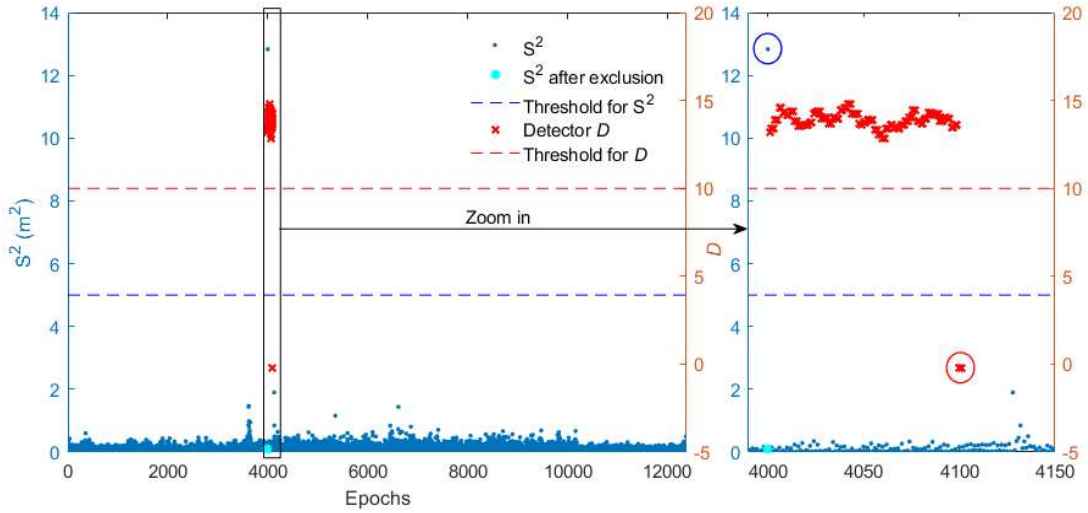

Figure 5-7: An example of the fault detection results for satellite SV10.

Table 5-3: Comparisons of algorithm performance with various values of error sources in Scenario 1.

Error Source (m)	Number of Test	Correct Detection rate (Proposed Method)	Correct Detection Rate (LSM based)
10	100	100%	0%
20	100	100%	0%
30	100	100%	64%
40	100	100%	72%
50	100	100%	81%

Table 5-4: Comparisons of algorithm performance with various values of error sources in Scenario 2.

Error Source (m)	Number of Test	Correct Detection Rate (Proposed Method)	Correct Detection Rate (LSM based)
10	100	100%	
20	100	100%	
30	100	100%	N/A
40	100	100%	
50	100	100%	

Table 5-5: Comparisons of algorithm performance with various values of error sources in Scenario 3.

Error Source (m)	Number of Test	Correct Detection Rate (Proposed Method)	Correct Detection Rate (LSM based)
20 and 50	100	100%	100%

Table 5-6: Comparison between the design method and LSM based method in Scenario 2.

	Proposed Method	LSM based method
Historical information required	Yes	No
Simultaneous multiple faults detection	Yes	No
The minimum number of SVs required for fault detection	>=4	>=5
The minimum number of SVs required for fault exclusion	>=4	>=6
Sensitive to small faults	Yes	No

Table 5-7: An example of windowing results in scenario 3.

Satellite ID	20	25	15	32	10	24	12	21
$c\Delta^2 dt_{R_k}$ (m)	100	100	100	100	100	100	100	100

Step error (m)	0	0	0	0	0	0	20	50
e_k (after sorting)	99.43	99.46	99.63	99.85	99.92	101.11	119.38	149.35
S^2	0.04				/	/	/	/
	0.05					/	/	/
	0.39						/	/
	54.55							/
	319.01							

Table 5-8: An example of windowing results in scenario 4.

Satellite ID	12	15	32	10	24	20	21	25
$c\Delta^2 dt_{R_k}$ (m)	150	150	150	150	150	150	150	150
Step error (m)	-60	-40	0	0	0	20	30	60
e_k (after sorting)	89.38	109.63	149.85	149.92	151.11	169.43	179.35	209.46
S^2	914.28				/	/	/	/
	/	413.66				/	/	/
	/	/	91.87				/	/
	/	/	/	206.65				/
	/	/	/	/	595.31			

In order further to investigate the effectiveness of the designed algorithm for the final positioning results, we have calculated the positioning solutions for the epochs with faulty satellites. The RMSE is used to evaluate the positioning results with the designed FDE algorithm applied one hundred times. In Scenario 1, pseudorange errors of between 10 and 50 meters were added in chosen satellite and the positioning results with different pseudorange errors and after applying the designed algorithm are shown in Figure 5-8. The statistical results of positioning errors are shown in Table 5-9. It is indicated that the 3D position accuracy RMSE was 4.47m with the designed algorithm applied, while, without the FDE, it was 13.79m, 24.15m, 34.15m, 45.00m and 55.44m for the single satellite with faults of 10m, 20m, 30m, 40m and 50m.

The positioning results with different pseudorange errors and after applying the designed algorithm in Scenario 2 are shown in Figure 5-9. It can be found that the positioning accuracy is significantly improved after applying the designed FDE algorithm. The positioning results with and without FDE algorithms in Scenario 2 and Scenario 3 were shown in

Table 5-10 and

Table 5-11 respectively. It is indicated that the 3D positioning accuracy was 10.79m after the proposed FDE applied, while it varied from 27.94m to 126.52m with the various magnitude of error added in the simulation in Scenario 2. The 3D positioning accuracy with FDE is 2.70m in Scenario 3, exhibiting an improvement of 93.6% over the positioning results without FDE.

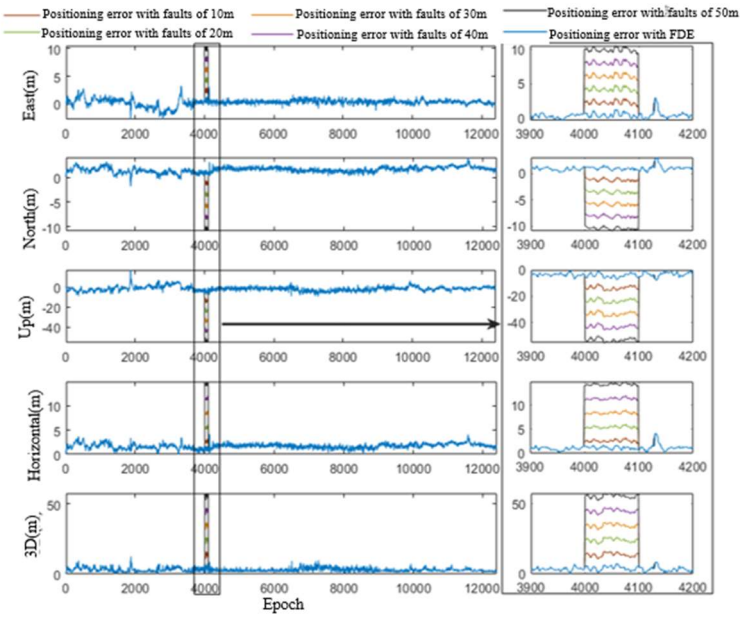

Figure 5-8: Positioning results in Scenario 1.

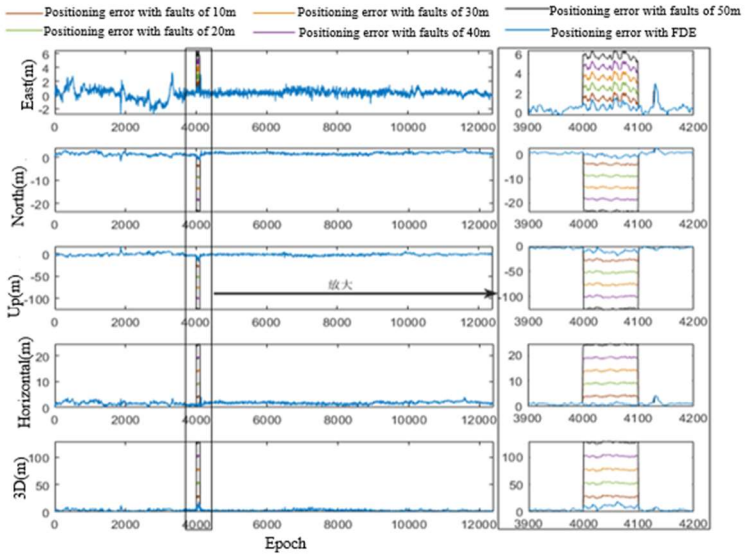

Figure 5-9: Positioning results in Scenario 2.

Table 5-9: The RMSE(m) of positioning results for Scenario 1.

Single Step Error (m)		10	20	30	40	50
East	RMSE(m)	2.31	4.21	6.10	8.00	9.90
	RMSE(m)(with FDE)			0.61		
North	RMSE(m)	1.19	3.48	5.78	8.08	10.38
	RMSE(m)(with FDE)			1.04		
Up	RMSE(m)	13.54	23.53	33.53	43.54	53.55
	RMSE(m)(with FDE)			4.31		
Horizontal	RMSE(m)	2.60	5.46	8.40	11.37	14.35
	RMSE(m)(with FDE)			1.20		

3D	RMSE(m)	13.79	24.15	34.56	45.00	55.44
	RMSE(m)(with FDE)			4.47		

Table 5-10: The RMSE(m) of positioning results for Scenario 2.

Double Step Error (m)		10	20	30	40	50
East	RMSE(m)	1.52	2.60	3.69	4.78	5.88
	RMSE(m)(with FDE)			0.77		
North	RMSE(m)	3.79	8.71	13.63	18.55	23.47
	RMSE(m)(with FDE)			0.58		
Up	RMSE(m)	27.64	51.76	75.90	100.04	124.19
	RMSE(m)(with FDE)			10.74		
Horizontal	RMSE(m)	4.09	9.09	14.12	19.15	24.19
	RMSE(m)(with FDE)			0.96		
3D	RMSE(m)	27.94	52.56	77.20	101.86	126.52
	RMSE(m)(with FDE)			10.79		

Table 5-11: The RMSE(m) of positioning results for Scenario 3.

Step Error (20 and 50m)	East	North	Up	Horizontal	3D
RMSE(m)	11.52	18.66	36.00	21.93	42.15
RMSE(m)(with FDE)	0.19	2.02	1.78	2.03	2.70

This project proposes a fault detection and exclusion model based on double detectors for single satellite and multi satellite faults, which can detect and eliminate satellite observations with faults in real time and online, and detect single or multi satellite faults at the same time, thus realizing real-time GNSS measurement quality control in dynamic positioning applications to meet the accuracy requirements in CAT II/III precision approaches. By adding errors to the pseudoranges of UAV data collected in an open environment for simulation, the effectiveness of the proposed algorithm can be seen from the experimental results. The fault detection rate of single satellite and multi satellite fault scenarios is 100%, so it has broad application prospects in G-ATM.

5.3. ADAPTIVE NOISE VARIANCE BASED FAULT DETECTION ALGORITHM

5.3.1. ALGORITHM DESIGN

ALGORITHM FRAMEWORK

The framework of the algorithm is shown in Figure 5-10: Firstly, the filtering parameters are initialized to predict the state vector of the next epoch, and then the variance matrix

of innovation and observed noise is calculated, and then the fault detection statistic is calculated and compared with the fault detection threshold to determine whether there is fault data. If there is fault data, fault identification is carried out and the fault data is eliminated. After fault detection and identification, the final state vector estimation of the epoch is calculated. Output the location result of this epoch, and then predict the state vector of the next epoch. Repeat the above steps.

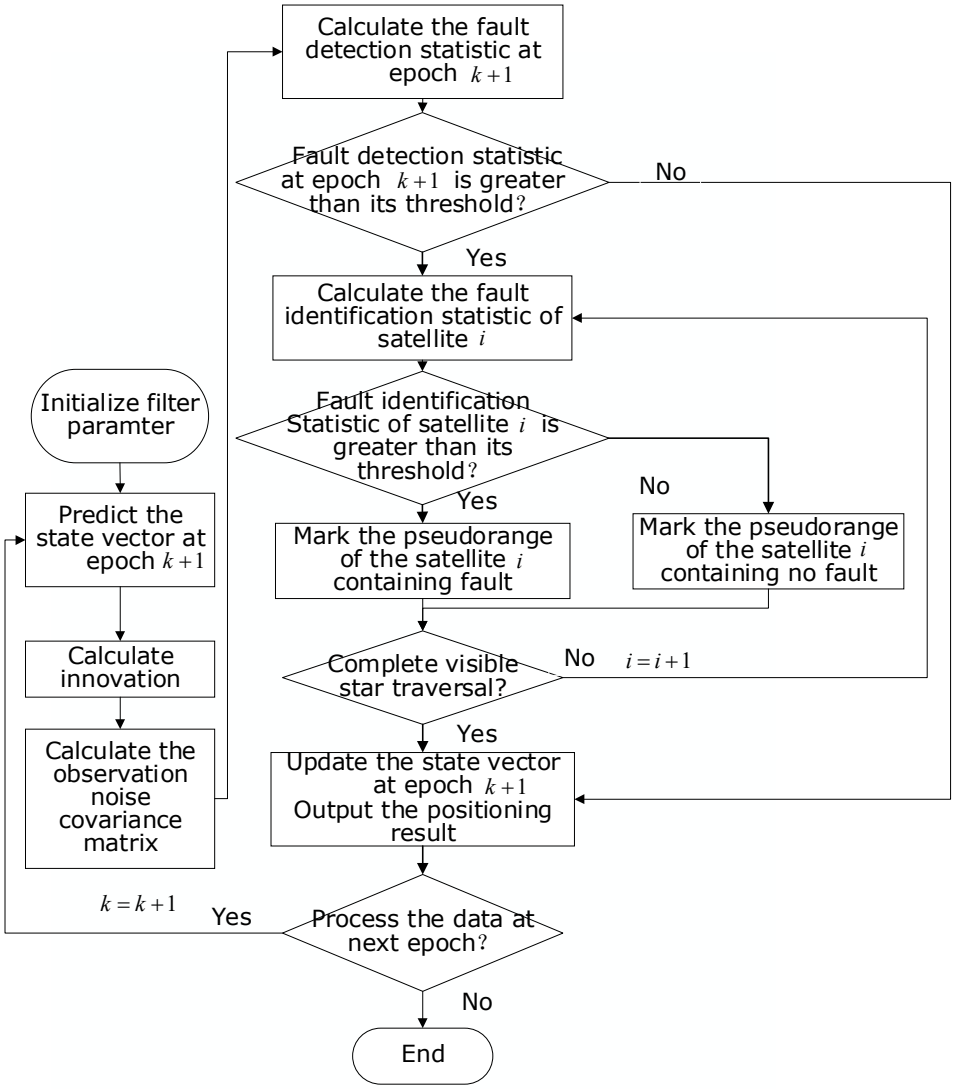

Figure 5-10: Framework of the proposed algorithm

STATE EQUATION AND MEASUREMENT EQUATION

State vector at k epoch

$$\mathbf{X}_k = [x_k, y_k, z_k, r_k, x_k', y_k', z_k', r_k']^T \quad (5\text{-}26)$$

where, x_k、y_k、z_k are X-axis, Y-axis and Z-axis coordinates of the receiver in the geostationary coordinate system at k epoch; r_k is receiver clock error multiplied by the speed of light at k epoch; x_k'、y_k'、z_k' are derivative of x, y, and z coordinates of the receiver with respect to time in the ECEF coordinate, Namely the velocity component of

the receiver in the x, y, and z axis at the epoch k; r_k' is the derivative of the receiver clock error times the speed of light with respect to time at k epoch; The superscript of x_k'、y_k'、z_k'、r_k' is the derivative of each variable with respect to time.

State equation:

$$\mathbf{X}_{k+1} = \mathbf{\Phi}_{k+1|k}\mathbf{X}_k + \mathbf{W}_k \tag{5-27}$$

where, $\mathbf{X}_{k+1}$ is the state vector at epoch $k+1$; $\mathbf{W}_k$ is the process noise, Assume that $\mathbf{W}_k$ is Gaussian white noise, its covariance matrix is $\mathbf{Q}$; $\mathbf{\Phi}_{k+1|k}$ is the state transition matrix, it is:

$$\mathbf{\Phi}_{k+1|k} = \begin{bmatrix} \mathbf{I}_{4\times4} & t\mathbf{I}_{4\times4} \\ \mathbf{0}_{4\times4} & \mathbf{I}_{4\times4} \end{bmatrix} \tag{5-28}$$

where, $\mathbf{I}_{4\times4}$ is the identity matrix of order 4; t is the time interval between k epoch and $k+1$ epoch; $\mathbf{0}_{4\times4}$ is zero matrix of order 4。

Observation equation:

$$\mathbf{Z}_{k+1} = \mathbf{H}_{k+1}\mathbf{X}_{k+1} + \mathbf{V}_{k+1} \tag{5-29}$$

where, $\mathbf{Z}_{k+1}$ is the observation vector; $\mathbf{H}_{k+1}$ is observation matrix; $\mathbf{V}_{k+1}$ is pseudorange observation noise, Assume that $\mathbf{V}_{k+1}$ is Gaussian white noise, its covariance is $\mathbf{R}_{k+1}$.

Observation vector:

$$\mathbf{Z}_{k+1} = \begin{bmatrix} \rho_{k+1,1} - \tilde{\rho}_{k+1,1} + m_{k+1,1}x_k + n_{k+1,1}y_k + l_{k+1,1}z_k \\ \rho_{k+1,2} - \tilde{\rho}_{k+1,2} + m_{k+1,2}x_k + n_{k+1,2}y_k + l_{k+1,2}z_k \\ \vdots \\ \rho_{k+1,N_{k+1}} - \tilde{\rho}_{k+1,N_{k+1}} + m_{k+1,N_{k+1}}x_k + n_{k+1,N_{k+1}}y_k + l_{k+1,N_{k+1}}z_k \end{bmatrix} \tag{5-30}$$

where, N_{k+1} is the number of visible satellites at epoch $k+1$; $\rho_{k+1,i}(i=1,2,\ldots N_{k+1})$ is the pseudorange after error correction of satellite i at epoch $k+1$; $\tilde{\rho}_{k+1,i}(i=1,2,\ldots,N_{k+1})$ is the distance between the approximated position (x_k, y_k, z_k) of $\tilde{\rho}_{k+1,i}(i=1,2,\ldots,N_{k+1})$ and satellite i; $m_{k+1,i}, n_{k+1,i}, l_{k+1,i}(i=1,2,\ldots,N_{k+1})$ are the direction cosine from (x_k, y_k, z_k) to satellite i at epoch $k+1$.

Observation matrix:

$$\mathbf{H}_{k+1} = \begin{bmatrix} \mathbf{D}_{k+1} & \mathbf{0}_{N_{k+1}\times4} \end{bmatrix} \tag{5-31}$$

where, $\mathbf{D}_{k+1} = \begin{bmatrix} m_{k+1,1} & n_{k+1,1} & l_{k+1,1} & 1 \\ m_{k+1,2} & n_{k+1,2} & l_{k+1,2} & 1 \\ \vdots & \vdots & \vdots & \vdots \\ m_{k+1,N_{k+1}} & n_{k+1,N_{k+1}} & l_{k+1,N_{k+1}} & 1 \end{bmatrix}$; $\mathbf{0}_{N_{k+1}\times4}$ is $N_{k+1}\times4$ dimensional zero matrix.

OBSERVATION NOISE VARIANCE MATRIX

One purpose of adaptive filtering is to use the observation information to estimate and correct the noise statistical characteristics or gain matrix in real time [Li 2012]. In this

project, the variance matrix of observation noise is estimated in real time by historical innovation sequence.

According to the equation of state, the prediction of the state vector at epoch $k+1$ is:

$$\mathbf{H}_{k+1} = \left[\mathbf{D}_{k+1} \quad \mathbf{0}_{N_{k+1} \times 4} \right] \tag{5-32}$$

where, $\hat{\mathbf{X}}_{k+1|k}$ is the one-step prediction of the state vector at epoch $k+1$; $\hat{\mathbf{X}}_k$ is the filter estimation of the state vector at epoch k。

The error covariance matrix of $\hat{\mathbf{X}}_{k+1|k}$ is:

$$\mathbf{P}_{k+1|k} = \mathbf{\Phi}_{k+1|k} \mathbf{P}_k \mathbf{\Phi}_{k+1|k}^{\mathrm{T}} + \mathbf{Q} \tag{5-33}$$

where, $\mathbf{P}_k$ is the error covariance matrix of the estimation $\hat{\mathbf{X}}_k$.

Calculate the innovation：

$$\boldsymbol{\eta}_{k+1} = \mathbf{Z}_{k+1} - \mathbf{H}_{k+1} \hat{\mathbf{X}}_{k+1|k} \tag{5-34}$$

In theory, the covariance matrix of innovation is:

$$\mathbf{C}_{\boldsymbol{\eta}_{k+1}} = \mathbf{H}_{k+1} \mathbf{P}_{k+1|k} \mathbf{H}_{k+1}^{\mathrm{T}} + \mathbf{R}_{k+1} \tag{5-35}$$

According to the maximum likelihood criterion，The best estimation of $\mathbf{C}_{\boldsymbol{\eta}_{k+1}}$ in a sliding window of length (assuming the visible satellites observed in the sliding window are the same) is [Brown 1992]

$$\hat{\mathbf{C}}_{\eta_{k+1}} = \frac{1}{L} \sum_{j=j_0}^{k} \boldsymbol{\eta}_j \boldsymbol{\eta}_j^{\mathrm{T}} \tag{5-36}$$

where, $j_0 = k - L + 1$.

In order to make the latest innovation the sliding window have a greater impact on the estimation of innovation covariance. Adjust Equation (5-36) as follows:

$$\hat{\mathbf{C}}_{\eta_{k+1}} = \frac{2}{L(L+1)} \sum_{j=j_0}^{k} (j - k + L) \boldsymbol{\eta}_j \boldsymbol{\eta}_j^{\mathrm{T}} \tag{5-37}$$

So the estimation of $\mathbf{R}_{k+1}$ is:

$$\hat{\mathbf{R}}_{k+1} = \frac{2}{L(L+1)} \sum_{j=j_0}^{k} (j - k + L) \boldsymbol{\eta}_j \boldsymbol{\eta}_j^{\mathrm{T}} - \mathbf{H}_{k+1} \mathbf{P}_{k+1|k} \mathbf{H}_{k+1}^{\mathrm{T}} \tag{5-38}$$

It is assumed that the pseudorange observation noise of each satellite are not correlated with each other. Meanwhile, in order to avoid the estimation results exceeding the reasonable range, the following constraints are applied to the estimation results. The pseudorange observation noise covariance matrix $\hat{\mathbf{R}}'_{k+1}$ after correction is:

$$\hat{\mathbf{R}}'_{k+1}(p,q)=\begin{cases}\hat{\mathbf{R}}_{k+1}(p,q) & \beta_2 \le \dfrac{\hat{\mathbf{R}}_{k+1}(p,q)}{\sigma_0^2} \le \beta_1, p=q \\ \beta_1\sigma_0^2 & \dfrac{\hat{\mathbf{R}}_{k+1}(p,q)}{\sigma_0^2} > \beta_1, p=q \\ \beta_2\sigma_0^2 & \dfrac{\hat{\mathbf{R}}_{k+1}(p,q)}{\sigma_0^2} < \beta_2, p=q \\ 0 & p \ne q \end{cases} \quad (5\text{-}39)$$

where, $\hat{\mathbf{R}}'_{k+1}(p,q)$ is the p row q column element of the matrix $\hat{\mathbf{R}}'_{k+1}$; $\hat{\mathbf{R}}_{k+1}(p,q)$ is the p row q column element of the matrix $\hat{\mathbf{R}}_{k+1}$; σ_0^2 is the general empirical value of the pseudorange observation noise variance(the user can set it according to the experience and the observation environment when using this algorithm); Empirical coefficient β_1 generally chooses 2~5, Empirical coefficient β_2 generally chooses 0.1~0.5.

The innovation covariance matrix based on $\hat{\mathbf{R}}'_{k+1}$ is:

$$\hat{\mathbf{C}}'_{\eta_{k+1}} = \mathbf{H}_{k+1}\mathbf{P}_{k+1|k}\mathbf{H}_{k+1}^{T} + \hat{\mathbf{R}}'_{k+1} \quad (5\text{-}40)$$

FAULT DETECTION

Construct fault detection statistic:

$$\lambda_{k+1} = \boldsymbol{\eta}_{k+1}^{T}(\hat{\mathbf{C}}'_{\boldsymbol{\eta}_{k+1}})^{-1}\boldsymbol{\eta}_{k+1} \quad (5\text{-}41)$$

According to statistical theory, when all the pseudorange observation do not have any fault at epoch $k+1$:

$$\lambda_{k+1} \sim \chi^2(N_{k+1}-4) \quad (5\text{-}42)$$

where, $\chi^2(N_{k+1}-4)$ is the chi-square distribution of $N_{k+1}-4$ degrees of freedom.

Given false alarm rate P_{FA}, fault detection threshold T_D can be determined according to Equation (5-43).

$$\int_0^{T_D} f_{\chi^2(N_{k+1}-4)}(x)dx = 1-P_{FA} \quad (5\text{-}43)$$

where, $f_{\chi^2(N_{k+1}-4)}(x)$ is the probability density function of the chi-square distribution of $N_{k+1}-4$ degrees of freedom.

Then the fault detection criteria can be obtained: If $\lambda_{k+1} \le T_D$, there is no fault occurs at this epoch; If $\lambda_{k+1} > T_D$, a fault occurs at this epoch.

FAULT IDENTIFICATION

If a fault is detected, it is further identified. Construct fault identification:

$$\varphi_{k+1,i} = \frac{|\eta_{k+1}(i)|}{\sqrt{\hat{C}'_{\eta_{k+1}}(i,i)}} \quad (5\text{-}44)$$

where, $\eta_{k+1}(i)$ is the ith element of the innovation η_{k+1}; $\hat{C}'_{\eta_{k+1}}(i,i)$ is the i row i column element of innovation covariance $\hat{C}'_{\eta_{k+1}}$, $i = 1,2,\ldots,N_{k+1}$。

The statistic $\varphi_{k+1,i}$ follows the standard normal distribution when the observation of satellite i has no fault. Thus, the following fault identification criteria can be obtained：If $\varphi_{k+1,i} \le T_R$, satellite i has no fault；If $\varphi_{k+1,i} > T_R$, the pseudorange of satellite i has fault. Where，T_R is the threshold of statistic $\varphi_{k+1,i}$, T_R can be determined according to Equation (5-45).

$$\int_{T_R}^{+\infty} \frac{1}{\sqrt{2\pi}} e^{-\frac{t^2}{2}} dt = \frac{P_{FA}}{2N_{k+1}} \quad (5\text{-}45)$$

where, e is natural base number.

ALGORITHM STEPS

Detailed steps of the proposed algorithm are given in this section.

Step 1 Initialize the filter parameter：$k=0$, Determine the initial state vector $\hat{X}_0$, determine $P_0, Q, L, P_{FA}, \sigma_0^2, \beta_1, \beta_2$ based on experience.

Step 2 Predict the state vector $\hat{X}_{k+1|k}$ at epoch $k+1$, calculate $P_{k+1|k}$ according to equation(5-33).

Step 3 Calculate innovation η_{k+1} according to equation (5-34).

Step 4 Determine the observation noise variance matrix $\hat{R}'_{k+1}$. If the length of the innovation sequence in the sliding window corresponding to all visible satellites at epoch $k+1$ is equal to L, calculate $\hat{R}'_{k+1}$ according to equation(5-39),Otherwise, $\hat{R}'_{k+1} = \sigma_0^2 I_{N_{k+1} \times N_{k+1}}$.Calculate $\hat{C}'_{\eta_{k+1}}$ according to equation (5-40).

Step 5 The fault detection statistic is calculated according to Equation (5-41), and the fault detection criteria are used to determine whether there is fault at this epoch.

Step 6 If there is no fault at this epoch, go to Step8. Otherwise, the fault identification statistic of each satellite is calculated according to Equation (5-44), and the fault satellite is identified according to the fault identification criteria.

Step 7 Adjust η_{k+1}:

$$\eta'_{k+1}(i) = \begin{cases} \sqrt{\hat{C}'_{\eta_{k+1}}(i,i)} & \varphi_{k+1,i} > T_R \\ \eta_{k+1}(i) & \varphi_{k+1,i} \le T_R \end{cases} \quad (5\text{-}46)$$

where, η'_{k+1} is the innovation sequence after adjustment，$\eta'_{k+1}(i)$ is the ith element of vector η'_{k+1}, $i = 1,2,\ldots,N_{k+1}$。

Step 8 Update the state vector $\hat{X}_{k+1}$ at epoch $k+1$. Output the positioning result:

The gain matrix is:

$$K_{k+1} = P_{k+1|k} H_{k+1}^T (\hat{C}'_{\eta_{k+1}})^{-1} \quad (5\text{-}47)$$

The state vector after updating at epoch $k+1$ is :

$$\hat{\mathbf{X}}_{k+1} = \hat{\mathbf{X}}_{k+1|k} + \mathbf{K}_{k+1}\boldsymbol{\eta}'_{k+1} \quad (5\text{-}48)$$

Calculate the error covariance of $\hat{\mathbf{X}}_{k+1}$:

$$\mathbf{P}_{k+1} = (\mathbf{I}_{8\times 8} - \mathbf{K}_{k+1}\mathbf{H}_{k+1})\mathbf{P}_{k+1|k} \quad (5\text{-}49)$$

The elements in $\hat{\mathbf{X}}_{k+1}$ are output as positioning results to complete the positioning solution process based on quality control.

Step 9 k add 1 and repeat Step 2.

5.3.2. SIMULATION VERIFICATION AND ANALYSIS

In this project, two static and dynamic experiments are designed to evaluate the fault detection performance of the proposed algorithm by adding corresponding pseudorange gross errors to the collected real static and dynamic data.

This project defines the indexes to evaluate the performance of the algorithm.

Fault detection rate（FDR）is:

$$R_{FD} = \frac{n_{FD}}{n_F} \times 100\% \quad (5\text{-}50)$$

where, n_F is the number of epochs the fault occurs in the experiment； n_{FD} is the number of epochs where the fault occurs and the algorithm successfully detects the fault in the experiment.

Fault identification rate（FIR）is:

$$R_{FI} = \frac{n_{FI}}{n_F} \times 100\% \quad (5\text{-}51)$$

where, n_{FI} is the number of epochs where the fault occurs and the algorithm correctly identifies the fault in the experiment.

False alarm rate（false alarm rate, FAR）is

$$R_{FA} = \frac{n_{FA}}{n_N} \times 100\% \quad (5\text{-}52)$$

where, n_N is the number of epochs where no fault occurs in the experiment； n_{FA} is the number of epochs where no fault occurs but the algorithm detects fault in the experiment.

Missed detection rate（MDR）is:

$$R_{MD} = \frac{n_{MD}}{n_F} \times 100\% \quad (5\text{-}53)$$

where, n_{MD} is the number of epochs where a fault occurs but the algorithm does not detect the fault in an experiment. Easy to know $R_{FD} + R_{MD} = 100\%$。

The least squares residual method and the fault detection method based on Kalman filter are used as the comparison algorithms in the fault detection algorithm and the evaluation method of positioning results. Their observation noise variance matrix is set to $\sigma_0^2 \mathrm{I}_{N_{k+1}\times N_{k+1}}$。

Step fault and slope fault are two common fault types. According to the number of simultaneous faults, it can be divided into single faults and multiple faults. In order to fully verify the performance of the proposed algorithm under different operating environments (static observation and dynamic observation) and different fault types, this project design the experiment scenario as shown in Table **5-12**.

Table 5-12: The designed scenarios

Data type	Fault type	Description
Static data (sampling rate 10Hz)	No fault	Raw static observation data
	single-step error	A step fault is added to the pseudorange of satellite G09 at observation time 150~200 s (including 150 s and 200 s, 501 epoch in total)
	single-slope error	A slope fault is added to the pseudorange of satellite G09 at observation time 100~200 s (including 100 s and 200 s, 1000 epoch in total)
	Multiple errors	A ramp fault is added to the pseudorange of satellite G09 at observation time 150~200 s (including 150 s and 200 s, 501 epoch in total)
Dynamic sampling rate 10Hz)	No fault	Raw dynamic observation data
	single-step error	A step fault is added to the pseudorange of satellite G10 at the observation time 300~400 s (including 300 s and 400 s, 1001 epoch in total)
	single-slope error	The slope fault is added to the pseudorange of satellite G10 at the observation time of 400~600 s (excluding 400 s, including 600 s, 2000 epoch in total)
	Multiple errors	The step fault is added to the pseudorange of satellite G10 and G12 at the observation time of 400~500 s (excluding 400 s, including 500 s, 1001 epoch in total)

SIMULATION EXPERIMENT BASED ON STATIC DATA

Simulation experiment based on static data

The static data used in this project was observed near the library in the campus of Jiangjun Road, Nanjing University of Aeronautics and Astronautics on December 29, 2019. Figure 5-11 shows the position and observation environment of the GNSS receiver used in the

experiment. The GNSS board type of the receiver is NovAtel OEM7500 and the sampling rate is 10 Hz. A total of 300 s GPS observation data from 10:45-10:50 am was selected for simulation experiment.

Figure 5-11: The environment of static observation experiment

The reference position of the receiver was obtained by calculating network real time kinematic (NRTK) technology provided by Qianxun to obtain GNSS observation data sustained for 1 h. The proposed algorithm uses the least square method to solve the data of the first epoch to get the initial state vector. Set initial filter parameter $\mathbf{P}_0 = \mathrm{diag}(1,1,1,1,0,0,0,1)$（diag represents a diagonal matrix, and the elements in () are diagonal elements）, $\mathbf{Q} = 0.1\mathrm{I}_{8\times 8}$, $\mathrm{L} = 100$, $\mathrm{P}_{\mathrm{FA}} = 0.01\%$, $\sigma_0^2 = 1\ \mathrm{m}^2$, β_1=5, $\beta_2 = 0.1$.

Experiment of raw static data

The fault detection statistic conducted by three fault detection methods on the raw static data is shown in Figure 5-12. In the experiment, their fault detection quantity did not exceed the threshold value, and the false alarm rate was 0。

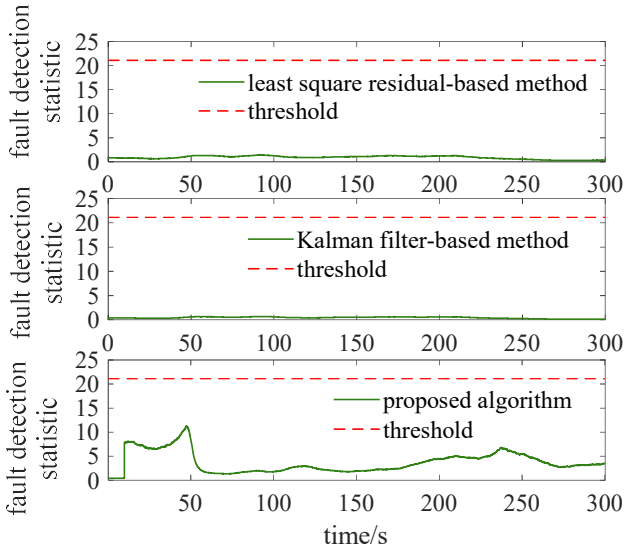

Figure 5-12: Fault detection statistics based on the original static data

Figure 5-13 shows the positioning error after the raw data is solved by the proposed algorithm. Table **5-13** compares the positioning accuracy indexes of the three algorithms. It can be seen that the horizontal root mean square error of the proposed algorithm is 0.191m, and the positioning accuracy in the horizontal direction is 13.96% higher than that of the least square-residual method and the fault detection method based on Kalman

filter. The 3D root mean square error of the proposed algorithm is 0.685 m, and the 3D positioning accuracy is improved by 26.11% and 25.46%, respectively, compared with the previous two algorithms.

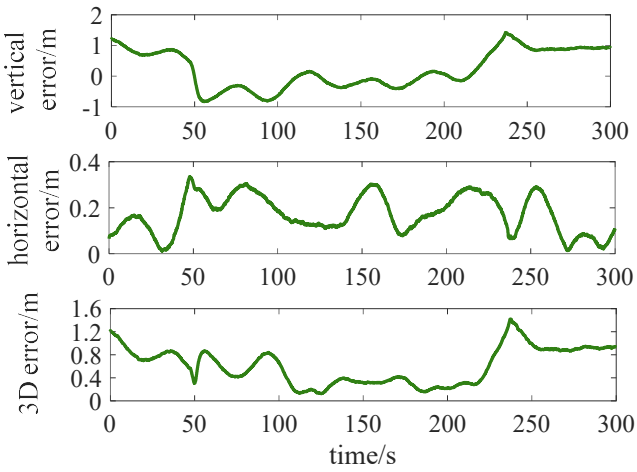

Figure 5-13: The positioning error of the proposed algorithm based on the original static data

Table 5-13: The positioning accuracy for the candidate algorithms based on the original static data

Positioning accuracy index	Direction	Maximum error /m	95%quantile error /m	RMSE /m
LSR-based	height	1.467	1.294	0.900
	horizontal	0.422	0.395	0.222
	3D	1.467	1.297	0.927
fault detection method based on Kalman filter	height	1.433	1.297	0.892
	horizontal	0.420	0.396	0.222
	3D	1.434	1.298	0.919
proposed algorithm	height	1.418	1.126	0.657
	horizontal	0.335	0.292	0.191
	3D	1.420	1.131	0.685

Experiment with static data of single step fault

The proposed algorithm and two comparison algorithms are used for fault detection after adding 5 m step fault to the pseudorange of visible satellite G09 during the observation time of 150~200 s (including 150 s and 200 s). The fault detection statistic is shown in Figure 5-14. At 150 s, the fault detection quantity of the proposed algorithm jumps to about 135 m and exceeds the threshold, and the fault detection quantity exceeds the threshold until 200 s. Although the fault detection quantity of the fault detection method based on Kalman filter and the least squares residual method also has a high order jump during the fault occurrence, it does not exceed the fault detection threshold, so no fault is detected. According to Figure 5-15, after the proposed algorithm detects a fault within 150~200 s, the amount of fault identification of G09 exceeds its threshold and is correctly marked as a satellite whose observation data contains a fault. As shown in Table **5-14**, both the fault detection rate and fault identification rate of the proposed algorithm are 100%, and the false alarm rate is 0. However, the least squares residual method and the fault detection method based on Kalman filter fail to detect the fault.

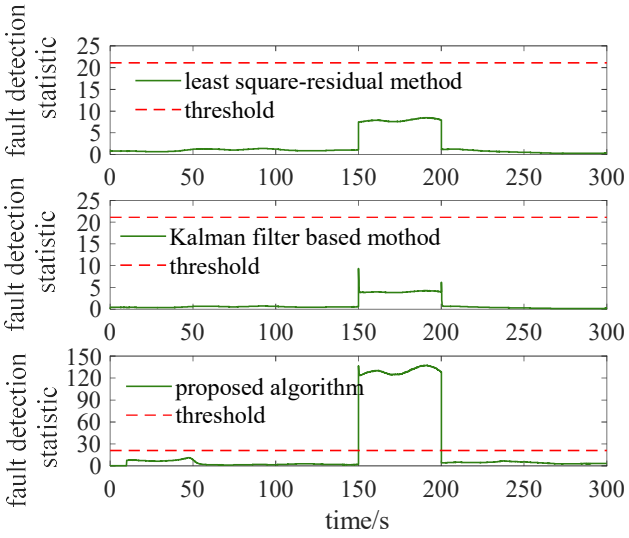

Figure 5-14: Fault detection statistics with a 5m step error added on the observations in the static mode

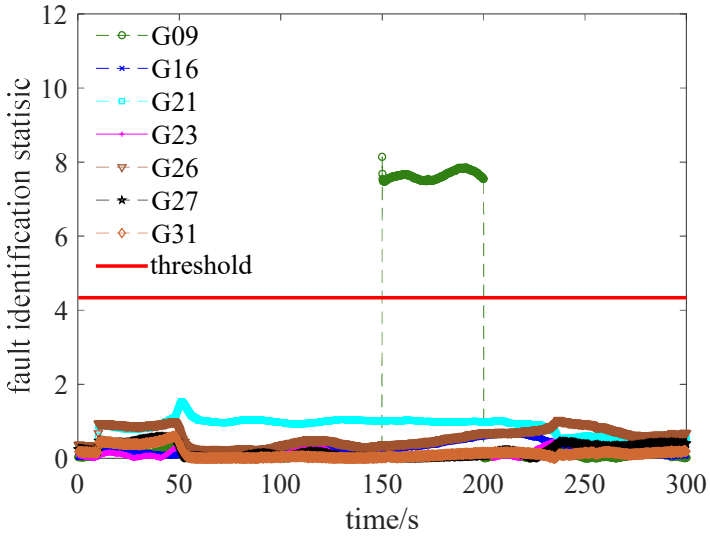

Figure 5-15: Fault identification statistics of the proposed algorithm with a 5 m step error added on the observations in the static mode

Table 5-14: Fault detection performance for a 5m step error added on the static data

Fault detection method	FDR	FIR	FAR	MDR
least square-residual method	0	0	0	100%
fault detection method based on Kalman filter	0	0	0	100%
proposed algorithm	100%	100%	0	0

According to Table 5-15, the horizontal root mean square error of the proposed algorithm is 0.192m and the 3D root mean square error is 0.687m. By comparing the accuracy indexes of the comparison algorithms, compared with the least square-residual method

and the fault detection method based on Kalman filter, the horizontal positioning accuracy of the proposed algorithm is improved by 82.14% and 82.17%, respectively, and the 3D positioning accuracy is improved by 71.67% and 71.68%, respectively.

Table 5-15: The positioning accuracy for the candidate algorithms based on the static data with a 5 m step error

Positioning accuracy index	Direction	Maximum error /m	%95 quantile error /m	Root mean square error /m
least square-residual method	height	5.122	5.008	2.174
	horizontal	2.794	2.711	1.075
	3D	5.741	5.664	2.425
fault detection method based on Kalman filter	height	5.556	5.025	2.174
	horizontal	2.925	2.704	1.077
	3D	6.270	5.657	2.426
proposed algorithm	height	1.418	1.126	0.659
	horizontal	0.335	0.286	0.192
	3D	1.420	1.131	0.687

If 0 m and 1 m are added to the pseudorange of visible satellite G09 from the observation time 150~200 s (including 150 s and 200 s), then 0 m,1 m... For a 10 m step fault, the fault detection rate, fault identification rate and 3D root mean square error of the three algorithms are shown in Figure 5-16. The false alarm ratio of the three algorithms is always 0, which is not shown in Figure 5-16. Since the sum of the missed detection rate and the fault detection rate is 1, it is not shown in Figure 5-16 for the sake of simplicity. It can be seen from that Figure 5-16 the proposed algorithm and the fault detection method based on Kalman filter reach 100% fault detection rate and fault identification rate when the single-satellite pseudorange fault exceeds 3 m and 8 m, respectively. When the fault of single satellite pseudorange is 8 m, the fault detection rate reaches 100%. When the single satellite pseudorange fault is 9 m, the fault identification rate reaches 100%. When the fault of the proposed algorithm is less than 2 m, the 3D root mean square error increases with the increase of the fault. When the fault is more than 3 m, the 3D root mean square error remains at 0.69 m because the proposed algorithm can detect and identify the fault 100%. The 3D root mean square error of the fault detection method based on Kalman filter gradually increases to about 3m as the fault increases to 6 m, and decreases to about 1 m when the fault exceeds 7 m. The 3D root mean square error of the least squares residual method exceeds 3m at 7 m fault and then decreases with the increase of the fault. The 3D root mean square error curve of the proposed algorithm is always below the other two algorithms, so the proposed algorithm has the highest positioning accuracy under different fault conditions.

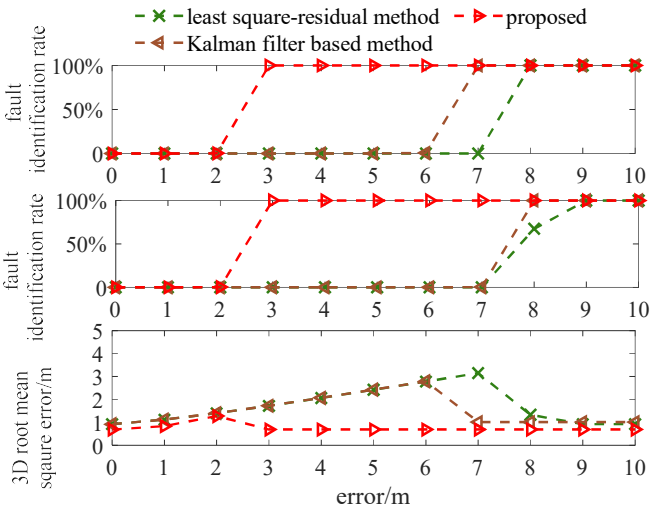

Figure 5-16: The FDR, FIR and 3D accuracy (RMSE) for the candidate algorithms based on the static data with various step errors

Experiment with static data including single slope fault

If a slope fault increasing at a rate of 0.2m /s is added to the pseudorage of visible satellite G09 at the observation time of 100-200 s (excluding 100 s, including 200 s), the fault detection statistics of the three algorithms is shown in Figure 5-17 (T_{SE} represents the slope fault duration; V_{SE} Represents the rate of slope failure). During the fault occurrence period, the fault detection amount of the three algorithms increases gradually and exceeds the threshold before 150 s. The proposed algorithm starts to detect slope faults slightly earlier than the other two algorithms.

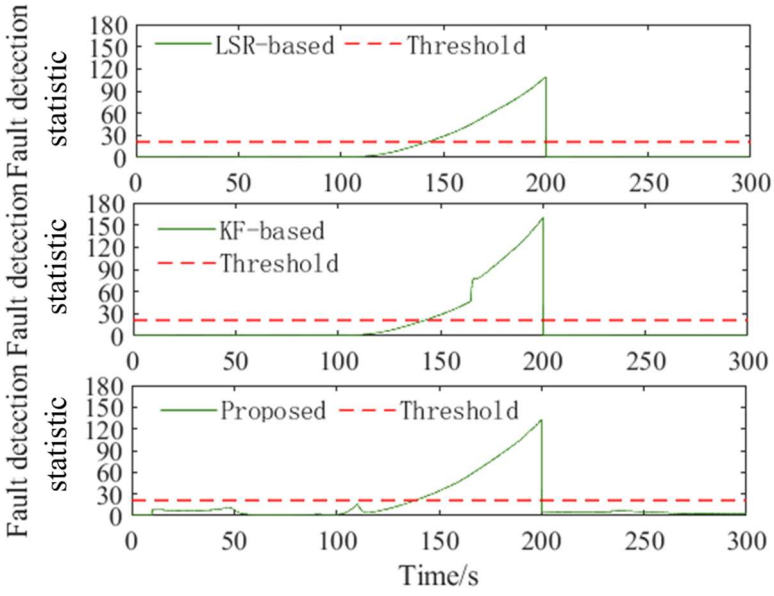

Figure 5-17: Fault detection statistics for the static data with a 0.2 m/s ramp error added for 100 s.

The fault identification statistic of G09 satellite calculated by the algorithm proposed in Figure 5-18, like its fault detection statistic, exceeds the threshold before 150 s, and its pseudo-distance is identified as containing faults. Figure 5-19 shows that the fault detection method based on Kalman filter correctly identifies faults after about 160 s. After the fault was identified, the fault identification statistic of G09 increased rapidly for a short time. Figure 5-20 shows that the least squares residual method correctly identified the fault only in about 20 s before 200 s.

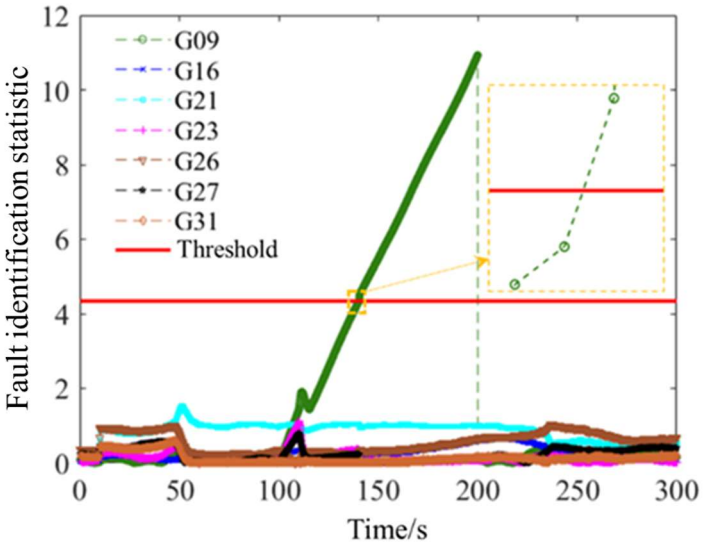

Figure 5-18: Fault identification statistics of the proposed algorithm with a 0.2 m/s ramp error added for 100 s in the static mode.

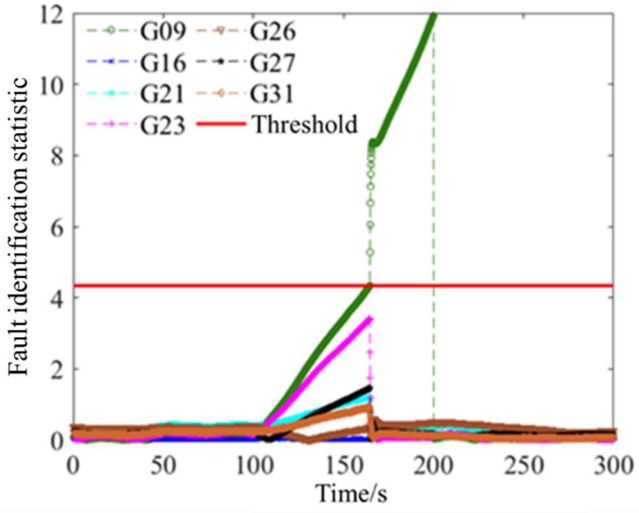

Figure 5-19: Fault identification statistics of the KF-based method with a 0.2 m/s ramp error added for 100 s in the static mode.

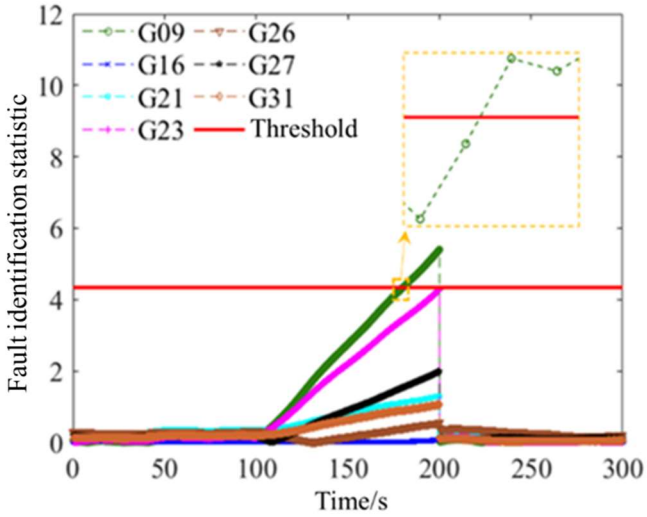

Figure 5-20: Fault identification statistics of the least square residual based method with a 0.2 m/s ramp error added for 100 s in the static mode.

Table 5-16 calculates the fault detection indexes of the three algorithms. The fault detection rate of the least squares residual method and the fault detection method based on Kalman filter is 57.8%. Although the fault detection rate of 61.6% of the proposed algorithm is not significantly higher than that of the two algorithms, the fault identification rate of 51.4% of the proposed algorithm is significantly higher than that of the other two algorithms of 20% and 35.2%.

Table 5-16: Fault detection performance for the candidate algorithms with a 0.2 m/s ramp error added for 100 s in the static mode.

Fault detection method	FDR	FIR	FAR	MDR
LSR-based	57.8%	20%	0	42.2%
KF-based	57.8%	35.2%	0	42.2%
Proposed	61.6%	51.4%	0	38.4%

Table 5-17 compares the positioning accuracy indexes of the three algorithms under this kind of fault. The 3D root mean square error(RMSE) of the proposed algorithm is 0.712 m, and the positioning accuracy is improved by 72.2% and 64.4% compared with the two control algorithms, respectively.

Table 5-17: The positioning accuracy for the candidate algorithms with a 0.2 m/s ramp error added for 100 s in the static mode.

Positioning accuracy indexes	Maximun error/m	%95 quantile positioning error /m	RMSE/m
LSR-based	4.198	3.595	1.595
	6.719	5.471	2.006
	7.923	6.548	2.563
KF-based	3.670	2.997	1.357
	5.444	4.219	1.472
	6.517	5.161	2.002
Proposed	1.418	1.125	0.657
	1.150	0.424	0.275
	1.420	1.134	0.712

Figure 5-21 shows the experimental results when the slope fault rate increases from 0 m/s to 0.5 m/s during the observation time of satellite G09 between 100 and 200 s (excluding 100 s, including 200 s). The fault detection rate of the three algorithms is close, but the fault detection rate of the proposed algorithm is significantly higher than that of the other two algorithms. The 3D root mean square error of the two control algorithms firstly

increases with the increase of slope fault rate, and then decreases. The maximum value is more than 2 m, but the 3D root mean square error of the proposed algorithm is always stable less than 1 m.

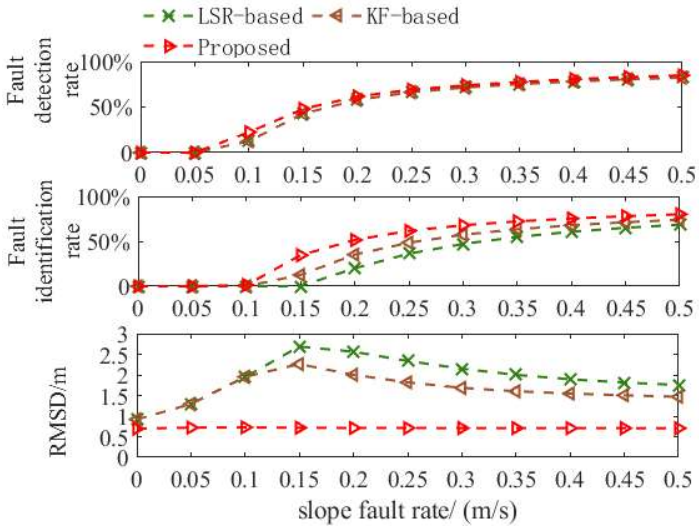

Figure 5-21: The FDR, FIR and 3D accuracy (RMSE) for candidate algorithms with various ramp errors in the static mode.

Experiment with static data including MUltiple faults

The least squares residual method is based on the single fault hypothesis, and each epoch can only eliminate one fault. Therefore, the experiments in Section 0 and Section 0 only take the fault detection method based on Kalman filter as the control group to verify the performance of the proposed algorithm for the detection of multiple faults.

A step fault of 5 m was added to the pseudorange of satellite G09 and G16 at the observation time of 150~200 s (including 150 s and 200 s). The fault detection statistics of the two algorithms is shown in Figure 5-22. During the fault occurrence, the fault detection statistics of the proposed algorithm is always higher than the threshold value, but the fault detection method based on Kalman filter does not detect the fault.

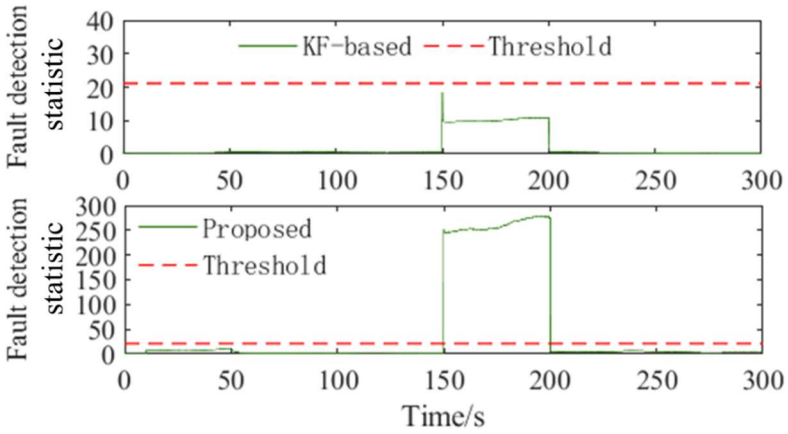

Figure 5-22: T Fault detection statistics for 5m step errors added on the pseudorange of G09 and G16 in the static mode.

As shown in Figure 5-23, during the fault occurrence, the fault identification statistics of satellite G09 and G16 of the proposed algorithm both exceeded the threshold.

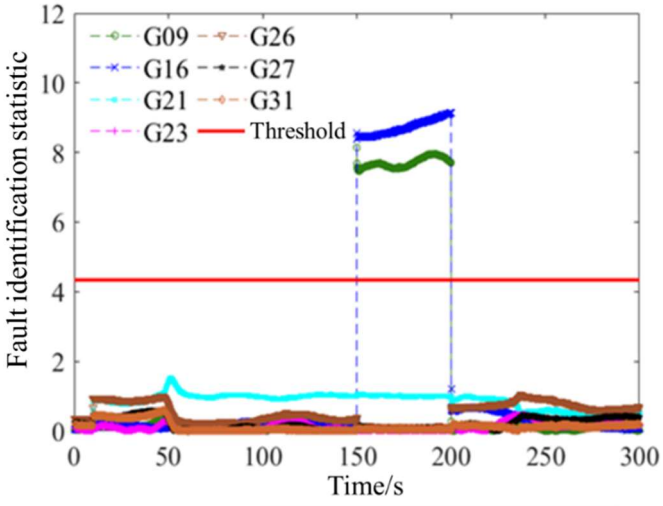

Figure 5-23: Fault detection statistics for 5m step errors added on the pseudorange of G09 and G16 in the static mode.

It can be seen from Table 5-18 that the proposed algorithm can detect and identify 100% of the 5 m step faults that exist simultaneously with the pseudorange of the two satellites. However, the detection rate and identification rate of the fault detection method based on Kalman filter are both 0.

Table 5-18: Fault detection performance for candidate algorithms with 5m step errors added on the pseudorange of G09 and G16 in the static mode.

Fault detection method	FDR	FIR	FAR	MDR
KF-based	0	0	0	100%
Proposed	100%	100%	0	0

The positioning accuracy indexes of the two algorithms are shown in Table 5-19. At this time, the 3D root mean square error of the fault detection method based on Kalman filter is 1.773m. The 3D root mean square error of the proposed algorithm is 0.704 m, and the positioning accuracy is improved by about 60.3%

Table 5-19: Positioning accuracy performance for candidate algorithms with 5m step errors added on the pseudorange of G09 and G16 in the static mode.

Positioning accuracy indexe	Maximun error/m	%95 quantile positioning error/m	RMSE/m
KF-based	1.432	1.301	0.813
	4.316	3.957	1.576
	4.328	3.965	1.773
Proposed	1.418	1.125	0.655
	0.687	0.553	0.260

	1.420	1.131	0.704

Figure 5-24 shows the fault detection and positioning after the step fault increases gradually with the addition of the pseudo-distance at the observation time 150-200 s (including 150 s and 200 s) of satellite G10 and G12. Under multiple faults of different sizes, the false alarm rate of the two algorithms is 0. The fault detection method based on Kalman filter can detect the multiple faults of more than 8 m 100% and identify the multiple faults of more than 10 m 100%. The proposed algorithm can detect and identify multiple faults 100% when the faults reach 3 m and 4 m respectively. When multiple faults are lower than 2 m, the 3D root mean square errors of the two algorithms are close. However, with the further increase of multiple faults, the 3D root mean square errors of the fault detection method based on Kalman filter always rise to more than 2 m when multiple faults are lower than 8 m, while the 3D root mean square of the proposed algorithm is always roughly kept below 1 m.

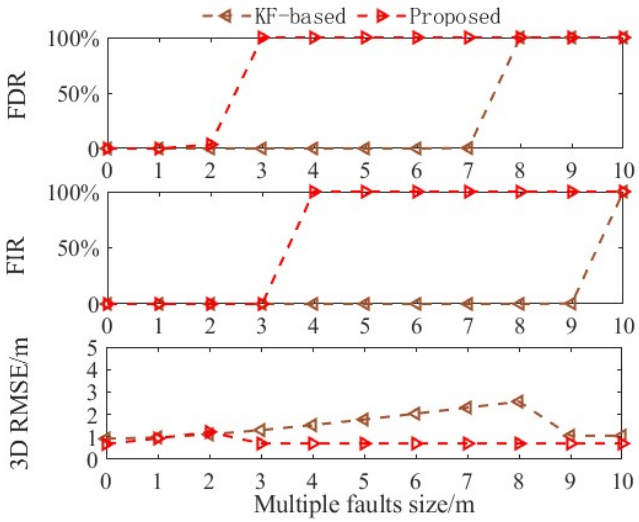

Figure 5-24: The FDR, FIR and 3D accuracy (RMSE) for candidate algorithms with various step errors on two satellites in the static mode.

SIMULATION EXPERIMENT BASED ON DYNAMIC DATA

The dynamic data used in this program are from the UAV dynamic observation experiment conducted in Nantou, Taiwan Province on January 31, 2018. The flight path of the UAV is shown in Figure 5-25. The onboard GNSS receiver model is Trimble BD 982, and the sampling rate is 10 Hz. The reference trajectory of the UAV used in the experiment was obtained by close-range photogrammetry using the onboard VLP-16 Velodyne Lidar, which has CM-level positioning accuracy.

Figure 5-25: Flight trajectory of the unmanned aerial vehicle (UAV).

The proposed algorithm uses the least square method to solve the first and second epoch data to get the initial state vector, and sets the initial filtering parameters $\mathbf{P}_0 = \mathrm{diag}(10,10,10,10,2,2,2,2)$, $\mathbf{Q} = 0.1\mathbf{I}_{8\times 8}$, $\mathrm{L} = 100$, $\mathbf{P}_{\mathrm{FA}} = 0.01\%$, $\sigma_0^2 = 5\ \mathrm{m}^2$, $\beta_1 = 2$, $\beta_2 = 0.2$.

Experiments with raw dynamic data

According to Figure 5-26, under the raw dynamic data, the fault detection statistics of the three algorithms in the whole process does not exceed the fault detection threshold, and the false alarm rate is 0.

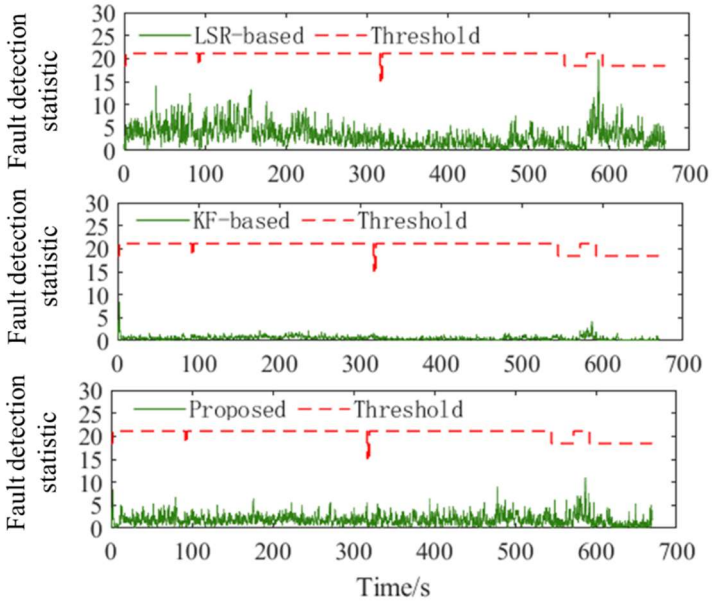

Figure 5-26: Fault detection statistics based on the original dynamic data.

The changes of positioning errors in each direction after the positioning solution of the original dynamic data by the proposed algorithm are shown in Figure 5-27 The positioning accuracy indexes are shown in Table **5-20** The horizontal root mean square error and 3D root mean square error of the proposed algorithm are 1.567m and 2.233m, respectively. Compared with the least squares residual method and the fault detection method based on Kalman filter, the horizontal positioning accuracy of the proposed algorithm is improved by 1.14% and 0.57%, respectively, and the positioning accuracy in 3D direction was improved by 33.4% and 32%, respectively.

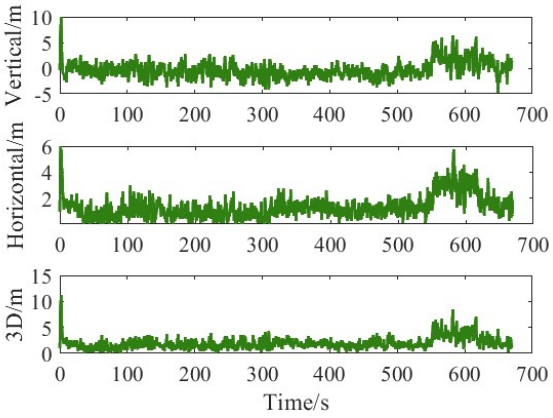

Figure 5-27: The positioning error of the proposed algorithm based on the original dynamic data.

Table 5-20: The positioning accuracy performance for the candidate algorithms based on the original dynamic data.

Positioning accuracy indexes	Direction	Maximun error/m	%95 quantile positioning error/m	RMSE/m
LSR-based	Vertical	6.481	4.765	2.955
	Horizontal	4.590	2.881	1.585
	3D	7.289	5.069	3.353
KF-based	Vertical	9.920	4.466	2.891
	Horizontal	5.976	2.933	1.558
	3D	11.267	4.743	3.284
Proposed	Vertical	9.920	3.007	1.591
	Horizontal	5.976	3.242	1.567
	3D	11.267	4.052	2.233

Experiment under dynamic data with single step fault

After adding 10 m step fault to the pseudorange of visible satellite G10 during the observation time 300~400 s (including 300 s and 400 s), the proposed algorithm and two control algorithms are used for fault detection.

As shown in Figure 5-28, the fault detection statistics of the proposed algorithm is higher than the fault detection threshold during 300~400 s of observation time, and lower than the threshold during the rest time. Among the control algorithms, the fault detection method based on Kalman filter is lower than the threshold value during the fault occurrence, and the fault detection rate is 0, while the least squares residual method has a higher fault detection rate. As shown in Figure 5-29, the fault identification statistics of satellite G10 of the proposed algorithm exceeds the corresponding threshold within 300~400 s, while the fault identification statistics of other visible satellites is all lower than the corresponding threshold during this period. Therefore, the proposed algorithm can correctly identify faults 100%. Figure 5-30 shows that the least squares residual method fails to correctly identify the fault in about half of the time periods in which the fault occurs.

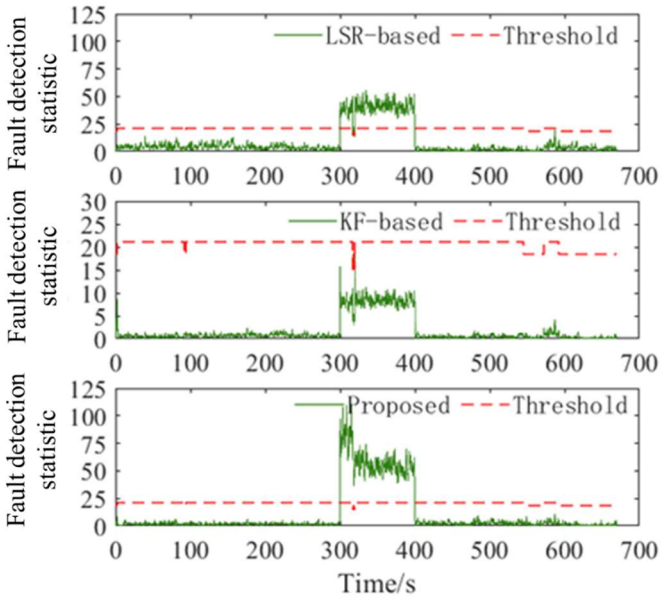

Figure 5-28: Fault detection statistics with a 10m step error added on the observations in the dynamic mode.

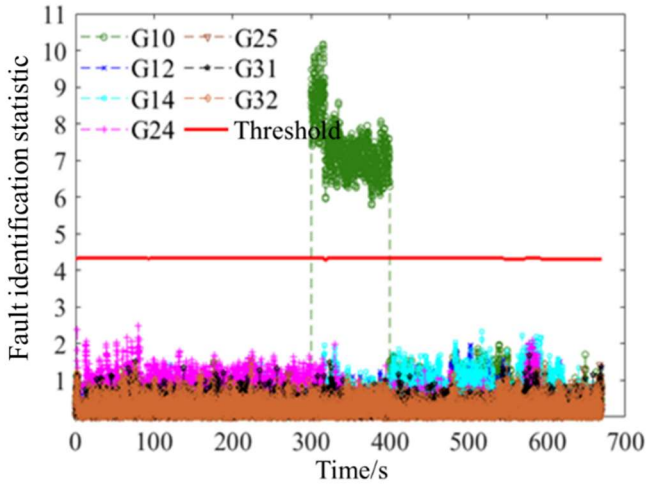

Figure 5-29: Fault identification statistics with a 10m step error added on the observations in the dynamic mode.

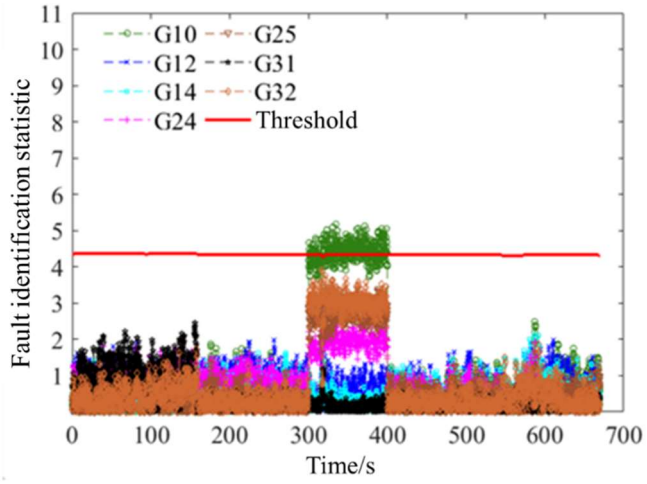

Figure 5-30: Fault identification statistics of least square residual based method with a 10m step error added on the observations in the dynamic mode.

As shown in Table 5-21, the proposed algorithm has a good fault detection performance when processing the dynamic data with a single satellite pseudorange containing 10 m faults. The fault detection rate and fault identification rate are both 100%, and the false alarm rate is 0. Although the fault detection rate of the least squares residual method reaches 98.7%, the fault identification rate is less than 60%. The fault detection method based on Kalman filter fails to detect the fault.

Table 5-21: Fault detection performance for candidate algorithms with a 10m step error added on the observations in the dynamic mode.

Fault detection method	FDR	FIR	FAR	MDR
LSR-based	98.7%	56.4%	0	1.3%
KF-based	0	0	0	100%
Proposed	100%	100%	0	0

Table 5-22 shows the positioning accuracy indexes of the proposed algorithm and two control algorithms when processing dynamic data containing faults. At this time, the

horizontal root mean square error and 3D root mean square error of the positioning results of the proposed algorithm are 1.592 m and 3.049 m, respectively. Compared with the least squares residual method, The horizontal positioning accuracy and 3D positioning accuracy were improved by 2.63% and 39.87%, respectively. Compared with the fault detection method based on Kalman filter, the horizontal positioning accuracy and 3D positioning accuracy are improved by 3.28% and 52.33% respectively.

Table 5-22: The positioning accuracy performance for the candidate algorithms with a 10m step error added on the observations in the dynamic mode.

Positioning accuracy indexes	Direction	Maximun error/m	%95 quantile positioning error/m	RMSE/m
LSR-based	Vertical	22.460	14.069	4.800
	Horizontal	4.590	2.947	1.635
	3D	22.668	14.401	5.071
KF-based	Vertical	18.823	14.622	6.180
	Horizontal	5.976	3.020	1.646
	3D	19.239	14.854	6.396
Proposed	Vertical	9.920	4.858	2.600
	Horizontal	5.976	5.239	1.592
	3D	11.267	3.208	3.049

If 0 m and 2 m are added successively to the pseudo distance of visible star G10 from 300~400s (including 300s and 400s)... ,18 m step fault. The fault detection effects of the three algorithms are shown in Figure 5-31. It can be seen from Figure 5-31 that in order for both the fault detection rate and the fault identification rate to reach 100%, the proposed algorithm and the fault detection method based on Kalman filter need faults exceeding 10 m and 16 m respectively. The fault detection rate of least squares residual method reaches 100% when the fault exceeds 10 m, and the fault identification rate reaches 100% when the fault exceeds 12 m. The 3D root mean square error of the proposed algorithm experienced a slow rise when the fault increased to 2 m, and then stabilized at 3 m. However, the 3D root mean square error of the fault detection method based on Kalman filter always increases before the fault reaches 14 m, and the 3D root mean square error of the highest point is more than 7 m. When the fault exceeds 16 m, the 3D root mean square error decreases to about 3.5 m. The 3D root mean square error of the least squares residual method reaches the maximum value of 6 m when the fault is 8 m. When the fault increases from 0 m to 18 m, the 3D root mean square error of the proposed algorithm is always the lowest among the three algorithms, so the proposed algorithm has higher positioning accuracy under different fault conditions.

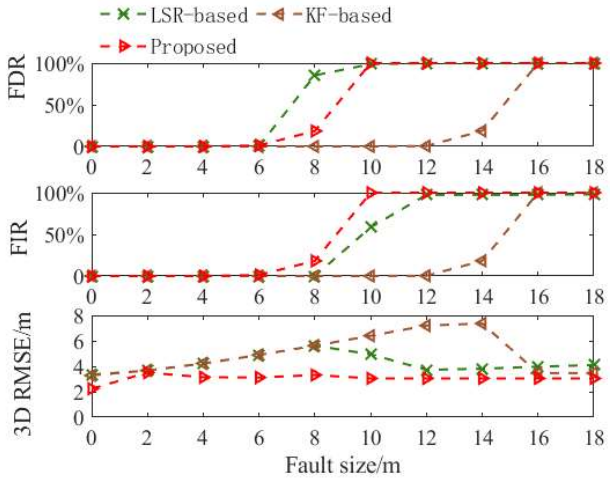

Figure 5-31: The FDR, FIR and 3D accuracy (RMSE) for the candidate algorithms based on dynamic data with various step errors.

Experiment under dynamic data with single slope fault

In the experiment in this section, a slope fault with a rate of 0.2 m/s from 400 to 600 s (excluding 400 s, including 600 s) from the observation time is added to the pseudorange of satellite G10.

The fault detection statistics of the three algorithms for dynamic data containing slope faults is shown in Figure 5-32. The fault detection statistics of the proposed algorithm starts to ramp up from 400 s and exceeds the threshold at about 450 s, and the algorithm begins to detect the slope fault. The control algorithm and the proposed algorithm have similar fault detection statistic variation. The time of first detection of slope failure is relatively close.

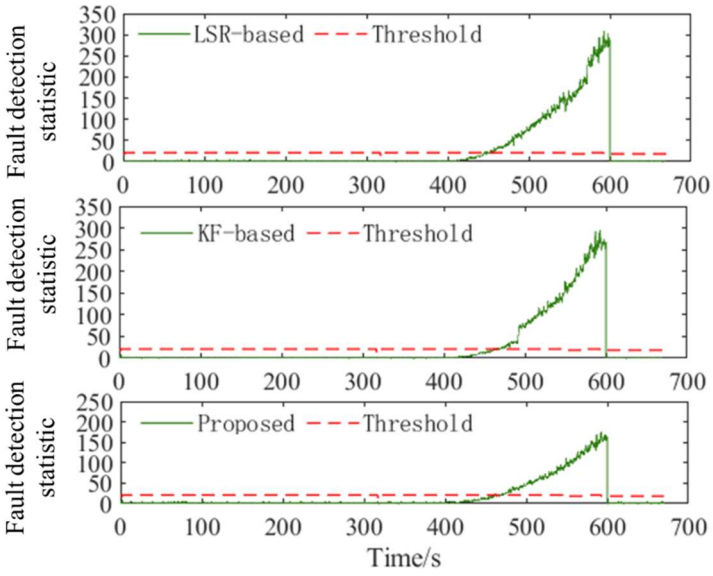

Figure 5-32: Fault detection statistics for the dynamic data with a 0.2 m/s ramp error added for 200 s.

As shown in Figure 5-33, the fault identification statistics of satellite G10 calculated by the proposed algorithm starts to ramp up from 400 s, and exceeds the threshold roughly at the same time when the algorithm detects the fault, and then the proposed algorithm can identify the fault correctly until the fault no longer occurs. Figure 5-34 shows that the fault detection method based on Kalman filter can identify faults later than the proposed algorithm. When the slope fault increases to a certain value, the fault identification statistics of multiple satellites exceeds the threshold, and the data corresponding to the

maximum value among them is marked as fault data. The fault identification results of the least squares residual method during the fault occurrence are shown in Figure 5-35. The least squares residual method fluctuates between correct fault identification and wrong fault identification within a short period of time after the first correct fault identification at around 440 s, and then the data containing slope faults can be correctly identified all the time.

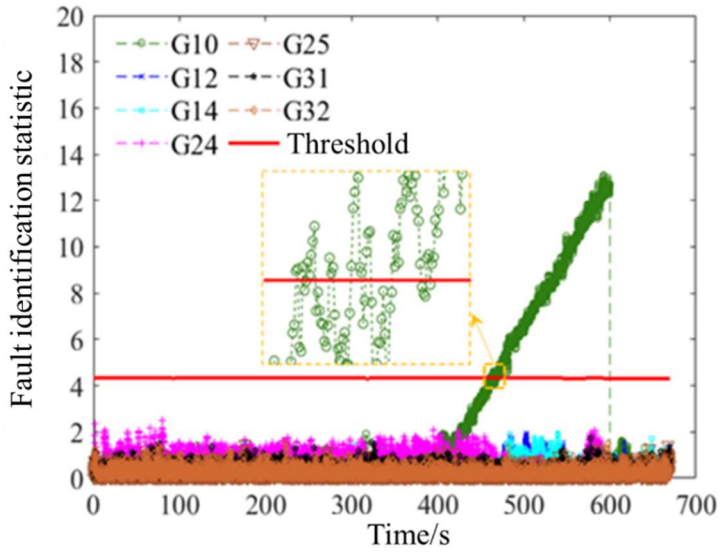

Figure 5-33: Fault identification statistics of the proposed algorithm with a 0.2 m/s ramp error added for 200s in the dynamic mode.

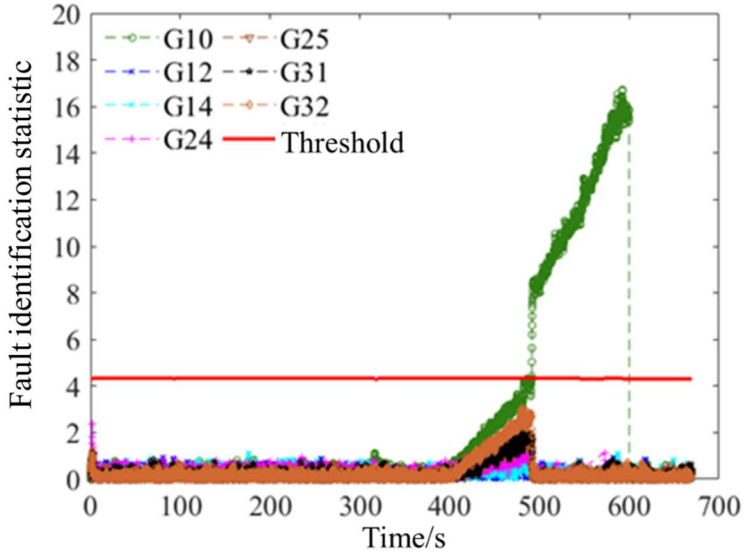

Figure 5-34: Fault identification statistics of the KF-based method with a 0.2 m/s ramp error added for 200 s in the dynamic mode.

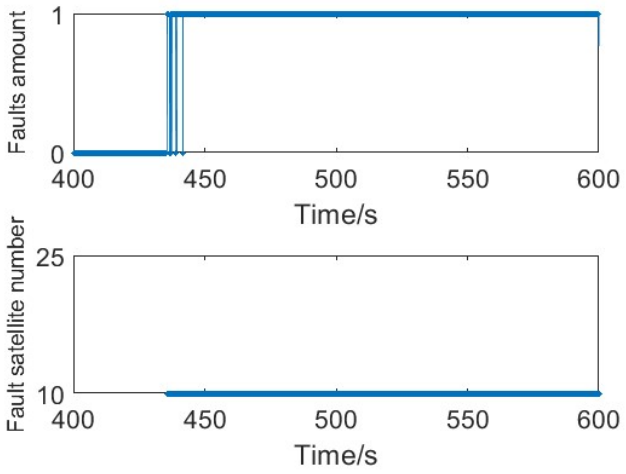

Figure 5-35: Fault identification result of the least square residual based method with a 0.2 m/s ramp error added for 200 s in the dynamic mode.

As can be seen from Table 5-23, under this slope fault condition, the fault detection ratE and identification rate of the proposed algorithm are both 66.25%. Although the fault detection rate of the least squares residual method and the fault detection method based on Kalman filter is slightly higher than that of the proposed algorithm, the fault identification rate of these two algorithms is significantly lower than that of the proposed algorithm.

Table 5-23: Fault detection performance for the candidate algorithm with a 0.2 m/s ramp error added for 200 s in the dynamic mode.

Fault detection method	FDR	FIR	FAR	MDR
LSR-based	75.1%	38.2%	0	24.9%
KF-based	66.75%	54.3%	0	33.25%
Proposed	66.25%	66.25%	0	33.75%

Table 5-24 calculates the positioning accuracy indexes of the three algorithms. The 3D root mean square error of the two control algorithms is 4.253m and 3.689m respectively, while the 3D root mean square error of the least squares residual method is 2.552m, which is 40% and 30.2% lower than that of the two control algorithms, respectively.

Table 5-24: The positioning accuracy for the candidate algorithms with a 0.2 m/s ramp error added for 200 s in the dynamic mode.

Positioning accuracy indexes	Direction	Maximun error/m	%95 quantile positioning error/m	RMSE/m
LSR-based	Vertical	18.743	4.570	2.575
	Horizontal	11.845	8.743	3.385
	3D	20.681	8.814	4.253
KF-based	Vertical	9.920	4.453	2.776
	Horizontal	8.845	5.956	2.429
	3D	11.267	6.124	3.689
Proposed	Vertical	9.920	3.942	1.975
	Horizontal	5.976	3.347	1.616

	3D	11.267	4.629	2.552

In Figure 5-36，if slope faults with increasing speed are added to the pseudoranges for G10 satellite during 400-600s (excluding 400s, including 600s), the fault detection rate of the least squares residual method is always slightly higher than that of the proposed algorithm, but the fault identification rate of the proposed algorithm is always higher than that of the other two control algorithms. In addition, the positioning accuracy of the proposed algorithm is always higher than that of the two control algorithms.

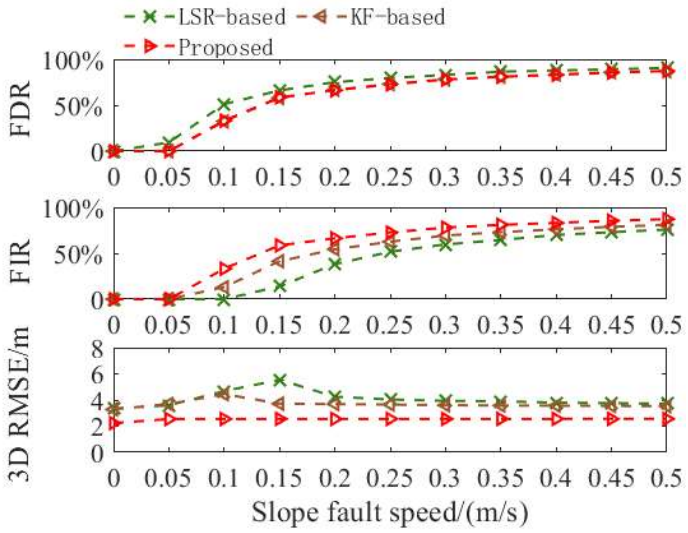

Figure 5-36: The FDR, FIR and 3D accuracy (RMSE) for candidate algorithms with various ramp errors in the dynamic mode.

Experiment under dynamic data with multiple faults

This section compares and analyzes the detection performance of the proposed algorithm on multiple faults. As shown in Figure 5-37, when the step fault of 10 m is injected into the pseudo-distance of the satellite G10 and G12 at the observation time of 400 ~500 s (including 400 s and 500 s), the fault detection method based on Kalman filtering can only detect the fault in very few epoch. The proposed algorithm can detect multiple faults 100%.

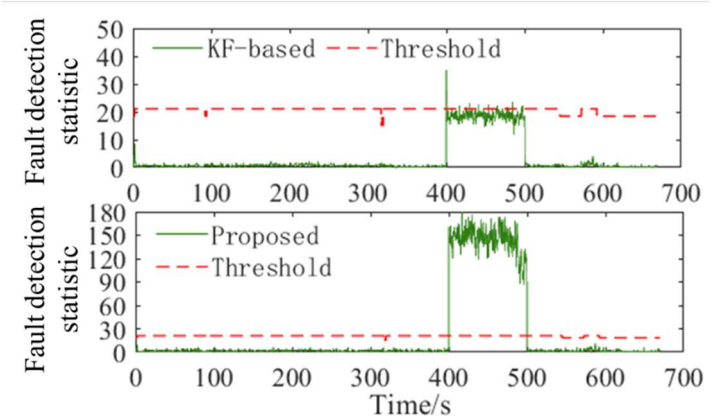

Figure 5-37: Fault detection statistics for 10m step errors added on the pseudorange of G10 and G12 in the dynamic mode.

The proposed algorithm and the fault identification statistics calculated based on the Kalman filter algorithm are shown in Figure 5-38 and Figure 5-39 respectively. It can be seen from Figure 5-38 that the proposed algorithm can basically identify multiple faults correctly. Only in a small number of epochs, the amount of fault identification of satellite G12 does not exceed the threshold and is not identificated. However, in Figure 5-39, only

in a very small number of epochs, the amount of fault identification of satellite G12 exceeds the threshold value, and even in these epochs, multiple faults cannot be fully identified.

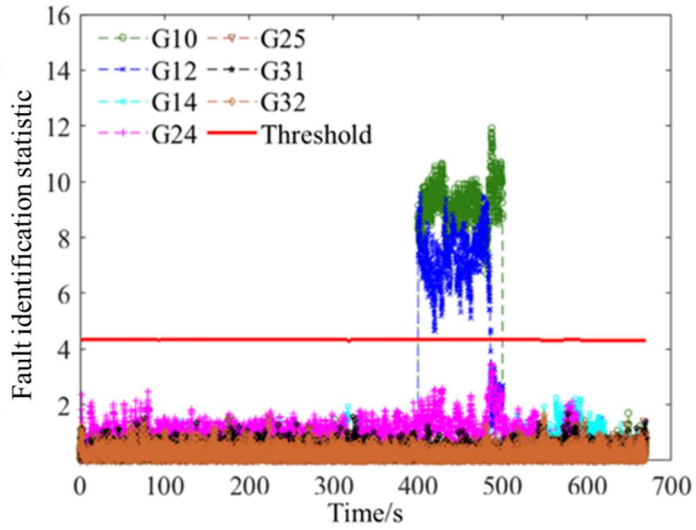

Figure 5-38: Fault identification statistics of the proposed algorithm with 10m step errors added on the pseudorange of G10 and G12 in the dynamic mode.

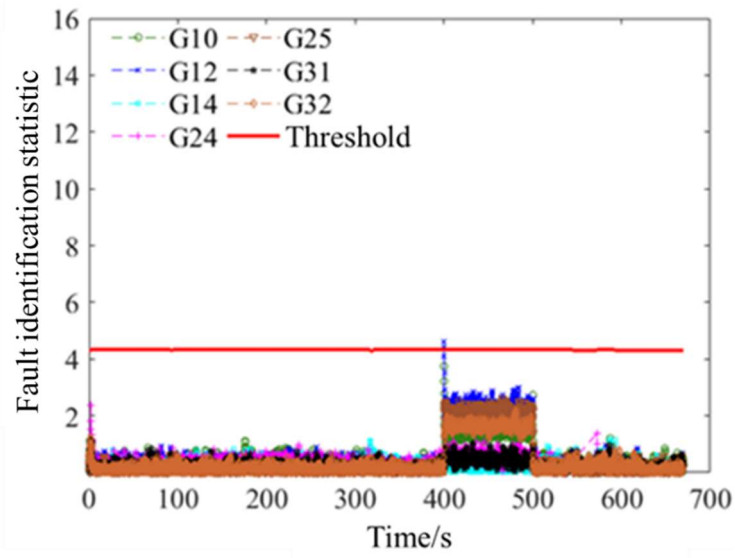

Figure 5-39: Fault identification statistics of the KF-based method with 10m step errors added on the pseudorange of G10 and G12 in the dynamic mode.

It can be seen from Table 5-25 that the fault detection method based on Kalman filter has a fault detection rate of only 3.7% and a fault identification rate of 0. The fault detection rate and fault identification rate of the proposed algorithm are 100% and 85.6% respectively, which is significantly better than the fault detection method based on Kalman filter.

Table 5-25: Positioning accuracy performance for the candidate algorithms with 10m step errors added on the pseudorange of G10 and G12 in the dynamic mode.

Fault detection method	FDR	FIR	FAR	MDR
KF-based	3.7%	0	0	96.3%
Proposed	100%	85.6%	0	0%

Table 5-26 compares the positioning accuracy indexes of the two algorithms. The 3D root mean square error of the proposed algorithm is 2.645 m, while the 3D root mean square error of the fault detection method based on Kalman filter is 6.618 m. Under the condition of multiple faults with 10 m dynamic data, the positioning accuracy of the proposed algorithm is improved by 60.03% compared with the control algorithm.

Table 5-26: The fault detection indexes of satellite G10 and G12 simultaneously contains 10 m fault in the dynamic data.

Positioning accuracy indexes	Direction	Maximun error/m	%95 quantile positioning error/m	RMSE/m
KF-based	Vertical	17.316	15.237	6.382
	Horizontal	5.976	3.018	1.756
	3D	17.476	15.496	6.618
Proposed	Vertical	11.851	4.118	2.064
	Horizontal	5.976	3.340	1.654
	3D	12.572	5.102	2.645

In order to further compare the performance of the two algorithms, Figure 5-40 shows the fault detection rate, fault identification rate and 3D root mean square error of the two algorithms when the pseudorange of the observation time of satellite G10 and G12 contains the step fault for 400~500 s (including 400 s and 500 s). The fault detection rate and fault identification rate of the proposed algorithm reach 100% when multiple faults exceed 8 m and 12 m, respectively. The fault detection rate and fault identification rate of Kalman filter based fault detection method reach 100% when multiple faults exceed 12 m and 14 m respectively. As the multiple faults increase from 0 to 18 m, the 3D root mean square error of the proposed algorithm is always stable at about 2 m because of the adaptive noise variance strategy adopted by the filtering algorithm and small multiple faults can be detected. However, when the multiple faults reach 12 m, the 3D root mean square error of the fault detection method based on Kalman filter also reaches the peak of 8 m.

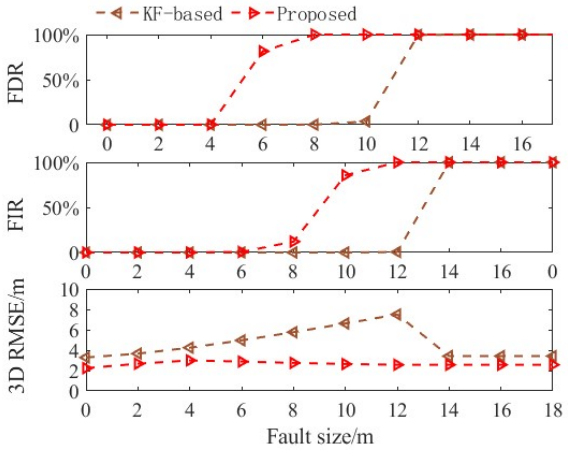

Figure 5-40: The FDR, FIR and 3D accuracy RMSE for candidate algorithms with various step errors on two satellites.

5.3.3. ALGORITHM SUMMARY

In this program, a fault detection algorithm for satellite positioning based on adaptive noise variance is proposed. The new information sequence in the sliding window is used to estimate the observation noise variance matrix in real time, which reduces the subjectivity of setting the observation noise matrix, and can better adapt to the actual observation

noise changes with the observation environment. Based on the adaptive noise variance, the fault detection statistics and fault identification statistics in this program can better meet the corresponding statistical probability distribution, and have a higher fault detection rate and identification rate, especially for small faults. After fault detection, the adaptive noise variance strategy also optimizes the Kalman gain matrix and improves the filtering accuracy to a certain extent. The experimental results show that:

1) If the step fault of the single star pseudorange increases gradually in the given static data, the fault detection rate and fault identification rate of the proposed algorithm reach 100% at the same time when the step fault exceeds 3 m. However, the fault detection method based on Kalman filter only reaches 100% when the step fault exceeds 8 m. When the step fault exceeds 8 m and the step fault exceeds 9 m, the least squares residual method achieves 100% fault detection rate and fault identification rate, respectively.

2) If the slope fault rate of the single star pseudorange increases gradually in the given static data, the change of the fault detection rate of the proposed algorithm and the control algorithm is close, but the fault identification rate of the proposed algorithm is significantly higher than that of the control algorithm.

3) If the number of faults in the given static data increases gradually, the proposed algorithm can detect and identify faults 100% when the number of faults exceeds 3 m and 4 m respectively; However, the fault detection method based on Kalman filter can detect and identify faults 100% when multiple faults exceed 8 m and 10 m respectively.

4) If the step faults of single star pseudorange increase gradually in the given dynamic data, the proposed algorithm needs faults exceeding 10 m in order to make the fault detection rate and identification rate reach 100% at the same time. The fault detection method based on Kalman filter requires the fault to exceed 16 m. Although the fault detection rate of the least squares residual method reaches 100% when the fault exceeds 10 m, the fault identification rate can only reach 100% when the fault exceeds 12 m.

5) If the slope fault rate of the single star pseudorange increases gradually in the given dynamic data, although the fault detection rate of the least squares residual method is slightly higher than that of the proposed algorithm, the fault identification rate of the proposed algorithm is always significantly higher than that of the other two control algorithms.

6) If the number of faults in the given dynamic data increases gradually, the proposed algorithm and the fault detection method based on Kalman filter can reach 100% fault detection rate when the fault exceeds 8 m and 12 m respectively. These two algorithms achieve 100% fault identification rate when the fault exceeds 12 m and 14m respectively.

Under all fault scenarios in this paper, since the proposed algorithm adopts the strategy of estimating the variance of observation noise according to the historical new information in the sliding window, the fault detection rate and identification rate of the fault detection method based on Kalman filter are improved, and the weight of each satellite in the measurement update is optimized. Therefore, the 3D root mean square error after applying the proposed algorithm to quality control does not change with the increase of the fault, and its positioning accuracy is always higher than that of the control algorithm.

6. HIGH-ACCURACY MULTI-CONSTELLATION GNSS POSITIONING MODEL FOR G-ATM

6.1. RESEARCH STATUS OF MULTI-CONSTELLATION GNSS POSITIONING MODEL

For multi frequency and multi-mode GNSS positioning model, different scholars have carried out many researchs from different aspects and achieved some results. [Yang 2010] described the advantages of multi frequency and multi-mode GNSS navigation in the article. The multi-frequency system of satellites is conducive to reducing the errors in the ionosphere and troposphere, making positioning faster. Due to different constellation systems, visual satellites will increase and improve the usability of multi constellation positioning. Therefore, the implementation of multi frequency and multi-mode GNSS will greatly improve the redundancy, positioning accuracy and flexibility of navigation and positioning, so as to improve the quality of navigation service. Many scholars have also evaluated the navigation effect of multi frequency and multi-mode GNSS through experiments. [Deng 2014] tested and analyzed the single epoch positioning performance of the GPS and Beidou joint system under short baseline conditions. The results showed that the single epoch ambiguity-fixed success rate of the GPS and Beidou joint system could be effectively improved compared with the single satellite system. [He 2014] analyzed the single frequency and dual frequency positioning performance of the GPS and BDS combined system. Compared with the single GPS system, the success rate and failure rate of ambiguity resolution of the multi system combined method were improved, and the single frequency positioning performance of the dual system gps/bds was basically equivalent to the dual frequency positioning performance of the single system. [Paziewski 2014] evaluated the positioning performance of the GPS+Galileo joint system and pointed out that the use of the joint system has significant advantages over a single system. [Geng 2021] have shown through experiments that compared with the single GPS system, the GNSS positioning ability of multi-frequency and multi-mode has been significantly improved. The accuracy of velocity measurement in horizontal and vertical directions of dual system combination is increased by 24% and 33% respectively. The combination of multiple GNSS systems can further improve the speed measurement accuracy, and the horizontal and elevation directions can be increased by 40% and 46% respectively. According to the above research, multi-frequency and multi-mode GNSS positioning can indeed enhance the positioning effect. However, some scholars have conducted relevant experiments to explore whether the more the number of systems, the better the optimization effect. [Wang 2015] analyzed the pARAIMeter estimation performance of GPS, BDS and GLONASS, and pointed out that the accuracy and reliability of pARAIMeter estimation of dual system GPS/BDS joint method has better performance than that of GPS/GLONASS and BDS/GLONASS joint method, while the accuracy and reliability of pARAIMeter estimation of three system GPS/BDS/GLONASS joint method was further improved than that of any dual system joint method. [Odolinski 2016] studied the RTK Positioning performance of the GPS/BDS/Galileo/QZSS four system combination. The experiment results show that the ambiguity fixation performance of the four system fusion strategy has been significantly improved compared with the single system, dual system and three system. For the multi-frequency and multi-mode GNSS positioning effect in the urban environment, [Pirti 2010] experiments explored the positioning performance of the GPS/GLONASS joint system. The experimental results showed that the accuracy and

reliability of the positioning results of the GPS/GLONASS joint system were better than that of the single GPS in the environment where the satellite signal was blocked by objects. [Pan 2017]proposed a robust sequential least squares method, which can effectively improve the positioning accuracy of GNSS, but requires historical data. [Wang 2018] studied the application of the total least squares method in GNSS positioning and concluded that the total least squares result is better than the least squares result. [Liu 2018] compared and analyzed the positioning accuracy of different weighted least squares methods, and concluded that each method has different performance in different situations. [Li 2011]proposed a weighted least squares method based on Doppler frequency shift assistance, and proved that the designed weighted least squares method can improve the positioning accuracy when the receiver can provide Doppler measurements.

6.2. ALGORITHM DESIGN

The acquisition of real-time dynamic and accurate navigation information is the key to the control of aircraft. G-ATM requires that during the flight of the aircraft, the accurate position of the aircraft must be mastered in real time, so that certain measures can be taken in advance to prevent the occurrence of dangerous events. Therefore, g-atm puts forward higher requirements for the accuracy of aircraft navigation and positioning information. According to the above requirements, this project analyzes the historical observation data of GNSS, and constructs a multi-frequency and multi-mode GNSS high-precision positioning model, that is, the least squares positioning quality control algorithm with real-time data-driven weight distribution function is used for aircraft navigation and positioning solution.

The basic principle of satellite positioning is that the satellite with known position continuously transmits signals to the receiver, and the receiver receives and processes the data to obtain pseudorange, which is the distance between the receiver and the satellite including various errors, as shown below:

$$\rho = \mathrm{r} + \mathrm{c}\left(\delta \mathrm{t}_{\mathrm{u}} - \delta \mathrm{t}^{\mathrm{s}}\right) + \mathrm{I}_{\rho} + \mathrm{T}_{\rho} + \varepsilon_{\rho} \tag{6-1}$$

where, ρ is the pseudorange measurement of the receiver. r represents the geometric distance between the satellite and the receiver; c denotes the speed of light in vacuum. $\delta \mathrm{t}_{\mathrm{u}}$ represents the receiver clock error, which needs to be calculated. $\delta \mathrm{t}^{\mathrm{s}}$ represents the satellite clock error, which can be obtained from the satellite ephemeris. I_{ρ} denotes the ionospheric error, T_{ρ} is the tropospheric error, these two parameters can be estimated by specific model. ε_{ρ} denotes random noise. r denotes as follows:

$$\mathrm{r} = \sqrt{\left(\mathrm{x}^{\mathrm{s}} - \mathrm{x}_{\mathrm{u}}\right)^{2} + \left(\mathrm{y}^{\mathrm{s}} - \mathrm{y}_{\mathrm{u}}\right)^{2} + \left(\mathrm{z}^{\mathrm{s}} - \mathrm{z}_{\mathrm{u}}\right)^{2}} \tag{6-2}$$

where $\left(\mathrm{x}^{\mathrm{s}},\ \mathrm{y}^{\mathrm{s}},\ \mathrm{z}^{\mathrm{s}}\right)$ is the coordinates of the satellite in the ECEF (Earth Center Earth Fixed) coordinate system which can be calculated from the satellite ephemeris. $\left(\mathrm{x}_{\mathrm{u}},\ \mathrm{y}_{\mathrm{u}},\ \mathrm{z}_{\mathrm{u}}\right)$ is the coordinate of the user receiver in ECEF coordinate system, which is the value we need to obtained. When the receiver receives *n* satellites, the observation equations of all satellites are established, and the equations represnets as follows:

$$\begin{cases} \rho^1 = r^1 + c\left(\delta t_u - \delta t_1^s\right) + I_\rho^1 + T_\rho^1 + \varepsilon_\rho^1 \\ \rho^2 = r^2 + c\left(\delta t_u - \delta t_2^s\right) + I_\rho^2 + T_\rho^2 + \varepsilon_\rho^2 \\ \vdots \\ \rho^i = r^i + c\left(\delta t_u - \delta t_i^s\right) + I_\rho^i + T_\rho^i + \varepsilon_\rho^i \end{cases} \quad (6\text{-}3)$$

After receiving these information, the user uses the method of spatial distance resection to calculate the three-dimensional position and motion speed of the receiver. In theory, three satellites can calculate the above required data. Satellite clock error, tropospheric error, ionospheric error and other errors in the satellite positioning system can be reduced or eliminated by various measures, while the receiver clock error can not be eliminated due to cost, technology and other reasons. Considering that the receiver clock error is equal to all satellite equations, it can be treated as an unknown pARAIMeter in the solution. Therefore, we need at least four satellites for positioning calculation. It is not convenient to solve due to the nonlinear characteristics of the original equations. When the number of satellites is greater than four, the receiver position can be solved by linearizing the equations and Newton iteration based on the least square.

The specific process is to linearize the equation by using Taylor formula at the approximate position of the receiver, and obtain :

$$\begin{cases} \rho^1 = r_0^1 + r_x^1\delta x + r_y^1\delta y + r_z^1\delta z + c\left(\delta t_u - \delta t_1^s\right) + I_\rho^1 + T_\rho^1 + \varepsilon_\rho^1 \\ \rho^2 = r_0^2 + r_x^2\delta x + r_y^2\delta y + r_z^2\delta z + c\left(\delta t_u - \delta t_2^s\right) + I_\rho^2 + T_\rho^2 + \varepsilon_\rho^2 \\ \vdots \\ \rho^i = r_0^i + r_x^i\delta x + r_y^i\delta y + r_z^i\delta z + c\left(\delta t_u - \delta t_i^s\right) + I_\rho^i + T_\rho^i + \varepsilon_\rho^i \end{cases} \quad (6\text{-}4)$$

Where, $r_0^i = \sqrt{\left(x_i^s - x_{u0}\right)^2 + \left(y_i^s - y_{u0}\right)^2 + \left(z_i^s - z_{u0}\right)^2}$, $\left(x_{u0},\ y_{u0},\ z_{u0}\right)$ is the approximate position of the user receiver in the ECEF coordinate system, which will converge quickly no matter where the approximate position starts; $\left[r_x^i, r_y^i, r_z^i\right] = \left[\frac{x_{u0} - x_i^s}{r_0^i}, \frac{y_{u0} - y_i^s}{r_0^i}, \frac{z_{u0} - z_i^s}{r_0^i}\right]$ is the unit vector pointing to the satellite from the approximate position of the receiverand the partial derivative of the three-dimensional position of the receiver for the pseudo range, which can be obtained from the satellite position and the calculated receiver position. $\boldsymbol{\Delta x} = \left(\delta x, \delta y, \delta z, c\delta t_u\right)$ include the receiver three-dimensional position correction value and receiver clock error. Each time a new correction value is proposed to correct the receiver position, and the position will converge to a stable result after several iterations.

Throung the item of equation (114), it is sorted into the following form :

$$\boldsymbol{G\Delta x} = \boldsymbol{b} \quad (6\text{-}5)$$

Where, $\boldsymbol{\Delta x}$ is the vector of unknown correction quantity; $\boldsymbol{G}$ is the cosine direction matrix of satellites:

$$\boldsymbol{G} = \begin{bmatrix} r_x^1 & r_y^1 & r_z^1 & 1 \\ r_x^2 & r_y^2 & r_z^2 & 1 \\ \vdots & \vdots & \vdots & \vdots \\ r_x^i & r_y^i & r_z^i & 1 \end{bmatrix}_{i\times 4} \quad (6\text{-}6)$$

Where, *i* is the number of visible satellites; $\boldsymbol{b}$ represents the residual vector of the pseudorange observation, which is the vector composed of the difference between the pseudorange observed by each satellite and the pseudorange obtained by calculating the receiver position.

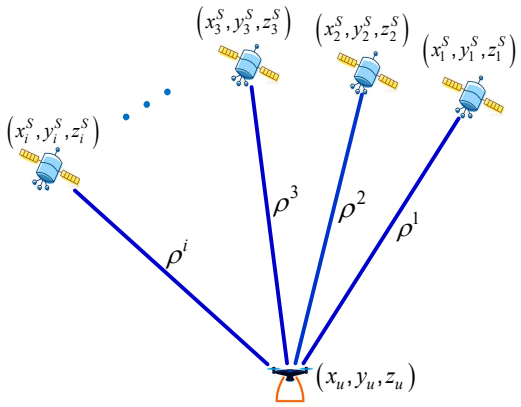

Figure 6-1: Principal of satellite positioning.

For BDS and Galileo dual constellation positioning,

$$\boldsymbol{\Delta x} = \left(\delta \mathrm{x}, \delta \mathrm{y}, \delta \mathrm{z}, \mathrm{c}\delta \mathrm{t}_{\mathrm{u,B}}, \mathrm{c}\delta \mathrm{t}_{\mathrm{u,G}}\right) \tag{6-7}$$

In which, $\delta \mathrm{t}_{\mathrm{u,B}}$ and $\delta \mathrm{t}_{\mathrm{u,G}}$ represent receiver clock bias of BDS and Galileo. Then the matrix $\boldsymbol{G}$ change to :

$$\boldsymbol{G} = \begin{bmatrix} \mathrm{r}_{\mathrm{x}}^{1,\mathrm{B}} & \mathrm{r}_{\mathrm{y}}^{1,\mathrm{B}} & \mathrm{r}_{\mathrm{z}}^{1,\mathrm{B}} & 1 & 0 \\ \vdots & \vdots & \vdots & \vdots & \vdots \\ \mathrm{r}_{\mathrm{x}}^{\mathrm{N_B}} & \mathrm{r}_{\mathrm{y}}^{\mathrm{N_B}} & \mathrm{r}_{\mathrm{z}}^{\mathrm{N_B}} & 1 & 0 \\ \mathrm{r}_{\mathrm{x}}^{1,\mathrm{G}} & \mathrm{r}_{\mathrm{y}}^{1,\mathrm{G}} & \mathrm{r}_{\mathrm{z}}^{1,\mathrm{G}} & 0 & 1 \\ \vdots & \vdots & \vdots & \vdots & \vdots \\ \mathrm{r}_{\mathrm{x}}^{\mathrm{N_G}} & \mathrm{r}_{\mathrm{y}}^{\mathrm{N_G}} & \mathrm{r}_{\mathrm{z}}^{\mathrm{N_B}} & 0 & 1 \end{bmatrix}_{(\mathrm{N_B}+\mathrm{N_G})\times 4} \tag{6-8}$$

Where, $\mathrm{N_B}$ and $\mathrm{N_G}$ are the number of visible satellites of BDS and Galileo respectively.

The double frequency pseudo range combined observation value for eliminating ionospheric delay lists below :

$$\rho' = \frac{\mathrm{f}_1^{\,2}}{\mathrm{f}_1^{\,2} - \mathrm{f}_2^{\,2}}\rho_1 - \frac{\mathrm{f}_2^{\,2}}{\mathrm{f}_1^{\,2} - \mathrm{f}_2^{\,2}}\rho_2 \tag{6-9}$$

Where, ρ_1 and ρ_2 are the pseudorange observation of carriers with frequencies f_1 and f_2 respectively.

According to the least square method, the most reliable value of the system should be obtained under the condition in which the sum of squares of residual errors is the minimum. But the premise of its establishment is that the measured values have equal accuracy. However, due to the position and motion of the satellite, the activity of the ionosphere and the change of the atmosphere, it is difficult for the satellite data received by the receiver to have a unified accuracy. In order to solve this problem, the weighted least square method is proposed for high accuracy. The basic principle of weighted least squares method is to give a higher degree of trust to reliable data sources, so that the whole result can reach a higher accuracy. The core and difficulty of weighted least squares method is the construction of weight matrix.

It should be considering that the weight between the output measurements is a relative quantity. Generally, if the error of the measured value is small, the corresponding weight value should be large. According to the maximum likelihood principle, when the weight of each measurement value is the reciprocal of the standard deviation of the measurement error, the system obtains the maximum likelihood solution :

$$\omega_i = \frac{1}{\sigma_i} \tag{6-10}$$

Where σ_i is the theoretical standard deviation of the random error of the measured value v_i. It should be noted that the systematic error of the measured value is generally not suitable to be solved by the weighted least square method, so it is necessary to reduce or eliminate the systematic error of the measured value as much as possible. In practical application, it is often impossible to get the true value of the standard deviation of the random error of the measured values of GNSS satellites. Therefore, the essence of various weighted least squares methods is to estimate the standard deviation of the random error of the measured value from different angles using various information.

To solve this problem, this project constructs a new real-time dynamic updating weight estimation algorithm based on the analysis of satellite historical data. If the receiver clock error is relatively stable, when the frequency of the receiver is high enough, it can be considered that the satellite and the receiver are moving in a uniform straight line in a short time. Thus, the pseudorange changes between adjacent epochs are approximately equal:

$$\rho_{k+1} - \rho_k = \rho_k - \rho_{k-1} + \varepsilon_{k+1} \tag{6-11}$$

Where, ρ_{k-1}, ρ_k and ρ_{k+1} are respectively the pseudorange of the same satellite measured with epoch $k-1$, k and $k+1$. ε_{k+1} represents random noise. Order :

$$E_{k+1} = \rho_{k+1} - 2\rho_k + \rho_{k-1} \tag{6-12}$$

Theoretically, the sample population follows the Gaussian distribution, and it can reflect the random noise size of the satellite pseudorange. In reality, the noise level of the satellite will also change slowly with the change of external conditions. Therefore, using the latest historical data to build a sliding window model can more accurately and adaptively estimate the size of the pseudorange random noise of the satellite.

$$\boldsymbol{N} = \left[E_{k-n+1} \cdots E_{k-1}\ E_k\right] \tag{6-13}$$

Where, n is the window length. So the sample variance list below :

$$S^2 = \frac{1}{n-1} \sum_{i=k-n+1}^{k} \left(E_i - \bar{E}\right)^2 \tag{6-14}$$

Since the sample variance S^2 is an unbiased estimate of the population variance σ^2, we can use the reciprocal of the sample standard deviation to estimate the weight of the measured value:

$$\omega_i = \frac{1}{S_i} \tag{6-15}$$

Where, S_i is the sample standard deviation. When the number of satellites is greater or equal than 5, the weighted least squares observation equation of satellite positioning is:

$$\boldsymbol{WG\Delta x} = \boldsymbol{Wb} \tag{6-16}$$

Where, $\boldsymbol{\Delta x}$ represnets the unknown correction vector, including four corrections of three-dimensional position and receiver clock difference. $\boldsymbol{b}$ denotes the residual vector of pseudorange observations. $\boldsymbol{G}$ is the cosine direction matrix of satellites. $\boldsymbol{W}$ is a diagonal matrix:

$$\boldsymbol{W} = \mathrm{diag}\left(\omega_1, \omega_2 \cdots \omega_i\right) \tag{6-17}$$

Where *i* is the number of visible satellites. Then, we can get the least square resolution:

$$\Delta x = \left(G^T C G\right)^{-1} G^T C b \tag{6-18}$$

Where, $C = W^T W$ is the weight matrix.

6.3. TEST AND ANALYSIS

In order to verify the effectiveness of the multi-frequency multi-mode GNSS high-precision positioning model for multi GNSS positioning designed in this project, which is the data-driven least squares positioning quality control algorithm. This project simulates the satellite data received by the receiver of the UAV during flight through simulation experiments. This simulation illustrated in Nanjing, Jiangsu Province. Six GNSS satellite data were generated by simulation. When setting the satellite observation error, the systematic errors such as troposphere and ionosphere should be eliminated as much as possible. In order to better verify the algorithm, the simulation was carried out three times, 20 minutes each time, and the sampling frequency was 10Hz. Each time the random error of each satellite is Gaussian white noise with a mean value of 0 and different standard deviations. The reference trajectory of the simulation is shown in Figure 6-1. The error settings of satellite number and different scenes are shown in Table **6-1**. In the data-driven weighted least squares method, the window length is set to 100. After the solution, compared with the ordinary least square method, the triaxial error results obtained in the geocentric geostationary coordinate system are shown in Figure 6-3, Figure 6-4, Figure 6-5. The statistical results of root mean square error (RMSE) of triaxial and 3D in each scene are shown in Table **6-2**, Table **6-3**, Table **6-4**. It can be seen that when the noise standard deviation of each satellite is similar, the weighted least square method can improve the positioning accuracy of UAV, but it is not different from the ordinary least square method. As the difference of random noise between satellites increases, the UAV positioning error based on the ordinary least squares method increases significantly, and the total root mean square error from Scene 1 to scene 3 increases by 52.9%. The results of weighted least square method increased by only 13.5% from Scene 1 to scene 3. By adaptively adjusting the weights of different satellites, the positioning error of UAV can be controlled within a certain range.

Therefore, the data-driven weighted least squares method proposed in this project has certain anti-interference ability, which can quickly adapt to the characteristics of satellite data in different environments, so as to give high-precision positioning and navigation solutions.

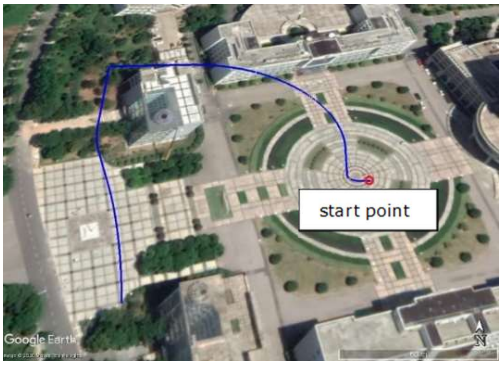

Figure 6-2: Trajectory of simulation UAV.

Table 6-1: Settings of satellite noise for different scene

PRN	Standard deviation (m)		
	Scene 1	Scene 2	Scene 3
3	0.5	0.4	0.4
14	0.6	0.6	0.6
16	0.6	0.8	0.8
22	0.8	1	1
23	0.9	1.2	1
16	1	1.4	4

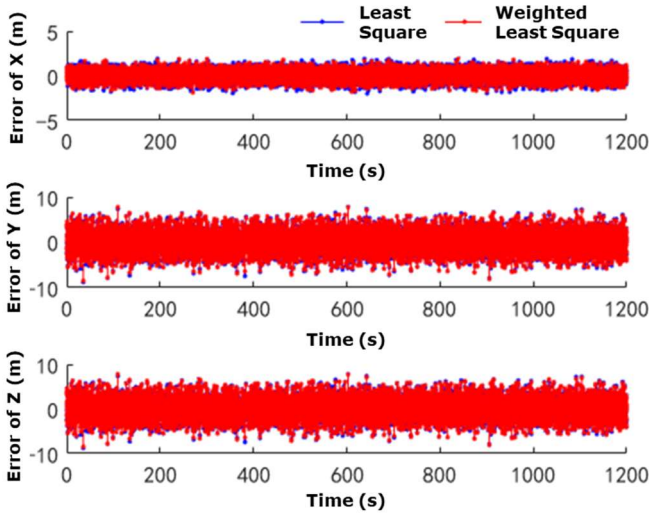

Figure 6-3: Error in scene 1.

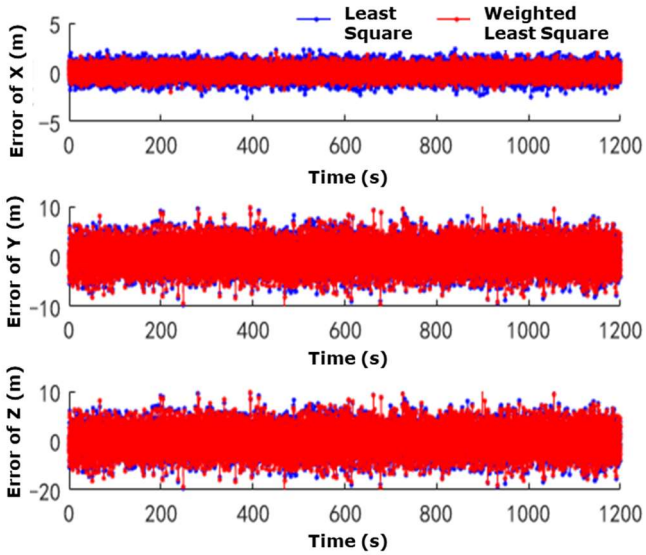

Figure 6-4: Error in scene 2.

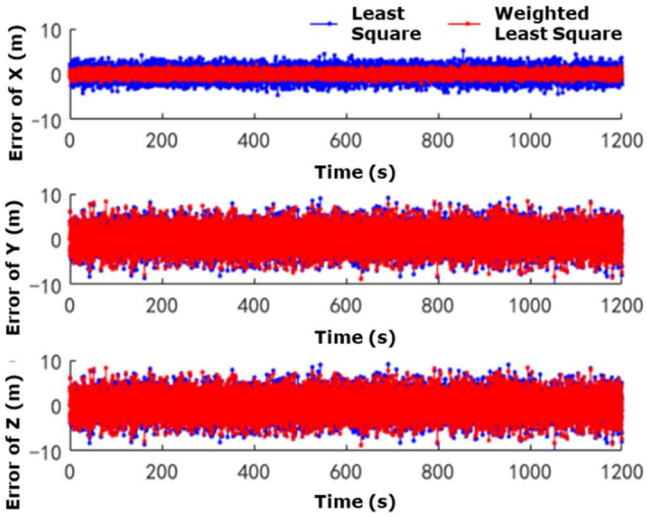

Figure 6-5: Error in scene 3.

Table 6-2: Root-Mean-Square Error of positioning in scene 1

RMSE (m)	Least Square	Weighted Least Square
X	0.56	0.52
Y	2.14	2.11
Z	0.98	0.94
3D	2.42	2.37

Table 6-3: Root-Mean-Square Error of positioning in scene 2

RMSE (m)	Least Square	Weighted Least Square
X	0.65	0.49
Y	2.57	2.53
Z	1.21	1.11
3D	2.91	2.81

Table 6-4: Root-Mean-Square Error of positioning in scene 3

RMSE (m)	Least Square	Weighted Least Square
X	1.20	0.53
Y	2.52	2.36
Z	2.43	1.17
3D	3.70	2.69

GNSS high-precision positioning is esential to satisfy the accuracy and integrity requirements of G-ATM. In this project, a multi-frequency and multi-mode GNSS high-precision positioning model and a data-driven GNSS fixed weight positioning quality control method are constructed. By comparing the proposed weighted least squares method with the traditional least squares method, the results show that the vertical positioning error of the algorithm is less than 2m and the horizontal error is less than 3m, and the algorithm meets the accuracy requirements of cat II/III precision approach

7. MULTI-CONSTELLATION GNSS PROTECTION LEVEL CALCULATION MODEL FOR G-ATM

At present, there are roughly two methods to provide real-time integrity enhancement and monitoring: system level (external enhancement) and user level (internal enhancement) integrity monitoring, mainly including Satellite Based Augmentation System (SBAS), Ground-Based Augmentation System (GBAS) and Air Based Augmentation System (ABAS). Among them, ABAS mainly provides integrity enhancement and monitoring at the user side, including traditional receiver autonomous integrity monitoring (RAIM) and advanced receiver autonomous integrity monitoring (ARAIM). These two models are based on the redundant observation data inside the receiver to independently detect and identify satellite faults to ensure the integrity performance of users. However, the traditional RAIM model is mainly aimed at GPS L1 users. Based on the assumption of single fault satellite, it can not monitor the satellite multi fault threat mode in multi-mode GNSS navigation, and can not accurately detect and identify the pseudorange deviation caused by small faults. Therefore, RAIM can only be used for horizontal guidance service during auxiliary route flight.

With the improvement of GNSS, developing RAIM to meet the vertical guidance service of precision approach has aroused great interest in the academic community, then ARAIM technology has been introduced. Compared with SBAS and GBAS technologies, ARAIM does not need a lot of infrastructure, with low cost and wide coverage, and can provide precision approach services for users in various regions (including polar regions). At the same time, because ARAIM adopts the consistency test method based on the position domain Multiple Hypothesis Solution Separation (MHSS) model, it can easily and effectively monitor a variety of potential satellite failure modes in the multi-mode dual frequency GNSS environment.

Protection level is a concept proposed in the integrity monitoring technology. In order to meet the integrity risk requirements, it is necessary to calculate the protection level in real time to form a protection area around the aircraft position domain. The protection level "protects" the user by quantifying the dangerous misleading rate in the navigation system as the position error limit value in the positioning estimation. The probability that the user's actual position is outside the protection area (i.e. the estimation error exceeds the protection level) should not be greater than the integrity risk requirements. In essence, the protection level is to inform the user whether the satellite geometry allows fault detection and exclusion. In this project, we mainly study the protection level in ARAIM technology.

7.1. RESEARCH STATUS OF PROTECTION LEVEL CALCULATION

The GNSS Evolutionary Architecture Study (GEAS) team [Panel 2010] in the United States is a major research team of ARAIM funded by FAA of the United States, which aims to assess the ability of GPS and Galileo to provide LPV-200 services worldwide from 2020 to 2025. Blanch, Walter and Enge, the main members of the GEAs team [Blanch 2010], have successively proved the principle of the ARAIM algorithm PHMI optimal allocation mathematically, and designed an ARAIM algorithm combined with ISM. For the first time, the requirements of LPV-200 users are brought into the framework of ARAIM, and the processing methods of multiple fault forms such as single fault, multiple fault and

constellation wide fault are studied. [Choi 2012] [Choi 2011] used the single fault and multiple fault hypotheses under the GPS/GLONASS combined measured data for ARAIM performance. [Blanch 2012, Blanch 2013] described in detail the definition of relevant variables, the calculation of protection level, the implementation of Fault Detection and Exclusion (FDE) in ARAIM, and described the contents and differences of two ARAIM ground architectures: offline ARAIM and online ARAIM [Blanch 2014]; Aiming at the problems of complex fault modes and too many solution operator sets of ARAIM in GNSS multi system combination, a smart fault joint model is proposed, and the availability of the model is analyzed [Walter 2014, Blanch 2018]. Researchers from the German Aerospace Center also carried out research on the ARAIM of GPS/galileo, analyzed the integrity performance under different ARAIM pARAIMeters [Rippl 2011] and designed the corresponding FDE module [Rippl 2012] Australian scholars have also studied the ARAIM performance of the time offset estimation method between multiple systems around ARAIM [Wu 2013], and proposed a new VPL optimization method [Jiang 2014]. At the same time, the real-time observation data (dual frequency and tri frequency data) are used to analyze the ARAIM performance under the combination of multi-mode and multi-frequency GNSS, as well as the corresponding error model, failure mode and pARAIMeters of satellite prior probability [El-Mowafy 2013, El-Mowafy 2016, El-Mowafy 2016, El-Mowafy 2017].

In order to make up for the inherent defect of low availability of ARAIM caused by the lack of available satellites in a single constellation, scholars have proposed to improve the availability of ARAIM by using multi constellation fusion [Joerger 2020, Zhai 2019, Luo 2020]. [Wang 2022] pointed out that among the existing GNSS constellations, BDS has obvious constellation advantages in the application of ARAIM by analyzing the global availability of ARAIM algorithm under the combination of multiple constellations. At the same time, optimal allocation of risk based on continuity and integrity is also an important method to improve availability [Wang 2019, Brown 1988, Blanch 2012, Joerger 2013]. [Blanch 2013] optimized the VPL by allocating integrity risk, which improved the availability of ARAIM. [Song 2017] proposed a polynomial coefficient optimization algorithm, which uses Gauss Newton method to solve the simplified VPL model, improving the availability of ARAIM. [Zheng 2018] optimized the calculation value of VPL by optimizing the distribution of continuity risk and integrity risk and using genetic algorithm. [Jing 2012] reduced the value of VPL and improved the availability of ARAIM through the VPL coefficient optimization method, but they did not consider the influence of the quantity determined in the VPL formula in the risk optimization allocation. [Han 2021]used a maximum minimization method to reasonably allocate the integrity risk and continuity risk, which improved the availability of single constellation ARAIM. [Wang 2021] optimized the allocation strategy of integrity risk and continuity risk based on PSO algorithm, effectively reducing the VPL value of dual constellation GNSS.

7.2. ARAIM

The ARAIM model is an extended integrity model, which enables the aircraft to carry out integrity detection in the vertical guidance LPV-200 phase. At present, ARAIM is still in development. When using dual frequency technology, ARAIM realizes consistency monitoring through redundant information received by multiple constellations or satellites. The purpose of ARAIM model is to ensure the seamless air navigation worldwide with fewer ground infrastructure. ARAIM is an extension and improvement of RAIM method.

At present, GEAS is considering the combination of GPS and other satellite navigation systems. The relatively complete satellite navigation systems in the world include Galileo in Europe, GLONASS in Russia and BDS in China. As of December 12, 2017, Galileo in Europe had 26 satellites, including 4 IOV satellites and 18 FOC satellites, and 4 satellites were launched further on July 25, 2018. As of June 21st, 2018, Russia's GLONASS had 26 satellites in orbit, including 24 GLONASS-M in operation, one retired satellite for the main developer's test and one GLONASS-K for flight parameter test. The Beidou navigation

system independently developed by China was officially completed and opened in 2020 to provide services worldwide. ARAIM using multiple constellations can improve the availability under the single fault assumption. In addition, ARAIM can further improve the design and detect the constellation wide fault.

The actual operation shows that the probability of failure is significantly reduced by using the enhanced system of ARAIM. The reason is that ARAIM can use more GNSS constellations, so there are more available signals for precise positioning. In addition, ARAIM can also save the maintenance cost of ground facilities, which attracts more researchers' attention for economy and effectiveness.

7.2.1. ARAIM SYSTEM ARCHITECTURE

The architecture of ARAIM system is composed of ground monitoring network, core constellation and airborne receiver. The main operation process list as follows:

- the ground monitoring network generates parameters Integrity Support Information (ISM) reflecting the inherent performance of the core constellation by observing the core constellation, and sends them to the airborne receiver.
- After receiving ISM, the airborne receiver will use the received satellite signal and ISM as the input value of the system algorithm to run MHSS algorithm, judging whether the satellite or constellation is faulty according to the operation results of the algorithm, and removeing the fault. If there is no fault, the protection level is calculated to determine whether the service is available.

7.2.2. ISM PARAMETERS

The Integrity Support Message (ISM) describes the nominal error of each satellite and the probability of satellite failure. The nominal error is given by two standard deviations and the maximum error set. The standard deviation is proposed for integrity, while the maximum error is proposed for accuracy and continuity. ISM mainly includes the following aspects:

- User Range Error (URE) / Signal-In-Space Error (SISE) .
- User Range Accuracy (URA) / Signal-In-Space Accuracy (SISA).
- The bias of integrity ecaluation ($b_{\max}$), which refers to the bias of the maximum value without satellite failure.
- Bias of evaluation accuracy and continuity (b_{cont}).
- Probability of satellite failure (P_{fault}).
- Probability of constellation failure (P_{const}).
- FLAG information, which indicates whether those information above exist in ISM

Before air traffic control department in civil aviation permits the application of ARAIM in the LPV-200 approach phase, the values of the above seven parameters must be verified, so that the performance of multi constellation ARAIM can be correctly evaluated.

When the airborne receiver is running the ARAIM algorithm, the parameters to be input are shown in the Table **7-1**.

Table 7-1: Input parameters of ARAIM

Parameters	Description	Source
PR_i	pseudorange of satellite *i* after dual frequency correction, tropospheric correction and smoothing are performed	Receiver
$\sigma_{URA,\mathrm{i}}$	standard deviation of satellite clock error and ephemeris error of satellite *i* for integrity	ISM
$\sigma_{URE,\mathrm{i}}$	Standard deviation of satellite clock error and ephemeris error of satellite *i* for accuracy and continuity	ISM
$b_{nom,i}$	Maximum nominal bias for satellite *i* for integrity detection	ISM
$P_{sat,i}$	prior probability of fault in satellite *i* per approach	ISM
$P_{const,j}$	prior probability of a fault affecting more than one satellite in constellation *j* per approach	ISM
$I_{const,i}$	index of satellites belonging to constellation *j*	Receiver
N_{sat}	number of satellites	Receiver
N_{const}	number of constellations	Receiver

These input parameters include ISM parameters and satellite signals received by the receiver. According to these input parameters, satellite faults can be detected and eliminated.

7.2.3. PURPOSE OF ARAIM

ARAIM aims to achieve global LPV-200 service. LPV-200 is an approach mode defined by the Federal Aviation Administration (FAA) of the United States, which can guide the aircraft to an altitude of 200ft (60m) above the ground according to the specified standards. The integrity index requirements defined by LPV-200 include:

- Probability of Hazard Misleading Information $\mathrm{PHMI} \le 1\times10^{-7}$ / approach.
- Protection Level must be less than alarm threshold: vertical protection level (VPL) is less than VAL of vertical protection threshold, and VAL = 35m. The horizontal error protection level HPL is less than the horizontal error protection limit Hal, and HAL = 40m.
- Alarm time TA≤6s.
- The probability of continuity risk is less than 8×10^{-6}.
- 95% vertical navigation error is less than 4m.

According to the context, the integrity requirements of LPV-200 service are shown in Table 7-2. When the protection level is less than the following alarm value, ARAIM's LPV-200 service is available.

Table 7-2: Requirement of integrity on LPV-200 service

Service level	LPV-200
Horizontal Protection Level Alarm Limit	40m
Vertical Protection Level Alarm Limit	35m
Vertical Effective Monitoring Threshold	15m
Integrity Risk Limit	2*10-7/approach

Compared with traditional methods, when using ARAIM algorithm for autonomous integrity detection to meet the requirements of LPV-200, it has no requiements of alarm time less than 6s. ARAIM has the complete availability prediction function, and it can predict the integrity of the flight phase in advance before the aircraft takes off, so there is no need to wait for the ground system to give an alarm to the user within 6s before selecting the corresponding navigation mode.

7.2.4. THREAT MODES AND MITIGAION

The threat of the navigation performance requirements for LPV-200 refers to the situation leading to 95% positioning error exceeding 4 m or positioning error greater than the protection level. Threats may affect the performance requirements of LPV-200, so it is necessary to analyze these threats and take corresponding measures to mitigate them during operation. In GNSS, the integrity threat of users is mainly due to the fact that the measured values from the receiver are vulnerable to faults including satellite and constellation faults. The main threats are divided into three types: nominal error, narrow fault error and wide fault error：

- Nominal error: nominal error can be characterized by known probability distribution. The nominal error does not necessarily exist, but is generally assumed to exist. Nominal errors include errors caused by signals in space (clock and ephemeris errors, nominal signal deformation, etc.), propagation errors (tropospheric delay, ionospheric delay) and local effects (multipath and receiver noise). These errors are basically characterized by Gaussian distribution with uncertain but bounded deviations.
- Narrow fault error: it is theoretically infeasible to characterize narrow fault and wide fault error by known distribution, because this method will lead to a wide range of error distribution, resulting in an unavailable range of positioning error. In these two categories, narrow faults can affect satellites independently. Generally speaking, the faults caused by satellite faults are narrow faults. For clock and ephemeris faults, it is necessary to determine the root cause of faults before classifying them as narrow faults.
- Wide fault error: wide fault can affect two or more satellites at the same time in a constellation (at this time, the constellation is defined as a satellite system operating on the same ground part), which is the most difficult fault category in RAIM. This is because in the worst case, a wide fault within a constellation will produce an error compatible with any movement of the user's position. These errors will produce completely wrong measurement results, but these measurement results are consistent, so redundancy detection cannot detect these errors. There are two possibilities for wide fault: one is that the fault is caused by continuous adjustment of clock reference. Another possibility is that these faults are caused by the damage of earth orientation parameters, which are common to all satellites.

In general, it is considered more important to mitigate the threat than to analyze the generation of the threat. Having identified the threat, it is proposed to mitigate it using three components: the ground monitoring stations of the satellite constellation and the satellite constellation itself, a separate ground segment and user receivers.

7.2.5. MHSS BASED ARAIM

At present, one of the most widely used integrity algorithms is the ARAIM algorithm based on the Multiple Hypothesis Solution Separation (MHSS), which is based on the multivariate hypothesis, defining H_0 for no fault and H_i for failure, including single satellite faults, double-satellite faults, and multi-satellite faults. With visible satellites of number n, there are n kinds of possible models under single satellite failure, C_n^2 kinds of possible models in double-satellite failures, and so on C_n^3、C_n^4, etc. However, the probability of faults of more than 3 satellites is small and basically negligible. The MHSS algorithm calculates the navigation and positioning solution of all satellites and the navigation and positioning solution after excluding satellites in the *i*-th model, if the difference between the two solutions is within a certain range, it can be determined that there is no fault, otherwise the *i*-th model is a fault model.

The availability analysis of the ARAIM, which does not require Probability of Missed Detection, Probability of False Alert and detection threshold, but calculates the Vertical Protection Level (VPL) of the aircraft during flight according to the integrity risk and continuity risk of the system requirements. After that, the VPL that satisfies the integrity risk probability and the continuity risk probability is compared with the Vertical Protection Limit (VAL). If the VPL is less than the VAL, the ARAIM algorithm is available, that is, the detection function can be performed normally.

The ARAIM algorithm monitors the following fault models: a) Single satellite faults; b) Single constellation faults; c) Any combinations of the above two cases. A particular satellite/constellation fault is called a fault model and the ARAIM algorithm performs a binary hypothesis test on all possible fault models at a given moment, the test thresholds are constructed as described in section 0 and the test quantities are constructed in the following way.

1）For fault model *k*, the satellite or constellation corresponding to fault model *k* that has failed is removed from the visible satellites, and the set consisting of the remaining satellites is called the subset *k*.

2）The receiver position ($X^{(0)}$, $Y^{(0)}$, $Z^{(0)}$) is obtained by locating all visible satellites contained in subset *k*.

3）The error caused by the satellite or constellation that has failed corresponding to subset *k* is converted from the pseudo-range domain to the positioning domain under the coordinate system of East North Up (ENU), and the result of the conversion is ($|X^{(k)}- X^{(0)}|$, $|Y^{(k)}- Y^{(0)}|$, $|Z^{(k)}- Z^{(0)}|$), which is the test quantity. When all the test statistics are less than the test threshold, the protection level (PL) and the vertical effective monitoring value (EMT) are then calculated and compared with the corresponding alarm values to determine whether the LPV-200 service is available. The flow chart of the MHSS-based ARAIM model is shown in the figure below.

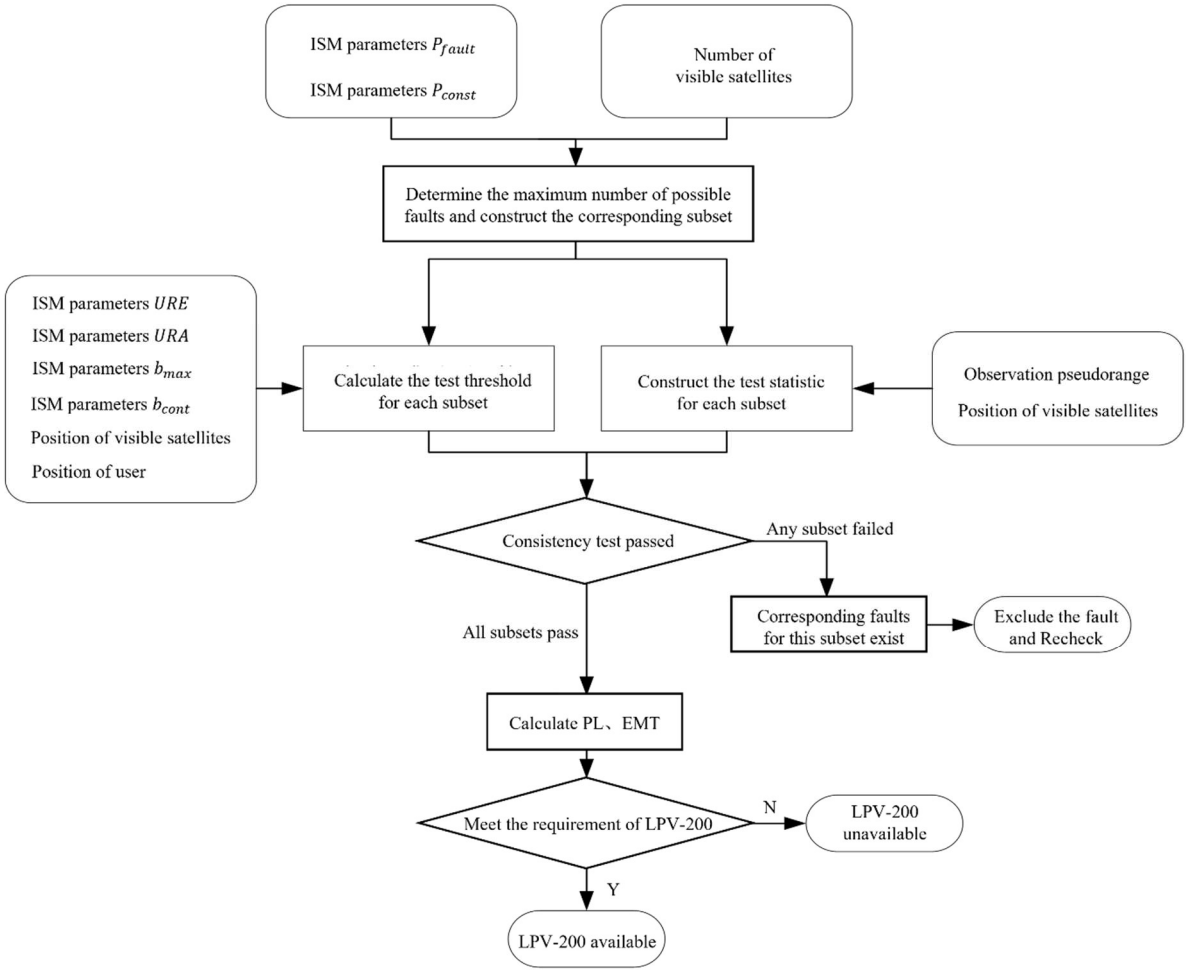

Figure 7-1: The flow chart of the MHSS-based ARAIM model

7.3. TLBO-BASED PROTECTION LEVEL CALCULATION MODEL

The value of the protection level affects the availability of the ARAIM, i.e. the determination of whether the satellite geometry allows the execution of fault detection and exclusion functions. Therefore, an appropriate protection level model needs to be constructed to improve the availability of the ARAIM in order to meet the integrity requirements of the LPV-200 phase. Based on the above, this project constructs a protection level model based on TLBO (Teaching-learning-based optimization).

7.3.1. MODEL DESIGN

The flow chart of the TLBO-based protection level model developed in this project is shown below.

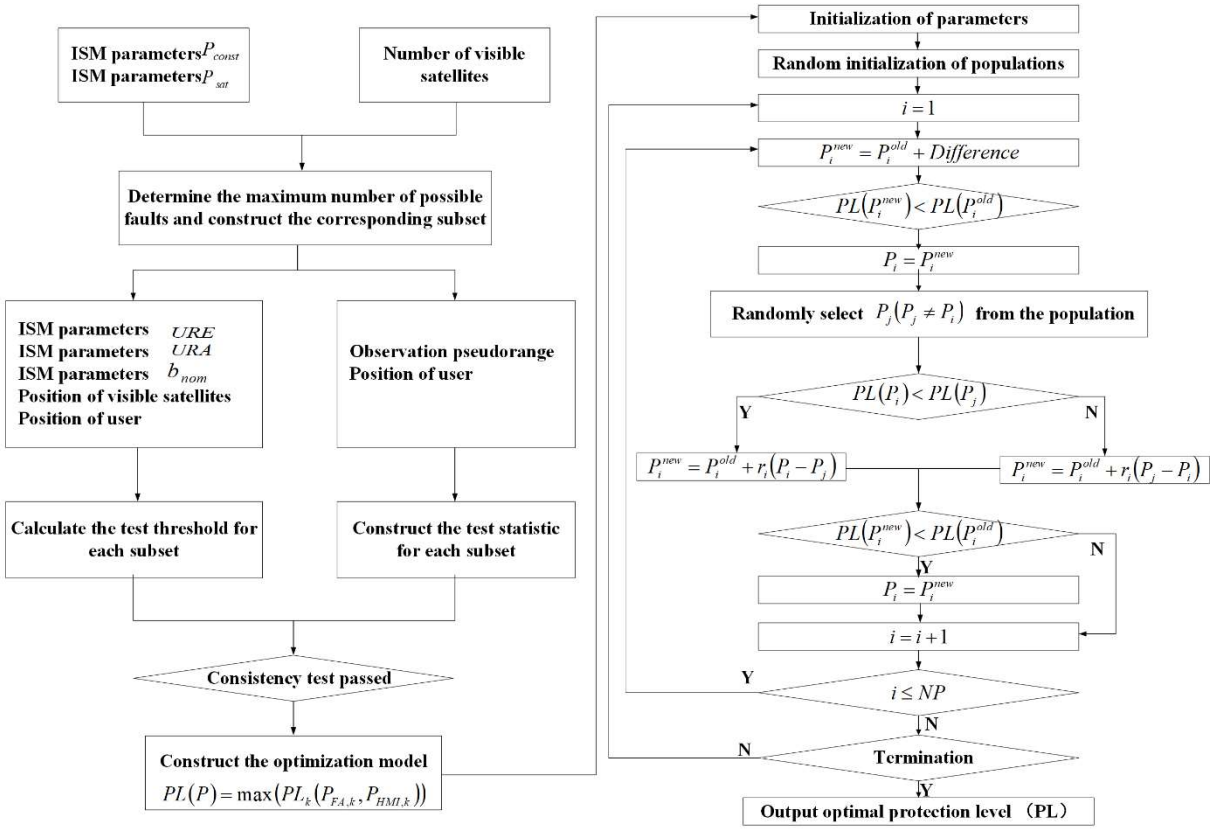

Figure 7-2: The flow chart of the TLBO-based protection level model

Firstly, the maximum number of faults is determined and the corresponding fault subsets are constructed based on the ISM parameters and the number of visible satellites, and the test quantity of each subset are constructed using the observed pseudorange of satellites and compared with the corresponding test threshold. After all the consistency tests are passed, the functional relationship between protection level and risk allocation is derived from the ARAIM protection level calculation equation to construct an optimization model. Then the TLBO algorithm is introduced into the process of continuity risk and intactness risk allocation, and the optimal risk allocation is achieved by the corresponding optimization-seeking rules in two stages of teaching and learning, and the optimal protection level is output after the termination condition is satisfied.

CALCULATION EQUATION FOR PROTECTION LEVEL

MHSS is recommended as the baseline user algorithm for ARAIM, and its core idea is to assume that there is one or more faulty satellites in the current epoch, and to make them excluded from the positioning solution by assigning a subset of satellites. In all satellite subsets, there exists at least one fault-free subset with corresponding intactness risk probability and some fault-tolerant subsets with corresponding intactness risk probability. The protection level of all subsets including the full set is solved, and the largest subset protection level is taken as the final user protection level, which is the upper limit of positioning error.

For GNSS visible satellites of N, the linearized fault-free pseudorange observation equation is as follows:

$$\mathrm{y} = \mathrm{Gx} + \varepsilon \tag{7-1}$$

where, y denotes the pseudorange residual; G denotes the observation matrix; x denotes the parameter vector to be estimated, which consists of three coordinate

parameters and the receiver clock offsets corresponding to each GNSS constellation system; and ε is the dimensional pseudorange error vector.

The weighted least squares localization solution for the full set is:

$$\hat{x}_0 = \left(G^T W_{URA} G\right)^{-1} G^T W_{URA} y = S_0 y \tag{7-2}$$

where, W_{URA} is the matrix for assessing integrity.

The positioning solution for the fault-tolerant subset of the k-th $\left(k = 1, 2, \ldots, N_{fault\_models}\right)$ failure mode is:

$$\hat{x}_k = \left(G^T M_i W_{URA} G\right)^{-1} G^T M_i W_{URA} y = S_k y \tag{7-3}$$

Where, M_i is the N-dimensional unit matrix with the i-th element being 0 to remove the observed pseudorange of the first satellite.

Define the test statistic for the k-th failure mode as follows:

$$\hat{x}_k = \left(\hat{x}_k - \hat{x}_0\right) = \left(S_k - S_0\right) y \tag{7-4}$$

The standard deviation of the error tolerant subset positioning solution is:

$$\sigma_k^{(q)} = \sqrt{\left(G^T M_i W_{URA} G\right)_{q,q}^{-1}} \tag{7-5}$$

Where, $q = 1, 2, 3$ represent the east, north and sky directions respectively.

The standard deviation of the fault-free full set positioning solution is:

$$\sigma_0^{(q)} = \sqrt{\left(G^T W_{URA} G\right)_{q,q}^{-1}} \tag{7-6}$$

The difference between the fault-tolerant subset positioning solution and the fault free full set positioning solution, i.e. the standard deviation of the solution separation test, is:

$$\sigma_{ss,k}^{(q)} = \sqrt{\left(S_k - S_0\right) C_{acc} \left(S_k - S_0\right)^T} \tag{7-7}$$

$$C_{acc} = W_{URE}^{-1} \tag{7-8}$$

Where, W_{URE} is the matrix for assessing accuracy and continuity.

Each fault model corresponds to the test threshold statistic in the East, North and Up directions, and the detection threshold corresponding to the fault model is defined as:

$$T_k^{(1)} = T_k^{(2)} = K_{FA\_HOR,k} \times \sigma_{ss,k}^{(1)} \tag{7-9}$$

$$T_k^{(3)} = K_{FA\_VERT,k} \times \sigma_{ss,k}^{(3)} \tag{7-10}$$

where the coefficient associated with the continuity risk is calculated based on the continuity risk budget allocated to the horizontal and vertical directions. The baseline ARAIM algorithm allocates the total continuity risk equally to each subset of faults other than the full set of fault-free ones, with:

$$K_{FA\_HOR,k} = -Q^{-1}\left(\frac{P_{FA\_HOR}}{4 \times N_{fault\_models}}\right) \tag{7-11}$$

$$K_{FA\_HOR,k} = -Q^{-1}\left(\frac{P_{FA\_HOR}}{4 \times N_{fault\_models}}\right) \tag{7-12}$$

Under the fault-free hypothesis, the vertical protection level VPL_0 corresponding to the full set of available satellites is expressed as

$$\mathrm{VPL}_0 = \mathrm{K}_{\mathrm{HMI\_VERT},0} \times \sigma_0^{(3)} + \sum_{i=1}^{N} \left|\mathrm{S}_0\left(3,i\right)\right| \times \mathrm{b}_{\mathrm{nom}} \tag{7-13}$$

where, $\mathrm{b}_{\mathrm{nom}}$ is the maximum pseudorange deviation in normal conditions used to assess integrity, as set by the ISM.

VPL_k is the vertical protection level corresponding to the remaining visible satellites after excluding the faulty satellite corresponding to the fault model, expressed as follows:

$$\mathrm{VPL}_k = \mathrm{T}_k^{(3)} + \mathrm{K}_{\mathrm{HMI\_VERT},k} \times \sigma_k^{(3)} + \sum_{i=1}^{N} \left|\mathrm{S}_k\left(3,i\right)\right| \times \mathrm{b}_{\mathrm{nom}} \tag{7-14}$$

where, the K-coefficient associated with the risk of integrity is defined as follows:

$$\mathrm{K}_{\mathrm{HMI\_VERT},0} = -\mathrm{Q}^{-1}\left(\frac{\mathrm{P}_{\mathrm{HMI\_VERT},0}}{2}\right) \tag{7-15}$$

$$\mathrm{K}_{\mathrm{HMI\_VERT},0} = -\mathrm{Q}^{-1}\left(\frac{\mathrm{P}_{\mathrm{HMI\_VERT},0}}{2}\right) \tag{7-16}$$

where, $\mathrm{P}_{\mathrm{prior},k}$ is the prior probability of fault model k. The baseline ARAIM algorithm allocates the total integrity risk equally between the fault-free modes and the component fault subsets, with:

$$\mathrm{P}_{\mathrm{HMI\_VERT},0} = \mathrm{P}_{\mathrm{HMI\_VERT},k} = \frac{\mathrm{PHMI\_VERT}}{\mathrm{N}_{\mathrm{fault\_models}} + 1} \tag{7-17}$$

The maximum VPL calculated for all fault models is finally taken as the user's current vertical protection level.

$$\mathrm{VPL} = \max\left\{\mathrm{VPL}_0, \max\left\{\mathrm{VPL}_k\right\}\right\} \tag{7-18}$$

The horizontal protection level is calculated in a similar way to the vertical protection level, with the difference that the horizontal protection level requires separate calculations for the eastward and northward components:

$$\mathrm{HPL}_0^{(1)} = \mathrm{HPL}_0^{(2)} = \mathrm{K}_{\mathrm{HMI\_HOR},0} \times \sigma_0^{(1)} + \sum_{i=1}^{N} \left|\mathrm{S}_0\left(1,i\right)\right| \times \mathrm{b}_{\mathrm{nom}} \tag{7-19}$$

$$\mathrm{HPL}_k^{(1)} = \mathrm{HPL}_k^{(2)} = \mathrm{T}_k^{(1)} + \mathrm{K}_{\mathrm{HMI\_HOR},k} \times \sigma_0^{(1)} + \sum_{i=1}^{N} \left|\mathrm{S}_0\left(1,i\right)\right| \times \mathrm{b}_{\mathrm{nom}} \tag{7-20}$$

where:

$$\mathrm{K}_{\mathrm{HMI\_HOR},0} = -\mathrm{Q}^{-1}\left(\frac{\mathrm{PHMI\_HOR}}{4 \times \left(\mathrm{N}_{\mathrm{fault\_models}} + 1\right)}\right) \tag{7-21}$$

$$\mathrm{K}_{\mathrm{HMI\_HOR},k} = -\mathrm{Q}^{-1}\left(\frac{\mathrm{PHMI\_HOR}}{2 \times \left(\mathrm{N}_{\mathrm{fault\_models}} + 1\right) \times \mathrm{P}_{\mathrm{prior},k}}\right) \tag{7-22}$$

The horizontal protection level is the root of the sum of the squares of the eastward and northward components:

$$\mathrm{HPL}_0 = \sqrt{\left(\mathrm{HPL}_0^{(1)}\right)^2 + \left(\mathrm{HPL}_0^{(2)}\right)^2} \tag{7-23}$$

$$\mathrm{HPL_k}=\sqrt{\left(\mathrm{HPL_k^{(1)}}\right)^2+\left(\mathrm{HPL_k^{(2)}}\right)^2} \tag{7-24}$$

Similarly, the maximum calculated for all failure modes is taken as the user's current level of protection.

$$\mathrm{HPL}=\max\left\{\mathrm{HPL_0},\max\left\{\mathrm{HPL_k}\right\}\right\} \tag{7-25}$$

When the satellite geometry configuration (determining the observation matrix G) and the error model (determining the weighting matrix $\mathrm{W_{URA}}$ and $\mathrm{W_{URE}}$) are known, the protection level for each fault subsets is a function of the probability of risk, and the final protection level is derived from the maximum value function. The equation for the protection level, expressed by the integrity risk and continuity risk instead of the risk coefficient, is as follows:

$$\begin{cases}\mathrm{VPL_0}=-\mathrm{Q}^{-1}\left(\dfrac{\mathrm{P_{HMI\_VERT,0}}}{2}\right)\times\sigma_0^{(3)}+\sum\limits_{\mathrm{i=1}}^{\mathrm{N}}\left|\mathrm{S_0}\left(3,\mathrm{i}\right)\right|\times\mathrm{b_{nom}}\\ \mathrm{VPL_k}=-\mathrm{Q}^{-1}\left(\dfrac{\mathrm{P_{FA\_VERT,k}}}{2}\right)\times\sigma_{\mathrm{ss,k}}^{(3)}+-\mathrm{Q}^{-1}\left(\dfrac{\mathrm{P_{HMI\_VERT,k}}}{\mathrm{P_{prior,k}}}\right)\times\sigma_{\mathrm{k}}^{(3)}\\ \qquad+\sum\limits_{\mathrm{i=1}}^{\mathrm{N}}\left|\mathrm{S_k}\left(3,\mathrm{i}\right)\right|\times\mathrm{b_{nom}}\\ \mathrm{VPL}=\max\left\{\mathrm{VPL_0},\max\left\{\mathrm{VPL_k}\right\}\right\}\end{cases} \tag{7-26}$$

$$\begin{cases}\mathrm{HPL_0}=\sqrt{2}\left(-\mathrm{Q}^{-1}\left(\dfrac{\mathrm{P_{HMI\_HOR,0}}}{2}\right)\times\sigma_0^{(1)}+\sum\limits_{\mathrm{i=1}}^{\mathrm{N}}\left|\mathrm{S_0}\left(1,\mathrm{i}\right)\right|\times\mathrm{b_{nom}}\right)\\ \mathrm{HPL_k}=\sqrt{2}\left(\begin{array}{l}-\mathrm{Q}^{-1}\left(\dfrac{\mathrm{P_{FA\_HOR,k}}}{2}\right)\times\sigma_{\mathrm{ss,k}}^{(1)}+-\mathrm{Q}^{-1}\left(\dfrac{\mathrm{P_{HMI\_HOR,k}}}{\mathrm{P_{prior,k}}}\right)\times\sigma_{\mathrm{k}}^{(1)}\\ \qquad+\sum\limits_{\mathrm{i=1}}^{\mathrm{N}}\left|\mathrm{S_k}\left(1,\mathrm{i}\right)\right|\times\mathrm{b_{nom}}\end{array}\right)\\ \mathrm{HPL}=\max\left\{\mathrm{HPL_0},\max\left\{\mathrm{HPL_k}\right\}\right\}\end{cases} \tag{7-27}$$

It's shown that the protection level is a function of the probability of continuity risk and the probability of integrity risk corresponding to each satellite subset, and the calculation of the protection level can be optimized by the risk allocation. Selecting VPL as the optimization objective, the continuity risk and integrity risk assigned to each fault subset as the optimization parameters, the optimization function is established as:

$$\begin{aligned}&\min\ \mathrm{VPL}\left(\mathrm{P_{FA\_VERT,0}},\mathrm{P_{FA\_VERT,1}},\ldots,\mathrm{P_{FA\_VERT,N_{fault\_models}}},\right.\\&\left.\mathrm{P_{HMI\_VERT,0}},\mathrm{P_{HMI\_VERT,1}},\ldots,\mathrm{P_{HMI\_VERT,N_{fault\_models}}}\right)\\&\text{s.t.}\begin{cases}\sum\limits_{\mathrm{k=0}}^{\mathrm{N_{fault\_models}}}\mathrm{P_{FA\_VERT,k}}\le\mathrm{P_{FA\_VERT}}\\ \sum\limits_{\mathrm{k=0}}^{\mathrm{N_{fault\_models}}}\mathrm{P_{HMI\_VERT,k}}\le\mathrm{P_{HMI\_VERT}}\end{cases}\end{aligned} \tag{7-28}$$

Similarly, the optimization function of HPL is established as

$$\begin{aligned}&\min\ \mathrm{HPL}\left(P_{FA\_HOR,0},P_{FA\_HOR,1},\ldots,P_{FA\_HOR,N_{fault\_models}},\right.\\&\left.P_{HMI\_HOR,0},P_{HMI\_HOR,1},\ldots,P_{HMI\_HOR,N_{fault\_models}}\right)\\&\text{s.t.}\begin{cases}\sum_{k=0}^{N_{fault\_models}}P_{FA\_HOR,k}\le P_{FA\_HOR}\\\sum_{k=0}^{N_{fault\_models}}P_{HMI\_HOR,k}\le P_{HMI\_HOR}\end{cases}\end{aligned}\qquad (7\text{-}29)$$

It is worth noting that the values of $P_{FA\_VERT,0}$ and $P_{FA\_HOR,0}$ are zero since the continuity risk is only assigned to each fault subset except the full fault-free set. The traditional algorithm which assigns the integrity and continuity risks equally to each fault subset assumes that each satellite contributes equally to the positioning error, which is an overly simplistic assumption, especially in complex and changing urban environments where the signal propagation error varies greatly from satellite to satellite. This risk allocation method inevitably leads to overly conservative values for the protection level and affects the availability of ARAIM. A suitable risk allocation strategy can reduce the maximum value of the protection level for a subset of satellites and achieve an optimized protection level. Therefore, the risk allocation for each satellite subset needs to be further optimized in order to reduce the protection level values and improve the availability of ARAIM.

The TLBO algorithm is one of the swarm intelligent optimization algorithms, which models the human learning process to design the algorithm process to obtain the global optimal solution. In this paper, the TLBO algorithm is adopted for optimisation based on the following two considerations: Firstly, since the variables are probability values, their values may tend to be infinitely small, and the solution to a decision variable that is infinitely close to 0 will lead to a singular solution. The choice of an intelligent optimization algorithm is able to solve the optimization function, which can avoid the above problems. Secondly, compared to other intelligent optimization algorithms, the TLBO algorithm has the advantages of fewer parameters, fast solution speed, high accuracy and strong convergence capability. Therefore, in this paper, the TLBO algorithm is chosen to solve the optimization equations, and the penalty function method is used for the adaptation degree calculation.

For the optimization problem $z=\min_{X\in S}f(X)$, the search space is $S=\left\{X\middle|x_m^L\le x_m\le x_m^U,m=1,2,\ldots,D\right\}$, $X=(x_1,x_2,\ldots,x_D)$ is any search point in the space, D denotes the number of design variables (i.e. the dimensionality of the space), x_i^L and x_i^U are the upper and lower bounds of each dimension respectively, and $f(X)$ is the objective function. In the algorithm, the class is the set of all points in the search space; the student is a point in the class, X_i denotes the i-th student; the teacher is the student with the best performance in the class, denoted by $X_{teacher}$; and D is the number of learning subjects. The algorithm is divided into two phases: the teaching phase is about learning from the teacher, and the learning phase is about students learning from each other, thus improving the learning of each individual.

In the protection level optimization problem, the objective function is $f(X)=PL(P)$, where $P=\left(P_{FA,0},P_{FA,1},\ldots,P_{FA,N_{fault\_models}},P_{HMI,0},P_{HMI,1},\ldots,P_{HMI,N_{fault\_models}}\right)$ represents the allocation pattern of continuity risk and integrity risk. The number of variables D is twice the number of fault models, and the upper and lower bounds are the upper and lower bounds of the risk probability of each fault model. For the randomly initialised risk allocation pattern, the protection level obtained for each risk allocation pattern is calculated and the risk allocation pattern corresponding to the optimal protection level is defined as the optimal risk allocation pattern, denoted as $P_{teacher}$, i.e. $P_{teacher}=P_{PL(P)=min}$.

TEACHING PHASE

In the teaching phase, each of the remaining risk allocation models is learned from the optimal risk allocation model, based on the direct difference between the optimal risk allocation model and the mean risk allocation model, as follows:

$$P_i^{new} = P_i^{old} + \text{Difference} \tag{7-30}$$

$$\text{Difference} = r_i \times \left(X_{teacher} - TF_i \times \text{Mean}\right) \tag{7-31}$$

where, P_i^{old} and P_i^{new} are the before-learning and after-learning values of the i-th risk allocation model respectively; $\text{Mean} = (1/NP)\sum_i^{NP} P_i$ is the mean of all risk allocation models; $TF_i = \text{round}\left[1 + \text{rand}(0,1)\right]$ is the teaching factor; and $r_i = \text{rand}(0,1)$ is the random factor, characterizing the learning rate.

LEARNING PHASE

In the learning phase, the i-th risk allocation model $P_i\left(i = 1,2,\ldots,NP\right)$ randomly selects another risk allocation model $P_j\left(j = 1,2,\ldots,NP, j \neq i\right)$, and implements learning by comparing and analyzing the differences between P_i and P_j.The learning process is as follows:

$$P_i^{new} = \begin{cases} P_i^{old} + r_i\left(P_i - P_j\right), PL\left(P_i\right) < PL\left(P_j\right) \\ P_i^{old} + r_i\left(P_j - P_i\right), PL\left(P_j\right) < PL\left(P_i\right) \end{cases} \tag{7-32}$$

Where, $r_i = \text{rand}(0,1)$ denotes the random factor of the risk allocation model P_i.

LEARNING PHASE

The TLBO is introduced into the process of assigning continuity risk and integrity risk according to the protection level optimisation function established in section 0 using the continuity risk and integrity risk assigned to each fault subset as optimization parameters, as follows:

1) Initializing the class: determining the optimization problem and designing the objective function $f(X)$. In the protection level optimization problem, the objective function is $f(X) = PL(P)$. where $P = \left(P_{FA,0}, P_{FA,1}, \ldots, P_{FA,N_{fault\_models}}, P_{HMI,0}, P_{HMI,1}, \ldots, P_{HMI,N_{fault\_models}}\right)$ represents the allocation pattern of continuity risk and integrity risk.

2) Initializing the parameters of the algorithm, i.e. designing the number of populations NP, determining the number of variables D, and the upper and lower bounds for each variable. In this problem, the number of variables D is twice the number of fault models N_{fault_models}.

3) Teaching phase: Calculate the value of the level of protection for each risk allocation model and consider the allocation model with the smallest value as the optimal risk allocation model, i.e. $P_{teacher} = P_{PL(P)=min}$. For the i-th risk allocation model, calculate P_i^{new}. If P_i^{new} has a better fitness value, accept it, otherwise reject it.

4) Learning phase: Randomly select the i-th risk allocation model P_i and the j-th risk allocation model $P_j = \left(P_{FA,0}^j, P_{FA,1}^j, \ldots, P_{FA,N_{fault\_models}}^j, P_{HMI,0}^j, P_{HMI,1}^j, \ldots, P_{HMI,N_{fault\_models}}^j\right)$, and complete mutual learning to obtain P_i^{new}. If P_i^{new} has a better fitness value, accept it, otherwise reject it.

5) Terminal conditions: end if terminal conditions are satisfied, otherwise repeat step 3).

7.3.2. MODEL EVALUATION AND VERIFICATION

In order to verify the usability of the multi-constellation GNSS protection level calculation model designed in this project for aviation approaches, the ARAIM baseline model was selected for comparison with the proposed TLBO-based protection level calculation model, and the software designed in this project was used to simulate the GNSS integrity monitoring function for LPV-200 application scenarios based on GPS, GAL and BDS multi-constellations.

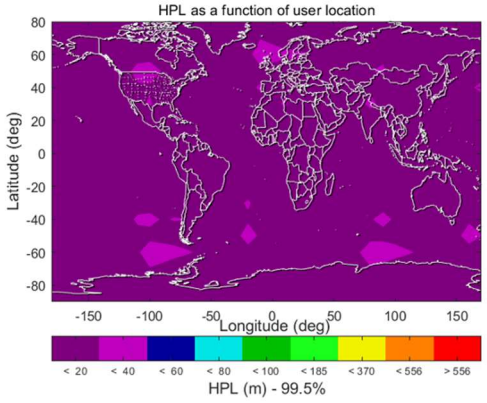

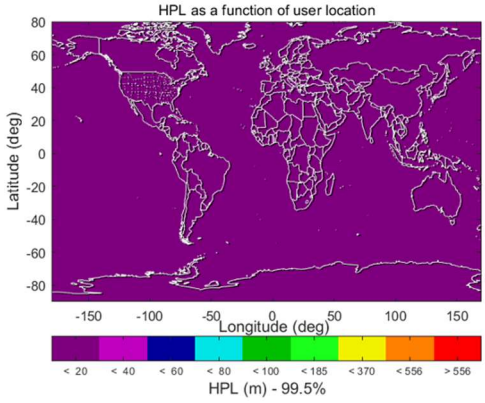

Figure 7-3: a)Global HPL (ARAIM model) **b) Global HPL (Proposed model)**

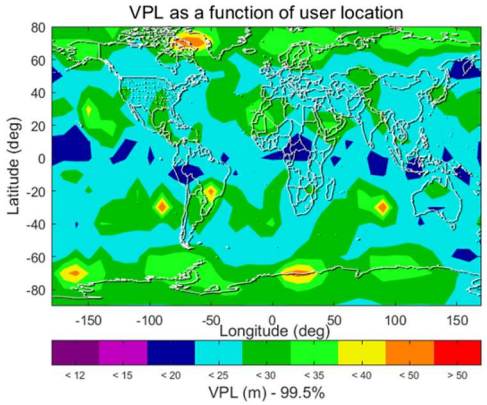

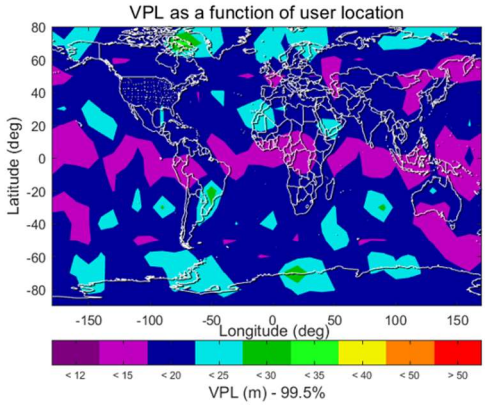

Figure 7-4: a)Global VPL (ARAIM model) **b) Global VPL (Proposed model)**

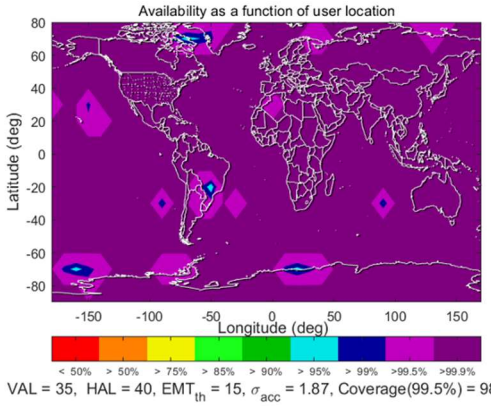

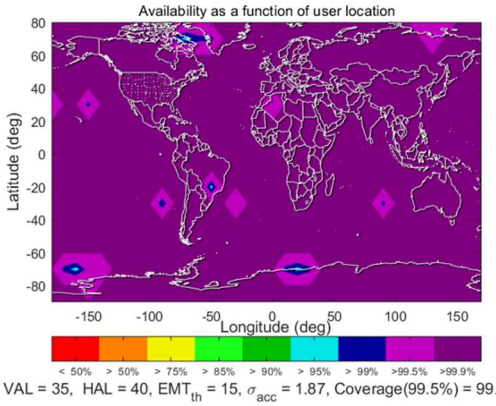

Figure 7-5: a)Global availability (ARAIM model) **b) Global availability (Proposed model)**

As shown in Figure 7-3 and Figure 7-4, using the TLBO-based protection level calculation model can effectively reduce the HPL and VPL, and Figure 7-3 and Figure 7-4 show that the vertical protection level in most areas is less than the vertical alarm threshold of 35 m in LPV-200 and the horizontal protection level in almost all areas is less than the horizontal alarm threshold of 40 m, satisfying the integrity requirements of LPV-200 phase, and proving that the proposed model can effectively separate the vertical protection level and horizontal protection level in different areas and realize the dynamic protection level calculation. Figure 7-5 shows that compared with the ARAIM baseline model, the availability of the model developed in this project has increased by 1.35% and the global availability has reached 99.65%, which proves that the proposed TLBO-based protection level calculation model can enable the global satellite configuration to achieve the integrity monitoring function in most of the locations worldwide.

8. SUMMARY

High-accuracy and high-reliability PNT information is critical for G-ATM. Therefore, multi-constellation GNSS based multi-mode augmentation technology has been developed in this subproject. The contributions are summarized below.

1) The requirement mode of navigation performance for G-ATM was constructed. Specifically, the accuracy and integrity indexes of each stage of flights were determined. The requirement analysis provided basis for the design and validation of the navigation and positioning algorithm supporting G-ATM in this subproject.

2) To deal with the low accuracy and transferability of current GNSS error models, machine learning theory was implemented to obtain GNSS error prediction rules from professional products of IGS. Hence, the GA-BP based ionospheric error model, the GMDH based tropospheric error model and the GBDT based multipath error model were constructed. In the experiment, these error models achieved a GNSS error prediction accuracy of more than 95%.

3) Since traditional fault detection and exclusion (FDE) algorithms are invalid in detecting simultaneous multiple faults, the online dataset based FDE algorithm was proposed. In particular, a sliding window, based on the pseudorange KF innovations from satellites in the normal satellite's dataset, is designed to check satellites maintaining normal data, while detector D, which is generated based on the difference between the predicted pseudorange and the observed pseudorange using data from satellites in the faulty satellite's dataset, is designed for checking faulty satellites or those just coming into view. In the field test, the fault detection rates of the proposed FDE method reached 100% in both single and multiple faults scenarios.

4) Since it is hard to detect minor or ramp faults with current FDE methods. The adaptive noise variance based fault detection algorithm was proposed. Its fault detection and identification statistics are generated based on the real-time observation noise variance matrix estimated from historical innovations with a sliding window. In the dynamic test, the proposed algorithm provided a 100% fault detection rate (FDR) and fault identification rate (FIR) of the minimum single-step error of 3m, and FDR and FIR improvements of over 20% for ramp faults.

5) Based on the proposed GNSS error models and FDE algorithms, the data-driven multi-mode and multi-frequency GNSS positioning model was constructed. The experiments proved that the navigation accuracy requirement of G-ATM was satisfied with the proposed positioning model.

6) The widely acknowledged ARAIM algorithm provides much conservative protection level because the integrity risk and the continuity risk are evenly assigned to each fault mode. It limits GNSS availability in many applications, such as precision approach. Therefore, the TLBO based protection level calculation algorithm was proposed by transforming the risk allocation problem to the single objective and multi-constraint problem. In the simulated experiment, the worldwide GNSS availability for LPV-200 of the proposed model reached 99.65%, with an improvement of over 1.35% compared to ARAIM.

In conclusion, the subproject greatly improves GNSS performance to support G-ATM. The required PNT information will be obtained with the proposed multi-constellation GNSS based multi-mode augmentation technology. This means great contributions for more efficient, safer and greener air traffic.

9. REFERENCES

[AFSC 1997] Command, A. F. S. (1997). Air force space command capstone requirements document for global position, velocity, and time determination capability.

[Bhatti 2007] Bhatti, U. (2007). Improved Integrity Algorithms for the Integrated GPS/INS Systems in the Presence of Slowly Growing Errors. Ph.D. Thesis, 2007, Imperial College London, London, UK.

[Bhatti 2007] Bhatti, U., and Ochieng, W. (2007). Failure modes and models for integrated GPS/INS systems. J. Navig., 2007, 60:327–348.

[Blanch 2010] Blanch, J., Walter, T. and Enge, P. (2010). RAIM with optimal integrity and continuity allocations under multiple failures. IEEE Transactions on Aerospace and Electronic Systems, 46(3), pp. 1235–1247.

[Blanch 2012] Blanch, J., Walter, T., Enge, P. Lee, Y., and Spletter, A. (2012). Advaced RAIM User Algorithm Description: Integrity Support Message Processing, Fault Detection, Exclusion, and Protection Level Calculation. Ion Institute of Navigation Global Navigation Satellite Systems Conference.

[Blanch 2012] Blanch, J., Walter, T., Enge, P., Lee, Y., Pervan, B., Rippl, M. and Spletter, A. (2012). Advanced RAIM user algorithm description: Integrity support message processing, fault detection, exclusion, and protection level calculation. Proceedings of the 25th International Technical Meeting of The Satellite Division of the Institute of Navigation (ION GNSS 2012), pp. 2828–2849.

[Blanch 2013] Blanch, J., Walter, T. and Enge, P. (2013). Optimal positioning for advanced RAIM. Navigation: Journal of the Institute of Navigation, 60(4), pp. 279–289.

[Blanch 2013] Blanch, J., Walter, T., Enge, P., Wallner, S., Amarillo Fernandez, F., Dellago, R., Ioannides, R., Fernandez Hernandez, I., Belabbas, B. and Spletter, A. (2013). Critical Elements for a Multi-Constellation Advanced RAIM. Navigation: Journal of The Institute of Navigation, 60(1), pp. 53–69.

[Blanch 2014] Blanch, J., Walter, T., Enge, P., Pervan, B., Joerger, M., Khanafseh, S., Burns, J., Alexander, K., Boyero, J. P. and Lee, Y.(2014). Architectures for advanced RAIM: Offline and online. Proceedings of the 27th International Technical Meeting of The Satellite Division of the Institute of Navigation (ION GNSS+ 2014), pp. 787–804.

[Blanch 2015] Blanch, J., Walter, T., and Enge, P. (2015). Efficient multiple fault exclusion with a large number of pseudorange measurements. Proceedings of the2015 International Technical Meeting of the Institute of Navigation, Dana Point, California, January, 2015, 696-701.

[Blanch 2018] Blanch, J., Walter, T. and Enge, P. (2018). Fixed Subset Selection to Reduce Advanced RAIM Complexity. Proceedings of the 2018 International Technical Meeting of The Institute of Navigation, pp. 88–98.

[Böhm 2015] Böhm, J. Möller, G. Schindelegger, M. Pain, G. and Weber, R. (2015). Development of an improved empirical model for slant delays in the troposphere (GPT2w). GPS solutions, 19(3), 433-441.

[Brown 1988] Brown, R. G. and McBurney, P. W. (1988). Self-Contained GPS Integrity Check Using Maximum Solution Separation. Navigation, 35(1), pp. 41–53.

[Brown 1992] Brown, R.G. (1992). A Baseline GPS RAIM Scheme and a Note on the Equivalence of Three RAIM Methods. Navigation 39(3): pp. 301–316.

[Brown 1997] Brown, R. (1997). Solution of the Two-Failure GPS RAIM Problem under Worst-Case Bias Conditions: Parity Space Approach. Navigation, 1997, 44:425-431.

[CAAC 2009] CAAC. (2009). Performance Based Navigation Implementation Roadmap for Civil Aviation of China.

[CHEN 2011] Chen, P. Yao, Y. and Wu, H. (2011). Prediction of Ionospheric TEC by time series analysis [J]. Journal of Wuhan University (Information Science Edition), 2011,36 (03): 267-270.

[Choi 2011] Choi, M., Blanch, J., Akos, D., Heng, L., Gao, G., Walter, T. and Enge, P. (2011). Demonstrations of multi-constellation advanced RAIM for vertical guidance using GPS and GLONASS signals. Proceedings of the 24th International Technical Meeting of The Satellite Division of the Institute of Navigation (ION GNSS 2011), pp. 3227–3234.

[Choi 2012] Choi, M., Blanch, J., Walter, T., Akos, D. and Enge, P. (2012). Evaluation of multi-constellation advanced RAIM for vertical guidance using GPS and GLONASS signals with multiple faults. Proceedings of the 25th International Technical Meeting of the Satellite Division of the Institute of Navigation (ION GNSS 2012), pp. 884–892.

[Deng 2014] Deng, C., Tang, W., Liu, J. and Shi, C. (2014). Reliable single-epoch ambiguity resolution for short baselines using combined GPS/BeiDou system. GPS Solutions, 18(3), pp. 375–386.

[DOD 2019] DOD. DOHS. DOT. (2019). 2019 Federal Radio Navigation Plan.

[DOD. 2008] DOD. (2008). CSO.

[El-Mowafy 2013] El-Mowafy, A. (2013). ARAIM for vertical guidance using GPS and BeiDou. Journal of Global Positioning Systems, 12(1), pp. 28–37.

[El-Mowafy 2016] El-Mowafy, A. (2016). Pilot evaluation of integrating GLONASS, Galileo and BeiDou with GPS in ARAIM. Artificial Satellites, 51(1), pp. 31–44.

[El-Mowafy 2016] El-Mowafy, A. and Yang, C. (2016). Limited sensitivity analysis of ARAIM availability for LPV-200 over Australia using real data. Advances in Space Research, 57(2), pp. 659–670.

[El-Mowafy 2017] El-Mowafy, A. (2017). Advanced receiver autonomous integrity monitoring using triple frequency data with a focus on treatment of biases. Advances in Space Research, 59(8), pp. 2148–2157.

[Enge 1996] Enge, P. Parkinson, B. Spilker Jr, J. and Axelrad, P. (1996). Global Positioning System: Theory and Applications, 2-Volume Set. American Institute of Aeronautics and Astronautics, Inc.

[FAA 1984] FAA. (1984). Criteria for Approach of Category III Landing Weather Minima(Advisory Circular).

[FAA 2002] FAA. (2002). Criteria for approval of Category I and Category II weather minima for approach.

[Feng 2012] Feng, S. (2012). Integrity Monitoring for GNSS. Shanghai Jiao Tong University.

[Gan 2008] Gan, X. (2008). Research on Perfect Monitoring Technology of GPS Local Area Augmentation System. Harbin Engineering University. Harbin, China.

[Gates 2011] Gates, R, M. La Hood, R, Napolitano J. (2011). 2010 Federal Radionavigation Plan[R]. John A. Volpe National Transportation Systems Center (US).

[Geng 2021] Geng, T., Ding, Z., Xie, X. and Lv, Y (2021). Accuracy Assessment of Multi-frequency and Multi-GNSS Velocity Estimation With Time Differenced Carrier Phase Method. Geomatics and Information Science of Wuhan University, pp. 0-0

[Groves 2011] Groves, P, D. (2011). Shadow matching: A new GNSS positioning technique for urban canyons[J]. Journal of Navigation, 2011, 64(3): 417-430.

[Groves 2013] Groves, P. D., Jiang, Z., Rudi, M., and Strode, P. (2013). A Portfolio Approach to NLOS and Multipath Mitigation in Dense Urban Areas. Proceedings of the 26th International Technical Meeting of the Satellite Division of the Institute of Navigation (ION GNSS+ 2013), Nashville, TN, September 2013, 3231-3247.

[Groves 2015] Groves, P.D. (2015). Principles of GNSS, inertial, and multisensor integrated navigation systems. Artech House.

[Han 2021] Han, Q., Wang, L., Luo, S., Shu, B. and Yue, C. (2021). Optimal allocation of risk probability based on ARAIM algorithm. Acta Geodaetica et Cartographica Sinica, 50(12), pp. 1751-1761.

[He 2014] He, H., Li, J., Yang, Y., Xu, J., Guo, H. and Wang, A. (2014). Performance assessment of single-and dual-frequency BeiDou/GPS single-epoch kinematic positioning. GPS Solutions, 18(3), pp. 393–403.

[Heinrichs 2004] Heinrichs, G. Lemke, N. Schmit, A. Neubauer, A. Kronberger, R. Rohmer, G. and Weigel, R. (2004). Galileo/GPS receiver architecture for high sensitivity acquisition. In Proc. of the International Symposium on Signals, Systems, and Electronics (ISSSE'04).

[Hewitson 2003] Hewitson, S. (2003). GNSS receiver autonomous integrity monitoring: A separability analysis. Proceedings of the 16th International Technical Meeting of the Satellite Division of The Institute of Navigation. 2003: 1502-1509.

[Hewitson 2004] Hewitson, S. Lee, H, K.and Wang, J. (2004). Localizability analysis for GPS/Galileo receiver autonomous integrity monitoring. The journal of Navigation, 2004, 57(2): 245-259.

[Hewitson 2006] Hewitson, S. (2006). Quality control for integrated GNSS and inertial navigation systems. UNSW, Sydney.

[Hewitson 2006] Hewitson, S. and Wang, J. (2006). GNSS Receiver Autonomous Integrity Monitoring (RAIM) Performance Analysis. GPS Solutions, 2006, 10(3): 155-170.

[Hopfield 1969] Hopfield H S. (1969). Two-quadratic Tropospheric Refractivity Profile for Correction Satellite Data[J]. Journal of Geophysical Research, 1969, 74(18):4487-4499.

[Hopfield 1971] Hopfiled H S. (1971). Tropospheric effect on electromagnetically measured range: Prediction from surface weather data[J]. Radio Science, 1971, 6(3):357-367.

[Hsu 2017] Hsu Li-Ta. (2017). GNSS multipath detection using a machine learning approach[C]. 2017 IEEE 20th International Conference on Intelligent Transportation Systems (ITSC). IEEE.

[Hsu 2017] Hsu, L. T., Tokura, H., Kubo, N., Gu, Y., and Kamijo, S. (2017). Multiple faulty gnss measurement exclusion based on consistency check in urban canyons. IEEE Sensors Journal,2017,99, 1-1.

[ICAO 2006] ICAO Navigation Systems Panel (NSP) A. (2006). International standards and recommended practices. aeronautical telecommunications (annex 10 to the convention on international civil aviation). volume I (radio navigation aids), sixth edition.

[ICAO 2008] International Civil Aviation Organization (2008). Performance-based Navigation (PBN) Manual. International Civil Aviation Organization.

[Ilcev 2011] Ilcev, D. S. (2011). Development and characteristics of African satellite augmentation system (ASAS) network. Telecommunication Systems, 52(1), 121-137.

[Jiang 2014] Jiang, Y. and Wang, J. (2014). A new approach to calculate the vertical protection level in A-RAIM. The Journal of Navigation, 67(4), pp. 711–725.

[Jin 2011] Jin, D. Jing, Z. and Wang, G. (2011). Avionics system for civil aircraft. Shanghai Jiao Tong University Press.

[Jing 2012] Jing, S., Zhan, X. and Su, X. (2012). Exploration of Advanced RAIM to Provide LPV-200 Service. Measurement & Control Technology, 31(11), pp. 75–79.

[Joerger 2013] Joerger, M., Stevanovic, S., Chan, F.-C., Langel, S. and Pervan, B. (2013). Integrity risk and continuity risk for fault detection and exclusion using solution separation ARAIM. Proceedings of the 26th International Technical Meeting of the Satellite Division of The Institute of Navigation (ION GNSS+ 2013), pp. 2702–2722.

[Joerger 2020] Joerger, M. and Pervan, B. (2020). Multi-constellation ARAIM exploiting satellite motion. Navigation, 67(2), pp. 235–253.

[Kaddour 2015] Kaddour, M., El Najjar, M. E., Naja, Z., Tmazirte, N. A., and Moubayed, N. (2015). Fault detection and exclusion for GNSS measurements using observations projection on information space. Fifth International Conference on Digital Information & Communication Technology& Its Applications. IEEE.2015.

[Kaplan 2017] Kaplan, E. D. and Hegarty, C. (Eds.). (2017). Understanding GPS/GNSS: Principles and applications. Artech house.

[KuusniemiH 2004] Kuusniemi, H., and Lachapelle, G. (2004). GNSS signal reliability testing in urban and indoor environments. Proc. ION NTM, 1-15, Aug., 2004.

[Lagler 2013] Lagler, K., Schindelegger, M., Böhm, J., Krásná, H., & Nilsson, T. (2013). GPT2: Empirical slant delay model for radio space geodetic techniques. Geophysical research letters, 40(6), 1069-1073.

[Lee 1986] Lee, Y, C. (1986) Analysis of Range and Position Comparison Methods as A Means to Provide GPS Integrity in the User Receiver.

[Lee 1986] Lee, Y.C. (1986). Analysis of range and position comparison methods as a means to provide GPS integrity in the user receiver. In Proceedings of the 42nd Annual Meeting of the Institute of Navigation (pp. 1-4).

[Lee 2004] Lee, Y. (2004). Analysis of Range and Position Comparison Methods as a Means to Provide GPS Integrity in the User Receiver. Proceedings of the 42nd Annual Meeting of the Institute of Navigation, Seattle, Washington, USA, 24-26, June, 2004.

[Li 2010] Li, S, H. (2010). Research on GPS ionospheric prediction based on chaos theory [D]. China University of Geosciences (Beijing), 2010.

[Li 2011] Li, L., Zhong, J. and Zhao, M. (2011). Doppler-aided GNSS position estimation with weighted least squares. IEEE Transactions on Vehicular Technology, 60(8), pp. 3615–3624.

[Li 2012] Li, L. (2012). Research on Positioning and Integrity Monitoring Technology of Ground-Based Augmentation System. Harbin Engineering University. Harbin, China.

[Li 2012] Li, W. Yuan, Y. Ou, J. Li, H. and Li, Z. (2012). A new global zenith tropospheric delay model IGGtrop for GNSS applications. Chinese science bulletin, 57(17), 2132-2139.

[Li 2013] Li, S, H. PENG, J, H. and XU, W, C. (2013). Prediction of short-term Ionospheric TEC changes using neural network [J]. Surveying and Mapping Science,38 (01): 8-9 + 12.

[Li 2015] Li, W. Yuan, Y. Ou, J. Chai, Y. Li, Z. Liou, Y. A. and Wang, N. (2015). New versions of the BDS/GNSS zenith tropospheric delay model IGGtrop. Journal of geodesy, 89(1), 73-80.

[Li 2021] LI, Y, T. ZHAO, A. and Li, J, W. (2021). Modeling and accuracy analysis of Ionospheric TEC in single station area [J/OL]. Journal of Wuhan University (Information Science Edition), {3}, {4} {5}: 1-12.

[Liu 2010] Liu, X, D. Song, L, J.and Yang, X, H. (2010). Ionospheric TEC short-term prediction based on wavelet neural network [J]. Marine surveying and mapping, 2010,30 (05): 49-51 + 55.

[Liu 2018] Liu, C. and Li, F. (2018). Comparison and analysis of different GNSS weighting methods. Science of Surveying and Mapping, 43(8), pp. 39–44.

[Luo 2020] Luo, S., Wang, L., Tu, R., Zhang, W., Wei, J. and Chen, C. (2020). Satellite selection methods for multi-constellation advanced RAIM advanced RAIM. Advances in Space Research, 65(5), pp. 1503–1517.

[Manesh 2017] Manesh, M.R. and Kaabouch N. (2017). Analysis of vulnerabilities, attacks, countermeasures and overall risk of the Automatic Dependent Surveillance-Broadcast (ADS-B) system. International Journal of Critical Infrastructure Protection 19: pp. 16-31.

[McGraw 1999] McGraw, G. A. and Braasch, M. S. (1999). GNSS multipath mitigation using gated and high resolution correlator concepts. In Proceedings of the 1999 national technical meeting of the institute of navigation (pp. 333-342).

[Meguro 2009] Meguro, J. I. Murata, T. Takiguchi, J. I. Amano, Y. and Hashizume, T. (2009). GPS multipath mitigation for urban area using omnidirectional infrared camera. IEEE Transactions on Intelligent Transportation Systems, 10(1), 22-30.

[Ober 2004] Ober, P. B. (2004). Integrity prediction and monitoring of navigation systems.

[Ochieng 2002] Ochieng, W. Y. Sheridan, K. F. Sauer, K. Han, X. Cross, P. A. Lannelongue, S. and Petit, K. (2002). An assessment of the RAIM performance of a combined Galileo/GPS navigation system using the marginally detectable errors (MDE) algorithm. GPS Solutions, 5(3), 42-51.

[Odolinski 2015] Odolinski, R., Teunissen, P.J.G. and Odijk, D. (2015). Combined BDS, Galileo, QZSS and GPS single-frequency RTK. GPS solutions, 19(1): pp. 151-163.

[Odolinski 2016] Odolinski, R., Teunissen, P. J. and Odijk, D. (2016). Combined GPS, BeiDou, Galileo, and QZSS single-epoch, single-frequency RTK performance analysis. 150th Anniversary with a Scientific Assembly, IAG 2013, pp. 643–649.

[Pan 2017] Pan, J., and Yang, M. (2017). Application of Robust Sequential LSQ Method in GNSS Positioning, Modern Surveying and Mapping, 2, pp. 30–32.

[Panel 2010] Panel, G. (2010). GNSS Evolutionary Architecture Study (GEAS) Phase II Panel Report. US: FAA, pp. 10–12.

[Parkinson 1988] Parkinson, B. and Axelrad, P. (1988) Autonomous GPS Integrity Monitoring Using the Pseudorange Residual. Navigation 35: pp. 255–274.

[Paziewski 2014] Paziewski, J. and Wielgosz, P. (2014). Assessment of GPS+ Galileo and multi-frequency Galileo single-epoch precise positioning with network corrections. Gps Solutions, 18(4), pp. 571–579.

[Pirti 2010] Pirti, A., Gümüş, K., Erkaya, H. and Hoşbaş, R. G. (2010). Evaluating repeatability of RTK GPS/GLONASS near/under forest environment. Croatian Journal of Forest Engineering: Journal for Theory and Application of Forestry Engineering, 31(1), pp. 23–33.

[Qu 1999] Qu, J, K. (1999). Reliability study of relevant observations [J] Journal of Surveying and Mapping, 28 (3): 6

[Rippl 2011] Rippl, M., Spleter, A. and Günther, C. (2011). Parametric performance study of advanced receiver autonomous integrity monitoring (ARAIM) for combined GNSS constellations. Proceedings of the 2011 International Technical Meeting of The Institute of Navigation, pp. 285–295.

[Rippl 2012] Rippl, M. (2012). Real Time Advanced Receiver Autonomous Integrity Monitoring in DLR's Multi-Antenna GNSS Receiver. Proceedings of the 2012 International Technical Meeting of The Institute of Navigation, pp. 1767–1776.

[RNPSORSG 2007] (RNPSORSG) IRSORSG. (2007). Performance Based Navigation Manual, Volume I (Concept and Implementation Guidance) Working Draft 5.1 – Final.

[Saastamoinen 1972] Saastamoinen, J. (1972). Atmospheric correction for the troposphere and stratosphere in radio ranging satellites. The use of artificial satellites for geodesy, 15, 247-251.

[Schüler 2013] Schüler, T. (2014). The TropGrid2 standard tropospheric correction model. GPS solutions, 18(1), 123-131.

[Socharoentum 2016] Socharoentum, M. Karimi, H. A. and Deng, Y. (2016). A machine learning approach to detect non-line-of-sight GNSS signals in Nav2Nav. In 23rd ITS World Congress (pp. 10-14).

[Soloviev 2008] Soloviev, A. and van Graas, F. (2008). Utilizing multipath reflections in deeply integrated GPS/INS architecture for navigation in urban environments. In 2008 IEEE/ION Position, Location and Navigation Symposium (pp. 383-393). IEEE.

[Song 2011] Song, S. Zhu, W. Chen, Q. and Liou, Y. (2011). Establishment of a new tropospheric delay correction model over China area. Science China Physics, Mechanics and Astronomy, 54(12), 2271-2283.

[Song 2017] Song, K. (2017). Research on GNSS Integrity Monitoring Algorithm. Doctoral thesis. Navigation Guidance and Control, Nanjing University of Aeronautics and Astronautics.

[Sturza 1988] Sturza, M. (1988). Navigation System Integrity Monitoring Using Redundant Measurements. Navigation, 35: pp.483–501.

[Sturza 1988] Sturza, M. A. (1988). Navigation system integrity monitoring using redundant measurements. Navigation, 35(4), 483-501.

[Su 2010] Su, X. L., Zhan, X., & Fang, H. (2010). Receiver autonomous integrity monitoring for GPS attitude determination with carrier phase FD/FDE algorithms. In Proceedings of the 23rd International Technical Meeting of the Satellite Division of The Institute of Navigation (ION GNSS 2010) (pp. 2168-2181).

[Tang 2019] Tang, H. Tang, S, H. and Chen, Y, T. (2019). Comparison of Holt winters and ARIMA models in the prediction of Ionospheric Total Electron Content [J]. Journal of Guilin University of technology, v.39 (04): 128-134.

[Thornberg 2003] Thornberg, D. B. Thornberg, D. S. DiBenedetto, M. F. Braasch, M. S. Van Graas, F. and Bartone, C. (2003). LAAS integrated multipath - limiting antenna. Navigation, 50(2), 117-130.

[Townsend 1994] Townsend, B. and Fenton, P. (1994). A practical approach to the reduction of pseudorange multipath errors in a L1 GPS receiver. In Proceedings of the 7th International Technical Meeting of the Satellite Division of the Institute of Navigation, Salt Lake City, UT, USA (pp. 20-23).

[Townsend 1995] Townsend, B. R., Fenton, P. C., Van Dierendonck, K. J., & Van Nee, D. R. (1995). Performance evaluation of the multipath estimating delay lock loop. Navigation, 42(3), 502-514.

[Van Dierendonck 1992] Van Dierendonck, A. J. Fenton, P. and Ford, T. (1992). Theory and performance of narrow correlator spacing in a GPS receiver. Navigation, 39(3), 265-283.

[Walter 2014] Walter, T., Blanch, J. and Enge, P. (2014). Reduced subset analysis for multi-constellation ARAIM. Proceedings of the 2014 International Technical Meeting of The Institute of Navigation, pp. 89–98.

[Wang 2013] Wang, D. (2013). Research on Performance Based Navigation (PBN) technology. Modern Navigation 23(1):5-10.

[Wang 2013] Wang, L. Groves, P. D. and Ziebart, M. K. (2013). GNSS shadow matching: Improving urban positioning accuracy using a 3D city model with optimized visibility scoring scheme. NAVIGATION: Journal of the Institute of Navigation, 60(3), 195-207.

[Wang 2015] Wang, L., Groves, P., and Ziebart, M. (2015). Smartphone Shadow Matching for Better Cross-street GNSS Positioning in Urban Environments. Journal of Navigation, 2015, 68(3):411-433.

[Wang 2015] Wang, L., Li, Z., Yuan, H. and Zhou, K. (2015). Validation and analysis of the performance of dual-frequency single-epoch BDS/GPS/GLONASS relative positioning. Chinese Science Bulletin, 9, pp. 857–868.

[Wang 2016] WANG S H. (2016). Study on regional ionospheric delay correction and prediction model [D]. SouthEast University,2016.

[Wang 2016] Wang, Y, D. (2016).Study on integrity monitoring technology of Beidou satellite foundation enhancement system [D]. Shenyang University of Aeronautics and Astronautics.

[Wang 2018] Wang, T. (2018). The Research on Algorithm of Total Least Squares in Combined Point Positioning of GNSS. Dissertation in Geodesy and Surveying Engineering, Anhui University of Science and Technology.

[Wang 2019] Wang, E., Sun, C., Tong, G., Guo, J., Wang, C. and Qu, P. (2021). Optimization method of multi-constellation GNSS vertical protection level based on particle swarm optimization algorithm. Journal of Beijing University of Aeronautics and Astronautics, 47(11), pp. 2175-2180.

[Wang 2019] Wang, E., Yang, D., Hong, C., Qu, P., Lan, X., Wang, C. and Pang, T. (2019). Research progress of ARAIM technology. Telecommunications Science, 35(8), pp. 128–138.

[Wang 2022] Wang, C., Yi, K., Li, R. and Teng, J. (2022). Global availability analysis of ARAIM algorithm in multiple constellations. Journal of Navigation and Positioning, 10(3), pp. 101-109.

[Wei 2014] Wei C, J. (2014). Ionospheric delay correction based on ground-based GNSS observation data [D]. Chang'an University, 2014.

[Weill 2002] Weill, L. and Fisher, B. (2002). U.S. Patent No. 6,370,207. Washington, DC: U.S. Patent and Trademark Office.

[Wieser 2000] Wieser, A., and Brunner, F. (2000). An extended weight model for GPS phase observations. Earth Planets Space, 2000, 52: 777-782.

[Wu 2013] Wu, Y., Wang, J. and Jiang, Y. (2013). Advanced receiver autonomous integrity monitoring (ARAIM) schemes with GNSS time offsets. Advances in Space Research, 52(1), pp. 52–61.

[Xie 2017] Xie, S, F. Chen, J. and Huang, L, K. (2017). Prediction of Ionospheric Total Electron Content Based on Holt-winters [J]. Geodesy and geodynamics, 37 (01): 72-76.

[Yang 2010] Yang, Y, X. (2010). Progress, contribution and challenge of Beidou satellite navigation system [J]. Journal of Surveying and Mapping,39(1): 1-6.

[Yao 2015] Yao, Y. Hu, Y. and Yu, C. (2015). An improved global zenith tropospheric delay model. Acta Geodaetica et Cartographica Sinica, 44(3), 242.

[Yu 2017] Yu, G. Zhang, B, H. and Lu, S, Y. (2017). Study on the integrity enhancement technology of Beidou GBAS assisted by pseudosatellite [J]. Surveying and Mapping Bulletin, (9): 1-5.

[Yuan 2018] Yuan, T, J. Chen, Y, H. and Liu, S, Q. (2018). Empirical prediction model of Ionospheric Total Electron Content Based on deep learning recurrent neural network [J]. Journal of space science,38 (01): 48-57.

[Zhai 2019] Zhai, Y., Zhan, X., Chang, J. and Pervan, B. (2019). ARAIM with more than two constellations. Proceedings of the ION 2019 Pacific PNT Meeting, pp. 925–941.

[Zhang 2001] Zhang, X, H. Li, Z, H. and Cai, C, S. (2001). Study on establishing small area ionospheric delay model with dual frequency GPS observations [J]. Journal of Wuhan University (Information Science Edition), {4} (02): 140-143 + 159.

[Zhang 2012] Zhang, L. (2012). Research on Ionospheric TEC prediction based on time series, neural network, grey and combined prediction [D]. Nanjing University of information engineering.

[Zhang 2014] Zhang, X, H. Ren, X, D. and Wu, F, B. (2014). Short term prediction of Ionospheric Total Electron Content Based on autoregressive moving average model [J]. Journal of Surveying and mapping, 43 (02): 118-124.

[Zhang 2021] Zhang, F, B. Zhou, C. and Wang, C. (2021). Global Ionospheric TEC prediction based on deep learning [J / OL]. Journal of radio wave science, 36(4), 553-561.

[Zhao 2015] Zhao, J, Y. Song, S, L. and Chen, Q, M. (2015). A New Global Tropospheric Zenith Delay Model GZTD [J] Journal of Geophysics, 56 (07): 2218-2227.

[Zheng 2018] Zheng, X., Xu, C., Fan, G. and Zhao, J. Multi-Constellation Protection Level Optimization Method Using Genetic Algorithm. Transactions of Beijing institute of Technology, 38(10), pp. 1046-1050

[Zhu 2015] Zhu, Y, X. Feng, L, P. Jia, X, L. Zhang, Q, H. and Ruan, R, Q. (2015). PPP accuracy analysis of Beidou regional navigation system [J]. Journal of Surveying and Mapping, 44(04): 377-383.

[Zhu 2018] Zhu, N. Marais, J. Bétaille, D. and Berbineau, M. (2018). GNSS position integrity in urban environments: A review of literature. IEEE Transactions on Intelligent Transportation Systems, 19(9), 2762-2778.